UNIVERSITY OF OKLAHOMA

GRADUATE COLLEGE

BUOYANCY-INDUCED HEAT AND MASS TRANSPORT

IN A POROUS MEDIUM NEAR A BURIED PIPE

A DISSERTATION

SUBMITTED TO THE GRADUATE FACULTY

in partial fulfillment of the requirements for the

degree of

Doctor of Philosophy

By

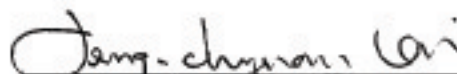CHEAN CHIN NGO
Norman, Oklahoma
2006

UMI Number: 3238557

UMI®
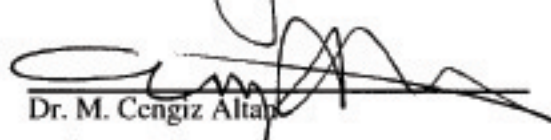
BUOYANCY-INDUCED HEAT AND MASS TRANSPORT
IN A POROUS MEDIUM NEAR A BURIED PIPE

A DISSERTATION APPROVED FOR THE
SCHOOL OF AEROSPACE AND MECHANICAL ENGINEERING

BY

_____
Dr. Feng Chyuan Lai (Chair)

_____
Dr. M. Cengiz Altan

_____
Dr. Rong Zhu Gan

_____
Dr. Ramkumar Parthasarathy

_____
Dr. Dimitrious V. Papavassiliou
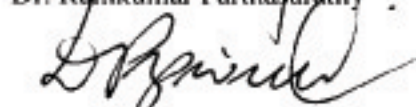
To
my wonderful parents
with love

ACKNOWLEDGMENT

TABLE OF CONTENTS

LIST OF TABLES

LIST OF FIGURES

ABSTRACT

The heat and mass transport in a porous medium induced by buoyancy from a buried heated pipe has been examined in this study. Due to the complexity and irregularity of geometry involved, body-fitted coordinate systems along with finite difference scheme were employed. First, the solutions for conduction and natural convection in a homogeneous porous medium were obtained and compared with the results available in the literature.

Realizing that the properties of porous medium immediate around the pipe are usually different from those of the surrounding medium, the objective of this particular study is to investigate how a step change in the permeability of the backfill would affect the flow patterns and heat transfer results. Numerical solutions have been obtained for natural convection in a heterogeneous porous medium induced by a buried heated pipe. The concept of imaginary nodal points has been used to derive the interface conditions. A wide range of governing parameters (e.g., base Rayleigh number and permeability ratio) for various backfill thicknesses have been covered in the computations. It is found that a more permeable backfill can minimize the heat loss and confine the flow to a region near the pipe.

Another area of interest is to predict how heat and mass transport when there is a breakage in the pipe. Numerical solutions are thus obtained for combined heat and mass transfer by mixed convection induced from a buried pipe with leakage. Two locations of leakage are considered in this study: one is on top of the pipe and the other is at the bottom of the pipe. The effects of Rayleigh number, Peclet number, Lewis number, and buoyancy ratio on the heat and mass transfer results have been

examined. The results suggest that both the Nusselt number and Sherwood number increase for the aiding flows and decrease for the opposing flows. For aiding flows, Sherwood number increases with an increase in the Lewis number but Nusselt number behaves otherwise.

Flow visualization experiments were conducted using two Hele-Shaw cells, which simulated a porous medium with distinct permeabilities, subjected to different pipe temperature for both permeable and impermeable top boundaries. Using time-elapsed photographs, it revealed that the flow fields for permeable and impermeable top boundaries displayed distinct characteristics. The flow fields predicted by numerical work for the impermeable top boundary were in good agreement with those observed in experiment.

CHAPTER I

INTRODUCTION AND LITERATURE REVIEW

1.1 Introduction

Porous materials are frequently encountered in our daily life. With a closer look, one realizes that from natural to manmade materials, a great constituent part of these materials are porous media. Examples of porous media include sand, crushed rocks, soils, fabrics, and biological tissues. Hence, one should not be surprised to find that heat transfer and fluid flow in porous media is involved in various applications of engineering disciplines such as agriculture, geological, petroleum, environmental, and mechanical engineering.

One of the oldest disciplines, which involves transport phenomena in porous media, is perhaps the soil physics. The knowledge of soil structure and its properties, air and water infiltration in soil, and uptake of soil moisture by plants are all parts of the study in soil physics (Hillel, 1982; Reddi and Inyang, 2000; Reddi, 2003). The study of soil physics is closely related to the applications in agricultural sector. From an agricultural engineer standpoint, crops production is directly related to water irrigation, as for how effective water is delivered and supplied to meet the needs of plant growth. Water irrigation is essential for countries with dry climates. Presently 70% of the global fresh water is accounted for irrigation usage according to the World Water Report (Ehrenman, 2003). Due in part to the increase of world populations and the pressure of producing more crops, the demand for water usage in irrigation is

expected to increase continuously. So is the increasing competition for freshwater from the industrial and domestic usage. Therefore, it is the responsibility for agricultural engineers to design and build more effective irrigation systems which consume less water. One possible technique is subsurface irrigation through perforated pipes for avoiding open water loss from evaporation (Withers and Vipond, 1980). In addition to water irrigation, drainage system and infrastructure to remove excess water from the agricultural land to prevent flooding, water-logging and salinity is equally important. Understanding the transport phenomena in soil is certainly beneficial for designing such water irrigation or drainage infrastructures.

Freshwater is one of the most precious resources on earth, and the soils underneath the earth are saturated with water. The task of exploring the presence and distributions of groundwater or aquifers lies in the hands of hydrologists and geological engineers. Monitoring and predicting the migration of the groundwater relies on our understanding of flow through porous media. For example, Donaldson (1962) examined convective water flows in the upper layers of the earth's crust. Geothermal reservoirs, where invaluable heat can be extracted economically for power generation or process heat, also exist underground. Countries such as the United States (e.g., the Geysers in northern California), Italy, New Zealand and Japan have converted geothermal energy to electricity through hydrothermal power plants. An alternative energy source such as geothermal energy relieves the burden of our dependence on fossil fuels. In such application, temperature becomes an important parameter in determining the capacity and useful lifespan of the geothermal reservoir. A more detailed discussion on geothermal energy resources is provided in a handbook

by Edwards et al. (1982).

In addition to water resources, invaluable energy resources such as crude oil or natural gas can also be found underneath the earth. To harvest the crude oil, oil is first driven from a reservoir to oil wells purely based on the existing high hydrostatics pressure inside the reservoir. This is referred to as the primary technique, and it generally accounts for the production of roughly 25% of the oil existing in the reservoir. The secondary technique involves the injection of fluid into the reservoir to maintain the reservoir pressure and further increases the oil production. In order to increase the extraction rate from oil fields, tertiary enhanced oil recovery (EOR) techniques (Schumacher, 1978 and Boberg, 1988) such as miscible flooding and thermal recovery are often employed. Take thermal recovery technique for example. The basic idea of this technique is to reduce the viscosity of oil by adding heat accompanied the gas or water injection, and thus increase the amount of oil displaced from the reservoir. The simulation and modeling of the oil reservoir obviously has become more complicated as it involves multiphase flow (Wang and Cheng, 1997), nevertheless it is still a transport phenomenon in porous media.

As the world's industries are booming and expanding, pollution gradually becomes a major concern and presents a threat to human health. As noted by Ehrenman (2003), pollution is one critical factor for the decline in the availability of freshwater resources. The transfer of pollutants from hazardous waste sites (e.g., municipal dump sites or underground nuclear waste repositories) and sanitary landfills to water aquifers or the irrigation backflow of pesticides and fertilizers from the agricultural runoff are undesirable. Sometimes the water source itself may have

contaminated with waterborne viruses. If the water is not properly treated before consumption, human is then exposed to the risks of viral disease outbreaks. In addition, hazardous waste materials and toxic substances from the industry may be introduced to the environment accidentally and threatened the quality of our lives. Environmental engineers are interested in understanding the transport of contaminants or pollutants in soil and how to safeguard us from the pollutants.

When the soil or groundwater has been contaminated, restoration and remediation processes are needed in the contaminated site for the protection of human health. In-situ techniques are often preferred over ex-situ techniques to avoid large scale excavation and transportation of contaminated soils for clean-up. Smith and Hinchee (1993) provided a summary of the in-situ thermal technologies presently available for site remediation. The review article of Dhir (2000) focuses on the remediation of soils contaminated with hydrocarbons due to oil spills. Species and solute transport as well as heat transfer in soil become an important issue for these treatments (Yong et al., 1992; Knox et al., 1993).

For applications in mechanical engineering, porous media are often found in insulation and barrier materials. Take the transportation of crude oil through buried pipelines for example. In order to reduce the pumping load and cost, crude oil is often heated to a higher temperature to reduce its viscosity for transport, and the pipelines are often surrounded by an insulation layer to reduce heat loss. For underground disposal of nuclear waste, natural and engineered barriers are often employed to prevent radiation leak. Transport phenomena in porous media also find its application in soil heating. In regions with cold climates, heated pipes are used to

prevent soil freezing. Fritton and Martsolf (1980) investigated the use of heated buried pipes for soil heating in orchard to prevent frosting. In addition, heat pipes can also be used to prevent the roadway or airport runway from freezing. The modeling for such applications is much more complicated and challenging due to the phase change in porous media.

The above-mentioned are just several examples of transport phenomena in porous media involved in various engineering disciplines. Other engineering applications, which involve porous media, include sintered bearings in tribology and lubrication (Khonsari and Booser, 2001), drying process and technology (Whitaker, 1998), and porous electrodes in fuel cell (Bejan et al., 2004). In addition, porous media also find applications in bioengineering. For example, Lew and Fung (1970) examined the possibility of using flow through deformable porous solid to model blood flow in the network of capillary blood vessels. Wulff (1974) modeled tissue as a porous medium and proposed a new bioheat equation which replaced the blood perfusion term in the original bioheat equation (Pennes, 1948) by a modified convective term in terms of Darcy blood velocity. As illustrated, transport phenomena in porous media have endless applications in our real world. A more in-depth discussion of porous media flow in modern technologies is given by Bejan et al. (2004).

1.2 Studies in Porous Media: A Brief Discussion

The study of heat transfer and fluid flow in porous media has received considerable attention in the past few decades, and it has gradually evolved into a

unique field of its own. This is evident through the amount of textbooks and handbooks published in recent years. The general discussion of the subject has been given by Bear (1972), Scheidegger (1974), Collins (1990), Bear and Bachmat (1990), Kaviany (1995), Holzbecher (1998), Nield and Bejan (1999), Vafai (2000), Pop and Ingham (2001), Ingham and Pop (1998, 2002) as well as Bejan et al. (2004). A remarkable account of the history, major milestones and development of the porous media studies in chronological order, has been provided by Kaviany (1995) and Reddi (2003). This section only presents a brief introduction of the study of porous media.

As mentioned in the previous section, the study of transport phenomena in porous media has diverse engineering applications as natural and manmade porous materials are encountered frequently in our daily life. But, what constitutes a porous medium and how to define it? A porous material is a medium consisting of a solid matrix with interconnected voids filled with fluids, as shown in Figure 1.1. Examples of porous materials include soils, sands, and lung tissues. The porosity (ϕ) of a
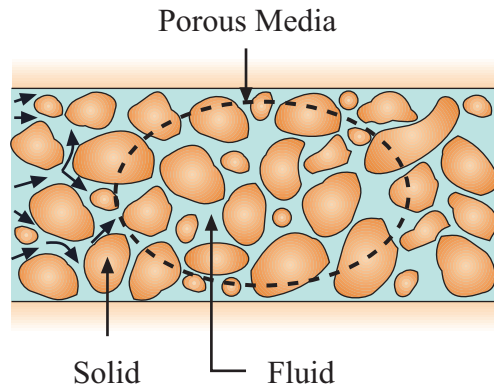
Figure 1.1 Flow through a porous medium.

porous medium is defined as the volume occupied by the voids over the total volume.

$$\phi = \frac{\text{volume of voids}}{\text{total volume}} \qquad [1.1]$$

For packing of uniform spheres, the porosity ranges from 0.255 for rhombohedral packing to 0.476 for cubic packing (Nield and Bejan, 1999).

The most fundamental equation governing fluid flow in porous media was derived by Darcy (1856) while he worked on the public fountains of Dijon in France. An excellent review of Darcy's original report was given by Lage (1998). According to Darcy's law, the volume-averaged velocity ($\mathbf{u}$) is directly proportional to the pressure gradient (∇p) and permeability ($\mathbf{K}$) but inversely proportional to the fluid viscosity (μ).

$$\mathbf{u} = -\frac{\mathbf{K}}{\mu}\nabla p \qquad [1.2]$$

Generally, permeability is an anisotropic property (directional-dependent), thus make it a tensor. If the material is assumed isotropic, permeability is then reduced to a scalar.

The permeability can be related to the porosity of a porous medium, and one widely used model is the Kozeny-Carman equation (Dullien, 1992) based on the hydraulic radius theory.

$$K = \frac{D_p^2 \phi^3}{180(1-\phi)^2} \qquad [1.3]$$

where D_p is the effective average particle diameter. The Kozeny-Carman equation provides the best estimate of the permeability value when a packed bed is formed by

spherical particles with narrow range of size distributions. Typical permeability values are: 10^{-7}-10^{-9} m^2 for clean gravel, 10^{-9}-10^{-12} m^2 for clean sand, and 10^{-11}-10^{-13} m^2 for peat (Nield and Bejan, 1999). In the study of hydrology, permeability is often lumped with other fluid properties and forms the hydraulic conductivity ($\overline{\mathbf{K}}$), which is defined as

$$\overline{\mathbf{K}} = \frac{\rho g \mathbf{K}}{\mu} \qquad [1.4]$$

where ρ and μ are the density and viscosity of the fluid, respectively.

Although Darcy's law has been used extensively to describe fluid flow in porous media, it has been recognized that Darcy's law is only valid for very low inertial flows (i.e., the order of Reynolds number based on the pore scale is much less than unity). As such, Darcy's law is applicable for most groundwater flows (Bear and Verruijt, 1987) and weak convective flows. For highly convective flows, the following equation, generally referred to as the Brinkman-Forchheimer-extended Darcy equation which accounts for the viscous and inertial effects, is more appropriate (Vafai and Tien, 1980 and 1981; Hsu and Cheng, 1990).

$$\rho \left[\frac{1}{\phi} \frac{\partial \mathbf{u}}{\partial t} + \frac{1}{\phi^2} (\mathbf{u} \cdot \nabla \mathbf{u}) \right] = -\nabla p + \mu_e \nabla^2 \mathbf{u} - \frac{\mu}{\mathbf{K}} \mathbf{u} - \frac{c_F \rho}{\mathbf{K}^{0.5}} |\mathbf{u}| \mathbf{u} \qquad [1.5]$$

where μ_e is the effective viscosity and c_F is the dimensionless form-drag coefficient. The local time-derivative and advective inertial terms are on the left-hand-side of Eqn. [1.5]. The Laplacian term is called the Brinkman viscous term while the last term on the right-hand-side of Eqn. [1.5] is the Dupuit-Forchheimer term. In general, both form-drag coefficient and effective viscosity depend on the geometry of the

porous medium. Note that when the permeability goes to infinity, Eqn. [1.5] reduces

to the Navier-Stokes equation. The discussion of the significant of each term is

described in details by Nield (2002) and Alazmi and Vafai (2000), and it is omitted

here for brevity.

1.3 Literature Review

For research involving porous media, some comprehensive reviews and

monographs on specific engineering application are well-documented in the literature.

For example, Cheng (1978) and McKibbin (1998) provided comprehensive reviews

on transport phenomena in geothermal systems. The literature review reported in this

dissertation is only focused on the studies related to a buried pipe in a porous medium.

It is the author's wish to provide an up-to-date comprehensive review on the research

progress made in this area. To do so effectively, the materials are organized

according to the mode of heat transfer involved (i.e., conduction, natural, mixed,

double-diffusive convection, etc.), and they are presented in the following sections.

1.3.1 Conduction

One of the earliest and most fundamental studies of heat transfer from a

cylinder buried in a semi-infinite medium was reported by Eckert and Drake (1959).

Analytical solutions for steady-state heat conduction were obtained using the source

and sink method, and heat transfer from the cylinder can be evaluated by

$$Q = \frac{2\pi k L (T_h - T_c)}{\ln(2d/r_i)}, \qquad [1.6]$$

where d and r_i are the depth and radius of the buried cylinder, respectively. The

above equation is valid only when $d/2r_i$ is much less than unity, and this result is often expressed in terms of the conduction shape factor given in most heat transfer textbooks (for example, Incropera and DeWitt, 1996; Mills, 1999). Eqn. [1.6] can also be expressed in terms of the thermal resistance as

$$R = \frac{\ln \left\{ \left[2\left(\frac{d}{r_i} \right)^2 - 1 \right] + 2\left(\frac{d}{r_i} \right)\sqrt{\left(\frac{d}{r_i} \right)^2 - 1} \right\}}{4\pi kL} \qquad [1.7]$$

and for large d/r_i the above expression is reduced to

$$R = \frac{\ln \left(2\frac{d}{r_i} \right)}{2\pi kL} \qquad [1.8]$$

Carslaw and Jaeger (1959) provided analytical solutions for transient temperature profiles in an infinite medium subject to a point heat source. The dimensionless temperature distribution was given in terms of the error function as

$$\Theta = \frac{1}{4\pi R}\,\mathrm{erfc}\left(\frac{R}{2\tau^{0.5}} \right) \qquad [1.9]$$

The expression for thermal resistance of a buried cylinder heated with constant flux was derived by Thiyagarajan and Yovanovich (1974). Analytical solutions were obtained by the method of separation of variables using bicylindrical coordinates. The thermal resistance for this case was given by

$$R = \frac{\eta_o}{2\pi k} + \frac{1}{\pi k}\sum_{n=1}^{\infty}\left[\frac{e^{-2n\eta_o}}{n}\tanh(n\eta_o) \right] \qquad [1.10]$$

where $\eta_o = \cosh^{-1}\left(\frac{d}{r_i} \right)$. By comparing the thermal resistances of these two heating conditions (i.e., Eqns. [1.7] and [1.8]) at various values of d/r_i, Thiyagarajan and

Yovanovich (1974) concluded that, for a burial depth of 5 pipe radii or deeper, the thermal resistance obtained from both models differed only by one percent.

Bau and Sadhal (1982) also provided analytical solutions for heat losses from a buried pipe. However, more realistic boundary conditions were applied to the pipe surface: (1) mixed convective boundary condition with uniform heat transfer coefficient was applied, which was best described when the fluid flowing inside the pipe was turbulent, and (2) fully-developed laminar flow was assumed, and the temperatures inside and outside of the pipe surface were determined simultaneously. The heat transfer results were expressed in terms of the shape factor given by

For case (1):
$$S = \frac{Bi}{\left(1 + Bi^2 \alpha_o^2 + 2Bi\,\alpha_o \coth \alpha_o\right)^{0.5}}$$
[1.11]

For case (2):
$$S = \frac{11}{24}(\frac{k_1}{k_2}) + \alpha_o + 2\sum_{n=1}^{\infty} \frac{(k_2/k_1)e^{-2n\alpha_o}}{n[\coth(n\alpha_o) + (k_2/k_1)]}$$
[1.12]

where Bi is the Biot number.

1.3.2 Natural Convection

Natural convection in porous media has been a vital part of the contemporary heat transfer research for the past few decades. Considerable work has been done in this area which included various types of porous enclosures. Oosthuizen (2000) has provided a comprehensive review on the subject. The literature review presented in this section only serves as a supplement to the earlier review and only focuses on the natural convection induced by a heated cylinder buried in a porous medium.

Wooding (1963) initiated the study of convection in a porous medium induced

by a point source and obtained similarity solutions for sufficiently large Rayleigh and Peclet numbers. Boundary layer approximation was employed to simplify the study such that the vertical gradients of velocity and temperature were neglected. He pointed out that the flow and temperature fields far away from the heat source closely resembled the solution for a laminar incompressible two-dimensional round jet obtained by Schlichting (1960). However, Yih (1965) argued that for similarity transformation which has the form of $\eta = (r/x)^n$, the omission of the terms involving vertical gradients was not justified for $n \geq 1$. To clarify the contradiction found in the literature, Lai (1990) reexamined the problem and obtained closed-form solutions using different set of similarity transformation parameters. The validity of the boundary layer approximation was examined through an order of magnitude analysis. It was concluded that Wooding's solution (1963) based on the boundary layer approximation was valid and applicable for Ra >> 1 and Yih's concerns (1965) were redundant after all.

Unlike Wooding's study (1963) which is valid for highly convective flows, Bejan (1978) employed perturbation method to analyze heat transfer from a concentrated heat source in an infinite porous medium at low Rayleigh numbers. Both transient and steady-state temperature and flow patterns in the vicinity of the point source were obtained. Bejan's results (1978) were valid for low Rayleigh numbers (i.e., Ra < 10 for transient solution and Ra < 20 for steady-state solution), and he emphasized that the limitation imposed was appropriate and consistent with the low inertial flow assumption of Darcy model. Similar to the work by Wooding

(1963), Merkin (1979) examined natural convection boundary layers on axisymmetric and two-dimensional bodies of arbitrary shape embedded in an infinite porous medium using similarity method, and he showed that similarity solution exists for all two-dimensional isothermal bodies of arbitrary shapes.   Cheng (1980) modified Merkin's approach (1979) and obtained a Nusselt number relation specifically for natural convection from an isothermal horizontal cylinder as

$$\mathrm{Nu} = 0.565\mathrm{Ra}_{\mathrm{D}}^{0.5}, \qquad\qquad [1.13]$$

where the Rayleigh number is based on the diameter D. This unpublished class notes of Cheng (1980) were reproduced in a paper by Fand et al. (1986).

Hickox and Watts (1980) generalized the earlier work of Wooding (1963) and Bejan (1978) such that their results were good for any Rayleigh number.   The governing equations were reduced to a set of nonlinear ordinary differential equations using similarity transformation suggested by Yih (1965).   Although the differential equations were greatly simplified through the transformation, no exact solution was available.   Approximate numerical solutions were sought using computer codes developed at Sandia National Laboratories (Scott and Watts, 1976 and 1977).   The results indicated that heat conduction was the dominated mode at low Rayleigh numbers, while plume-like boundary layer behaviors were observed for high Rayleigh number flows, as reported by Wooding (1963).

The literature reviewed thus far mostly considered free convection from a concentrated heat source in an infinite porous medium. As time progressed, more research efforts were devoted to and centered on modeling the porous medium as a

semi-infinite medium. This was partly due to an increasing interest in examining the possibility of disposal of nuclear wastes in oceanic basins (Bishop and Hollister, 1974). The emphasis of Hickox's study (1981) was on the analysis of nuclear waste disposal in the sediment below a seabed. He first performed perturbation analysis to study convection from a concentrated heat source in an unbounded porous medium by retaining only the leading terms of the power series expansion. The solutions obtained were thus linear and valid for low Rayleigh numbers. Because of the linearity, solutions for natural convection from a concentrated heat source buried in a semi-infinite porous medium with a permeable top boundary could then be obtained by the method of superposition. For the case of the nuclear waste disposal in a generic site located in the Central North Pacific, the anticipated Rayleigh number was approximately 10^{-3}, which satisfied the assumption of the mathematical model.

Fernandez and Schrock (1982) performed both experimental and numerical study to investigate natural convection from a heated cylinder buried in a porous medium bounded above by an isothermal liquid layer. To the best knowledge of author's, this was the first known attempt to experimentally study convection from a deeply buried heat source. The porous medium was simulated using two standard and reproducible sands (Monterey Crystal Amber and Ottawa Silica). The sands were saturated with water, and a water column of 15 cm was retained above the sand surface. The heated cylinder was simulated using a heater of various lengths (L) and radii (r_i) with 5 different burial depths (d). Temperature distributions were measured using thermocouples. To numerically model the interface between the porous medium and the fluid layer, a boundary condition similar to that of transpiration

cooling was imposed to account for the energy transferred. The numerical and experimental data were in qualitatively good agreement. The correlation for the Nusselt number was given by

$$Nu = Nu_{cond}\left[1.6 - 0.6\tanh\left(2.67 - 1.67\frac{f\,Ra^{0.514}}{Nu_{cond}}\right)\right] \quad \text{for } 0 \le \frac{f\,Ra^{0.514}}{Nu_{cond}} \le 1.6 \quad [1.14a]$$

$$Nu = f\,Ra^{0.514} \qquad\qquad\qquad\qquad \text{for } \frac{f\,Ra^{0.514}}{Nu_{cond}} \ge 1.6 \qquad [1.14b]$$

where $Nu_{cond} = \dfrac{2}{\displaystyle\sum_{m=1}^{M}\frac{1}{m}\left(1-\frac{r_i}{d+a}\right)^m + \frac{L/2r_i - M}{M+1}\left(1-\frac{r_i}{d+a}\right)^{M+1}}$, M is the largest integer

$\le L/2r_i$, $a = \sqrt{d^2 - r_i^2}$, and $f = 0.015 + 1.23\exp(-0.534\,\eta_S)$. Here, η_S is the bi-cylindrical coordinate at the source surface. The standard deviation of the experimental and numerical data from the correlation was 11.4%. The ranges of variables covered in the study were $10^{-2} \le Ra \le 10^4$, $1 \le \dfrac{L}{2r_i} \le \infty$, and $0.8 \le \dfrac{d}{2r_i} \le 23.7$.

Note that the Rayleigh number presented in this study was based on the length scale of $\sqrt{d^2 - r_i^2}$.

Bau (1984) studied natural convection from a pipe buried in a semi-infinite porous medium. Both impermeable and permeable inclined top surfaces were considered in his study. The problem was formulated using bi-cylindrical coordinates to solve for the temperature and flow fields at low Rayleigh numbers using perturbation method. A correlation for the Nusselt number was obtained in the form of a power series in terms of the Rayleigh number.

$$Nu = 1 + \frac{(a^2 N_2 Ra)^2}{a^2 N_2 - a^3 N_3 Ra \cos\theta} \qquad [1.15a]$$

where

$$a^2 N_2 = 10^{-3}(-10.12 + 9.335d + 1.523d^2 - 0.034d^3), \qquad [1.15b]$$

$$a^3 N_3 = 10^{-3}(1.599 - 1.865d^2 + 0.148d^3 - 0.005d^4), \qquad [1.15c]$$

θ is the inclined angle and d is the burial depth. The correlation given in Eqn. [1.15a]

is valid for impermeable top surface, $0 \leq \theta < \frac{\pi}{2}$, $2 \leq d \leq 14$, and $\left(Ra\frac{d}{r_i}\right) \leq 60$.

Shanks's nonlinear transformation (1955) was applied to obtain Eqn. [1.15a] to

increase the range of validity of the correlation. Bau (1984) revealed the existence of

an optimal burial depth at which heat transfer from the pipe is minimal. This finding

can be applied in the design of pipelines to save energy. Later, Himasekhar and Bau

(1987) conducted a similar study, but for which the top surface was assumed to be

impermeable and Robin convective condition was imposed. Again, by means of

Shanks's transformation (1955), the Nusselt number can be given as a function of the

Rayleigh number, Biot number and the burial depth:

$$Nu = \frac{1 + A Ra + B Ra^2}{1 + A Ra}, \qquad [1.16a]$$

where $A = a_1 d^{a_2}$, $\qquad [1.16b]$

$$B = 10^{-2} d\left(b_1 d^{b_2} + b_3\right), \qquad [1.16c]$$

$$a_1 = 0.28 + \frac{0.058}{Bi} - \frac{0.0029}{Bi^2}, \qquad [1.16d]$$

$$a_2 = 0.4 - \frac{0.048}{Bi} + \frac{0.0042}{Bi^2}, \qquad\qquad [1.16e]$$

$$b_1 = 1.084 - \frac{1.016}{Bi} + \frac{0.091}{Bi^2}, \qquad\qquad [1.16f]$$

$$b_2 = 0.393 + \frac{0.593}{Bi} - \frac{0.053}{Bi^2}, \qquad\qquad [1.16g]$$

$$b_3 = 3.85 \tanh\left(\frac{0.45}{Bi}\right) - 0.71. \qquad\qquad [1.16h]$$

Analogous to the finding of previous work by Bau (1984), the existence of an optimal burial depth was also observed for the boundary condition of a convective top surface. The magnitude of this optimal burial depth decreases with the Biot number.

An in-depth experimental investigation was conducted by Fand et al. (1986) to study heat transfer from a horizontal cylinder buried in randomly packed glass spheres saturated by either water or silicone oil. Two flow regimes, where the Nusselt number behaves differently, were identified based on the Reynolds numbers. Darcy flow regime corresponds to low Reynolds number flows while Forchheimer flow regime represents high Reynolds number flows. The change of properties with temperature and the wall effect on porosity were also considered in this study. The following correlations were obtained based on their experimental results.

(a) Darcy Flow Regime ($0.001 < Re_{max} \le 3$)

$$Nu\,Pr^{0.124} = 0.653\,Ra^{0.649} + 9.97 \times 10^6\,Ge\,\mathrm{sech}(Ra) \quad \text{for } \varepsilon_w, j = 0.5 \qquad [1.17a]$$

$$Nu\,Pr^{0.0877} = 0.618\,Ra^{0.698} + 8.54 \times 10^6\,Ge\,\mathrm{sech}(Ra) \quad \text{for } \varepsilon_w, j = 0.32 \qquad [1.17b]$$

(b) Forchheimer Flow Regime ($3 < Re_{max} \le 100$)

$$\text{Nu}\,\text{Pr}^{0.124} = 1.65\,\text{Ra}^{0.319}\left(\frac{C_1 D}{C_2}\right)^{0.0585} \qquad \text{for } \varepsilon_w, j = 0.5 \qquad\qquad [1.18a]$$

$$\text{Nu}\,\text{Pr}^{0.0877} = 0.766\,\text{Ra}^{0.374}\left(\frac{C_1 D}{C_2}\right)^{0.173} \qquad \text{for } \varepsilon_w, j = 0.32 \qquad\qquad [1.18b]$$

where Ge is the Gebhart number, ε_w is the wall corrected porosity, j is a numerical constant determined the reference temperature, D is the diameter of the cylinder, C_1 and C_2 are the Forchheimer coefficients.

Nakayama and Koyama (1987) presented similarity solutions for free convective heat transfer from a nonisothermal body of arbitrary shape embedded in a porous medium using boundary layer approximation with Kármán-Pohlhausen integral method. The obtained ordinary differential equation is identical to that of natural convection from a vertical flat plate with exponential wall temperature distribution, which has been solved by Cheng and Minkowycz (1977).

Ingham and Pop (1987) studied natural convection induced from a heated cylinder in an unbounded porous medium. Numerical solutions were obtained for finite Rayleigh numbers. The variation of the average Nusselt number with the Rayleigh number is determined to be

$$\text{Nu} = 0.3995\,\text{Ra}^{0.5} + 0.78 - 1.9\,\text{Ra}^{-0.5} \qquad\qquad [1.19]$$

The numerical results agreed well with the experimental data of Fand et al. (1986) for Rayleigh number on the order of unity. However, there was discrepancy between the numerical and experimental results when Rayleigh number increases to 10^2, an indication that Darcy's law may be no longer applicable.

It was the objective of Farouk and Shayer (1988) to perform numerical analysis to obtain steady-state solution for natural convection around a heated cylinder in a semi-infinite porous medium. A combination of grid systems, which involved both polar and Cartesian meshes, has been employed for the computations. The semi-infinite porous medium was bounded above by a liquid layer; hence both permeable and convective conditions were applied to this medium surface. It has been found that the flow behavior and the variation of Nusselt number at various burial depths were quite different for conduction and convection cases.

Himasekhar and Bau (1988) investigated natural convection around a cylinder heated with constant flux buried in a box filling with porous materials. Both experimental and numerical solutions were obtained. The experimental results indicated the existence of a critical Rayleigh number below which the flow was two-dimensional and time independent. Once this critical Rayleigh number was exceeded, the flow became three-dimensional and time dependent. For numerical computations, the physical domain of the problem was transformed to a rectangular domain via boundary-fitted coordinates. Once again, both numerical and experimental results agreed well at low Rayleigh numbers, and deviated as Rayleigh number was increased.

The consistent discrepancy between experimental data and theoretical results found in the literature has prompted Hsiao et al. (1992) to investigate the non-uniform porosity and thermal dispersion effects on convection from a heated cylinder in an enclosed porous medium using finite difference method with body-fitted coordinates. Both isothermal and constant flux heating conditions were imposed on the surface of

the cylinder. It was concluded that by including the effects of thermal dispersion and non-uniform porosity simultaneously, the predicted heat transfer results were in better agreement with the experimental data. The discussion of this subject could also be found in a recent review article by Chen and Hsiao (1998).

More recently, Christopher and Wang (1993) examined the non-Darcy effects by using Forchheimer-extended Darcy flow model. Finite element code MARIAH (Gartling and Hickox, 1980) was used to solve for the flow and temperature fields. It was concluded that the Dupuit-Forchheimer term should be included when the Reynolds number was five and above.

The majority of the literatures reviewed thus far have all assumed steady-state in their analysis. Ingham et al. (1983) investigated the unsteady collision effects of free convection boundary layers arise from a heated cylinder in a porous medium with particular interest on the flow behavior near the top and bottom stagnation points. No singularity in the solution was observed within a finite time, which was contrary to the findings of other studies dealing with a similar problem (Simpson and Stewartson, 1982; Brown and Simpson, 1982).

Using the method of matched asymptotic expansions, Pop et al. (1993) studied transient natural convection from an isothermal cylinder embedded in a porous medium at small times. Later, they extended the study to consider constant surface flux condition (Pop et al., 1996). In both studies, it was found that the solutions contain terms that were not included in the solutions based on boundary layer approximation. The formation of vortices was also observed at both sides of the cylinder. Bradean et al. (1997) then solved the problem numerically and their

solutions were valid for all times. Their numerical results at small times compared well with the analytical solutions of Pop et al. (1993). At very large times, the results at the vicinity of the cylinder agreed reasonably well with the steady-state solution of Ingham and Pop (1987).

1.3.3 Mixed Convection

In the last section, the literature reviewed was focused on the studies of free convective flow. Other than natural convection, mixed convection in porous media is also of practical interest. As pointed out by Lai (2000), research in mixed convection was called for in the early 1960s because of the need for better understanding of the movement of the groundwater in the geothermal region of Wairakei, New Zealand. In addition, the knowledge of convective transport around a nuclear waste repository was also desired, which eventually prompted the study of mixed convection. Since Lai (2000) has provided a comprehensive review on mixed convection in porous media for different flow regimes and geometries, the literature reviewed in this section is only focused on mixed convection around a cylinder buried in a porous medium

Using a similarity transformation previously employed by Merkin (1979) for natural convection, Cheng (1982) obtained similarity solutions with boundary layer approximation for mixed convection induced from an isothermal cylinder or a sphere in a fluid saturated porous medium. The transformed equations were found to be identical to those of an earlier study by Cheng (1977) about mixed convection from a vertical surface in a porous medium. Huang et al. (1986) also conducted a similar

study with uniform heat flux condition imposed on the surface of the cylinder and sphere. Minkowycz et al. (1985) extended the study of Cheng (1982) and considered non-isothermal surface temperature for a cylinder and a sphere in their model. Numerical solutions up to three levels of truncation were obtained based on the local non-similarity method. All these three theoretical studies (Cheng, 1982; Minkowycz et al., 1985 and Huang et al., 1986) have invoked boundary layer approximation.

Fand and Phan (1987) reported an experimental study on combined forced and natural convection from a cylinder in a porous medium. The porous medium was composed of randomly packed glass spheres saturated with water, and only horizontal cross flow condition was simulated in their experiment. It has been found that the predominant heat transfer mechanism is forced convection for $\mathrm{Gr_K}/\mathrm{Re_D^2} \leq 0.5$, and the effects of natural convection are important for $0.5 \leq \mathrm{Gr_K}/\mathrm{Re_D^2} \leq 4$. Their results were consistent with the findings of another study by Fand and Keswani (1973) on mixed convection from a heated cylinder in water.

Badr and Pop (1988) investigated both aiding and opposing flows (i.e., parallel and counter flows) over a heated cylinder in a porous medium. Finite difference scheme with modified polar coordinates was employed to obtain the transient solutions. The numerical results agreed well with the theoretical results obtained by Cheng (1982) and Minkowycz et al. (1985) except for a region near $\theta = 0$, where the boundary layer approximation failed. In view of the unusual temperature profiles and flow patterns reported by Badr and Pop (1988), Zhou and Lai (2002) reexamined the problem using body-fitted coordinates, and their results were in good

agreement with those of Badr and Pop (1988) for small Reynolds numbers and Gr/Re. However, there was a significant discrepancy between the studies for large Re or Gr/Re. Also, oscillatory solutions, which contradicted to the steady-state solutions obtained by Badr and Pop (1988), were observed for opposing flows at Re $\geq$ 50 and Gr/Re $\geq$ 4. They suspected that the discrepancy may be attributed to the truncation errors from the series solutions reported by Badr and Pop (1988).

In 1993, Sano investigated mixed convection around a cylinder immersed in a Darcy flow at small Peclet number with Gr/Re on the order of unity. Solutions have been obtained using the method of matched asymptotic expansions. Bradean et al. (1998) performed both analytical and numerical analysis on mixed convection around a suddenly heated cylinder buried in a porous medium. A series solution with the matched asymptotic expansion was employed to determine the solutions at small times while a finite difference scheme was used to obtain the solutions at all times.

1.3.4 Double-Diffusive Convection

Another type of convection, which involves simultaneous heat and mass transfer, can be frequently found in nature as well as in engineering applications. These include seawater flow, mantle flow in the earth's crust, casting and solidification of metal alloy, transport of contaminant in soils and exploitation of geothermal reservoir. This type of convection is also referred to as thermohaline, thermosolutal or double-diffusive convection.

Trevisan and Bejan (1990) presented a comprehensive review on combined heat and mass transfer by natural convection in a porous medium, which summarized

the research work conducted in the 1970s and 1980s. Mojtabi and Charrier-Mojtabi (2000) and Mamou (2002) also reviewed the work on double-diffusive convection. The majority of the work they reviewed was related to convection in a cavity or enclosure. Hence, the literature review presented in this section will only supplement these earlier reviews by focusing on double-diffusive convection induced from a cylinder in a porous medium. Other areas such as combined heat and mass transfer from a cylinder immersed in a pure fluid (the phenomenon of fingering), Neilson and Incropera (1987) have presented a comprehensive review. Similarly for double diffusive convection in an unsaturated porous medium, interested readers can refer to the work by Chang and Weng (2002).

Equally important in engineering applications are the transport phenomena of double diffusive convection, where the buoyancy due to the concentration difference is as significant as the thermal buoyancy. Unfortunately, there are only limited studies reported in the literature that deal with double diffusive convection from a buried cylinder.

Slegel and Davis (1977) looked into the idea of using waste heat from power plants for soil heating and subsurface irrigation to maintain the temperature and moisture of the soils. Finite difference scheme has been employed to solve for temperature and moisture content subject to typical weather conditions of the Willamette Valley in Oregon. It was concluded that irrigation through perforated pipe provided better soil warming and higher moisture content compared with surface irrigation. They suggested that a further analysis was needed to find the optimum pipe spacing, depth and size for increasing crop yield, but they also realized such

analysis could be difficult to perform. Fritton and Martsolf (1980) also proposed using soil heating technique to prevent frosting for growing orchards.

As an extension to Bejan's work (1978) on natural convection in an infinite porous medium with a concentrated heat source, Poulikakos (1985) studied the effects due to the added concentration point source using perturbation analysis of Darcy flow model. It was determined that the transport of chemical species induced from a concentration gradient has a great impact on the buoyancy flow. The flow resulted from a concentration difference can either oppose or aid the flow induced by a thermal gradient. However, the results obtained in this study were only valid for low Rayleigh numbers. Ganapathy (1994) performed a similar analysis as Poulikakos (1985) but using the Brinkman model. He recommended that the inclusion of both the viscous shear and the local acceleration terms was important in capturing all the salient features of the early stages of flow development, especially for small and moderate values of Prandtl numbers.

Phillips (1991) discussed the modeling of the dispersal of solutes using a point source at the boundary of a permeable layer by assuming the distribution is axisymmetry. According to the solutions obtained by Bird et al. (1960), the solute decreased with the distance from the source in an exponential manner. As pointed out by Stoessell (1987), this solution was pertinent to the concentration distribution around a small dissolving grain, particularly for the dissolution of plagioclase grains and the precipitation of kaolinite in an asymmetrical halo frequently found in limestones.

Nakayama and Ashizawa (1996) employed boundary layer analysis to investigate the coupled heat and mass transfer by natural convection from concentrated point and line sources embedded in porous media. The Lewis number (Le) and buoyancy ratio (N) were identified as the two critical parameters governing this double diffusive flow. It was also reported that the Lewis number was more sensitive to concentration field than the velocity and temperature fields.

Later, Cheng and Lai (1997) obtained a first order solution of combined heat and mass transfer from a buried pipe in a semi-infinite porous medium using the perturbation method. Both permeable and impermeable top surfaces were considered in their study. The analysis was conveniently done in bi-cylindrical coordinates. More recently, Yih (1999) performed a numerical study on coupled heat and mass transfer by natural convection adjacent to a permeable horizontal cylinder in an infinite porous medium. Finite difference scheme along with the modified Keller box method was employed in his study. The results were presented in terms of the Nusselt number and Sherwood number. The Nusselt number obtained in this study compared well with those obtained by Merkin (1979).

Two years later, Chamkha and Quadri (2001) extended the study of Yih (1999) to include the external magnetic field and internal heat generation or absorption effects. The governing equations were transformed using non-similarity form and were solved using finite difference method. It was found that both Nusselt and Sherwood numbers increased with the suction/injection parameter and buoyancy ratio, but decreased with the Hartmann number and the inertia parameter.

1.3.5 Homogeneous versus Heterogeneous Medium

All previous work reviewed thus far have considered homogeneous porous media. However, a heterogeneous or a layered porous medium is encountered more frequently in engineering applications. Considerable efforts have been made by numerous researchers to investigate flow and heat transfer in planar porous layers. For example, Rana et al. (1979) studied the effect of layered structure in rock formation on natural convection in a geothermal reservoir. A planar system comprising three porous layers with different permeabilities was used to represent the reservoir. The middle layer was assumed the least permeable; this layer has imposed a restriction on the flow producing a multi-cellular convection pattern and a lower overall heat transfer rate. It was found that the convection pattern was dependent on the permeability ratio and the boundary conditions.

McKibbin and O'Sullivan (1980) investigated the onset of convection in a system with an arbitrary number of layers. Linear stability analysis was performed in their study. The results showed that with an increase in the non-homogeneity in permeability, a transition of the flow patterns was observed with the convection cells tending to localize in the more permeable layers. Later McKibbin and O'Sullivan (1981) extended their earlier study to examine convection at slightly supercritical Rayleigh numbers. It was concluded that for a layered system, the heat transfer was strongly dependent on the cell width.

Poulikakos and Bejan (1983) studied natural convection in vertically and horizontally layered porous media heated from the side. Particular attention was

placed on the effects of inhomogeneity in permeability and thermal diffusivity on the overall heat transfer results. A correlation for the Nusselt number was developed via a general scaling law. These are just a few of the studies dealing with a layered planar porous system. A detailed literature review on this subject has been given by Ngo (1999); hence it is not repeated here for brevity.

Previous studies that were most closely resembled the problem of interest were those reported by Muralidhar et al. (1986) and Ngo and Lai (2000) in which a layered porous annulus was considered. Muralidhar et al. (1986) numerically and experimentally studied natural convection in a horizontal annulus with a step change in permeability. The agreement between numerical solution and experimental data has been satisfactory in general. However, when the porous layer next to the heated surface has a higher permeability, the Nusselt number predicted using Darcy's law was consistently lower than that of experimental data. They attributed the deviation to the non-Darcy effects. Ngo and Lai (2000) reexamined the study and attempted to find an effective permeability such that a lumped system approach can be employed for a layered porous annulus. Three averaging techniques (i.e., arithmetic, harmonic, and volumetric) were proposed for the evaluation of the effective permeability in their numerical study. The results showed that the harmonic technique has the best prediction in heat transfer rate among the three examined.

1.3.6 Superimposed Fluid and Porous Layers

Another research subject of interest is for a fluid layer overlying a layer of porous medium. Nield (1977) performed linear stability analysis for a system

28

comprising of a fluid layer and a porous medium layer heated from below. He included the possibility of Marangoni effect at the deformable upper surface. Beavers and Joseph (1967) condition was applied at the interface. The results obtained in this study for constant heat flux condition were qualitatively useful for estimating the stability criterion for other cases involving different thermal boundary conditions.

Somerton and Catton (1982) also considered a superposed system in their study with the objective of predicting the onset of convection. In this analysis, Brinkman viscous term was retained in the porous medium model along with the interface conditions suggested by Neale and Nader (1974). Normal stability manipulations were carried out to obtain the governing equations, which were approximated using the Galerkin method. An external Rayleigh number based on the fluid layer was identified as the sole stability parameter. It was concluded that either a large thermal conductivity ratio (fluid to porous layer) or a small Darcy number lead to a more stable fluid layer.

Motivated by the application of solidifying casting, Beckermann et al. (1987) conducted both numerical and experimental study on natural convection in an enclosure vertically divided into fluid and porous layers. The porous layer was modeled using the Brinkman-Forchheimer-extended Darcy equation, and solved numerically using the SIMPLER algorithm (Patankar, 1980). The continuity of temperature, heat flux, normal and tangential velocities, pressure, normal and shear stresses was implemented at the fluid-porous interface. Their experiment used spherical glass beads saturated with glycerin and water. The flow visualization results obtained from experiment compared well with the numerical results. The

penetration by convection in the porous layer from the fluid layer became significant when the product of Rayleigh number and Darcy number was greater than 50.

Chen and Chen (1988) performed linear stability analysis on the onset of salt-finger convection in a superposed fluid and porous layers. The porous layer was modeled using the Darcy's law while Beavers and Joseph (1967) condition was applied at the interface. A critical depth ratio, the thickness of fluid layer to porous layer, was identified by the linear stability analysis. The theoretical predictions obtained in this study were later confirmed by an experimental study (Chen and Chen, 1989). The convective cells were found to be three-dimensional in general. The same authors (Chen and Chen, 1992) then extended their studies to include a numerical investigation. The porous medium layer was modeled using the Brinkman-Forchheimer-extended Darcy equation. A combined Galerkin and finite difference scheme was employed. The numerical results were in good agreement with the experimental results obtained earlier (Chen and Chen, 1989).

More recently, Choi and Waller (1997) examined water flow over porous media using the Brinkman-Forchheimer-extended Darcy equation. Five different porous media typically found in natural and engineered systems were selected for the study. The interface conditions implemented were the continuity of longitudinal and transverse velocities, pressure, normal and shear stresses. The effective viscosity was assumed to be the same as the viscosity (i.e., $\mu_{eff} = \mu$). Finite difference method was employed to solve the partial differential equations expressed in terms of the stream function and vorticity. It was concluded that Darcy number of the porous medium

played an important role in determining the degree of flow penetration, and Darcy's law alone would not provide a full description of the flow field near the interface.

Previous work which closely resembled the present work was the study of Oosthuizen and Naylor (1996). They studied free convection from a cylinder in an enclosure partly filled with a porous medium. The cylinder was buried in the porous medium while the top portion of the enclosure was saturated with air. The objective of the study was to determine how heat transfer rate from the cylinder was affected by the air gap on top. The governing equations were solved using a Galerkin based finite element procedure. It has been found that there exists a critical thickness of air layer which will minimize the heat transfer rate from the cylinder.

1.3.7 Interfacial Conditions

A layered system is encountered quite frequently in engineering applications. In general, there are two types of layered systems: (a) porous-porous layer, and (b) porous-fluid layer, as shown in Figure 1.2. Over the years, the conditions needed to be satisfied at these interfaces have been a subject of research interest. An outstanding review was reported by Nield (2002) recently, which provided an updated development and implement of the interface conditions. The literature review in this section only summarizes the milestones achieved on this subject over the past few decades.

One of the pioneer studies in the determination of the interface condition between a fluid and a porous medium was conducted by Beavers and Joseph (1967). Viscous flow over a porous medium was considered. Navier-Stokes equations
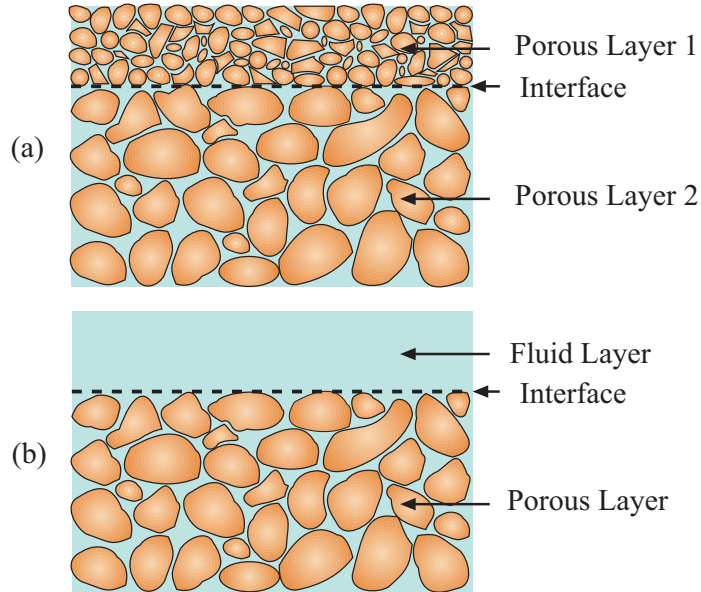
Figure 1.2 Common layered systems: (a) porous-porous layers,
and (b) porous-fluid layers.

governed the flow in the fluid layer while Darcy's law applied to the flow in the

porous medium. Based on their experimental study, they have proposed a slip-flow

model as the interface condition for flow over a porous medium, which is given

below (Figure 1.3b).

$$\frac{\partial u_f}{\partial y} = \frac{\alpha_{BJ}}{\sqrt{K}}\left(u_f - u_{pm}\right)$$ [1.20]

where u_f is the velocity of fluid; u_{pm} is the velocity in the porous medium; K is the

permeability; and α_{BJ} is the Beavers and Joseph slip coefficient. In general, the slip

coefficient needs to be determined through experiments, and it depends on the

structure of the medium, flow direction, Reynolds number, etc. The Beavers and

Joseph condition has been further verified and confirmed through experiments by

Beavers et al. (1970, 1974). Taylor (1971) and Richardson (1971) also independently
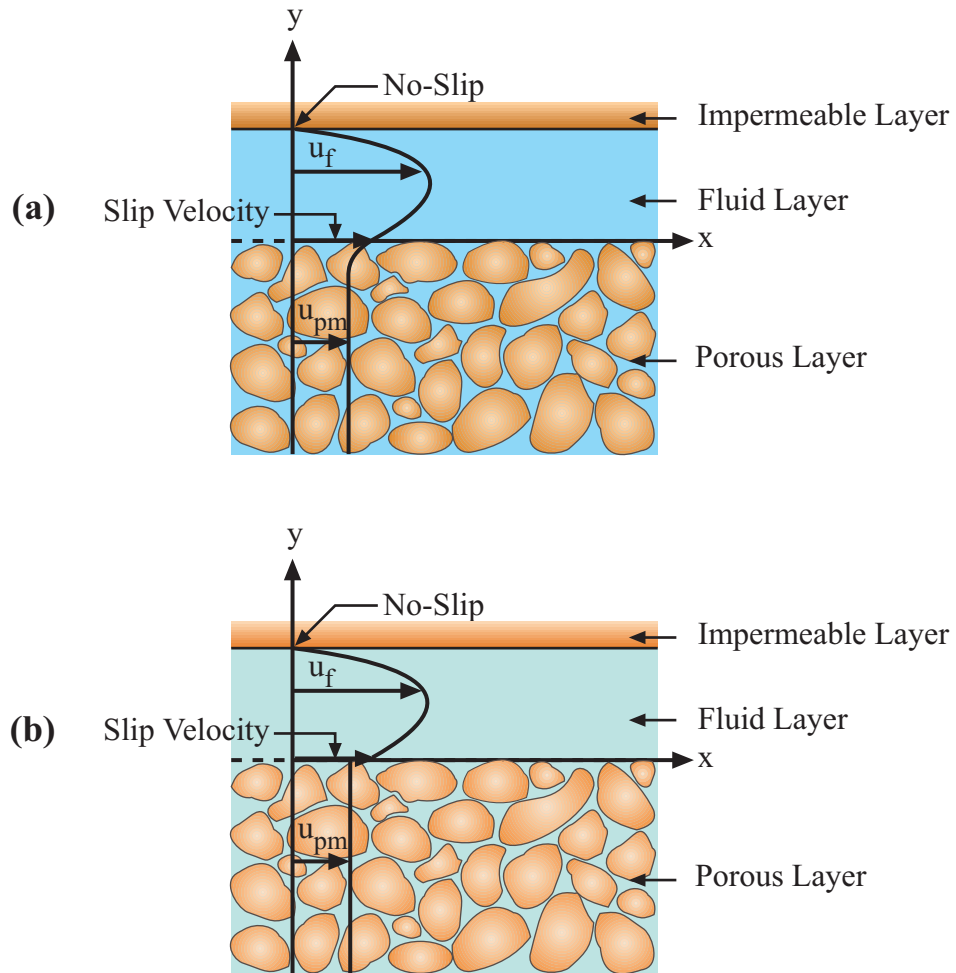
Figure 1.3 Schematic for illustrating (a) the actual velocity profile, and (b) Beavers-Joseph condition.

studied the Couette-type flow bounded by a permeable material analytically and experimentally. Their results obtained from the slip velocity model agreed well with the experimental data.

Neale and Nader (1974) employed the extended-Brinkman equation to simulate flows in porous media in conjunction with the implementation of continuity in both velocity and velocity gradient at the interface. They found that the velocity

profile near the boundary obtained herein was identical to those using Darcy's law along with the Beavers-Joseph (1967) conditions. Their interfacial conditions were expressed in terms of $\sqrt{\mu_{\text{eff}}/\mu}$ instead of the Beavers and Joseph slip coefficient (α_{BJ}). However, the proper value of μ_{eff}/μ was not available at the time but it was said that the results compared reasonably well by setting it as unity. Note that the determination of accurate effective viscosity has been a challenging subject over the years (Lundgren, 1972; Kolodziej, 1988; Givler and Altobelli, 1994).

One of the first comprehensive studies on interface conditions was performed by Vafai and Thiyagaraja (1987). They analyzed the flow and heat transfer conditions for three types of interfacial conditions (i.e., porous medium-porous medium, fluid-porous medium, and impermeable solid-porous medium). Explicit analytical expressions for the velocity and temperature distributions at the interface were derived based on matched asymptotic perturbation expansions. It was found that the analytical results were in excellent agreement with the numerical results.

In a time span of six years, Vafai and Kim (1990 and 1995) had a series of discussions with Nield (1991 and 1996) on the treatment of interface conditions between porous medium and fluid. Vafai and Kim (1990) provided an exact solution for the description of flow at the interface between a fluid layer and a porous medium, which accounted for both the boundary and inertial effects but with a constant porosity assumption. Nield (1991) argued that Vafai and Kim (1990) have over-determined the physical problem by using the continuity of tangential and normal stresses interface conditions. Further, the variation of the porosity should be

accounted for when Brinkman formulation was employed to model a dense porous medium. He also suggested that the interface between a porous medium and a fluid layer interface could be best handled by dropping the Brinkman term and using the Beavers-Joseph (1967) interface condition. In response to Nield's comments (1991), Vafai and Kim (1995) emphasized and reconfirmed that the Brinkman model with the continuity of velocities and stresses at the interface were appropriate, and the previous numerical solutions based on this formulation have been shown to be consistent with the experimental results (Beckermann et al., 1987). Furthermore, according to Vafai and Kim (1995), the slip coefficient in the Beavers-Joseph (1967) condition is a function of too many parameters, which make this condition difficult to implement. They agreed with Nield (1991) that a variable porosity might be needed to model a dense porous medium, but a constant porosity was sufficient for simulating a porous medium with high porosity. In a closure statement on the issue, Nield (1996) stood by his earlier comments (Nield, 1991), and recommended that more experimental studies in this area were needed to distinguish between the models.

Sahraoui and Kaviany (1992) examined the slip and no-slip boundary conditions for velocity at the interface of porous and plain media. Their two-dimensional model was simulated using porous medium made of cylinders arranged in periodic fashion, which allowed both parallel and oblique flows as opposed to only parallel flows (i.e., Poiseuille or Couette flow) considered previously (e.g., Beavers and Joseph, 1967; Neale and Nader, 1974). The numerical results suggested that the Beavers-Joseph slip coefficient was not just a function of the porous structure but also dependent on the flow direction, Reynolds number, the extent of the plain medium,

and the non-uniformities in the arrangement of the surface particles. It was also shown that Brinkman formulation along with a constant effective viscosity did not describe the flow field near the interface accurately. A variable effective viscosity model was recommended. As an extension of their earlier study, Sahraoui and Kaviany (1994) then proceeded to examine the temperature interface condition in a similar manner. Slip and no-slip temperature conditions with a constant and variable transverse total diffusivity were examined, respectively. The thermal slip coefficient was determined to be a function of the bulk Peclet number, the thermal conductivity ratio (solid-to-fluid), and the gap width of the medium.

Between 1995 and 1997, Ochoa-Tapia and Whitaker (1995a, 1995b and 1997) conducted a series of studies on the momentum and heat transfer at the interface of a porous medium and a fluid. First, they (1995a) derived a jump condition in stress using a non-local form of volume averaged momentum equation. This jump condition connected the Darcy's model with the Brinkman correction to the Navier-Stokes equations and produced a smooth transition of velocity profile at the interface. The jump interface condition was expressed in terms of a coefficient, which is determined by experimental measurements. In their follow-up study (Ochoa-Tapia and Whitaker, 1995b), they compared stress jump condition with the experimental results provided by Beavers and Joseph (1967), and showed that they were in good agreement. The possibility of using a variable porosity model for the stress jump condition was also evaluated in their study. However, the comparison between the theory and experimental data was not successful, and more detailed experimental and numerical studies were needed to yield a significant improvement on the present

model.

Ochoa-Tapia and Whitaker (1997) then developed a flux jump condition at the interface between a porous medium and a fluid where the condition of local thermal equilibrium was invalid. The heat transfer between the two phases (i.e., fluid and solid phases) was accounted for by inclusion of an excess heat exchange term. However, the excess surface heat exchange coefficient needed to be determined by experiments.

As an extension to the analytical approach proposed by Vafai and Kim (1990) and addressing the concerns raised by Nield (1991), Kuznetsov (1997) analytically obtained a new set of interface conditions utilizing the stress jump condition proposed by Ochoa-Tapia and Whitaker (1995a, b). It was shown that the difference between effective viscosity and fluid viscosity played an important role in determining the velocity profile.

In a recent paper by James and Davis (2001), flow at the interface of a model fibrous porous medium (i.e., a channel partially filled with an array of widely spaced circular cylinders against one wall) was investigated. For the spacing considered, singularity methods were employed to obtain solutions for both Couette and Poiseuille flows at the interface region. It was suggested that the Brinkman model was not suitable to predict flow at the interface of a low-solidity porous medium.

By far the most comprehensive and detailed review on the interface conditions between a porous medium and a fluid layer was given by a recent work of Alazmi and Vafai (2001). They critically examined different types of interfacial conditions for fluid flow and heat transfer that have been used in the previous work. In general, it

has been found that the variances (e.g., Darcy number, inertial parameter, Reynolds number, porosity and slip coefficient) have a more prominent effect on the velocity than the temperature distribution.   For most practical applications, the results produced by all the interfacial conditions examined were quite close to each other with the discrepancy only appeared for large Reynolds or Darcy numbers.

1.4 Motivation and Objective of Present Study

For applications in underground pipelines for the transportation of natural gas and crude oil, power cables and the disposal of nuclear wastes, the pipe or canister temperature is usually higher than the surroundings due to artificial (viscosity reduction for oil transportation) or natural causes (ohm heating for transmission cables and decay heating for nuclear wastes). As a result, a buoyancy-induced flow is initiated in the soils.

From the literature review presented in the previous sections, most of the previous studies have considered a homogeneous porous medium despite that heterogeneous or layered porous media are encountered more frequently. For buried pipes, the soil structure near the buried site is usually modified from its original state in the excavation process. A similar situation is found in the mining process for a nuclear waste repository.   In addition to the changes brought about by the excavation/mining process, it is customary to add backfill to the buried pipes and waste canisters. As a result, the soil or bed rock that hosts the pipes and waste canisters is never homogeneous, but heterogeneous instead.

For the problem considered (Figure 1.4), the properties of the excavation

disturbed zone and backfill around the buried pipe would be different from those of the soil far away from the pipe. Among the properties involved, permeability is perhaps the most important one because of its direct influences on the convective flow. Therefore, it is the objective of the present study to examine the effects of permeability contrast in the porous medium on the fluid flow and heat transfer results.

Another area of interest is when leakage from the pipe is induced accidentally (i.e., oil spill) or artificially (i.e., subsurface irrigation). In the event of a leakage developed from the crude oil pipeline, one would be interested to know the spreading patterns of the crude oil over the surrounding environment. Another application is the usage of waste heat for soil heating. Sometimes it is also desirable to let water seep through the buried pipe to provide subsurface irrigation and maintain the moisture level in the soil (Slegel and Davis, 1977). For either application, a prior knowledge of the flow, temperature and concentration distributions would certainly improve the
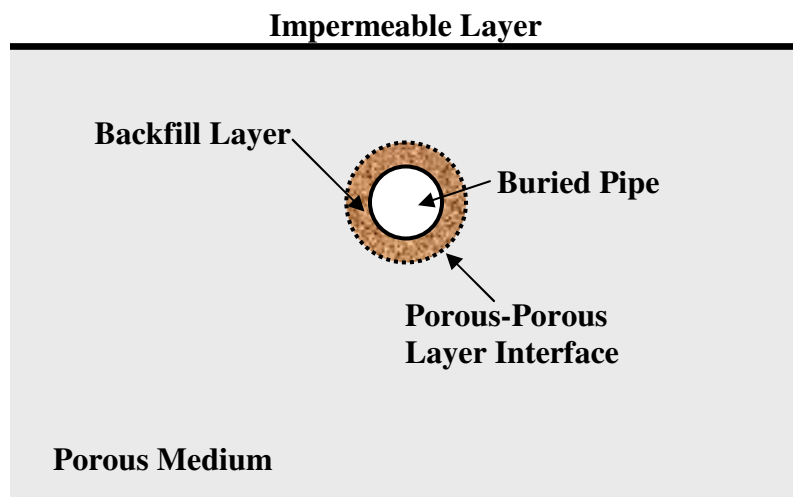
Figure 1.4 A horizontal pipe embedded in a porous medium with a backfill layer.

effectiveness in confining the pollutants or providing heating and irrigation to soil. Hence, the objective of the present study is to investigate the coupled heat and mass transfer by mixed convection induced by a leakage from a buried pipe (Figure 1.5). In addition to the numerical studies, experimental flow visualization using Hele-Shaw analogy is conducted to obtain the flow field for comparison.

1.5 Dissertation Overview

This dissertation is consisted of three major studies (Chapters 4-6) with each focused on different aspects of heat transfer and fluid flow induced by a heated cylinder buried in a porous medium. Some of the results have been presented at national heat transfer conferences and subsequently published in the corresponding conference proceedings or archival journals. This dissertation is written with the intention to be a good reference source for students, researchers and engineering practitioners in this specific subject.
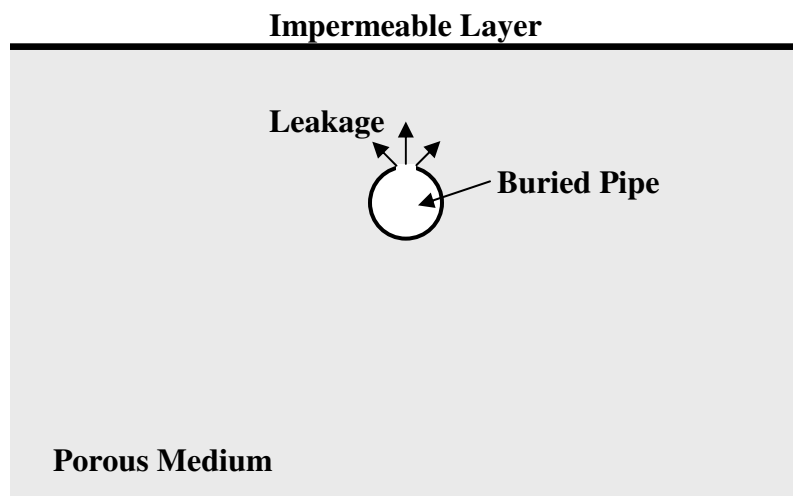
Figure 1.5 Leakage from a horizontal pipe embedded in a porous medium.

Chapter 1 presents a first glimpse at the research interests in porous media and their engineering applications. A brief introduction to the study of heat transfer and fluid flow in porous media is included here. The literature review presented in this chapter summarizes all the important work that has been done in the past. It also discusses the trend of the current research. The scope and objectives of the present study are also clearly defined in this chapter.

In Chapter 2, the concept and fundamental theory of body-fitted coordinates system is briefly introduced. Since an elliptic grid generation is the preferred technique for the present study, it is discussed in more detail here. The effects of the grid control functions are demonstrated through various examples.

Chapter 3 is centered on conduction and natural convection from a cylinder buried in a homogeneous porous medium. Mathematical formulation along with the finite difference method is presented here in detail. The results obtained are compared with and validated by those of previous studies. The proper size of the computational domain for studies reported in the subsequent chapters is determined based on the analysis presented here.

Chapter 4 examines natural convection from a buried pipe with a layer of backfill. Flow patterns and heat transfer results subject to a step change in the permeability of the backfill are presented. Numerical calculations have been performed to cover a wide range of governing parameters (i.e., $10 \leq Ra_1 \leq 500$ and $0.1 \leq K_1/K_2 \leq 10$) for various backfill thicknesses ($0.5 \leq t/r_i \leq 2$) (Ngo and Lai, 2005).

Chapter 5 addresses the numerical study on combined heat and mass transfer by mixed convection induced from a buried pipe with leakage. A parametric study

has been performed to investigate the effects of Rayleigh number, Peclet number, Lewis number, and buoyancy ratio (i.e., Ra $\leq$ 500, Le $\leq$ 10, Pe $\leq$ 10, and $|N| \leq 5$) on the heat and mass transfer results. The results have already been published in the Proceedings of the 2003 National Heat Transfer Conference (Ngo and Lai, 2003).

The flow visualization experiment conducted in the present study is presented in Chapter 6. Flow patterns in a porous medium induced by a heated cylinder are visualized using Hele-Shaw cell and qualitatively compared to the numerical results. In this chapter, a brief introduction of the available experimental techniques is presented. A review of literature on the Hele-Shaw analogy is also included in this chapter.

The final chapter summarizes the conclusions drawn from the present study and provides recommendations for the future work.

CHAPTER II

BODY-FITTED COORDINATES

2.1 Introductory Remarks

Flow and heat transfer problems encountered in engineering practice often involve complex geometries. Closed-form analytical solutions are, therefore, difficult and nearly impossible to obtain for most real world problems. One alternative approach is to mathematically model and predict the physical processes using numerical methods such as finite difference method (FDM) and finite element method (FEM). Owing to its simplicity in computations, FDM is the preferred method when the problem involved has a simple geometry which can be readily modeled using coordinate systems such as the Cartesian, cylindrical and spherical coordinates. On the other hand, FEM is better suited for problems with irregular geometries. The drawback associated with FEM is that the coding can be tedious and lengthy in time.

One numerical technique which is capable of dealing with complex and irregular geometries and yet maintaining the computational simplicity of FDM is by way of the body-fitted coordinates. Due to its flexibility, body-fitted coordinates have been used to tackle a variety of engineering problems. Just to name a few, Yost (1984) analyzed fluid flow and solidification problems in arbitrarily shaped domains; Koo and Leap (1998) modeled three-dimensional groundwater flows; and Strohle et al. (2000) performed numerical simulations for radiation from coal-fired furnaces. All have used body-fitted coordinates. In additions, most commercial computational

fluid dynamics (CFD) software such as FLUENT, FLOW-3D and ALGOR provide

grid generator with body-fitted coordinates.

The concept of the body-fitted coordinate method is to obtain a curvilinear

coordinate system by mapping an arbitrary shape in the physical domain onto a

regular shape in the computational domain. The curvilinear coordinates in the

physical domain are generally not orthogonal. Figure 2.1 shows a simply connected

physical domain and its corresponding computational domain. As the name of the

body-fitted coordinate implies, the chosen boundary points in the physical domain

intersect with the coordinate lines in the computational domain. Segments AB and

DC correspond to constant ξ_o and ξ_m lines, respectively. The value of η varies

monotonically (from η_o to η_n) along segments AB and DC. Likewise, η is constant on

segments AD and BC (i.e., η_o for AD and η_n for BC), and ξ varies monotonically
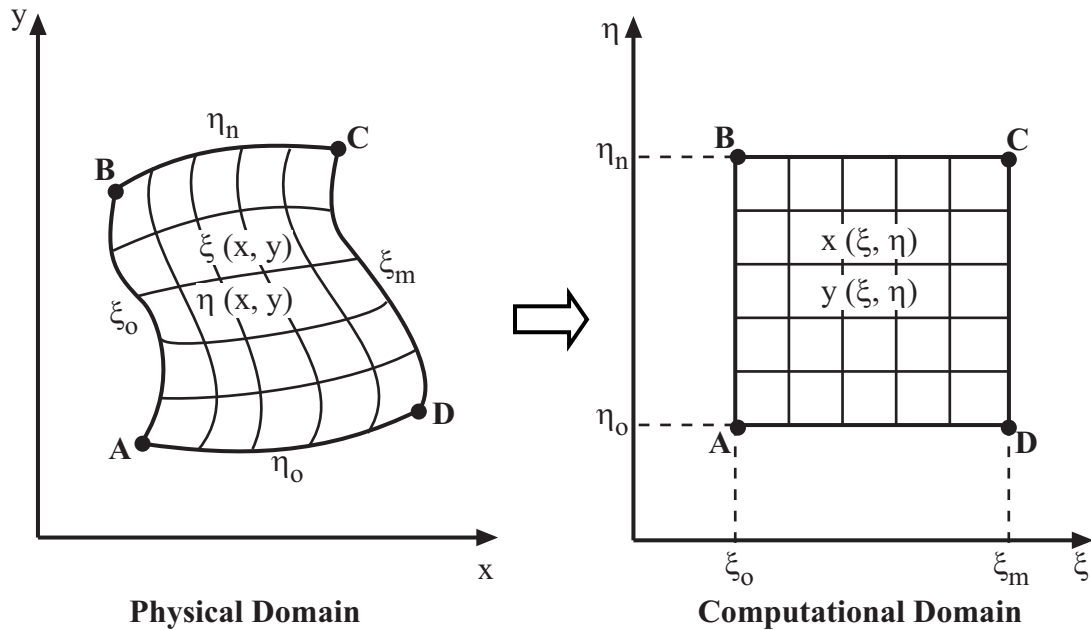
Figure 2.1 Physical and computational domains of the body-fitted
coordinate transformation.

along them. In the physical domain, the Cartesian coordinates x and y are the independent variables whereas the curvilinear coordinates ξ and η are the dependent variables. The dependent and independent variables are interchanged in the computational domain. The computational domain consists of uniform square grids. Therefore, the discretization process becomes greatly simplified and straightforward.

This chapter presents a brief introduction of the body-fitted coordinates with the focus on the elliptic grid generation. For an in-depth discussion of other numerical grid generation methods, one may refer to Thompson (1982), Thompson et al. (1982, 1999) and Knupp and Steinberg (1993) for more information.

2.2 Elliptic Grid Generation

Elliptic grid generation is widely used in computational fluid mechanics problems. It is preferred over other methods for the following reasons, (a) the grid generated is fairly smooth, and (b) the boundary slope discontinuities are not propagated into the interior nodes. In addition, this approach has been successfully used in the previous studies by Himasekhar and Bau (1988) and Hsiao et al. (1992) involving a similar geometry. As such, it is chosen over other available coordinate transformations for the present study.

The simplest form of an elliptic generating system is the Laplace equation:

$$\frac{\partial^2 \xi}{\partial x^2} + \frac{\partial^2 \xi}{\partial y^2} = 0, \qquad\qquad [2.1a]$$

$$\frac{\partial^2 \eta}{\partial x^2} + \frac{\partial^2 \eta}{\partial y^2} = 0. \qquad\qquad [2.1b]$$

It has been shown that this coordinate transformation is unique (one-to-one mapping) and has a non-vanishing Jacobian for any simply connected domain mapped onto rectangular domain (Knupp and Steinberg, 1993; Mastin and Thompson, 1978). The grid generated using Laplace equation is evenly spaced and by far the smoothest, but the major drawback is that one has little control over the distributions of the interior nodes. As a result, grid generation using the Laplace equation is not practical for most engineering problems.

The preferred coordinate transformation is through an elliptic Poisson-type generating system given as follows

$$\frac{\partial^2 \xi}{\partial x^2} + \frac{\partial^2 \xi}{\partial y^2} = \overline{P}, \qquad\qquad [2.2a]$$

$$\frac{\partial^2 \eta}{\partial x^2} + \frac{\partial^2 \eta}{\partial y^2} = \overline{Q}, \qquad\qquad [2.2b]$$

where $\overline{P}$ and $\overline{Q}$ are the grid control functions. The non-homogeneous nature of the Poisson-type grid generation allows for the control of the grid line distributions. Having introduced the grid control functions, the uniqueness of the coordinate transformation is no longer preserved; hence one should be cautious to make sure that the grid generated is not overlapped or folded (i.e., points fall outside of the prescribed domain). More discussion on this subject will be given at the end of this chapter.

By interchanging the dependent and independent variables in Eqn. [2.2], the transformed equations in the computational domain become

$$\overline{\alpha}\frac{\partial^2 x}{\partial \xi^2} - 2\overline{\beta}\frac{\partial^2 x}{\partial \xi \partial \eta} + \overline{\gamma}\frac{\partial^2 x}{\partial \eta^2} + J^2\left(\overline{P}\frac{\partial x}{\partial \xi} + \overline{Q}\frac{\partial x}{\partial \eta}\right) = 0,$$ [2.3a]

$$\overline{\alpha}\frac{\partial^2 y}{\partial \xi^2} - 2\overline{\beta}\frac{\partial^2 y}{\partial \xi \partial \eta} + \overline{\gamma}\frac{\partial^2 y}{\partial \eta^2} + J^2\left(\overline{P}\frac{\partial y}{\partial \xi} + \overline{Q}\frac{\partial y}{\partial \eta}\right) = 0,$$ [2.3b]

where
$$\overline{\alpha} = \left(\frac{\partial x}{\partial \eta}\right)^2 + \left(\frac{\partial y}{\partial \eta}\right)^2,$$ [2.3c]

$$\overline{\beta} = \frac{\partial x}{\partial \xi}\frac{\partial x}{\partial \eta} + \frac{\partial y}{\partial \xi}\frac{\partial y}{\partial \eta},$$ [2.3d]

$$\overline{\gamma} = \left(\frac{\partial x}{\partial \xi}\right)^2 + \left(\frac{\partial y}{\partial \xi}\right)^2,$$ [2.3e]

$$J = \frac{\partial x}{\partial \xi}\frac{\partial y}{\partial \eta} - \frac{\partial x}{\partial \eta}\frac{\partial y}{\partial \xi}.$$ [2.3f]

J is the Jacobian of the coordinate transformation. $\overline{\alpha}$, $\overline{\beta}$ and $\overline{\gamma}$ are the coefficients of the transformation.

The grid control function is an attractive feature that elliptic Poisson-type generating system has to offer. It provides the much needed flexibility for the users to control and adjust the grid distribution. One type of grid control is through an adaptive control system where the distribution of the grid is coupled with the physical solution. As the region with high gradient of field variables (e.g., temperature, concentration and pressure) changes with time, the grid distribution is adjusted accordingly. Adaptive grid control is ideal for problems involving a moving boundary (e.g., solidification and high speed compressible flows). The grid can be reconstructed and concentrated in regions near the freezing front or shock wave.

Another type of grid control is pre-specified by the users so that the regions, where high gradients of field variables are anticipated, have concentrated grid distributions. The prescribed grid control functions employed in the present study are given by

$$\overline{P}(\xi,\eta) = -\sum_{i=1}^{m}\overline{ap}_i \text{sign}(\xi-\xi_i)\exp(-\overline{cp}_i|\xi-\xi_i|)$$
$$-\sum_{j=1}^{n}\overline{bp}_j\text{sign}(\xi-\xi_j)\exp\left\{-\overline{dp}_j\left[(\xi-\xi_j)^2+(\eta-\eta_j)^2\right]^{1/2}\right\},$$

[2.4a]

$$\overline{Q}(\xi,\eta) = -\sum_{k=1}^{o}\overline{aq}_k\text{sign}(\eta-\eta_k)\exp(-\overline{cq}_k|\eta-\eta_k|)$$
$$-\sum_{l=1}^{p}\overline{bq}_l\text{sign}(\eta-\eta_l)\exp\left\{-\overline{dq}_l\left[(\xi-\xi_l)^2+(\eta-\eta_l)^2\right]^{1/2}\right\}.$$

[2.4b]

Thompson et al. (1982) introduced these grid control functions to attract grids to selected coordinate lines and points. Grid control function $\overline{P}$ is to attract coordinate lines in the direction of ξ. In particular, the amplitude factors $\overline{ap}_i$ and $\overline{bp}_j$ move the ξ-coordinate lines towards line ξ_i and point (ξ_j, η_j), respectively. The extent of attraction effect is determined by both the amplitude factors ($\overline{ap}_i$ and $\overline{bp}_j$) and decay factors ($\overline{cp}_i$ and $\overline{dp}_j$). The "sign" operator ensures that the attraction of coordinate lines acts from both sides of line ξ_i and point (ξ_j, η_j). Similarly, grid control function $\overline{Q}$ attracts coordinate lines in the direction of η. The selection of adequate amplitude and decay factors is based on a trial and error process until a reasonable grid is obtained. The effects of the grid control functions will be illustrated in Chapter 2.4.

2.3 Numerical Methods

Finite difference method is used to discretize the partial differential equation

given in Eqn. [2.3]. Based on the Taylor series expansion, the central difference

approximations for the first and second derivatives are given as follows,

$$\frac{\partial \Phi}{\partial \xi} = \frac{\Phi_E - \Phi_W}{2\Delta\xi}, \qquad\qquad \frac{\partial \Phi}{\partial \eta} = \frac{\Phi_N - \Phi_S}{2\Delta\eta}, \qquad\qquad \text{[2.5a, b]}$$

$$\frac{\partial^2 \Phi}{\partial \xi^2} = \frac{\Phi_E + \Phi_W - 2\Phi_P}{(\Delta\xi)^2}, \qquad \frac{\partial^2 \Phi}{\partial \eta^2} = \frac{\Phi_N + \Phi_S - 2\Phi_P}{(\Delta\eta)^2}, \qquad \text{[2.5c, d]}$$

where Φ represents either the coordinate x or y. $\Delta\xi$ and $\Delta\eta$ are the grid spacing in ξ-

and η-direction, respectively. The nodes involved in Eqn. [2.5] are illustrated in

Figure 2.2. Similarly, the mixed derivative is approximated by applying the first

derivative in the η-direction and then in the ξ-direction,

$$\frac{\partial^2 \Phi}{\partial \xi \partial \eta} = \frac{\Phi_{NE} - \Phi_{SE} - \Phi_{NW} + \Phi_{SW}}{4\Delta\xi\Delta\eta}. \qquad\qquad \text{[2.6]}$$
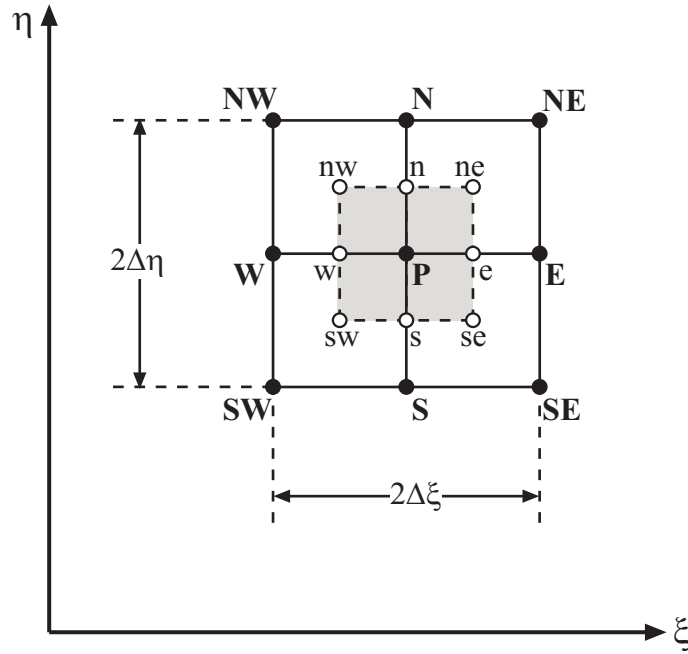
Figure 2.2 Nodes involved in the finite difference equation.

For the present study, uniform grid is used. As such, $\Delta\xi$ and $\Delta\eta$ are assumed unity. Notice that the accuracy of the above approximations can be improved by including additional terms from the Taylor series expansion if necessary.

The discretized equations are then obtained as follows,

$$x_P = A_1(x_{SE} - x_{NE} - x_{SW} + x_{NW}) + (A_2 + A_4\overline{P})x_E + (A_2 - A_4\overline{P})x_W$$
$$+ (A_3 + A_4\overline{Q})x_N + (A_3 - A_4\overline{Q})x_S, \qquad [2.7a]$$

$$y_P = A_1(y_{SE} - y_{NE} - y_{SW} + y_{NW}) + (A_2 + A_4\overline{P})y_E + (A_2 - A_4\overline{P})y_W$$
$$+ (A_3 + A_4\overline{Q})y_N + (A_3 - A_4\overline{Q})y_S, \qquad [2.7b]$$

where $\quad A_1 = \dfrac{\overline{\beta}_P}{4(\overline{\alpha}_P + \overline{\gamma}_P)}, \qquad A_2 = \dfrac{\overline{\alpha}_P}{2(\overline{\alpha}_P + \overline{\gamma}_P)}, \qquad$ [2.7c, d]

$$A_3 = \dfrac{\overline{\gamma}_P}{2(\overline{\alpha}_P + \overline{\gamma}_P)}, \qquad A_4 = \dfrac{J_P^{\,2}}{4(\overline{\alpha}_P + \overline{\gamma}_P)}, \qquad [2.7e,\ f]$$

$$\overline{\alpha}_P = \frac{1}{4}\left[(x_N - x_S)^2 + (y_N - y_S)^2\right], \qquad [2.7g]$$

$$\overline{\beta}_P = \frac{1}{4}\left[(x_E - x_W)(x_N - x_S) + (y_E - y_W)(y_N - y_S)\right], \qquad [2.7h]$$

$$\overline{\gamma}_P = \frac{1}{4}\left[(x_E - x_W)^2 + (y_E - y_W)^2\right], \qquad [2.7i]$$

$$J_P = \frac{1}{4}\left[(x_E - x_W)(y_N - y_S) - (x_N - x_S)(y_E - y_W)\right]. \qquad [2.7j]$$

The above algebraic equations are then programmed using Fortran90 and solved with Gauss-Seidel iterative scheme (Chapra and Canale, 2002) subject to the specified boundary locations.

A successive over-relaxation parameter is employed to accelerate or improve the convergence of the results.

$$\Phi_{i,j}^{k+1} = \Phi_{i,j}^{k} + r\left(\phi_{i,j}^{k+1} - \Phi_{i,j}^{k}\right), \qquad\qquad [2.8]$$

where   k: iteration level,

$\phi_{i,j}^{k+1}$: the most recent value calculated from the Gauss-Seidel procedure,

$\Phi_{i,j}^{k}$: the adjusted value from the previous iteration,

$\Phi_{i,j}^{k+1}$: the newly adjusted value at the k+1 iteration level, and

r: relaxation parameter.

The selection of adequate relaxation parameter is more of an art; it depends on experience and some insights to the problem. Over-relaxation parameter (values between 1 and 2) is used in the present study to generate the grid.

To determine if a solution has converged, the following convergence criterion is employed:

$$\max\left|\Phi_{i,j}^{k+1} - \Phi_{i,j}^{k}\right| \leq \delta, \qquad\qquad [2.9]$$

where the quantity Φ represents either x- or y-coordinate, k is the iteration level, and δ is the allowable error, which is set to be 10^{-8} in the present study. The iteration process is terminated once this criterion is met. The solution procedures are summarized in the flow chart shown in Figure 2.3.

2.4 Effects of Grid Control Function

To demonstrate the effects of grid control function, let's take the geometry considered in the present study (as shown in Figure 2.4) for example. The mapping is chosen such that segments EF and DC are constant ξ-coordinate lines while segments

```
        ┌─────────────┐
        │    Start     │
        └──────┬───────┘
               │
               ▼
   ╱─────────────────────────╱
  ╱  Input the Amplitude and Decay ╱
 ╱  Factors for the Grid Control Functions ╱
╱   and the Relaxation Parameters   ╱
╱─────────────────────────╱
               │
               ▼
   ╱─────────────────────────╱
  ╱   Input the Boundary Locations  ╱
 ╱─────────────────────────╱
               │
               ▼
   ┌─────────────────────────┐
   │ Determine the Grid Control Functions and │
   │   Transformation Coefficients   │
   └────────────┬────────────┘
               │
               ▼
   ┌─────────────────────────┐
   │  Solving for the Interior Nodes:  │
   │        x(i,j), y(i,j)       │
   └────────────┬────────────┘
               │
               ▼
          ◇ decision ◇
```

Start

Input the Amplitude and Decay Factors for the Grid Control Functions and the Relaxation Parameters

Input the Boundary Locations

Determine the Grid Control Functions and Transformation Coefficients

Solving for the Interior Nodes: x(i,j), y(i,j)

Is $\max \left| \Phi_{i,j}^{k+1} - \Phi_{i,j}^{k} \right| \leq 10^{-8}$?

For $\Phi = x$ and y

No

$\Phi_{i,j}^{k+1} = \Phi_{i,j}^{k} + r\left(\phi_{i,j}^{k+1} - \Phi_{i,j}^{k} \right)$

Yes

Output the Required Results

End

Figure 2.3 Flow chart of the numerical procedures for grid generation.
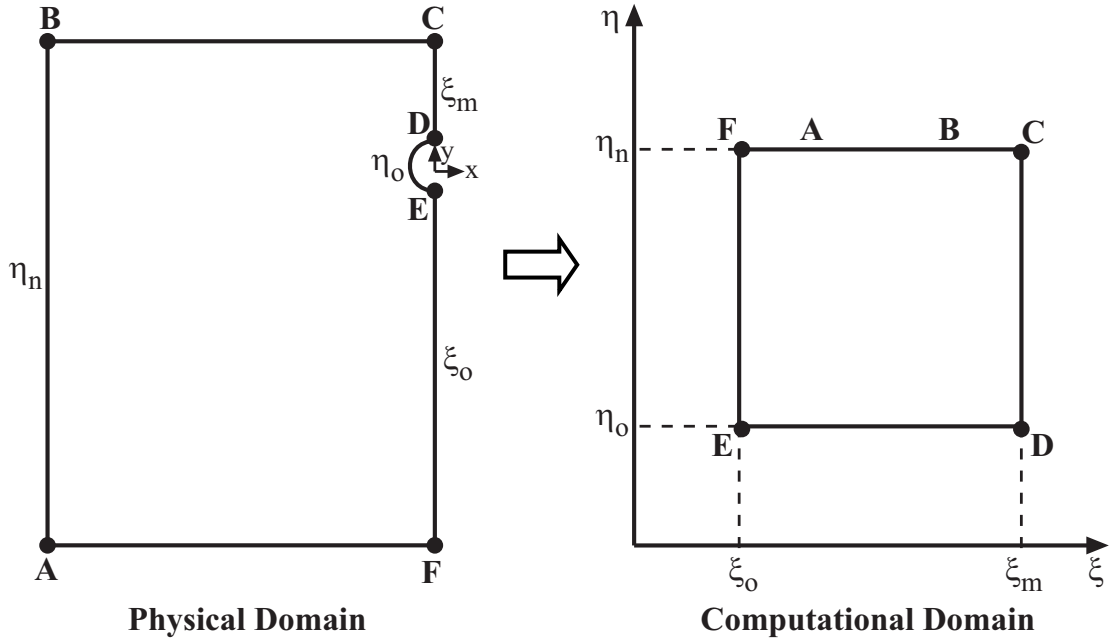
Figure 2.4 Physical and computational domains of the geometry considered.

ED and FABC represent constant η_o and η_n lines, respectively. Sample meshes are then constructed with different combinations of the grid control functions.

For the purpose of comparison, the meshes shown in Figure 2.5(a) and 2.6(a) are generated using the Laplace equation (i.e., $\overline{P} = \overline{Q} = 0$). The following grid control functions (a special case of Eqn. [2.4]) are introduced:

$$\overline{P}(\xi,\eta) = -\overline{ap}\,\text{sign}(\xi-61)\exp(-\overline{cp}|\xi-61|)$$
$$-\overline{bp}\,\text{sign}(\xi-61)\exp\left\{-\overline{dp}\left[(\xi-61)^2+(\eta-101)^2\right]^{1/2}\right\}, \qquad [2.10a]$$

$$\overline{Q}(\xi,\eta) = -\overline{aq}\,\text{sign}(\eta-101)\exp(-\overline{cq}|\eta-101|)$$
$$-\overline{bq}\,\text{sign}(\eta-101)\exp\left\{-\overline{dq}\left[(\xi-61)^2+(\eta-101)^2\right]^{1/2}\right\}. \qquad [2.10b]$$

where the amplitude and decay factors used to generate the mesh are summarized in

53

(a)

(b)

(c)

(d)
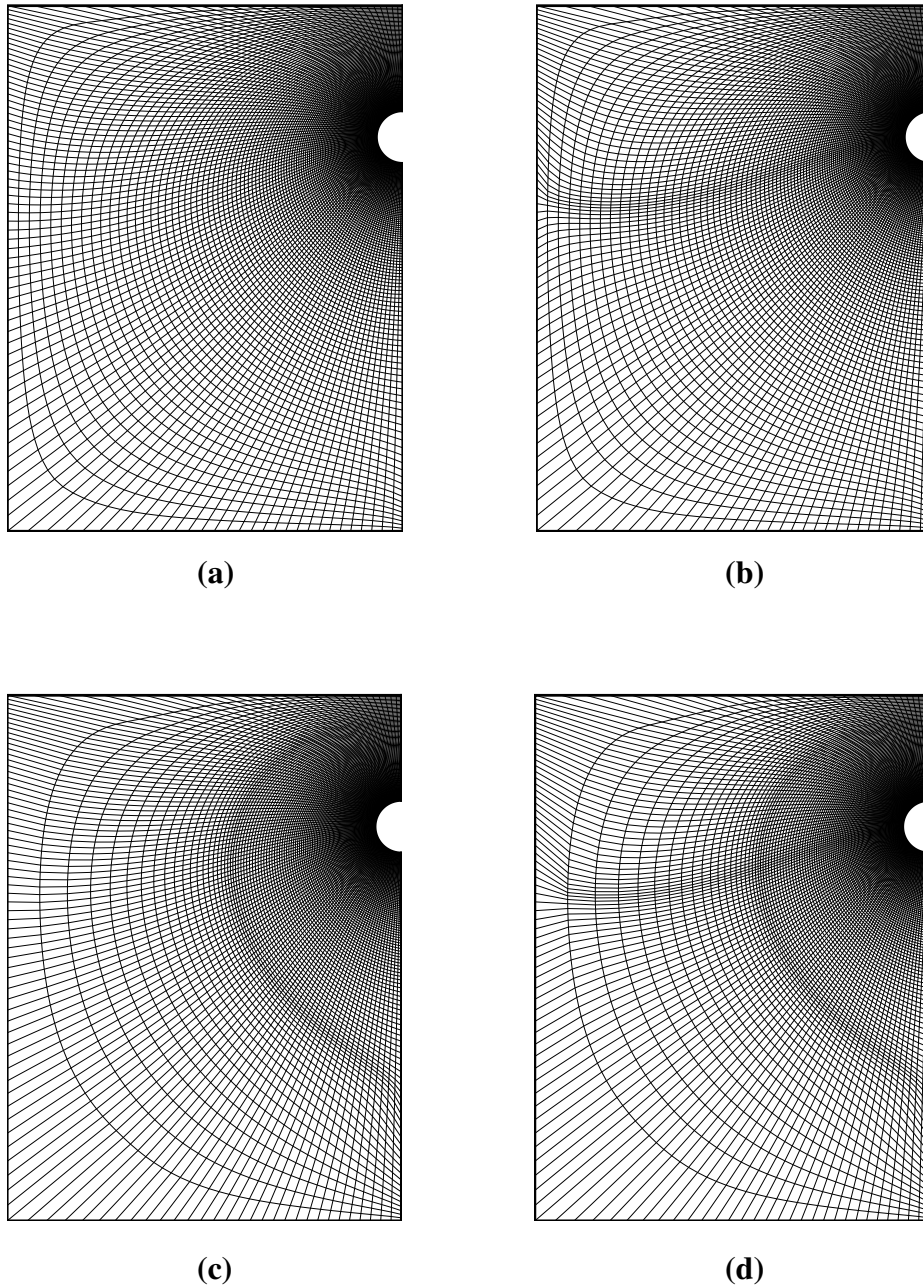
Figure 2.5 Mesh generated with (a) no grid control function ($\overline{P} = \overline{Q} = 0$);
(b) grid control function $\overline{P}$ attracted to line $\xi = 61$;
(c) grid control function $\overline{Q}$ attracted to line $\eta = 101$;
(d) both grid control functions $\overline{P}$ and $\overline{Q}$ attracted to lines $\xi = 61$ and $\eta = 101$
[number of nodes = 121×121].

(a)

(b)

(c)

(d)
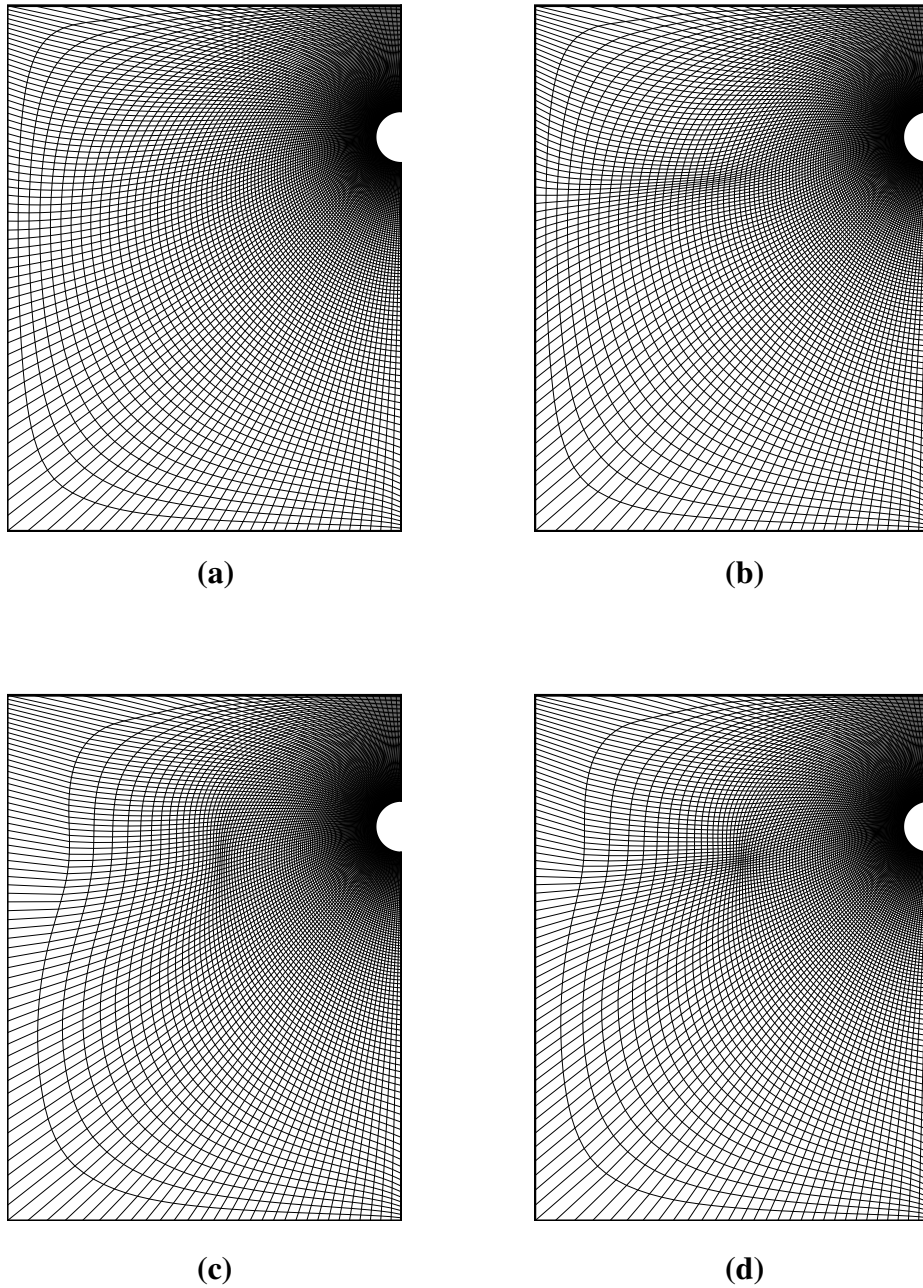
Figure 2.6 Mesh generated with (a) no grid control function ($\overline{P} = \overline{Q} = 0$);
(b) grid control function $\overline{P}$ attracted to point ($\xi = 61$, $\eta = 101$);
(c) grid control function $\overline{Q}$ attracted to point ($\xi = 61$, $\eta = 101$);
(d) both grid control functions $\overline{P}$ and $\overline{Q}$ attracted to point ($\xi = 61$, $\eta = 101$)
[number of nodes = 121×121].

Table 2.1. Figure 2.5(b) illustrates the attraction of ξ-coordinate lines towards $\xi = 61$ while Figure 2.5(c) shows the attraction of η-coordinate lines towards $\eta = 101$. The simultaneous effects of both grid control functions $\overline{P}$ and $\overline{Q}$ are shown in Figure 2.5(d).

On the other hand, the attraction of coordinate lines towards a single point ($\xi = 61$, $\eta = 101$) is illustrated in Figure 2.6. In particular, the grid control function $\overline{P}$ is employed to attract ξ-coordinate lines towards point ($\xi = 61$, $\eta = 101$) in Figure 2.6(b) while grid control function $\overline{Q}$ is employed to attract η-coordinate lines towards point ($\xi = 61$, $\eta = 101$) in Figure 2.6(c). Both grid control functions are used in Figure 2.6(d) for the concentration of coordinate lines. In this section, the concentration of coordinate lines towards a specified line or point is demonstrated separately. It is noted that they can be employed simultaneously to obtain the level of grid concentration needed.

Table 2.1 Amplitude and decay factors employed in Figures 2.5, 2.6 and 2.8.

Figure No.	$\overline{ap}$	$\overline{bp}$	$\overline{cp}$	$\overline{dp}$	$\overline{aq}$	$\overline{bq}$	$\overline{cq}$	$\overline{dq}$	Remarks
2.5a	---	---	---	---	---	---	---	---	No Grid Control Functions
2.5b	10	---	0.25	---	---	---	---	---	Line Attraction with $\overline{P}$
2.5c	---	---	---	---	10	---	0.25	---	Line Attraction with $\overline{Q}$
2.5d	10	---	0.25	---	10	---	0.25	---	Line Attraction with $\overline{P}$ & $\overline{Q}$
2.6a	---	---	---	---	---	---	---	---	No Grid Control Functions
2.6b	---	20	---	0.2	---	---	---	---	Point Attraction with $\overline{P}$
2.6c	---	---	---	---	---	20	---	0.2	Point Attraction with Q
2.6d	---	20	---	0.2	---	20	---	0.2	Point Attraction with $\overline{P}$ & $\overline{Q}$
2.8	---	30	---	0.1	---	30	---	0.1	Point Attraction with $\overline{P}$ & $\overline{Q}$

2.5 Grid Quality

For a given geometry, often there is more than one way to generate the mesh. Two different meshes are constructed and shown in Figure 2.7 for the geometry considered in the present study. The first mesh is constructed as described in Chapter 2.4 (same as Figure 2.4). That is, the mapping is chosen such that segments EF and DC are constant ξ-coordinate lines while segments ED and FABC represent constant η_o and η_n lines, respectively. The grid is generated with only grid control function $\overline{Q}$ to attract η-coordinate lines towards η_o and η_n lines:

$$\overline{P}(\xi,\eta) = 0, \tag{2.11a}$$

$$\overline{Q}(\xi,\eta) = -\overline{aq}\left\{ \text{sign}(\eta - \eta_o)\exp\left(-\overline{cq}|\eta - \eta_o|\right) + \text{sign}(\eta - \eta_n)\exp\left(-\overline{cq}|\eta - \eta_n|\right) \right\} \tag{2.11b}$$

where $\overline{aq}$ and $\overline{cq}$ are set to 10 and 0.25, respectively. The second mapping is constructed such that segments AB and FEDC are constant ξ-coordinate lines while segments AF and BC represent constant η-coordinate lines. No grid control function is employed to obtain this grid.

Since there are several possible ways of generating meshes for a given geometry, the question is what guidelines one should follow in generating the mesh. Generally the grid construction is problem dependent. The rule of thumb is to construct a grid which closely resembles the actual flow conditions (i.e., grid profile aligned with streamlines or isotherms). For the present study, the first mesh would be ideal for simulating flows induced from a heated cylinder with an impermeable top boundary (segment BC). On the other hand, the mesh generated using the second

Mapping #1
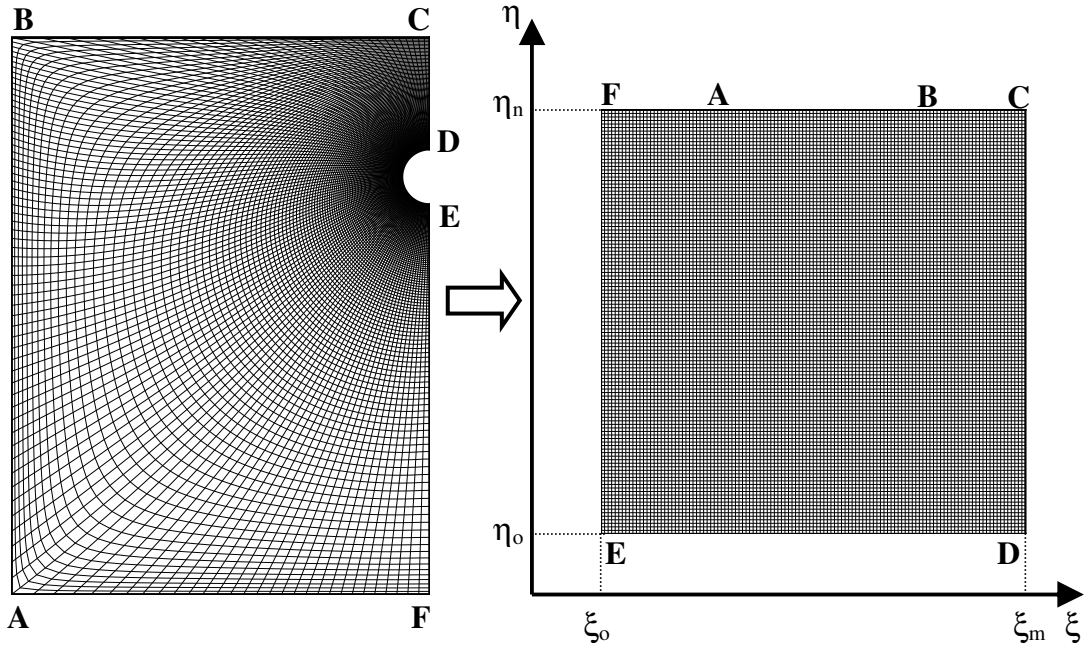
Mapping #2
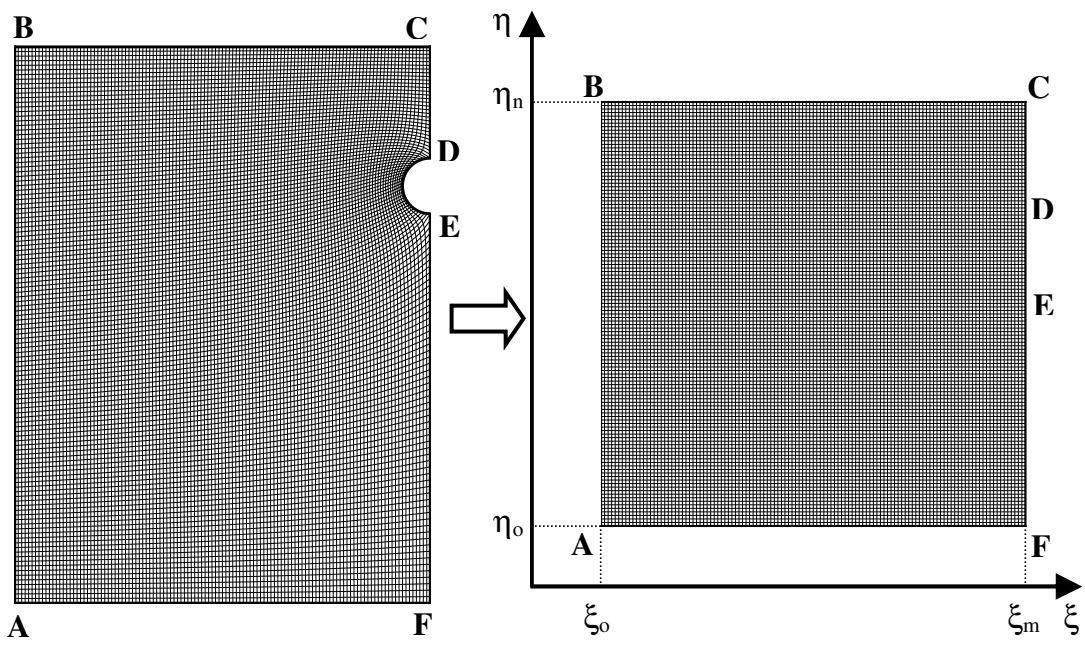
Figure 2.7 Two different mappings for a given geometry [number of nodes = 121×121].

mapping would be better suited for a permeable top boundary.

Generally speaking, the accuracy of the numerical results depends highly on the grids. The generated grid should not be highly distorted or with extreme skewness. It is also desirable to maintain the grid as much orthogonal as possible. The computational results obtained should be independent of the grid. It is always a good practice to undergo a grid refinement test to find the optimal number of nodes so that one can achieve a balance between the accuracy of the results and computational efficiency in terms of time and cost.

As briefly mentioned in Chapter 2.2, grid generation using Poisson equation no longer guarantees the mapping is one-to-one. The selection of the amplitude and decay factors becomes an important factor to avoid overlapped or folded grid. Figure 2.8 shows a folded grid generated using grid control functions $\overline{P}$ and $\overline{Q}$ to attract the coordinate lines to point (ξ = 61, η = 101). This is essentially the same functions employed in Figure 2.6(d) but with different values of the amplitude and decay factors ($\overline{bp} = \overline{bq}$ = 30, $\overline{dp} = \overline{dq}$ = 0.1). As seen from Figure 2.8, this combination of the amplitude and decay factors greatly amplifies the extent of the grid attraction. As a result, a folded grid with overlapped coordinate points is generated.
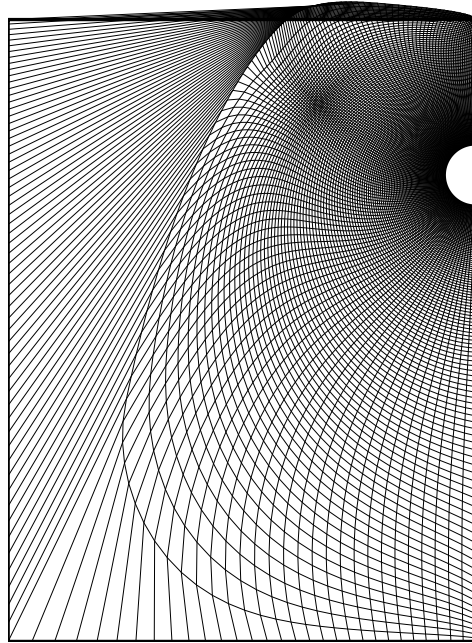
Figure 2.8 Folded grid generated with both grid control functions $\overline{P}$ and $\overline{Q}$ for attracting the coordinate lines to point ($\xi = 61$, $\eta = 101$) [number of nodes = 121×121].

CHAPTER **III**

HEAT CONDUCTION AND NATURAL CONVECTION FROM A PIPE BURIED IN A HOMOGENEOUS POROUS MEDIUM

3.1 Introductory Remarks

Heat transfer from a buried pipe has been a subject of great interest for many decades because of its important applications in engineering, which include the underground pipelines for gas and oil, power cables and the disposal of nuclear wastes. For these applications, the surface temperature of pipe or canister is usually higher than that of surroundings due to artificial (reduction of viscosity for oil transportation) or natural (ohm heating for transmission cables and decay heating for nuclear wastes) causes. In this chapter, the numerical results of heat conduction are first presented. The study of natural convection is then conducted to investigate the flow and heat transfer induced by buoyancy in a porous medium. The numerical schemes employed to tackle the present problem are described in details. The conclusions are expressed in generic terms such that they can also be applied to other similar situations (e.g., mixed convection study in Chapter 5). Through the studies of heat conduction and natural convection, one can determine the appropriate domain size for the porous medium which can accurately represent a semi-infinite medium. The results obtained in this chapter not only validate the present numerical approach but also serve as a basis for comparison with the results obtained from subsequent studies in the later chapters.

3.2 Heat Conduction

One of the earliest studies concerning heat transfer from a buried pipe was performed by Eckert and Drake (1959), in which they determined the analytical solutions using the heat source and sink method. For the present study, it is appropriate to begin with solving the conduction problem numerically. The results thus obtained can be served as a validation of the proposed mathematical model and used as a reference in the determination of the proper dimensions for the present model to represent a semi-infinite medium.

3.2.1 Problem Statement and Mathematical Formulation

Consider a cylindrical heat source with a radius of r_i embedded in a porous medium at a depth of d beneath the top surface (Figure 3.1). This cylindrical heat source may represent a heated pipe for crude oil transportation, a heated electric
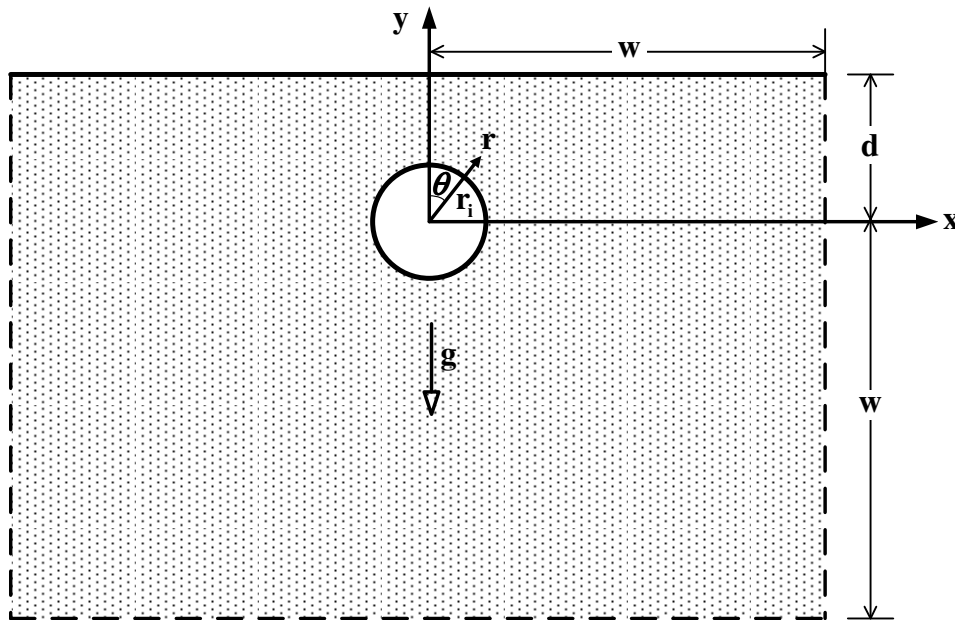
Figure 3.1 A horizontal heated pipe embedded in a porous medium.

cable or a nuclear waste storage container. Both isothermal and convective conditions are considered for the top surface while insulated conditions are applied to all other boundaries. Since heat conduction is the primary heat transfer mode of interest here, the two-dimensional steady-state heat conduction equation expressed in Cartesian coordinates is given by

$$\frac{\partial^2 T}{\partial x^2} + \frac{\partial^2 T}{\partial y^2} = 0. \tag{3.1}$$

The above equation can be written in dimensionless form as

$$\frac{\partial^2 \Theta}{\partial X^2} + \frac{\partial^2 \Theta}{\partial Y^2} = 0, \tag{3.2}$$

where the temperature is normalized by the temperature difference between the pipe and the top surface for isothermal top boundary (or the temperature difference between the pipe and the ambient air for convective top boundary, $\Theta = \dfrac{T - T_c}{T_h - T_c}$). The radius of the buried pipe is taken as the characteristic length. The heat conduction equation can then be transformed to the computational domain using the transformation described in Chapter 2, and the equation becomes

$$\nabla^2_{\xi\eta}\Theta = 0, \tag{3.3a}$$

where $\quad \nabla^2_{\xi\eta} = \dfrac{\overline{\alpha}}{J^2}\dfrac{\partial^2}{\partial\xi^2} - \dfrac{2\overline{\beta}}{J^2}\dfrac{\partial^2}{\partial\xi\partial\eta} + \dfrac{\overline{\gamma}}{J^2}\dfrac{\partial^2}{\partial\eta^2} + \overline{P}\dfrac{\partial}{\partial\xi} + \overline{Q}\dfrac{\partial}{\partial\eta} \tag{3.3b}$

is the Laplacian operator in the computational domain. Grid control function $\overline{Q}$ is employed to control the grid line distribution in the direction of η toward the boundaries η_0 and η_n (Thompson, 1982),

$$\overline{Q} = -A_1 \{ \text{sign}(\eta - \eta_0) \exp[-A_2 |\eta - \eta_0|]$$
$$+ \text{sign}(\eta - \eta_n) \exp[-A_2 |\eta - \eta_n|] \}, \qquad [3.4]$$

where A_1 and A_2 are the amplitude and decay factors, respectively. No grid control is

needed in the direction of ξ (i.e., $\overline{P} = 0$). The values of A_1 and A_2 for various domain

sizes (w/r_i) are summarized in Table 3.1. The grid generated for a domain size of w/r_i

= 30 is shown in Figure 3.2 using 121 x 121 nodes.

Table 3.1 Amplitude factor A_1 and decay factor A_2 values employed in this study.

w/r_i	A_1	A_2
15	10.0	0.25
20	8.0	0.50
25	5.0	0.50
30	4.0	0.50
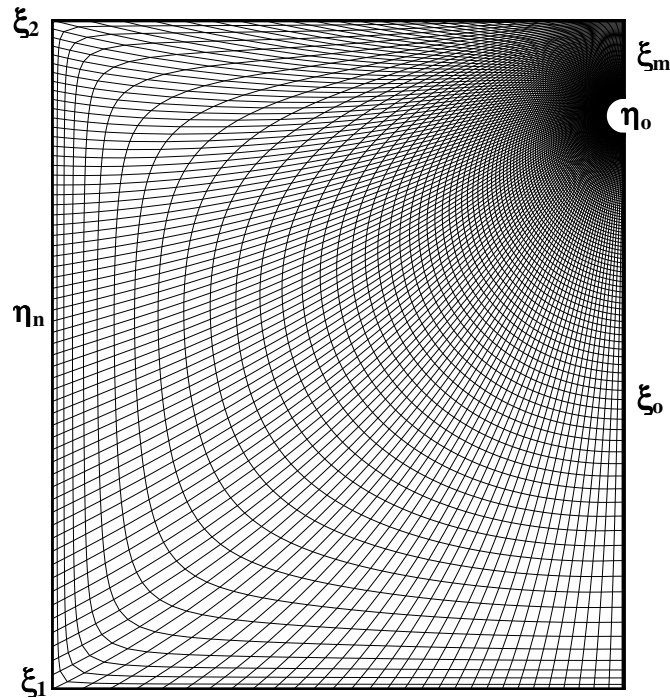
Figure 3.2 Grid for the domain with w/r_i = 30 and 121 x 121 nodes.

3.2.2 Boundary Conditions and Numerical Methods

For the present study, the dimensionless burial depth is fixed at five (i.e., d/r_i = 5). Various geometry dimensions (i.e., w/r_i = 15, 20, 25 and 30) are tested to obtain the optimum size for the domain to represent a semi-infinite medium. The cylindrical heat source is assumed to maintain at a higher temperature while both isothermal and convective conditions are considered for the top surface. Insulated conditions are applied to all other boundaries. Only one half of the domain ($-w \leq x \leq 0$ and $-w \leq y \leq d$) is considered for computations due to symmetry. The dimensionless boundary conditions are illustrated in Figure 3.3.

Isothermal: $\Theta = 0$; Convective: $\dfrac{\partial \Theta}{\partial Y} = -Bi \cdot \Theta$

$\dfrac{\partial \Theta}{\partial X} = 0$

$\Theta = 1$

$\dfrac{\partial \Theta}{\partial X} = 0$

$\dfrac{\partial \Theta}{\partial X} = 0$

$\dfrac{\partial \Theta}{\partial Y} = 0$
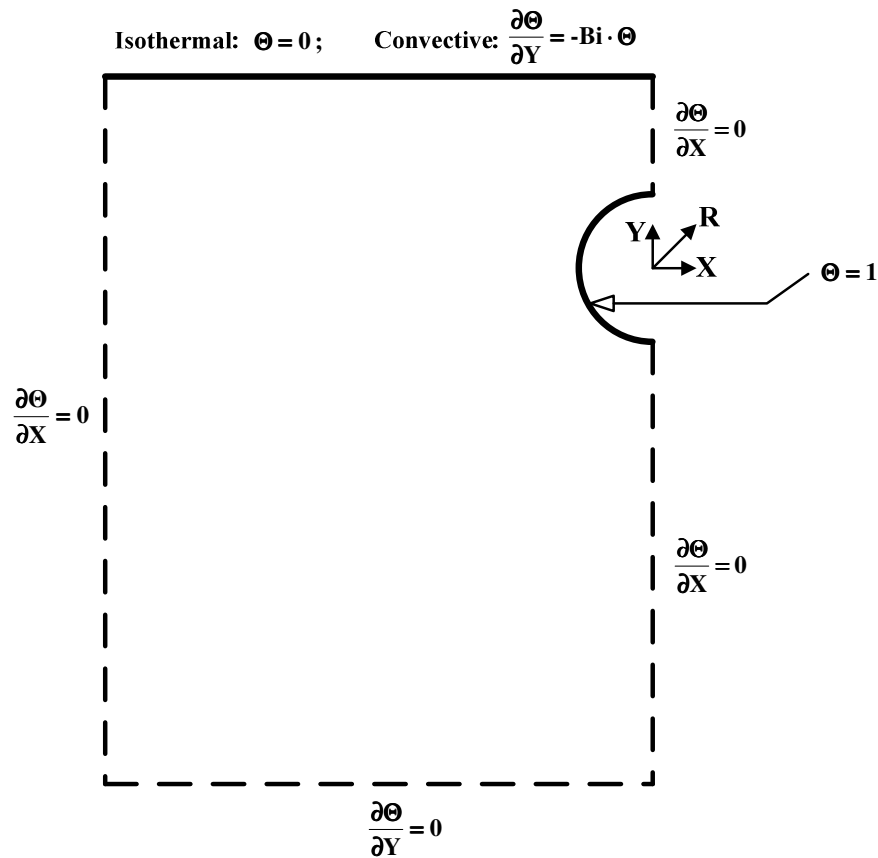
Figure 3.3 Dimensionless boundary conditions for the study of heat conduction from a buried pipe.

For the convective boundary condition on the top surface, it is expressed in terms of the Biot number, which is defined as follows,

$$Bi = \frac{hr_i}{k},$$ [3.5]

where h is the convective heat transfer coefficient and k is the thermal conductivity of the medium. The Biot number represents the ratio of heat convection at the top surface to heat conduction within the porous medium.

The discretization of the governing equation (Eqn. [3.3]) follows the finite difference method described in Chapter 2.3. The discretized equation for the temperature is given by

$$\Theta_P = A_1(\Theta_{SE} - \Theta_{NE} - \Theta_{SW} + \Theta_{NW}) + (A_2 + A_4\overline{P})\Theta_E + (A_2 - A_4\overline{P})\Theta_W$$
$$+ (A_3 + A_4\overline{Q})\Theta_N + (A_3 - A_4\overline{Q})\Theta_S,$$ [3.6]

where the A coefficients are defined in Eqn. [2.7]. The numerical procedure for solving the above algebraic equation has been given previously; hence the discussion is omitted here for brevity. The algorithm for the numerical procedure is summarized using the flow chart in Figure 3.4.

The heat transfer results are expressed in the dimensionless forms as follows

$$Q_{in} = -\int_\pi^{2\pi} \frac{\partial \Theta}{\partial R}\Big|_{R=1} d\theta,$$ [3.7a]

and
$$Q_{out} = -\int_{-w/r_i}^0 \frac{\partial \Theta}{\partial Y}\Big|_{Y=d/r_i} dX,$$ [3.7b]

where Q_{in} is the heat transfer through the pipe and Q_{out} represents heat loss through the top surface. Since all other boundaries are insulated, Q_{in} should equal to Q_{out} in

```
                    ┌──────────────┐
                    │    Start     │
                    └──────────────┘
                           │
                           ▼
              ╱─────────────────────────╲
             ╱  Input the Grid Generated  ╲
             ╲   and the Relaxation         ╱
              ╲   Parameters               ╱
               ╲──────────────────────────╱
                           │
                           ▼
              ╱─────────────────────────╲
             ╱    Input the Boundary      ╲
             ╲      Conditions             ╱
               ╲──────────────────────────╱
                           │
                           ▼
         ┌─────────────────────────────────┐
         │ Solving for the Temperature: Θ(i,j) │
         └─────────────────────────────────┘
                           │
                           ▼
                      ◇ decision ◇
                                              No
                           │ Yes
                           ▼
              ╱─────────────────────────╲
             ╱  Output the Required Results ╲
               ╲──────────────────────────╱
                           │
                           ▼
                    ┌──────────────┐
                    │     End      │
                    └──────────────┘
```

$$\Phi_{i,j}^{k+1} = \Phi_{i,j}^{k} + r\left(\phi_{i,j}^{k+1} - \Phi_{i,j}^{k}\right)$$

Is $\max \left|\Phi_{i,j}^{k+1} - \Phi_{i,j}^{k}\right| \leq 10^{-4}$?

For $\Phi = \Theta$
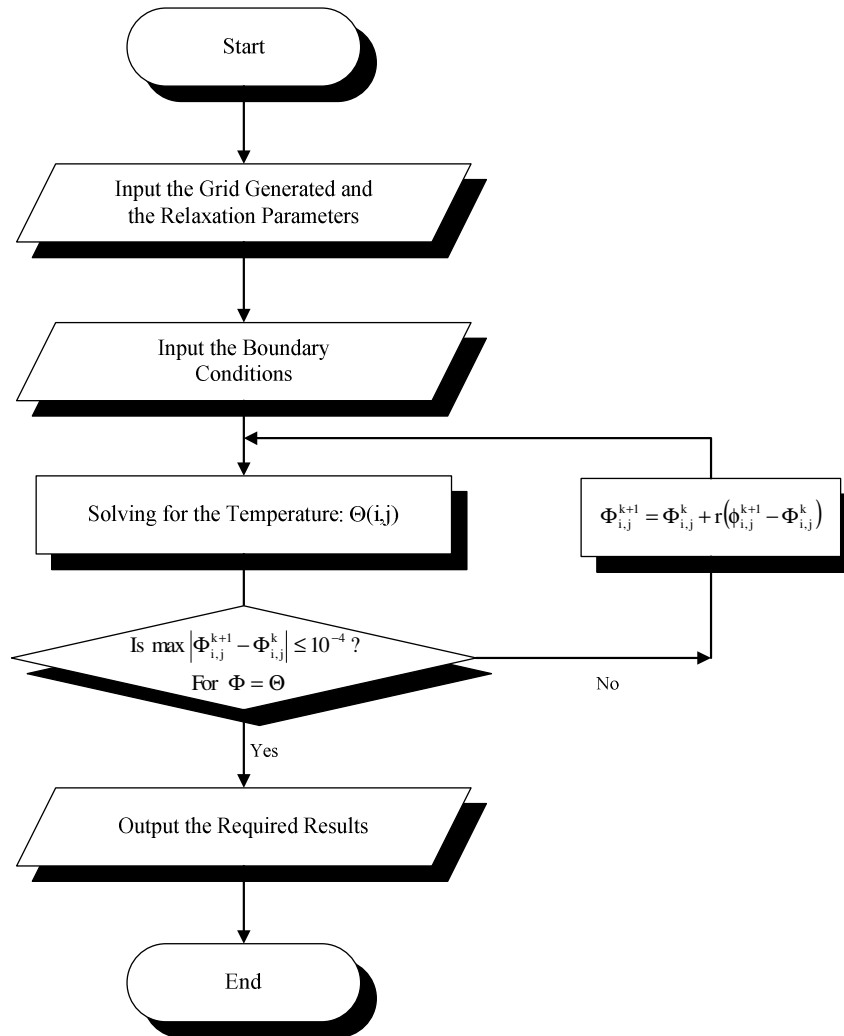
Figure 3.4 Flow chart of the numerical procedures for the study of conduction from a buried pipe.

order to achieve an energy balance.

3.2.3 Results and Discussion

The results for the isothermal top surface are first examined. Based on the analytical study of Eckert and Drake (1959), it has been found that for $d/2r_i \gg 1$, the heat transfer from the cylinder can be evaluated by

$$Q = \frac{2\pi kL(T_h - T_c)}{\ln(2d/r_i)} . \qquad [3.8]$$

This result is often expressed in terms of the conduction shape factor given in most heat transfer textbooks (e.g., Incropera and DeWitt, 1996; Mills, 1999). For comparison with the present numerical results, the equation is recast into a dimensionless form. For $d/r_i = 5$ the dimensionless heat transfer rate from a half cylinder can be calculated by

$$Q_{\substack{\text{dimensionless,} \\ \text{half domain}}} = \frac{Q}{2L(T_h - T_c)k} = \frac{\pi}{\ln(2d/r_i)} = \frac{\pi}{\ln(10)} = 1.36 \qquad [3.9]$$

The dimensionless heat transfer results obtained from the present study for different physical domain sizes are summarized in Table 3.2. The energy balance is satisfied within 1% and the amount of heat transfer approaches 1.43 as the domain size is increased. The results agree quite well with the analytical solution by Eckert and Drake (1959), with only 5% deviation. The temperature distributions around a buried heat source obtained analytically by Eckert and Drake (1959) are reproduced in Figure 3.5. It is noted that the temperature fields are represented by concentric circles. The centers of these circular isotherms shift downward as the radii increase. Same

Table 3.2 Heat conduction results for different physical domain size.

w/r_i	Q_{in}	Q_{out}	% Err
15	1.35	1.34	0.4
20	1.42	1.41	0.7
25	1.43	1.42	0.5
30	1.43	1.43	0.3
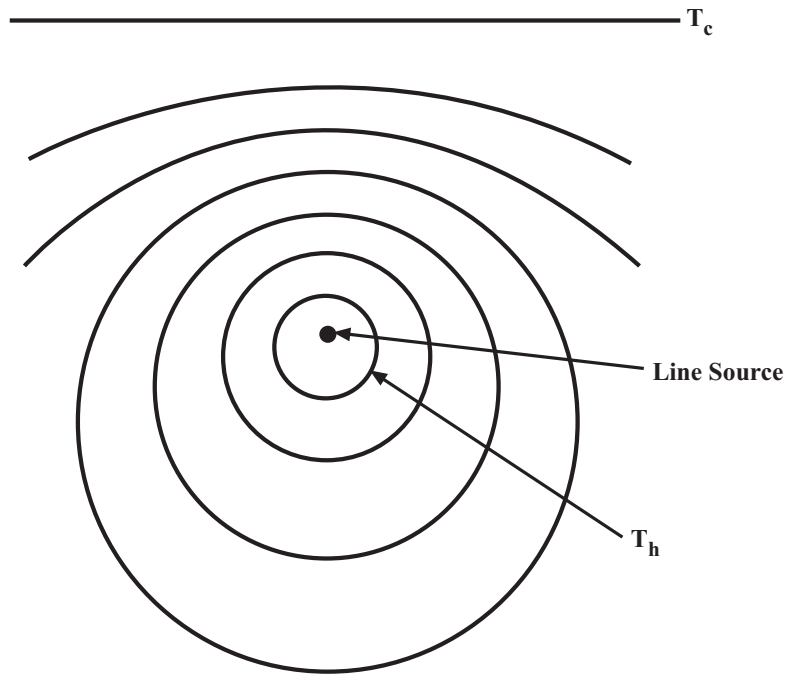
Figure 3.5 Analytical temperature distribution around
a buried heat source [Eckert and Drake (1959)].
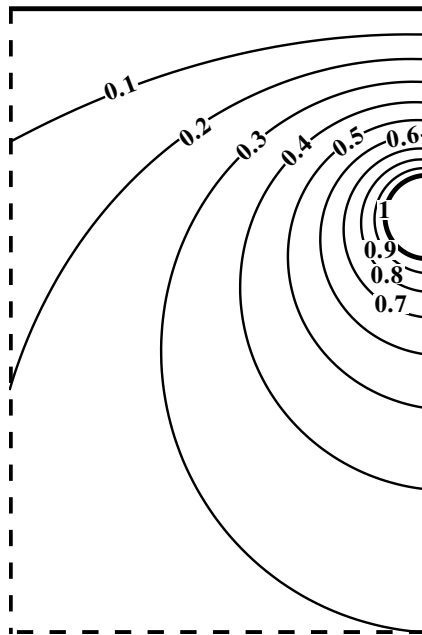
Figure 3.6 Temperature field for conduction with
isothermal top surface ($\Delta\Theta = 0.1$).

trend can be observed from the present numerical results shown in Figure 3.6. In this chapter, only partial results are presented in the figures ($-10 \leq X \leq 0$, $-10 \leq Y \leq 5$) in order to better observe the temperature field at the vicinity of the buried pipe.

Once again as indicated in Table 3.2, the heat transfer approaches an asymptotic value of 1.43 as the domain size is increased. However, it is not conclusive to state that a domain with $w/r_i = 30$ is sufficient to represent a semi-infinite medium based on the conduction results alone. The results obtained herein at least provides clues for the necessary domain size, confirmation still awaits the study of natural convection.

The results for convective top surface are discussed next. The temperature fields for various Biot numbers are presented in Figure 3.7. When the convective heat transfer is sufficiently small (i.e., $Bi \leq 1$), virtually no heat is transferred through the medium. As the Biot number increases (i.e., a highly convective top surface), the temperature at the top surface approaches that of the ambient air. The convective condition essentially reduces to an isothermal boundary condition when the Biot number becomes infinitely large. Based on the heat transfer results (Table 3.3) and the isotherms (Figure 3.7), it is realized that when Biot number has a value of 10 or greater, the results depict those of isothermal top condition. Note the similarity of temperature distributions in Figure 3.7(f) and Figure 3.6. The dimensionless heat transfer rate also approaches 1.43 as the Biot number increases.

3.3 Natural Convection

Heat conduction involving a buried heated pipe in a semi-infinite porous

70

(a) Bi = 0.01 **(b) Bi = 0.05** **(c) Bi = 0.1**
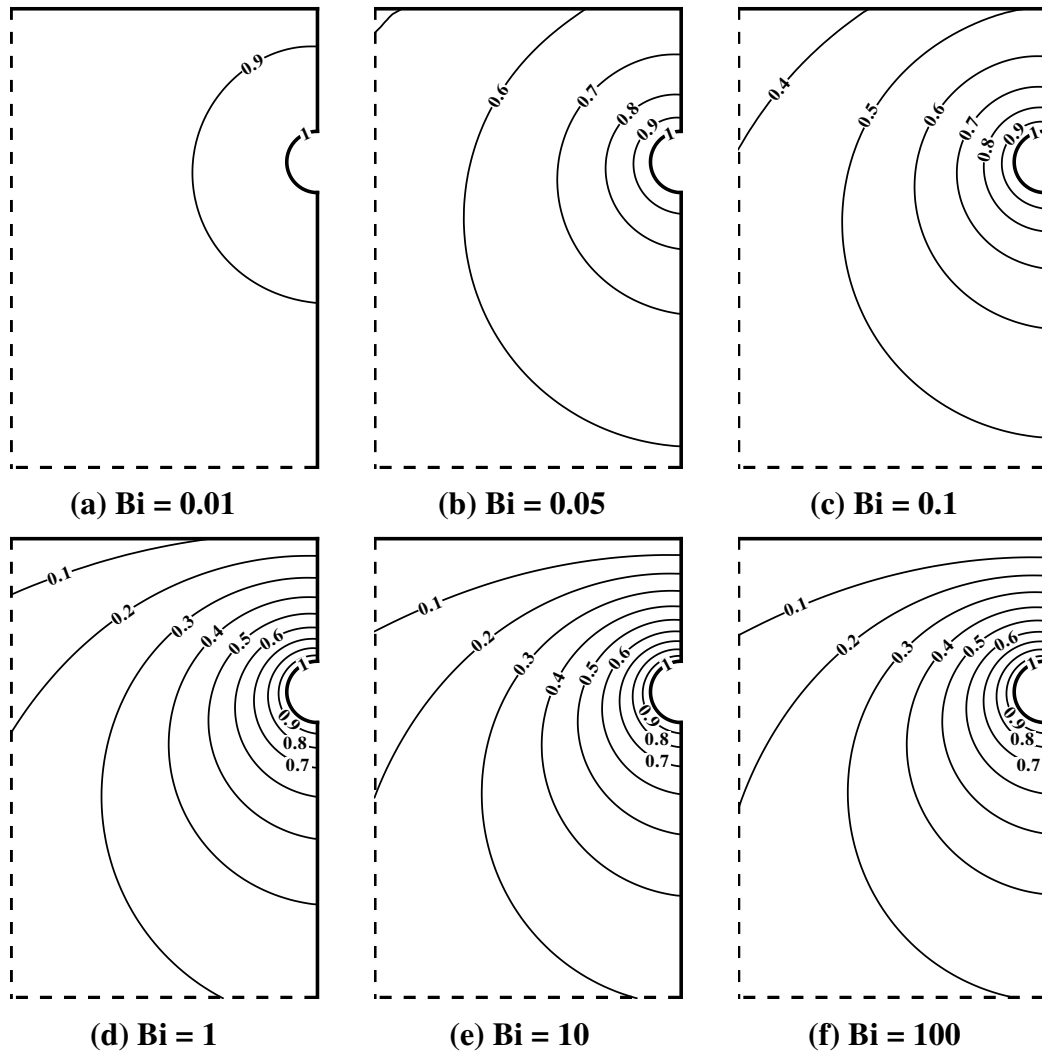
(d) Bi = 1 **(e) Bi = 10** **(f) Bi = 100**

Figure 3.7 Temperature fields for conduction with convective top surface (a) Bi = 0.01, (b) Bi = 0.05, (c) Bi = 0.1, (d) Bi = 1, (e) Bi = 10, (f) Bi = 100 ($\Delta\Theta = 0.1$).

Table 3.3 Heat transfer results for conduction with convective top surface ($w/r_i = 30$).

Bi	Q_{in}	Q_{out}	% Err
0.01	0.24	0.24	0.7
0.05	0.71	0.71	1.2
0.1	0.93	0.94	1.7
1.0	1.35	1.35	0.3
10.0	1.41	1.44	1.5
100.0	1.43	1.44	1.1

medium has been considered in the previous section. However, since the porous medium is saturated with fluid, a buoyancy-induced flow is likely to initiate when the temperature difference is large. Therefore, it is crucial to take into the account of the buoyancy effects. Previous studies have considered various configurations and models of porous media. For example, Bau (1984) has obtained analytical solutions for heat convection from a pipe buried in a semi-infinite porous medium using the perturbation method. Farouk and Shayer (1988) as well as Christopher and Wang (1993) have obtained numerical results using Darcy and non-Darcy formulations, respectively. Experimental results have been reported by Fernandez and Schrock (1982) as well as Fand et al. (1986). Particularly, an excellent review of this subject has been presented by Nield and Bejan (1999).

3.3.1 Problem Statement and Mathematical Formulation

The model considered here is the same as shown previously in Figure 3.1. The top surface is impermeable and isothermal (T_c) while the pipe is maintained at a higher temperature T_h. Again, only one half of the physical domain is considered for computations due to symmetry. For the present study, it is assumed that the properties of the fluid and porous medium are homogeneous and isotropic. The solid matrix of the porous medium is in local thermodynamics equilibrium with the saturating fluid. It is further assumed that Darcy's law is applicable and thus the inertial and viscous effects are neglected.

The governing equations based on Darcy's law in Cartesian coordinate system are given by

Continuity:
$$\frac{\partial u}{\partial x} + \frac{\partial v}{\partial y} = 0,$$
[3.10]

X-Momentum:
$$u = -\frac{K}{\mu}\frac{\partial p}{\partial x},$$
[3.11]

Y-Momentum:
$$v = -\frac{K}{\mu}\left[\frac{\partial p}{\partial y} + \rho g\right],$$
[3.12]

Energy Equation:
$$u\frac{\partial T}{\partial x} + v\frac{\partial T}{\partial y} = \alpha\left[\frac{\partial^2 T}{\partial x^2} + \frac{\partial^2 T}{\partial y^2}\right].$$
[3.13]

In accordance with Darcy's law, the volume-averaged velocity is directly proportional to the pressure gradient and the permeability K, but inversely proportional to the viscosity of the saturating fluid μ. α in the energy equation represents the thermal diffusivity of the porous medium.

All physical properties are assumed constant except the density in the body force term of the y-momentum equation. Boussinesq approximation is invoked to account for the changes in density due to temperature difference, and it is assumed that density is a linear function of the temperature difference:

$$\rho = \rho_c\left[1 - \beta_T(T - T_c)\right],$$
[3.14]

where β_T is the coefficient of thermal expansion. This approximation is valid only for small temperature difference, i.e., $(T - T_c) \leq O(1)$ (Gebhart el al., 1988).

The following dimensionless parameters are introduced to normalize the governing equations.

$$X = \frac{x}{r_i}, \qquad Y = \frac{y}{r_i}, \qquad U = \frac{u}{\alpha/r_i}, \qquad V = \frac{v}{\alpha/r_i},$$
[3.15a, b, c, d]

$$\Theta = \frac{T - T_c}{T_h - T_c}, \qquad Ra = \frac{Kg\beta_T (T_h - T_c) r_i}{\alpha\nu}. \qquad\qquad [3.15e, f]$$

The characteristic length is the radius of the buried pipe while the velocity is normalized using α/r_i. Temperature is normalized with the temperature difference between the buried pipe and the top surface. Ra is the modified Rayleigh number, and it represents the ratio of buoyancy force to viscous force.

Then, stream function is introduced to further simplify the governing equations,

$$U = \frac{\partial\Psi}{\partial Y}, \qquad V = -\frac{\partial\Psi}{\partial X}. \qquad\qquad [3.16a, b]$$

The continuity equation is satisfied automatically by introducing stream function.

After cross-differentiating the momentum equations (Eqn. [3.11] and [3.12]) to eliminate the pressure terms, one obtains the dimensionless governing equations in terms of stream function as follows.

$$\frac{\partial^2\Psi}{\partial X^2} + \frac{\partial^2\Psi}{\partial Y^2} = -Ra\frac{\partial\Theta}{\partial X}, \qquad\qquad [3.17]$$

$$\frac{\partial\Psi}{\partial Y}\frac{\partial\Theta}{\partial X} - \frac{\partial\Psi}{\partial X}\frac{\partial\Theta}{\partial Y} = \frac{\partial^2\Theta}{\partial X^2} + \frac{\partial^2\Theta}{\partial Y^2}. \qquad\qquad [3.18]$$

The above governing equations are transformed to the computational domain by employing the elliptic transformation described in Chapter 2. The resultant equations are given by

$$\nabla^2_{\xi\eta}\Psi = -\frac{Ra}{J}\left[\frac{\partial\Theta}{\partial\xi}\frac{\partial Y}{\partial\eta} - \frac{\partial\Theta}{\partial\eta}\frac{\partial Y}{\partial\xi}\right], \qquad\qquad [3.19]$$

$$\nabla_{\xi\eta}^2 \Theta = \frac{1}{J}\left[\frac{\partial\Theta}{\partial\xi}\frac{\partial\Psi}{\partial\eta} - \frac{\partial\Theta}{\partial\eta}\frac{\partial\Psi}{\partial\xi}\right],$$

[3.20]

where $\quad \nabla_{\xi\eta}^2 = \dfrac{\overline{\alpha}}{J^2}\dfrac{\partial^2}{\partial\xi^2} - \dfrac{2\overline{\beta}}{J^2}\dfrac{\partial^2}{\partial\xi\partial\eta} + \dfrac{\overline{\gamma}}{J^2}\dfrac{\partial^2}{\partial\eta^2} + \overline{P}\dfrac{\partial}{\partial\xi} + \overline{Q}\dfrac{\partial}{\partial\eta}.$

[3.21]

3.3.2 Boundary Conditions

The governing equations are then solved with respect to the prescribed boundary conditions. For this study, the buried pipe is assumed to be impermeable; hence the normal velocity vanishes while a slip velocity is allowed along the pipe surface according to Darcy's formulation. The pipe is maintained at a higher temperature while the top surface is impermeable and isothermal. In view of the symmetry of the mathematical model, only half of the domain is considered for computations. Hence, symmetrical conditions are applied to the vertical mid-plane. For the far-field boundaries (i.e., left and bottom boundaries), it is assumed that the domain considered is sufficiently large so that adiabatic conditions are appropriate, and the tangential velocities vanish. This is essentially implying that these boundaries are permeable (constant pressure) such that fluid flows past the boundaries perpendicularly.

Mathematically, the boundary conditions are stated as follows.

At $r = r_i$, $\pi \le \theta \le 2\pi$, $\qquad\qquad u_r = 0$, $\qquad T = T_h$. [3.22a, b]

At $y = d$, $-w \le x \le 0$, $\qquad\qquad v = 0$, $\qquad T = T_c$. [3.22c, d]

At $x = -w$, $-w \le y \le d$, $\qquad\qquad v = 0$, $\qquad \dfrac{\partial T}{\partial x} = 0$. [3.22e, f]

At $y = -w$, $-w \leq x \leq 0$, $u = 0$, $\dfrac{\partial T}{\partial y} = 0$.   [3.22g, h]

At $x = 0$, $r_i \leq y \leq d$, $u = 0$, $\dfrac{\partial T}{\partial x} = 0$.   [3.22i, j]

At $x = 0$, $-r_i \leq y \leq -w$, $u = 0$, $\dfrac{\partial T}{\partial x} = 0$.   [3.22k ,l]

Figure 3.8 shows a schematic of the dimensionless boundary conditions. The boundary conditions in terms of the dimensionless parameters and stream function are given below.

At $R = 1$, $\pi \leq \theta \leq 2\pi$, $\Psi = 0$, $\Theta = 1$.   [3.23a, b]

At $Y = d/r_i$, $-w/r_i \leq X \leq 0$, $\Psi = 0$, $\Theta = 0$.   [3.23c, d]

At $X = -w/r_i$, $-w/r_i \leq Y \leq d/r_i$, $\dfrac{\partial \Psi}{\partial X} = 0$, $\dfrac{\partial \Theta}{\partial X} = 0$.   [3.23e, f]

At $Y = -w/r_i$, $-w/r_i \leq X \leq 0$, $\dfrac{\partial \Psi}{\partial Y} = 0$, $\dfrac{\partial \Theta}{\partial Y} = 0$.   [3.23g, h]

At $X = 0$, $1 \leq Y \leq d/r_i$, $\Psi = 0$, $\dfrac{\partial \Theta}{\partial X} = 0$.   [3.23i, j]

At $X = 0$, $-1 \leq Y \leq -w/r_i$, $\Psi = 0$, $\dfrac{\partial \Theta}{\partial X} = 0$.   [3.23k, l]

Similar to the governing equations, the boundary conditions are transformed to the computational domain using the elliptic transformation described in Chapter 2 and they become,

At $\eta = \eta_o$, $\xi_o \leq \xi \leq \xi_m$, $\Psi = 0$, $\Theta = 1$.   [3.24a, b]

At $\eta = \eta_n$, $\xi_o \leq \xi \leq \xi_l$, $\dfrac{\partial \Psi}{\partial \eta} \dfrac{\partial X}{\partial \xi} - \dfrac{\partial \Psi}{\partial \xi} \dfrac{\partial X}{\partial \eta} = 0$,   [3.24c]
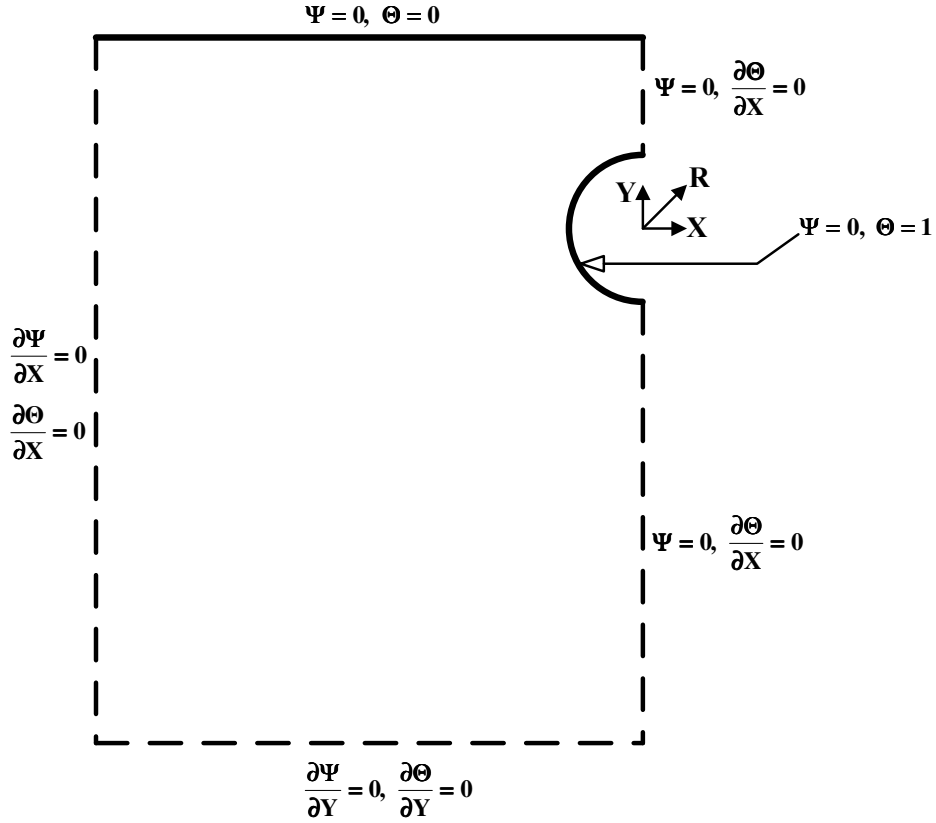
Figure 3.8 Dimensionless boundary conditions for the study of natural convection from a buried pipe.

$$\frac{\partial \Theta}{\partial \eta} \frac{\partial X}{\partial \xi} - \frac{\partial \Theta}{\partial \xi} \frac{\partial X}{\partial \eta} = 0. \qquad [3.24\text{d}]$$

$$\xi_1 \le \xi \le \xi_2, \qquad \frac{\partial \Psi}{\partial \xi} \frac{\partial Y}{\partial \eta} - \frac{\partial \Psi}{\partial \eta} \frac{\partial Y}{\partial \xi} = 0, \qquad [3.24\text{e}]$$

$$\frac{\partial \Theta}{\partial \xi} \frac{\partial Y}{\partial \eta} - \frac{\partial \Theta}{\partial \eta} \frac{\partial Y}{\partial \xi} = 0. \qquad [3.24\text{f}]$$

$$\xi_2 \le \xi \le \xi_m, \qquad \Psi = 0, \qquad \Theta = 0. \qquad [3.24\text{g, h}]$$

At $\xi = \xi_o$, $\quad \eta_o \le \eta < \eta_n$, $\qquad \Psi = 0$, $\qquad \dfrac{\partial \Theta}{\partial \xi} \dfrac{\partial Y}{\partial \eta} - \dfrac{\partial \Theta}{\partial \eta} \dfrac{\partial Y}{\partial \xi} = 0.$ $\quad$ [3.24i, j]

At $\xi = \xi_m$, $\quad \eta_o \leq \eta < \eta_n$, $\quad \Psi = 0$, $\quad \dfrac{\partial \Theta}{\partial \xi}\dfrac{\partial Y}{\partial \eta} - \dfrac{\partial \Theta}{\partial \eta}\dfrac{\partial Y}{\partial \xi} = 0.$ [3.24k, l]

3.3.3 Numerical Methods

In this section, the numerical techniques used to discretize the governing equations will be discussed in details. The derivations will be expressed in a generic form so that the results obtained here can be applied to the related studies that will be discussed in the later chapters with minimum modifications. As such, the numerical details will not be repeated elsewhere in the dissertation.

The transformed governing equations along with the boundary conditions are reduced to a set of algebraic equations using the finite difference and finite volume method (Coulter and Güceri, 1985; Yost, 1984). Successive algebraic equations for the field variables such as the temperature, concentration and stream function at discrete points in the selected domain are sought. A computer program is then written and executed to solve for the solutions. The control volume approach is used to derive the finite difference equations. A schematic of the control volume for the computational domain is shown in Figure 3.9. The shaded area represents the control volume centered at node P. For diffusion terms, a central difference approximation is employed. The convective terms in the energy or transport equation are discritized using the upwind scheme. The derivations given here are based on uniform grids (i.e., $\Delta \xi = \Delta \eta$).
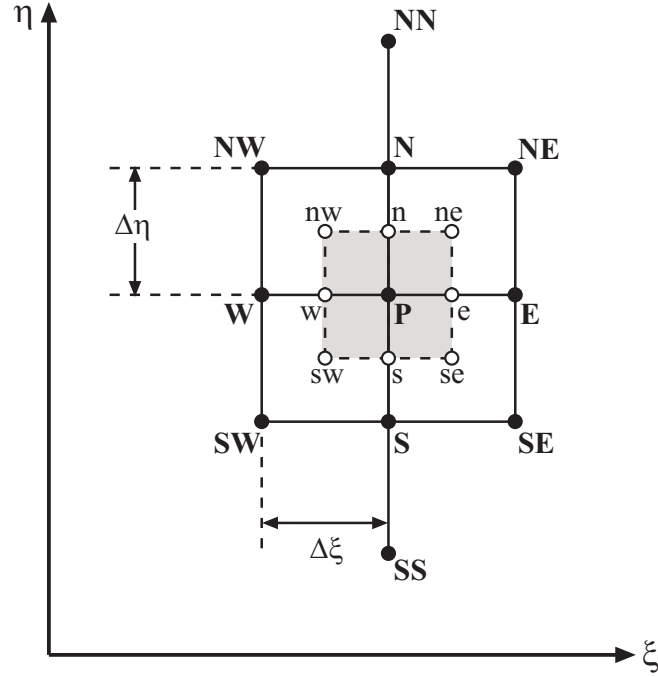
Figure 3.9 A control volume in a two-dimensional computational domain.

3.3.3.1 Discretization of Momentum Equation

The discretization of the momentum equation (Eqn. [3.19]) is fairly straightforward, and it can be obtained using the central-difference approximation expressed in Eqn. [2.5]. After considerable manipulations, the stream function at node P is given by the following algebraic equation,

$$\Psi_P = \frac{1}{2(\overline{\alpha}_P + \overline{\gamma}_P)}\left[F_1 + F_2 + F_3 + F_4 + F_5\right], \tag{3.25a}$$

where $F_1 = \overline{\alpha}_P\left(\Psi_E + \Psi_W\right),$ [3.25b]

$$F_2 = \overline{\gamma}_P\left(\Psi_N + \Psi_S\right), \tag{3.25c}$$

$$F_3 = -\frac{\overline{\beta}_P}{2}\left(\Psi_{NE} - \Psi_{SE} - \Psi_{NW} + \Psi_{SW}\right), \tag{3.25d}$$

$$F_4 = \frac{J_P^2}{2}\left[\overline{P}(\Psi_E - \Psi_W) + \overline{Q}(\Psi_N - \Psi_S)\right],$$ [3.25e]

$$F_5 = \frac{Ra \cdot J_P}{4}\left[(\Theta_E - \Theta_W)(Y_N - Y_S) - (\Theta_N - \Theta_S)(Y_E - Y_W)\right].$$ [3.25f]

The transformation coefficients $\overline{\alpha}_P$, $\overline{\beta}_P$, $\overline{\gamma}_P$ and J_P are given in Eqn. [2.7]. Note that the discretized momentum equation can also be obtained by integration over a control volume (finite volume method). However, it is realized that both approaches yield the same results when uniform grids are used (as in the present study). Also, the accuracy of the above approximations can be improved by including additional terms from the Taylor series expansion if necessary.

3.3.3.2 Discretization of Energy Equation

In general, central difference scheme can also be used to discretize the energy equation including the convective terms on the right-hand side of Eqn. [3.20]. However, as pointed out by Lai (1988), for high Reynolds or Peclet numbers (as in the study of forced and mixed convection), this discretization approach may lead to numerical instabilities. To overcome this drawback, upwind scheme is one of the numerical schemes that provide the advantages of simplicity and numerical stability for convection-dominated problems. In the present study, the upwind scheme is only applied to the convective terms.

The energy equation is integrated over the control volume as shown in Figure 3.9.

$$\int_{\eta,s}^{\eta,n}\int_{\xi,w}^{\xi,e} \nabla_{\xi\eta}^2\Theta \, d\xi d\eta = \int_{\eta,s}^{\eta,n}\int_{\xi,w}^{\xi,e} \frac{1}{J}\left[\frac{\partial\Theta}{\partial\xi}\frac{\partial\Psi}{\partial\eta} - \frac{\partial\Theta}{\partial\eta}\frac{\partial\Psi}{\partial\xi}\right]d\xi d\eta,$$ [3.26]

The treatment of diffusion and convective terms will be described separately in the following sections. Now, let's consider the convective terms on the right-hand side of the energy equation.

(a) Convective Terms

The integrand in the convective terms can be recast in the following manner.

$$< \text{Convective Terms} > = \int_{\eta,s}^{\eta,n} \int_{\xi,w}^{\xi,e} \frac{1}{J} \left[\frac{\partial \Phi}{\partial \xi} \frac{\partial \Psi}{\partial \eta} - \frac{\partial \Phi}{\partial \eta} \frac{\partial \Psi}{\partial \xi} \right] d\xi d\eta$$

$$= \frac{1}{J_P} \int_{\eta,s}^{\eta,n} \int_{\xi,w}^{\xi,e} \left[\frac{\partial}{\partial \xi} \left(\Phi \frac{\partial \Psi}{\partial \eta} \right) - \frac{\partial}{\partial \eta} \left(\Phi \frac{\partial \Psi}{\partial \xi} \right) \right] d\xi d\eta, \qquad [3.27]$$

where the Jacobian for the given control volume is evaluated at the central node P. By taking the integration once, Eqn. [3.27] becomes,

$$< \text{Convective Terms} > = \frac{1}{J_P} \left[\int_{\eta,s}^{\eta,n} \Phi_e \left(\frac{\partial \Psi}{\partial \eta} \right)_e d\eta - \int_{\eta,s}^{\eta,n} \Phi_w \left(\frac{\partial \Psi}{\partial \eta} \right)_w d\eta \right.$$
$$\left. - \int_{\xi,w}^{\xi,e} \Phi_n \left(\frac{\partial \Psi}{\partial \xi} \right)_n d\xi + \int_{\xi,w}^{\xi,e} \Phi_s \left(\frac{\partial \Psi}{\partial \xi} \right)_s d\xi \right]. \qquad [3.28]$$

Now, consider the first term in Eqn. [3.28],

$$I_{C1} = \int_{\eta,s}^{\eta,n} \Phi_e \left(\frac{\partial \Psi}{\partial \eta} \right)_e d\eta. \qquad [3.29]$$

Based on the second theorem of mean for integrals (Chapra and Canale, 2002), it is known that there exists a value $\overline{\Phi}_e$ in the interval between the values of Φ_e at upper and lower integration limits, such that

$$\overline{\Phi}_e = \frac{\int_{\eta,s}^{\eta,n} \Phi_e \left(\frac{\partial \Psi}{\partial \eta}\right)_e d\eta}{\int_{\eta,s}^{\eta,n} \left(\frac{\partial \Psi}{\partial \eta}\right)_e d\eta} \approx \frac{I_{C1}}{(\Psi_{ne} - \Psi_{se})}, \qquad [3.30]$$

which leads to the following simplifications,

$$I_{C1} \approx \overline{\Phi}_e (\Psi_{ne} - \Psi_{se}). \qquad [3.31]$$

In accordance with the upwind scheme, $\overline{\Phi}_e$ only takes the value of Φ_e at the upstream face of the control volume, which can be stated mathematically as follows.

$$\overline{\Phi}_e = \Phi_P, \qquad \text{if } \Psi_{ne} - \Psi_{se} > 0; \qquad [3.32a]$$

$$\overline{\Phi}_e = \Phi_E, \qquad \text{if } \Psi_{ne} - \Psi_{se} < 0. \qquad [3.32b]$$

The above argument can be written in a more compact form and combined with Eqn. [3.31] to give

$$I_{C1} \approx \Phi_E \left[\frac{(\Psi_{ne} - \Psi_{se}) - |\Psi_{ne} - \Psi_{se}|}{2}\right] + \Phi_P \left[\frac{(\Psi_{ne} - \Psi_{se}) + |\Psi_{ne} - \Psi_{se}|}{2}\right]. \qquad [3.33]$$

Other convective terms (I_{C2}, I_{C3}, and I_{C4}) can be obtained in a similar fashion.

Further, by assuming the stream function at the corner of the control volume takes the average value of those at the four neighboring nodes, one can obtain

$$\Psi_{ne} \approx \frac{\Psi_{NE} + \Psi_E + \Psi_P + \Psi_N}{4}, \qquad \Psi_{se} \approx \frac{\Psi_{SE} + \Psi_E + \Psi_P + \Psi_S}{4}, \qquad [3.34a, b]$$

$$\Psi_{nw} \approx \frac{\Psi_{NW} + \Psi_N + \Psi_P + \Psi_W}{4}, \qquad \Psi_{sw} \approx \frac{\Psi_{SW} + \Psi_S + \Psi_P + \Psi_W}{4}. \qquad [3.34c, d]$$

Combine these results for all four convective terms, one obtains the following expression.

$$< \text{Convective Terms} > = A_E(\Phi_P - \Phi_E) + A_W(\Phi_P - \Phi_W) + A_N(\Phi_P - \Phi_N) + A_S(\Phi_P - \Phi_S),$$

[3.35a]

where $A_E = \dfrac{1}{8J_P}\left[(\Psi_{SE} + \Psi_S - \Psi_{NE} - \Psi_N) + \left|\Psi_{SE} + \Psi_S - \Psi_{NE} - \Psi_N\right|\right],$ [3.35b]

$$A_W = \dfrac{1}{8J_P}\left[(\Psi_{NW} + \Psi_N - \Psi_{SW} - \Psi_S) + \left|\Psi_{NW} + \Psi_N - \Psi_{SW} - \Psi_S\right|\right],$$ [3.35c]

$$A_N = \dfrac{1}{8J_P}\left[(\Psi_{NE} + \Psi_E - \Psi_{NW} - \Psi_W) + \left|\Psi_{NE} + \Psi_E - \Psi_{NW} - \Psi_W\right|\right],$$ [3.35d]

$$A_S = \dfrac{1}{8J_P}\left[(\Psi_{SW} + \Psi_W - \Psi_E - \Psi_{SE}) + \left|\Psi_{SW} + \Psi_W - \Psi_E - \Psi_{SE}\right|\right].$$ [3.35e]

(b) Diffusion Terms

Now, let's turn our attention to the diffusion terms given as follows

$$< \text{Diffusion Terms} > = \int_{\eta,s}^{\eta,n}\int_{\xi,w}^{\xi,e}\left[\frac{\overline{\alpha}}{J^2}\frac{\partial^2\Phi}{\partial\xi^2} - \frac{2\overline{\beta}}{J^2}\frac{\partial^2\Phi}{\partial\xi\partial\eta} + \frac{\overline{\gamma}}{J^2}\frac{\partial^2\Phi}{\partial\eta^2} + \overline{P}\frac{\partial\Phi}{\partial\xi} + \overline{Q}\frac{\partial\Phi}{\partial\eta}\right]d\xi d\eta.$$

[3.36]

The integration of diffusion terms will be explained term-by-term in the following sections.

(i) $\underline{1^{st}\ \text{Term}}$

The first diffusion term can be rewritten as follows,

$$\begin{aligned}I_{D1} &= \int_{\eta,s}^{\eta,n}\int_{\xi,w}^{\xi,e}\frac{\overline{\alpha}}{J^2}\frac{\partial^2\Phi}{\partial\xi^2}d\xi d\eta\\ &= \int_{\eta,s}^{\eta,n}\int_{\xi,w}^{\xi,e}\left\{\frac{\partial}{\partial\xi}\left(\frac{\overline{\alpha}}{J^2}\frac{\partial\Phi}{\partial\xi}\right) - \left[\frac{\partial}{\partial\xi}\left(\frac{\overline{\alpha}}{J^2}\right)\right]\frac{\partial\Phi}{\partial\xi}\right\}d\xi d\eta.\end{aligned}$$

[3.37]

The first diffusion term can be divided into two separate terms I_{D1A} and I_{D1B}. By integrating once with respect to ξ, the term I_{D1A} becomes,

$$
\begin{aligned}
I_{D1A} &= \int_{\eta,s}^{\eta,n} \int_{\xi,w}^{\xi,e} \frac{\partial}{\partial \xi}\left(\frac{\overline{\alpha}}{J^2}\frac{\partial \Phi}{\partial \xi}\right)d\xi d\eta \\
&= \int_{\eta,s}^{\eta,n}\left[\left(\frac{\overline{\alpha}}{J^2}\right)_e\left(\frac{\partial \Phi}{\partial \xi}\right)_e - \left(\frac{\overline{\alpha}}{J^2}\right)_w\left(\frac{\partial \Phi}{\partial \xi}\right)_w\right]d\eta \\
&= \frac{1}{2}\left[\left(\frac{\overline{\alpha}}{J^2}\right)_E + \left(\frac{\overline{\alpha}}{J^2}\right)_P\right]\left[\frac{\Phi_E - \Phi_P}{\Delta \xi}\right]\Delta\eta - \frac{1}{2}\left[\left(\frac{\overline{\alpha}}{J^2}\right)_W + \left(\frac{\overline{\alpha}}{J^2}\right)_P\right]\left[\frac{\Phi_P - \Phi_W}{\Delta \xi}\right]\Delta\eta \\
&= B_{1AE}\left(\Phi_E - \Phi_P\right) + B_{1AW}\left(\Phi_W - \Phi_P\right)
\end{aligned}
\qquad [3.38a]
$$

where $B_{1AE} = \dfrac{1}{2}\left[\left(\dfrac{\overline{\alpha}}{J^2}\right)_E + \left(\dfrac{\overline{\alpha}}{J^2}\right)_P\right]$, and $B_{1AW} = \dfrac{1}{2}\left[\left(\dfrac{\overline{\alpha}}{J^2}\right)_W + \left(\dfrac{\overline{\alpha}}{J^2}\right)_P\right]$. $\qquad [3.38b,\ c]$

It has been assumed that the quantities $\dfrac{\overline{\alpha}}{J^2}$ and Φ vary only in the direction of ξ. As mentioned before, uniform grid is employed in the present study (i.e., $\Delta\xi = \Delta\eta = 1$).

Once again, with the assumption that $\dfrac{\overline{\alpha}}{J^2}$ and Φ vary only in the direction of ξ, the second integral of the first diffusion term can be obtained as follows,

$$
\begin{aligned}
I_{D1B} &= \int_{\eta,s}^{\eta,n}\int_{\xi,w}^{\xi,e}\left[\frac{\partial}{\partial \xi}\left(\frac{\overline{\alpha}}{J^2}\right)\right]\frac{\partial \Phi}{\partial \xi}d\xi d\eta \\
&= \frac{1}{2\Delta\xi}\left[\left(\frac{\overline{\alpha}}{J^2}\right)_E - \left(\frac{\overline{\alpha}}{J^2}\right)_W\right]\int_{\eta,s}^{\eta,n}\int_{\xi,w}^{\xi,e}\frac{\partial \Phi}{\partial \xi}d\xi d\eta \\
&= \frac{1}{2\Delta\xi}\left[\left(\frac{\overline{\alpha}}{J^2}\right)_E - \left(\frac{\overline{\alpha}}{J^2}\right)_W\right]\frac{(\Phi_E - \Phi_W)}{2}\Delta\eta \\
&= B_{1B}\left(\Phi_E - \Phi_W\right)
\end{aligned}
\qquad [3.39a]
$$

where $B_{1B} = \dfrac{1}{4}\left[\left(\dfrac{\overline{\alpha}}{J^2}\right)_E - \left(\dfrac{\overline{\alpha}}{J^2}\right)_W\right]$. $\qquad [3.39b]$

Combining the results of both integrations, the first diffusion term is given by

$$I_{D1} = B_{1AE}\left(\Phi_E - \Phi_P\right) + B_{1AW}\left(\Phi_W - \Phi_P\right) - B_{1B}\left(\Phi_E - \Phi_W\right).$$ [3.40]

(ii) $\underline{2^{nd}\ Term}$

Rewrite the second diffusion term as follows,

$$I_{D2} = \int_{\eta,s}^{\eta,n} \int_{\xi,w}^{\xi,e} -\frac{2\overline{\beta}}{J^2} \frac{\partial^2 \Phi}{\partial\xi\partial\eta} \, d\xi d\eta$$

$$= \int_{\eta,s}^{\eta,n} \int_{\xi,w}^{\xi,e} \left\{ \frac{\partial}{\partial\xi}\left(-\frac{2\overline{\beta}}{J^2}\frac{\partial\Phi}{\partial\eta}\right) - \left[\frac{\partial}{\partial\xi}\left(-\frac{2\overline{\beta}}{J^2}\right)\right]\frac{\partial\Phi}{\partial\eta} \right\} d\xi d\eta.$$ [3.41]

By integrating once and assuming $-\dfrac{2\overline{\beta}}{J^2}$ and Φ vary in the direction of ξ and η,

respectively. The first integral I_{D2A} can be obtained as follows,

$$I_{D2A} = \int_{\eta,s}^{\eta,n} \int_{\xi,w}^{\xi,e} \frac{\partial}{\partial\xi}\left(-\frac{2\overline{\beta}}{J^2}\frac{\partial\Phi}{\partial\eta}\right) d\xi d\eta$$

$$= \int_{\eta,s}^{\eta,n} \left[\left(-\frac{2\overline{\beta}}{J^2}\right)_e \left(\frac{\partial\Phi}{\partial\eta}\right)_e - \left(-\frac{2\overline{\beta}}{J^2}\right)_w \left(\frac{\partial\Phi}{\partial\eta}\right)_w\right] d\eta$$ [3.42a]

$$= \frac{1}{2}\left[\left(-\frac{2\overline{\beta}}{J^2}\right)_E + \left(-\frac{2\overline{\beta}}{J^2}\right)_P\right][\Phi_{ne} - \Phi_{se}] - \frac{1}{2}\left[\left(-\frac{2\overline{\beta}}{J^2}\right)_W + \left(-\frac{2\overline{\beta}}{J^2}\right)_P\right][\Phi_{nw} - \Phi_{sw}]$$

$$= B_{2AE}\left(\Phi_{NE} + \Phi_N - \Phi_S - \Phi_{SE}\right) - B_{2AW}\left(\Phi_{NW} + \Phi_N - \Phi_S - \Phi_{SW}\right)$$

where $B_{2AE} = \dfrac{1}{4}\left[\left(-\dfrac{\overline{\beta}}{J^2}\right)_E + \left(-\dfrac{\overline{\beta}}{J^2}\right)_P\right]$, and $B_{2AW} = \dfrac{1}{4}\left[\left(-\dfrac{\overline{\beta}}{J^2}\right)_W + \left(-\dfrac{\overline{\beta}}{J^2}\right)_P\right].$ [3.42b, c]

Note that the values of Φ_{ne}, Φ_{se}, Φ_{nw} and Φ_{sw} are taken as the average value of the

neighboring nodes. Perform the integration of the second integral I_{D2B}, one yields

$$I_{D2B} = \int_{\eta,s}^{\eta,n} \int_{\xi,w}^{\xi,e} \left[\frac{\partial}{\partial \xi} \left(-\frac{2\overline{\beta}}{J^2} \right) \right] \frac{\partial \Phi}{\partial \eta} d\xi d\eta$$

$$= \frac{1}{2\Delta\xi} \left[\left(-\frac{2\overline{\beta}}{J^2} \right)_E - \left(-\frac{2\overline{\beta}}{J^2} \right)_W \right] \int_{\eta,s}^{\eta,n} \int_{\xi,w}^{\xi,e} \frac{\partial \Phi}{\partial \eta} d\xi d\eta \qquad\qquad \text{[3.43a]}$$

$$= \frac{1}{2\Delta\xi} \left[\left(-\frac{2\overline{\beta}}{J^2} \right)_E - \left(-\frac{2\overline{\beta}}{J^2} \right)_W \right] \frac{(\Phi_N - \Phi_S)}{2} \Delta\xi$$

$$= B_{2B}(\Phi_N - \Phi_S)$$

where $\quad B_{2B} = \frac{1}{2} \left[\left(-\frac{\overline{\beta}}{J^2} \right)_E - \left(-\frac{\overline{\beta}}{J^2} \right)_W \right].$ $\qquad\qquad\qquad$ [3.43b]

The second diffusion term is thus given by

$$I_{D2} = B_{2AE}(\Phi_{NE} + \Phi_N - \Phi_S - \Phi_{SE})$$
$$- B_{2AW}(\Phi_{NW} + \Phi_N - \Phi_S - \Phi_{SW}) - B_{2B}(\Phi_N - \Phi_S). \qquad \text{[3.44]}$$

(iii) 3rd Term

Similar to the treatment of the first diffusion term, rewrite the third diffusion term in the following manner.

$$I_{D3} = \int_{\eta,s}^{\eta,n} \int_{\xi,w}^{\xi,e} \frac{\overline{\gamma}}{J^2} \frac{\partial^2 \Phi}{\partial \eta^2} d\xi d\eta$$

$$\qquad\qquad\qquad\qquad\qquad\qquad\qquad\qquad\qquad \text{[3.45]}$$

$$= \int_{\eta,s}^{\eta,n} \int_{\xi,w}^{\xi,e} \left\{ \frac{\partial}{\partial \eta} \left(\frac{\overline{\gamma}}{J^2} \frac{\partial \Phi}{\partial \eta} \right) - \left[\frac{\partial}{\partial \eta} \left(\frac{\overline{\gamma}}{J^2} \right) \right] \frac{\partial \Phi}{\partial \eta} \right\} d\xi d\eta$$

Now, with the assumption that $\dfrac{\overline{\gamma}}{J^2}$ and Φ vary only in the direction of η, both

integrations of the third diffusion term can be obtained as follows,

$$I_{D3A} = \int_{\eta,s}^{\eta,n} \int_{\xi,w}^{\xi,e} \frac{\partial}{\partial\eta}\left(\frac{\bar{\gamma}}{J^2}\frac{\partial\Phi}{\partial\eta}\right) d\xi d\eta$$

$$= \int_{\xi,w}^{\xi,e} \left[\left(\frac{\bar{\gamma}}{J^2}\right)_n \left(\frac{\partial\Phi}{\partial\eta}\right)_n - \left(\frac{\bar{\gamma}}{J^2}\right)_s \left(\frac{\partial\Phi}{\partial\eta}\right)_s\right] d\xi \qquad\qquad [3.46a]$$

$$= \frac{1}{2}\left[\left(\frac{\bar{\gamma}}{J^2}\right)_N + \left(\frac{\bar{\gamma}}{J^2}\right)_P\right]\left[\frac{\Phi_N - \Phi_P}{\Delta\eta}\right]\Delta\xi - \frac{1}{2}\left[\left(\frac{\bar{\gamma}}{J^2}\right)_S + \left(\frac{\bar{\gamma}}{J^2}\right)_P\right]\left[\frac{\Phi_P - \Phi_S}{\Delta\eta}\right]\Delta\xi$$

$$= B_{3AN}(\Phi_N - \Phi_P) + B_{3AS}(\Phi_S - \Phi_P)$$

where $B_{3AN} = \frac{1}{2}\left[\left(\frac{\bar{\gamma}}{J^2}\right)_N + \left(\frac{\bar{\gamma}}{J^2}\right)_P\right]$, and $B_{3AS} = \frac{1}{2}\left[\left(\frac{\bar{\gamma}}{J^2}\right)_S + \left(\frac{\bar{\gamma}}{J^2}\right)_P\right]$. $\qquad$ [3.46b, c]

$$I_{D3B} = \int_{\eta,s}^{\eta,n} \int_{\xi,w}^{\xi,e} \left[\frac{\partial}{\partial\eta}\left(\frac{\bar{\gamma}}{J^2}\right)\right]\frac{\partial\Phi}{\partial\eta} d\xi d\eta$$

$$= \frac{1}{2\Delta\eta}\left[\left(\frac{\bar{\gamma}}{J^2}\right)_N - \left(\frac{\bar{\gamma}}{J^2}\right)_S\right]\int_{\eta,s}^{\eta,n} \int_{\xi,w}^{\xi,e} \frac{\partial\Phi}{\partial\eta} d\xi d\eta \qquad\qquad [3.47a]$$

$$= \frac{1}{2\Delta\eta}\left[\left(\frac{\bar{\gamma}}{J^2}\right)_N - \left(\frac{\bar{\gamma}}{J^2}\right)_S\right]\frac{(\Phi_N - \Phi_S)}{2}\Delta\xi$$

$$= B_{3B}(\Phi_N - \Phi_S)$$

where $B_{3B} = \frac{1}{4}\left[\left(\frac{\bar{\gamma}}{J^2}\right)_N - \left(\frac{\bar{\gamma}}{J^2}\right)_S\right]$. $\qquad\qquad\qquad\qquad\qquad\qquad$ [3.47b]

Finally, the third diffusion term is given by

$$I_{D3} = B_{3AN}(\Phi_N - \Phi_P) + B_{3AS}(\Phi_S - \Phi_P) - B_{3B}(\Phi_N - \Phi_S). \qquad\qquad [3.48]$$

(iv) 4th Term

Once again, rewrite the fourth diffusion term using the product rule of differentiation.

$$I_{D4} = \int_{\eta,s}^{\eta,n} \int_{\xi,w}^{\xi,e} \bar{P}\frac{\partial\Phi}{\partial\xi} d\xi d\eta = \int_{\eta,s}^{\eta,n} \int_{\xi,w}^{\xi,e}\left[\frac{\partial}{\partial\xi}(\bar{P}\Phi) - \frac{\partial\bar{P}}{\partial\xi}\Phi\right] d\xi d\eta. \qquad [3.49]$$

By integrating once with respect to ξ and assuming the quantity ($\overline{P}\Phi$) varies linearly in the direction of ξ only, the first integral is obtained as follows,

$$
\begin{aligned}
I_{D4A} &= \int_{\eta,s}^{\eta,n} \int_{\xi,w}^{\xi,e} \left[\frac{\partial}{\partial \xi}(\overline{P}\Phi) \right] d\xi d\eta \\
&= \int_{\eta,s}^{\eta,n} \left[(\overline{P}\Phi)_e - (\overline{P}\Phi)_w \right] d\eta \\
&= \frac{(\overline{P}\Phi)_E - (\overline{P}\Phi)_W}{2} \Delta\eta \\
&= B_{4AE}\Phi_E - B_{4AW}\Phi_W
\end{aligned}
\qquad [3.50a]
$$

where $B_{4AE} = \dfrac{1}{2}\overline{P}_E$, and $B_{4AW} = \dfrac{1}{2}\overline{P}_W$. $\qquad$ [3.50b, c]

Similarly, the second integral can be integrated to yield,

$$
\begin{aligned}
I_{D4B} &= \int_{\eta,s}^{\eta,n} \int_{\xi,w}^{\xi,e} \frac{\partial \overline{P}}{\partial \xi} \Phi d\xi d\eta \\
&= \overline{\Phi} \int_{\eta,s}^{\eta,n} \int_{\xi,w}^{\xi,e} \frac{\partial \overline{P}}{\partial \xi} d\xi d\eta \\
&= \frac{1}{4}(\Phi_n + \Phi_w + \Phi_s + \Phi_e)\frac{(\overline{P}_E - \overline{P}_W)}{2}\Delta\eta \\
&= \frac{1}{16}(\Phi_N + \Phi_W + \Phi_S + \Phi_E + 4\Phi_P)(\overline{P}_E - \overline{P}_W) \\
&= B_{4B}(\Phi_N + \Phi_W + \Phi_S + \Phi_E) + B_{4BP}\Phi_P
\end{aligned}
\qquad [3.51a]
$$

where $B_{4BP} = \dfrac{1}{4}(\overline{P}_E - \overline{P}_W)$, and $B_{4B} = \dfrac{1}{4}B_{4BP}$. $\qquad$ [3.51b, c]

Combine and rearrange terms, the fourth diffusion term becomes,

$$
I_{D4} = B_{4AE}\Phi_E - B_{4AW}\Phi_W - B_{4B}(\Phi_N + \Phi_W + \Phi_S + \Phi_E) - B_{4BP}\Phi_P. \qquad [3.52]
$$

(v) 5<u>th</u> Term

Follow the same procedures as described above for the fourth diffusion term, the last diffusion term can be obtained as follows,

$$I_{D5} = \int_{\eta,s}^{\eta,n} \int_{\xi,w}^{\xi,e} \overline{Q} \frac{\partial \Phi}{\partial \eta} d\xi d\eta = \int_{\eta,s}^{\eta,n} \int_{\xi,w}^{\xi,e} \left[\frac{\partial}{\partial \eta} (\overline{Q}\Phi) - \frac{\partial \overline{Q}}{\partial \eta} \Phi \right] d\xi d\eta.$$ [3.53]

The first integral is determined to be

$$
\begin{aligned}
I_{D5A} &= \int_{\eta,s}^{\eta,n} \int_{\xi,w}^{\xi,e} \left[\frac{\partial}{\partial \eta} (\overline{Q}\Phi) \right] d\xi d\eta \\
&= \int_{\xi,w}^{\xi,e} [(\overline{Q}\Phi)_n - (\overline{Q}\Phi)_s] d\xi \\
&= \frac{(\overline{Q}\Phi)_N - (\overline{Q}\Phi)_S}{2} \Delta\xi \\
&= B_{5AN}\Phi_N - B_{5AS}\Phi_S
\end{aligned}
$$ [3.54a]

where $B_{5AN} = \frac{1}{2}\overline{Q}_N$, and $B_{5AS} = \frac{1}{2}\overline{Q}_S$. [3.54b, c]

And the second integral is given by

$$
\begin{aligned}
I_{D5B} &= \int_{\eta,s}^{\eta,n} \int_{\xi,w}^{\xi,e} \frac{\partial \overline{Q}}{\partial \eta} \Phi d\xi d\eta \\
&= \overline{\Phi} \int_{\eta,s}^{\eta,n} \int_{\xi,w}^{\xi,e} \frac{\partial \overline{Q}}{\partial \eta} d\xi d\eta \\
&= \frac{1}{4}(\Phi_n + \Phi_w + \Phi_s + \Phi_e) \frac{(\overline{Q}_N - \overline{Q}_S)}{2} \Delta\xi \\
&= \frac{1}{16}(\Phi_N + \Phi_W + \Phi_S + \Phi_E + 4\Phi_P)(\overline{Q}_N - \overline{Q}_S) \\
&= B_{5B}(\Phi_N + \Phi_W + \Phi_S + \Phi_E) + B_{5BP}\Phi_P
\end{aligned}
$$ [3.55a]

where $B_{5BP} = \frac{1}{4}(\overline{Q}_N - \overline{Q}_S)$, and $B_{5B} = \frac{1}{4}B_{5BP}$. [3.55b, c]

The 5th diffusion term is then given by

$$I_{D5} = B_{5AN}\Phi_N - B_{5AS}\Phi_S - B_{5B}(\Phi_N + \Phi_W + \Phi_S + \Phi_E) - B_{5BP}\Phi_P$$ [3.56]

Thus far, all the diffusion terms have been discretized term-by-term. Combine the results of all five diffusion terms, one yields

$$
\begin{aligned}
< \text{Diffusion Terms} > &= I_{D1} + I_{D2} + I_{D3} + I_{D4} + I_{D5} \\
&= B_{1AE}(\Phi_E - \Phi_P) + B_{1AW}(\Phi_W - \Phi_P) - B_{1B}(\Phi_E - \Phi_W) \\
&\quad + B_{2AE}(\Phi_{NE} + \Phi_N - \Phi_S - \Phi_{SE}) - B_{2AW}(\Phi_{NW} + \Phi_N - \Phi_S - \Phi_{SW}) - B_{2B}(\Phi_N - \Phi_S) \\
&\quad + B_{3AN}(\Phi_N - \Phi_P) + B_{3AS}(\Phi_S - \Phi_P) - B_{3B}(\Phi_N - \Phi_S) \\
&\quad + B_{4AE}\Phi_E - B_{4AW}\Phi_W - B_{4B}(\Phi_N + \Phi_W + \Phi_S + \Phi_E) - B_{4BP}\Phi_P \\
&\quad + B_{5AN}\Phi_N - B_{5AS}\Phi_S - B_{5B}(\Phi_N + \Phi_W + \Phi_S + \Phi_E) - B_{5BP}\Phi_P
\end{aligned}
$$

[3.57]

Equate and rearrange the results obtained for both diffusion and convective terms, the temperature at the central node is then determined to be

$$
\Theta_P = \frac{T_{SUM2}}{T_{SUM1}},
$$

[3.58a]

where $\quad T_{SUM1} = A_{SUMT1} + B_{SUMT1}$, [3.58b]

$$
T_{SUM2} = A_{SUMT2} + B_{SUMT2},
$$

[3.58c]

$$
A_{SUMT1} = A_E + A_W + A_N + A_S,
$$

[3.58d]

$$
B_{SUMT1} = B_{1AE} + B_{1AW} + B_{3AN} + B_{3AS} + B_{4BP} + B_{5BP},
$$

[3.58e]

$$
B_{T1} = B_{1AE}\Theta_E + B_{1AW}\Theta_W - B_{1B}(\Theta_E - \Theta_W),
$$

[3.58f]

$$
\begin{aligned}
B_{T2} &= B_{2AE}(\Theta_{NE} + \Theta_N - \Theta_S - \Theta_{SE}) - B_{2AW}(\Theta_{NW} + \Theta_N - \Theta_S - \Theta_{SW}) \\
&\quad - B_{2B}(\Theta_N - \Theta_S),
\end{aligned}
$$

[3.58g]

$$
B_{T3} = B_{3AN}\Theta_N + B_{3AS}\Theta_S - B_{3B}(\Theta_N - \Theta_S),
$$

[3.58h]

$$
B_{T4} = B_{4AE}\Theta_E - B_{4AW}\Theta_W - B_{4B}(\Theta_N + \Theta_W + \Theta_S + \Theta_E),
$$

[3.58i]

$$
B_{T5} = B_{5AN}\Theta_N - B_{5AS}\Theta_S - B_{5B}(\Theta_N + \Theta_W + \Theta_S + \Theta_E).
$$

[3.58j]

A Fortran90 code has been developed to perform the numerical calculations using Gauss-Seidel iterative scheme incorporated with the relaxation parameters (Eqn. [2.8]). The numerical iteration is terminated once the convergence criterion (Eqn. [2.9]) is met. The allowable error δ is set to be 10^{-4} in the present study for all field variables (i.e., temperature, concentration and stream function). The algorithm for the present numerical procedures is summarized in Figure 3.10.

The heat transfer results are expressed in terms of the overall Nusselt number, and it is defined below (in the physical domain).

$$\text{Nu} = -\int_{-w/r_i}^{0} \left.\frac{\partial \Theta}{\partial Y}\right|_{Y=d/r_i} dX. \qquad [3.59]$$

The Nusselt number represents the total heat flux through the top wall. As an additional check on the accuracy of the results obtained, an overall energy balance has been performed after each calculation. The relaxation parameters were adjusted to reduce the relative errors to within 3%. The definitions of the relative errors are given as follows,

$$\% \text{ Error E} = \left|\frac{\text{Nu}_{in} - \text{Nu}_{out}}{\text{Nu}_{in}}\right| \times 100\%, \qquad [3.60a]$$

where

$$\text{Nu}_{in} = \int \left(-\frac{\partial \Theta}{\partial R}R\right)_{R=1} d\theta + \int \left(U \cdot \Theta\right)_{X=-w/r_i} dY + \int \left(V \cdot \Theta\right)_{Y=-w/r_i} dX, \qquad [3.60b]$$

$$\text{Nu}_{out} = \int \left(-\frac{\partial \Theta}{\partial Y}\right)_{Y=d/r_i} dX. \qquad [3.60c]$$

In the expression of Eqn. [3.60b], it has been assumed that the velocities U and V are in the positive direction. When performing the energy balance, the directions of the velocities were obtained prior to the determination if the energy transfer was going into or coming out of the control volume.
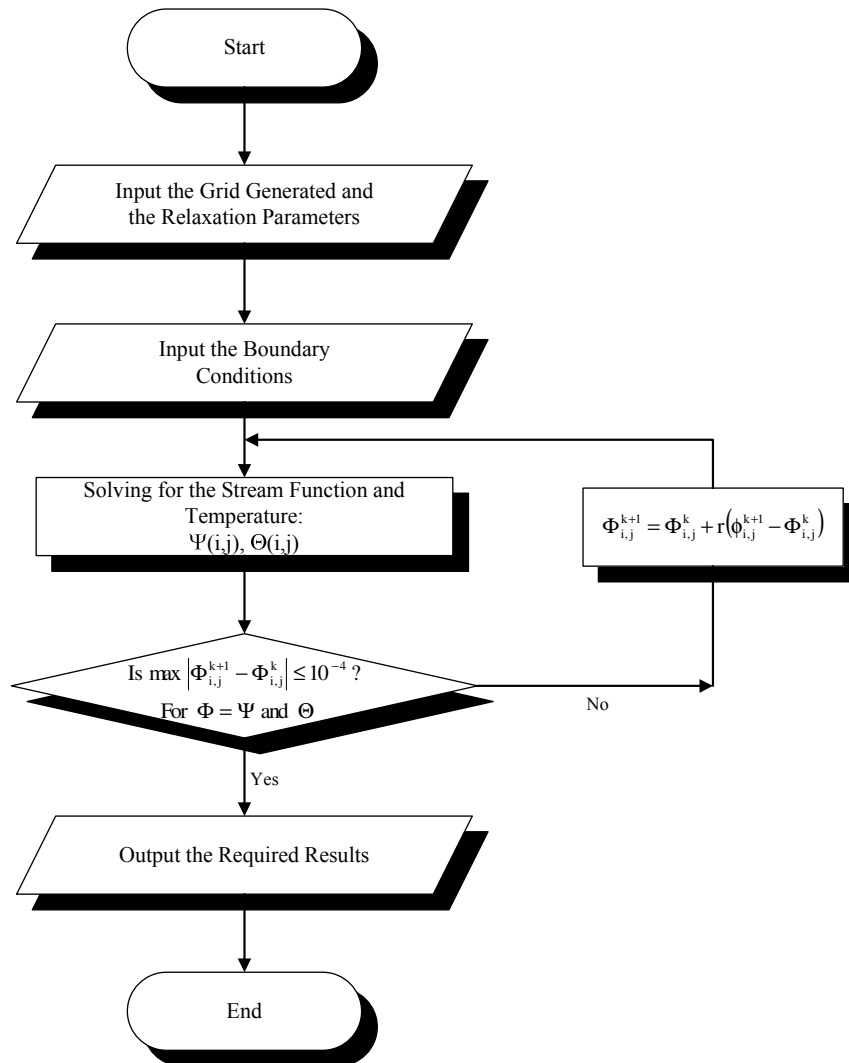
Figure 3.10 Flow chart of the numerical procedures for the study of natural convection from a buried pipe.

3.3.4 Results and Discussion

One immediate concern of the present study that needs to be addressed is to determine the width (w/r_i) of the physical domain so that the present model can adequately represent a semi-infinite porous medium. For the case of natural convection due to thermal buoyancy alone, heat transfer results have been obtained for various Rayleigh numbers, and they are summarized in Table 3.4. It is noted that for all Rayleigh numbers, the total heat transfer approaches an asymptotic value as the width of the domain increases. When a small domain is employed, the flow field becomes unstable and no converged solution can be obtained for high Rayleigh numbers. Based on the analysis, it is concluded that a dimensionless width w/r_i of 30 is sufficient for the present model to represent a semi-infinite medium. This finding is also consistent with the experimental observation by Fand et al. (1986). Based on their experimental results, they established that for a burial depth (d/r_i) of 22.2, a horizontal dimensionless width of 17.6 and a vertical dimensionless width of 22.2 are adequate for the enclosed porous medium to be considered as infinite.

Table 3.4 Heat transfer results for various physical domain size.

w/r_i	Nu_{in}	Nu_{out}	% Err	Nu_{in}	Nu_{out}	% Err	Nu_{in}	Nu_{out}	% Err
	Ra = 25			Ra = 50			Ra = 75		
15	5.069	5.063	0.1	7.148	7.179	0.4	8.741	8.659	0.9
25	5.188	5.200	0.2	7.459	7.409	0.7	9.090	9.111	0.2
30	5.214	5.198	0.3	7.499	7.482	0.2	9.149	9.166	0.2
	Ra = 100			Ra = 200			Ra = 500		
15	10.201	9.855	3.4	Not Converged			Not Converged		
25	10.485	10.479	0.1	14.499	14.505	0.0	Not Converged		
30	10.549	10.542	0.1	14.586	14.695	0.7	21.459	21.498	0.2

Once the dimensions of the physical domain are fixed, a grid refinement test is performed to determine the effect of grid size. For the present study, a mesh of 121×121 is used. A further grid refinement does not produce any significant improvement in the heat transfer results.

Next, the present results are compared with those reported by Himasekhar and Bau (1987) as well as Merkin (1979) for the case of natural convection from a heated pipe embedded in a porous medium. The heat transfer results in terms of the Nusselt number are shown in Figure 3.11. For the present study, heat transfer results can be correlated as

$$Nu = Ra^{0.5}. \tag{3.61}$$

As seen from Figure 3.11, the numerical results obtained from the present study compared very well with the analytical solutions reported by Himasekhar and
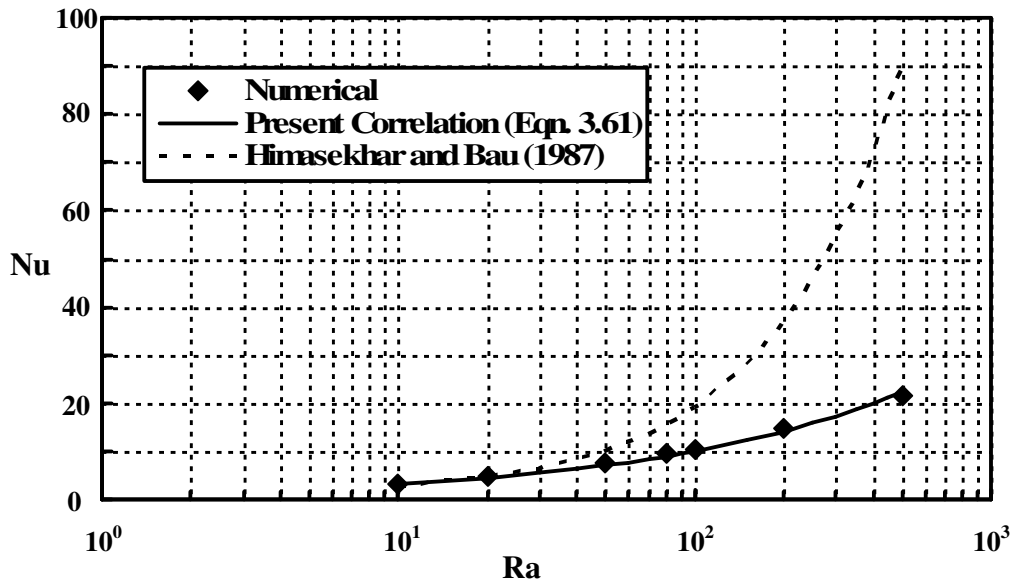
Figure 3.11 Validation of the present numerical code for the study of natural convection from a buried pipe.

Bau (1987) at low Rayleigh numbers (Ra ≤ 20). This is expected since the correlation of Himasekhar and Bau (1987) was obtained from the perturbation analysis, which is only good for small Rayleigh numbers.

Merkin (1979) has also obtained a correlation of the Nusselt number from natural convection from a cylinder buried in an infinite porous medium using similarity method,

$$\mathrm{Nu} = 0.565\mathrm{Ra}_{\mathrm{D}}^{0.5}, \tag{3.62}$$

where Nu is the average Nusselt number and the Rayleigh number is based on the diameter D. By comparing the correlation from Merkin (1979) with the present study, it is noted that for both correlations, the Nusselt number is proportional to the square root of the Rayleigh number. The only difference is the proportional constants, which may be attributed to the difference in the modeled problem domain (i.e., semi-infinite porous medium vs infinite porous medium).

The streamlines and isotherms for various Rayleigh numbers are shown in Figure 3.12 and 3.13, respectively. As observed, heated fluid rises along the pipe surface to the top boundary and then discharges to the left boundary. The flow field is replenished by cold fluid entering from the lower boundaries. Due to thermal buoyancy, there is a large recirculating cell. The strength of this recirculating cell increases with the Rayleigh number. Corresponding to this flow motion, a thermal plume is observed to develop from the top surface of the buried pipe, especially at high Rayleigh numbers. Quantitatively, the plots of the streamlines and isotherms agree well with those reported by Himasekhar and Bau (1987).
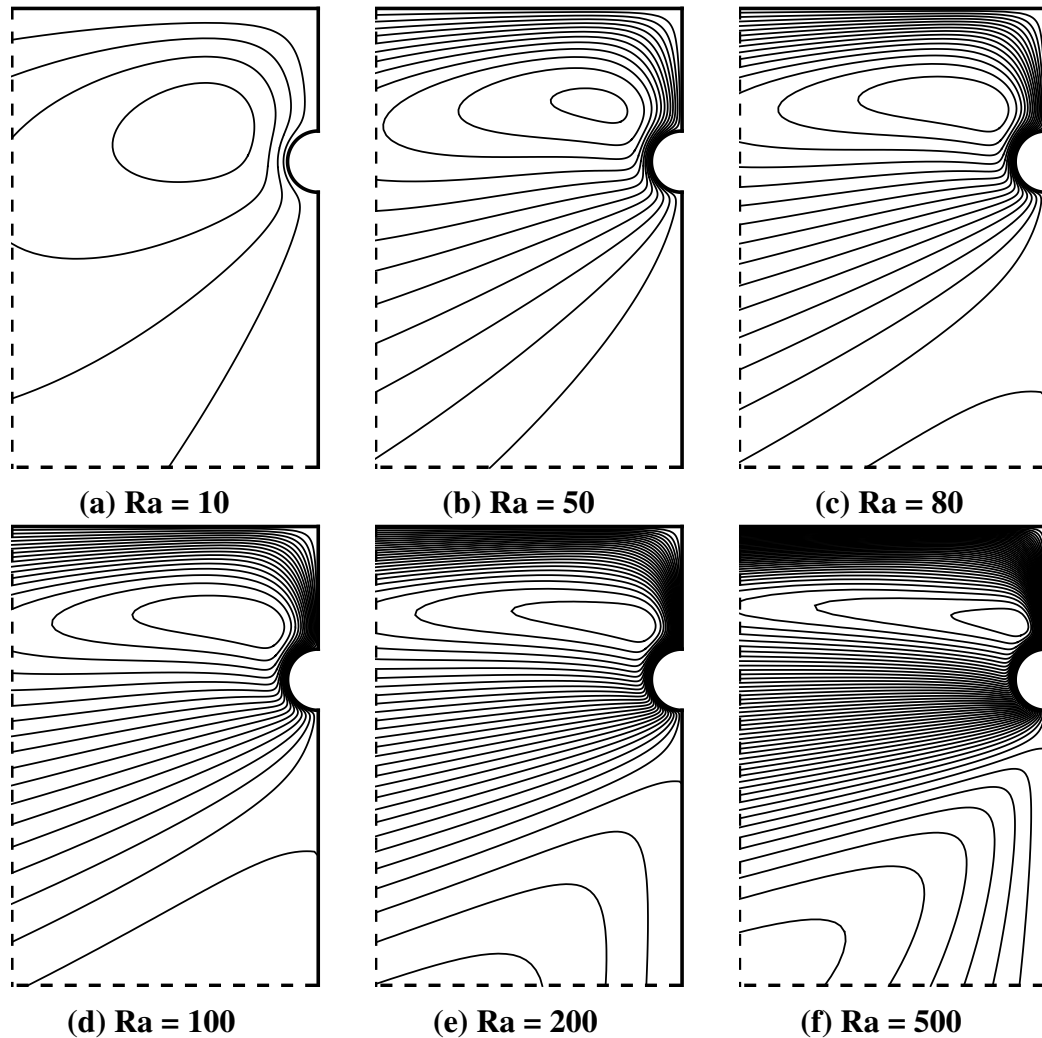
Figure 3.12 Flow fields for natural convection from a buried heated pipe
(a) Ra = 10, (b) Ra = 50, (c) Ra = 80, (d) Ra = 100, (e) Ra = 200,
(f) Ra = 500 ($\Delta\Psi = 1$).

3.4 Concluding Remarks

Based on the results obtained for conduction and natural convection induced

from a pipe buried in a homogeneous porous medium, it is concluded that a

dimensionless width (w/r_i) of 30 is appropriate for the model to represent a semi-

infinite medium. The validity of the present model has been confirmed by the
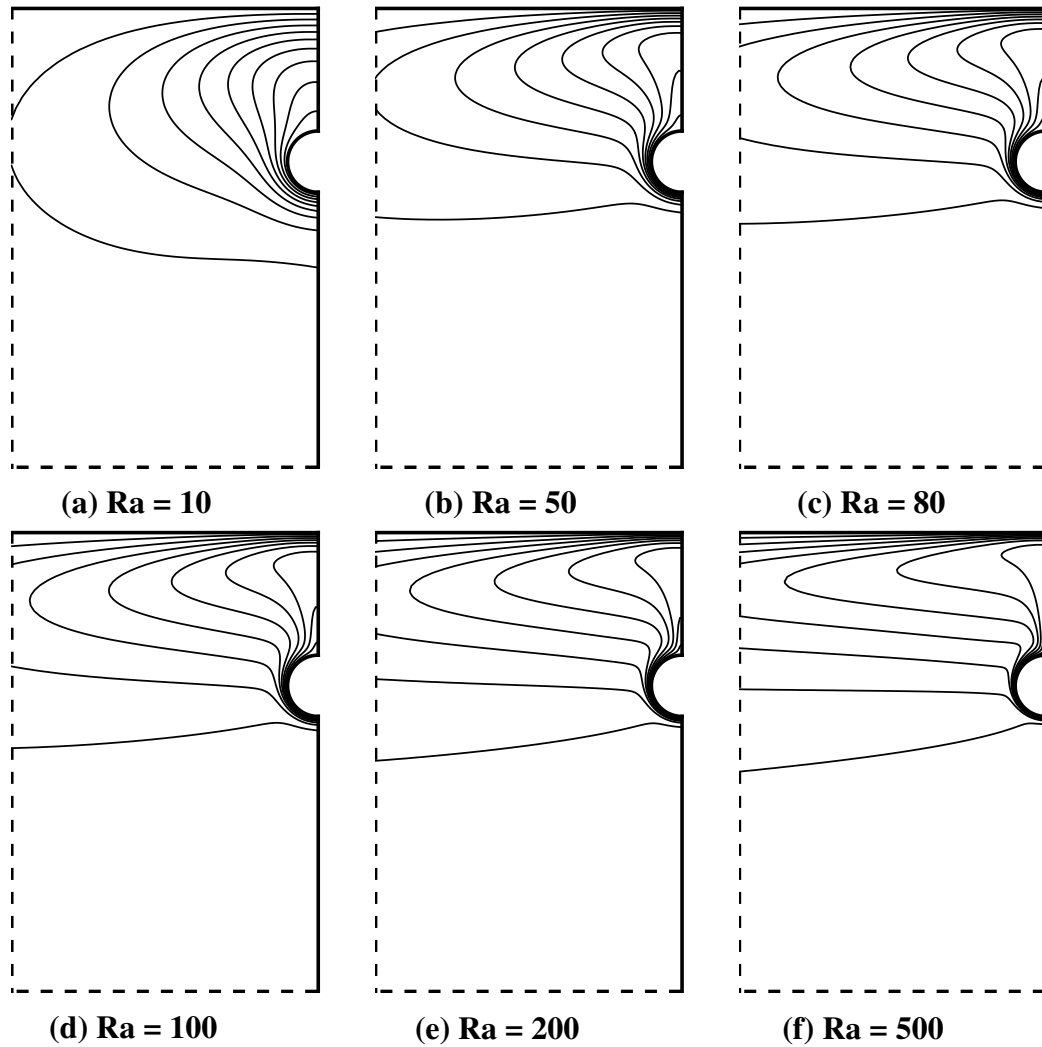
Figure 3.13 Temperature fields for natural convection from a buried heated pipe (a) Ra = 10, (b) Ra = 50, (c) Ra = 80, (d) Ra = 100, (e) Ra = 200, (f) Ra = 500 ($\Delta\Theta = 0.1$).

excellent agreement between the present numerical solutions and those of the previous analytical work. The conductive heat transfer for an isothermal top surface is determined to be 1.43, which is within 5% of the analytical solution provided by Eckert and Drake (1959). As for the convective top surface, the heat transfer results approach those of isothermal top surface when the Biot number is equal to or greater

than 10. As for the study of natural convection, Nusselt number is found to be a function of the square root of the Rayleigh number. The results also compare well with the perturbation solutions provided by Himasekhar and Bao (1987) for small Rayleigh numbers.

CHAPTER IV

NATURAL CONVECTION FROM A PIPE BURIED IN A HETEROGENEOUS POROUS MEDIUM

4.1 Introductory Remarks

In Chapter 3, heat conduction and natural convection induced from a heated pipe buried in a porous medium has been examined. The porous medium considered has been assumed to be homogeneous; however in reality heterogeneous or layered porous media are encountered more frequently in engineering applications. For buried pipes, the soil structure near the buried site is usually modified from its original state in the excavation process. A similar situation is found in the mining process for a nuclear waste repository. In addition to the changes brought about by the excavation/mining process, it is customary to add backfill to the buried pipes and waste canisters. As a result, the soil or bed rock that hosts the pipes and waste canisters are never homogeneous, but heterogeneous instead.

A review of the literature reveals that only limited deal with heat convection from a buried pipe in a heterogeneous porous medium (Hsiao et al., 1992). Previous studies that most closely resemble the problem at hand are those reported by Muralidhar et al. (1986) and Ngo and Lai (2000) in which a layered porous annulus was considered. For the problem considered here, the properties of the excavation disturbed zone and backfill around the buried pipe would be different from those of the soil far away from the pipe. Among the properties involved, permeability is

perhaps the most important because of its direct influence on the convective flow. Therefore, it is the objective of the present study to examine the effects of permeability variation in the porous medium on the heat transfer results.

4.2 Mathematical Formulation

The geometry considered is a horizontal pipe with a radius of r_i buried in a saturated porous medium at a depth of d beneath the top surface (Figure 4.1). The top surface is assumed impermeable and maintained at a constant temperature T_c while the buried pipe is maintained at a higher temperature T_h. The excavation disturbed zone and backfill immediate around the buried pipe is assumed to form a layer of thickness t and which has a distinct permeability from the soil outside of this region (far field). Since the physical domain is symmetric, only one half of the domain (-w $\leq$ x $\leq$ 0 and -w $\leq$ y $\leq$ d) is considered for computations.
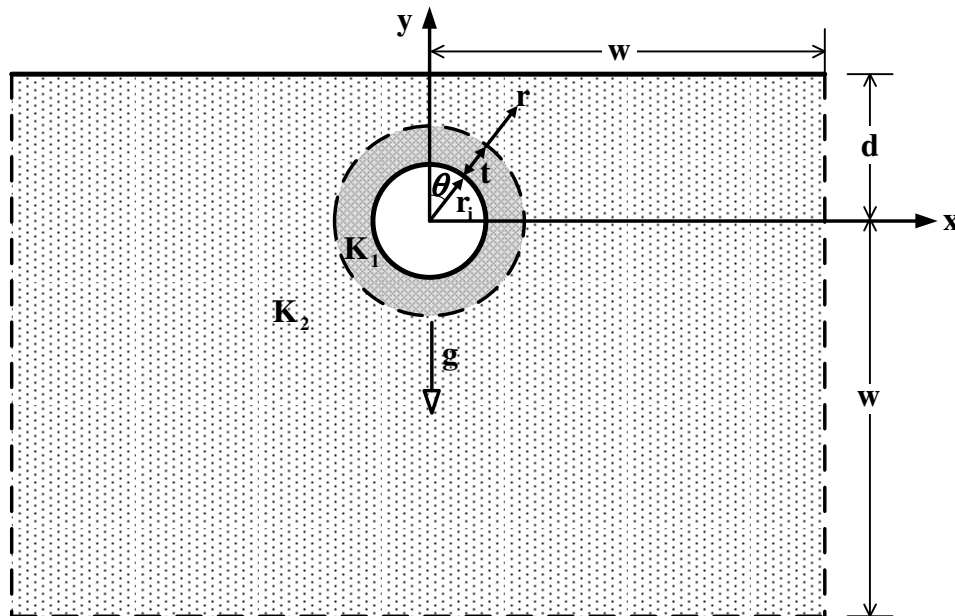
Figure 4.1 A horizontal pipe with a backfill layer in a saturated porous medium.

The governing equations based on Darcy's law in the computational domain
are the same as those presented in Chapter 3.

$$\nabla^2_{\xi\eta}\Psi_i = -\frac{Ra_i}{J}\left[\frac{\partial\Theta_i}{\partial\xi}\frac{\partial Y}{\partial\eta} - \frac{\partial\Theta_i}{\partial\eta}\frac{\partial Y}{\partial\xi}\right], \tag{4.1}$$

$$\nabla^2_{\xi\eta}\Theta_i = \frac{1}{J}\left[\frac{\partial\Theta_i}{\partial\xi}\frac{\partial\Psi_i}{\partial\eta} - \frac{\partial\Theta_i}{\partial\eta}\frac{\partial\Psi_i}{\partial\xi}\right], \tag{4.2}$$

where $\quad \nabla^2_{\xi\eta} = \frac{\overline{\alpha}}{J^2}\frac{\partial^2}{\partial\xi^2} - \frac{2\overline{\beta}}{J^2}\frac{\partial^2}{\partial\xi\partial\eta} + \frac{\overline{\gamma}}{J^2}\frac{\partial^2}{\partial\eta^2} + \overline{P}\frac{\partial}{\partial\xi} + \overline{Q}\frac{\partial}{\partial\eta},$ $\tag{4.3}$

and the subscript i ($= 1, 2$) denotes the inner and outer regions of the porous medium,
respectively. The mesh for both physical and computational domain is shown in
Figure 4.2. Only grid control function $\overline{Q}$ is employed in the outer region of the
porous medium to control the grid line distributions in the direction of η toward the
boundary η_n (Thompson, 1982), i.e.,

$$\overline{P} = 0, \tag{4.4}$$

$$\overline{Q} = -A_1 \text{sign}(\eta - \eta_n)\exp[-A_2|\eta - \eta_n|], \tag{4.5}$$

with $A_1 = 4$ and $A_2 = 0.5$.

4.3 Boundary and Interface Conditions

The boundary conditions for this problem are given as follows:

At $r = r_i$, $\pi \le \theta \le 2\pi$, $\qquad\qquad$ $T_1 = T_h$, $\qquad$ $u_{r1} = 0.$ $\qquad$ [4.6a, b]

At $y = d$, $-w \le x \le 0$, $\qquad\qquad$ $T_2 = T_c$, $\qquad$ $v_2 = 0.$ $\qquad$ [4.6c, d]

At $x = -w$, $-w \le y \le d$, $\qquad\qquad$ $\dfrac{\partial T_2}{\partial x} = 0$, $\qquad$ $v_2 = 0.$ $\qquad$ [4.6e, f]
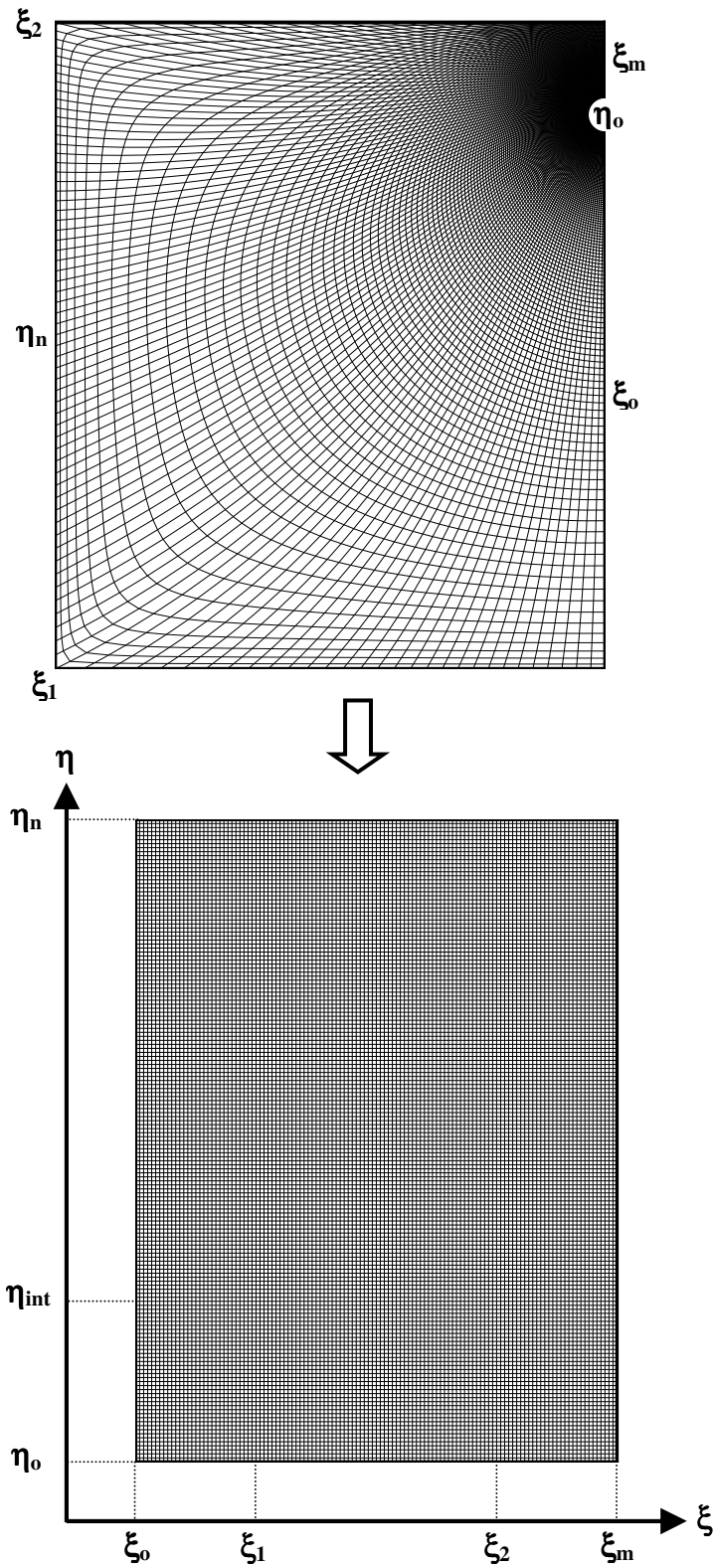
Figure 4.2 Mesh generated in the physical and computational domain.

At $y = -w$, $-w \le x \le 0$, $\qquad \dfrac{\partial T_2}{\partial y} = 0$, $\qquad u_2 = 0$. $\qquad\qquad$ [4.6g, h]

At $x = 0$, $\pm r_i \le y < \pm (r_i + t)$, $\qquad \dfrac{\partial T_1}{\partial x} = 0$, $\qquad u_1 = 0$. $\qquad\qquad$ [4.6i, j]

$(r_i + t) < y \le d$, $\qquad \dfrac{\partial T_2}{\partial x} = 0$, $\qquad u_2 = 0$. $\qquad\qquad$ [4.6k, l]

$-(r_i + t) < y \le -w$, $\qquad \dfrac{\partial T_2}{\partial x} = 0$, $\qquad u_2 = 0$. $\qquad\qquad$ [4.6m, n]

For better understanding, the dimensionless boundary conditions are shown in Figure 4.3.
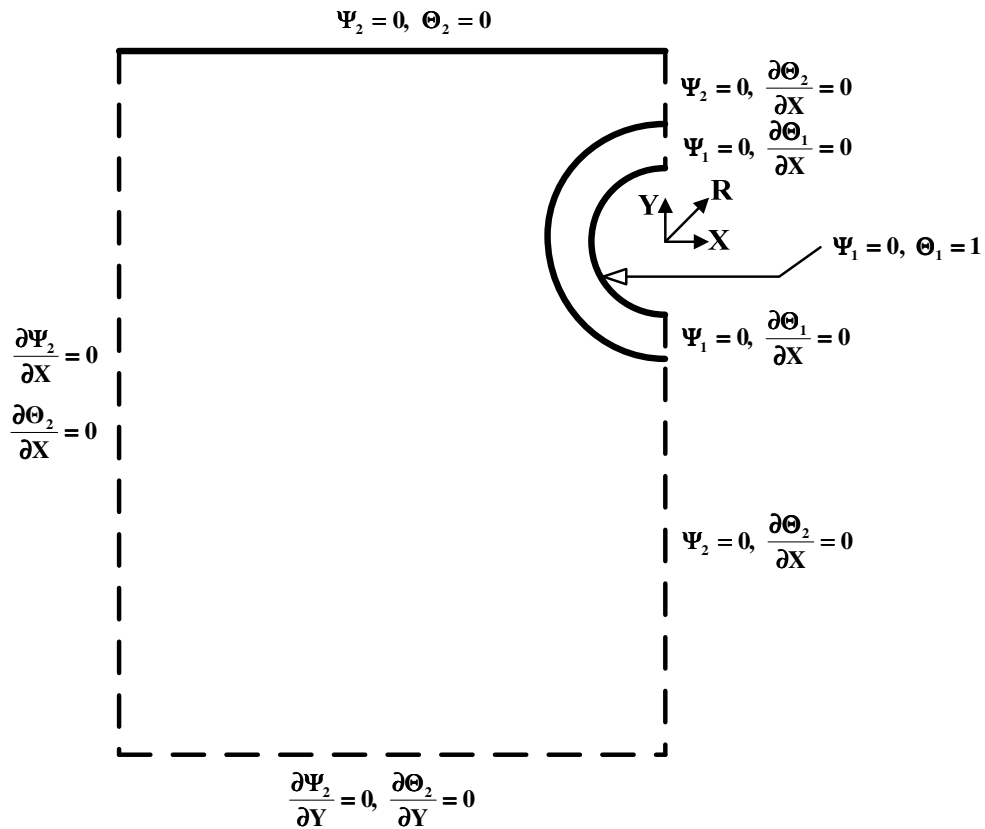
Figure 4.3 Dimensionless boundary conditions for the study of natural convection from a buried pipe with a backfill layer.

In addition to the boundary conditions, appropriate conditions need to be specified at the interface between the two porous regions and they are the continuity of pressure, temperature, radial flow and heat flux:

$$p_1 = p_2,$$ [4.7a]

$$T_1 = T_2,$$ [4.7b]

$$u_{r1} = u_{r2},$$ [4.7c]

$$k_1 \frac{\partial T_1}{\partial r} = k_2 \frac{\partial T_2}{\partial r}.$$ [4.7d]

The justification of these interface conditions has been given by Rana et al. (1979) as well as by McKibbin and O'Sullivan (1981). In a separate study by Pan and Lai (1996), it has been shown that the application of these interface conditions does produce a better agreement with experimental results.

The boundary conditions in the transformed domain are given below.

At $\eta = \eta_o$, $\quad \xi_o \le \xi \le \xi_m$, $\qquad \Theta_1 = 1$, $\qquad \Psi_1 = 0.$ [4.8a, b]

At $\eta = \eta_n$, $\quad \xi_o \le \xi \le \xi_1$, $\qquad \dfrac{\partial \Theta_2}{\partial \eta} \dfrac{\partial X}{\partial \xi} - \dfrac{\partial \Theta_2}{\partial \xi} \dfrac{\partial X}{\partial \eta} = 0,$ [4.8c]

$$\frac{\partial \Psi_2}{\partial \eta} \frac{\partial X}{\partial \xi} - \frac{\partial \Psi_2}{\partial \xi} \frac{\partial X}{\partial \eta} = 0.$$ [4.8d]

$\xi_1 \le \xi \le \xi_2$, $\qquad \dfrac{\partial \Theta_2}{\partial \xi} \dfrac{\partial Y}{\partial \eta} - \dfrac{\partial \Theta_2}{\partial \eta} \dfrac{\partial Y}{\partial \xi} = 0,$ [4.8e]

$$\frac{\partial \Psi_2}{\partial \xi} \frac{\partial Y}{\partial \eta} - \frac{\partial \Psi_2}{\partial \eta} \frac{\partial Y}{\partial \xi} = 0.$$ [4.8f]

$\xi_2 \le \xi \le \xi_m$, $\qquad \Theta_2 = 0$, $\qquad \Psi_2 = 0.$ [4.8g, h]

At $\xi = \xi_o$ and $\xi = \xi_m$,

$$\eta_o \leq \eta < \eta_{int}, \qquad \frac{\partial \Theta_1}{\partial \xi}\frac{\partial Y}{\partial \eta} - \frac{\partial \Theta_1}{\partial \eta}\frac{\partial Y}{\partial \xi} = 0, \qquad \Psi_1 = 0. \qquad [4.8i, j]$$

$$\eta_{int} < \eta \leq \eta_n, \qquad \frac{\partial \Theta_2}{\partial \xi}\frac{\partial Y}{\partial \eta} - \frac{\partial \Theta_2}{\partial \eta}\frac{\partial Y}{\partial \xi} = 0, \qquad \Psi_2 = 0. \qquad [4.8k, l]$$

where the subscript "int" refers to the location of the interface.

Similarly, the transformed dimensionless interface conditions are,

$$\sin\theta\left[\frac{\partial \Psi_1}{\partial \xi}\frac{\partial Y}{\partial \eta} - \frac{\partial \Psi_1}{\partial \eta}\frac{\partial Y}{\partial \xi}\right] + \cos\theta\left[-\frac{\partial \Psi_1}{\partial \xi}\frac{\partial X}{\partial \eta} + \frac{\partial \Psi_1}{\partial \eta}\frac{\partial X}{\partial \xi}\right]$$

$$= \frac{\alpha_2}{\alpha_1}\frac{K_1}{K_2}\left\{\sin\theta\left[\frac{\partial \Psi_2}{\partial \xi}\frac{\partial Y}{\partial \eta} - \frac{\partial \Psi_2}{\partial \eta}\frac{\partial Y}{\partial \xi}\right]\right.$$

$$\left. + \cos\theta\left[-\frac{\partial \Psi_2}{\partial \xi}\frac{\partial X}{\partial \eta} + \frac{\partial \Psi_2}{\partial \eta}\frac{\partial X}{\partial \xi}\right]\right\}, \qquad [4.9a]$$

$$\Theta_1 = \Theta_2, \qquad [4.9b]$$

$$\cos\theta\left[\frac{\partial \Psi_1}{\partial \xi}\frac{\partial Y}{\partial \eta} - \frac{\partial \Psi_1}{\partial \eta}\frac{\partial Y}{\partial \xi}\right] - \sin\theta\left[-\frac{\partial \Psi_1}{\partial \xi}\frac{\partial X}{\partial \eta} + \frac{\partial \Psi_1}{\partial \eta}\frac{\partial X}{\partial \xi}\right]$$

$$= \frac{\alpha_2}{\alpha_1}\left\{\cos\theta\left[\frac{\partial \Psi_2}{\partial \xi}\frac{\partial Y}{\partial \eta} - \frac{\partial \Psi_2}{\partial \eta}\frac{\partial Y}{\partial \xi}\right]\right.$$

$$\left. - \sin\theta\left[-\frac{\partial \Psi_2}{\partial \xi}\frac{\partial X}{\partial \eta} + \frac{\partial \Psi_2}{\partial \eta}\frac{\partial X}{\partial \xi}\right]\right\}, \qquad [4.9c]$$

$$\sin\theta\left[\frac{\partial \Theta_1}{\partial \xi}\frac{\partial Y}{\partial \eta} - \frac{\partial \Theta_1}{\partial \eta}\frac{\partial Y}{\partial \xi}\right] + \cos\theta\left[-\frac{\partial \Theta_1}{\partial \xi}\frac{\partial X}{\partial \eta} + \frac{\partial \Theta_1}{\partial \eta}\frac{\partial X}{\partial \xi}\right]$$

$$= \frac{\alpha_2}{\alpha_1}\left\{\sin\theta\left[\frac{\partial \Theta_2}{\partial \xi}\frac{\partial Y}{\partial \eta} - \frac{\partial \Theta_2}{\partial \eta}\frac{\partial Y}{\partial \xi}\right]\right.$$

$$\left. + \cos\theta\left[-\frac{\partial \Theta_2}{\partial \xi}\frac{\partial X}{\partial \eta} + \frac{\partial \Theta_2}{\partial \eta}\frac{\partial X}{\partial \xi}\right]\right\}. \qquad [4.9d]$$

4.4 Numerical Methods

The governing equations along with the boundary conditions are solved by finite difference method (see Chapter 3 for the derivation). The expressions of the discretized stream function and temperature for the inner and outer regions are given by Eqn. 3.25 and Eqn. 3.58, respectively. The interface conditions are implemented using imaginary nodal points (Figure 4.4) as described by Rana et al. (1979). The location of the interface is indicated by η_{int}, along with solid circles representing the actual grid points and open circles as the imaginary nodal points. The interface conditions for stream function and temperature can be reduced to the following algebraic forms:

$$\Psi_{1P} = \frac{1}{I_{F0}}\left(I_{F1} + I_{F2} + I_{F3} + I_{F4} + I_{F5} - I_{F6}\right), \qquad [4.10a]$$

where

$$I_{F0} = 2(\overline{\alpha} + \overline{\gamma})\left(1 + \frac{K_1}{K_2}\right) + \frac{3}{2}J^2\frac{K_1}{K_2}, \qquad [4.10b]$$

$$I_{F1} = \overline{\alpha}\left(1 + \frac{K_1}{K_2}\right)\left(\Psi_{1E} + \Psi_{1W}\right), \qquad [4.10c]$$

$$I_{F2} = 2\overline{\gamma}\left(\Psi_{1S} + \frac{K_1}{K_2}\frac{\alpha_2}{\alpha_1}\Psi_{2N}\right), \qquad [4.10d]$$

$$I_{F3} = -\overline{\gamma}\frac{\sin\theta(Y_S - Y_N) - \cos\theta(X_S - X_N)}{\sin\theta(Y_E - Y_W) - \cos\theta(X_E - X_W)}\left(1 - \frac{K_1}{K_2}\right)\left(\Psi_{1E} - \Psi_{1W}\right), \qquad [4.10e]$$

$$I_{F4} = -\overline{\beta}\left[\left(\Psi_{1E} - \Psi_{1SE} - \Psi_{1W} + \Psi_{1SW}\right) + \frac{K_1}{K_2}\frac{\alpha_2}{\alpha_1}\left(\Psi_{2NE} - \Psi_{2NW}\right) - \frac{K_1}{K_2}\left(\Psi_{1E} - \Psi_{1W}\right)\right], \quad [4.10f]$$
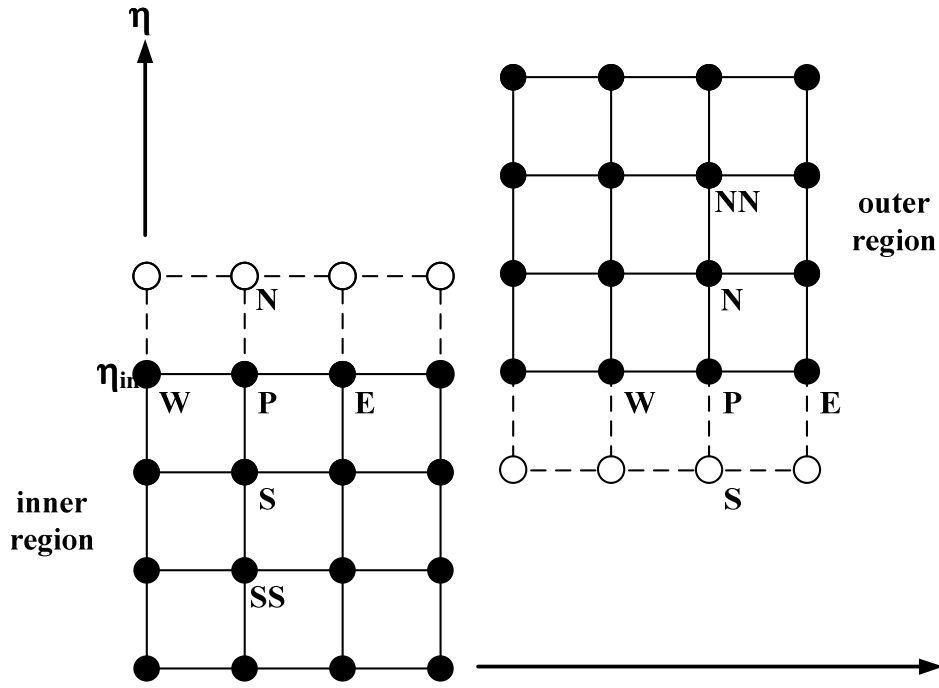
Figure 4.4 Imaginary nodal points for the implementation of interface conditions.

$$I_{F5} = \frac{1}{2}J^2\frac{K_1}{K_2}\frac{\alpha_2}{\alpha_1}\overline{Q}_2(4\Psi_{2N} - \Psi_{2NN}), \tag{4.10g}$$

$$I_{F6} = -\frac{J}{4}Ra_1[2(\Theta_{1E} - \Theta_{1W})(Y_N - Y_S) + (4\Theta_{1S} - 4\Theta_{2N} + \Theta_{2NN} - \Theta_{1SS})(Y_E - Y_W)], \tag{4.10h}$$

$$\Theta_{1P} = \frac{1}{I_{T1}}\left[\frac{I_{T3}}{I_{T2}}(\Theta_{1E} - \Theta_{1W}) - 4\Theta_{1S} + \Theta_{1SS} - \frac{\alpha_2}{\alpha_1}(4\Theta_{2N} - \Theta_{2NN})\right], \tag{4.11a}$$

where $$I_{T1} = -3\left(\frac{\alpha_2}{\alpha_1} + 1\right), \tag{4.11b}$$

$$I_{T2} = \sin\theta(Y_E - Y_W) - \cos\theta(X_E - X_W), \tag{4.11c}$$

$$I_{T3} = \sin\theta\left[\frac{\alpha_2}{\alpha_1}(-3Y_P + 4Y_N - Y_{NN}) - (3Y_P - 4Y_S + Y_{SS})\right]$$
$$- \cos\theta\left[\frac{\alpha_2}{\alpha_1}(-3X_P + 4X_N - X_{NN}) - (3X_P - 4X_S + X_{SS})\right]. \tag{4.11d}$$

Also, note that the grids near the interface have been constructed carefully to preserve the smoothness and near orthogonality, as can be seen from Figure 4.5.

For the present study, the dimensionless buried depth is fixed at five ($d/r_i = 5$) and the thermal diffusivity ratio is set to unity ($\alpha_1/\alpha_2 = 1$). Since the porous medium is assumed to be saturated with the same fluid, the thermal diffusivity ratio is equal to the thermal conductivity ratio ($\alpha_1/\alpha_2 = k_1/k_2$). Numerous trial runs have been conducted to ensure that the heat transfer results obtained from the present study are independent of the physical domain and mesh size. It has been found that a dimensionless width (w/r_i) of 30 is sufficient to represent the domain as a semi-infinite medium (see Chapter 3). A uniform grid of 121×161 in the computational domain (i.e., 121×41 for the inner region and 121×121 for the outer region) is the best
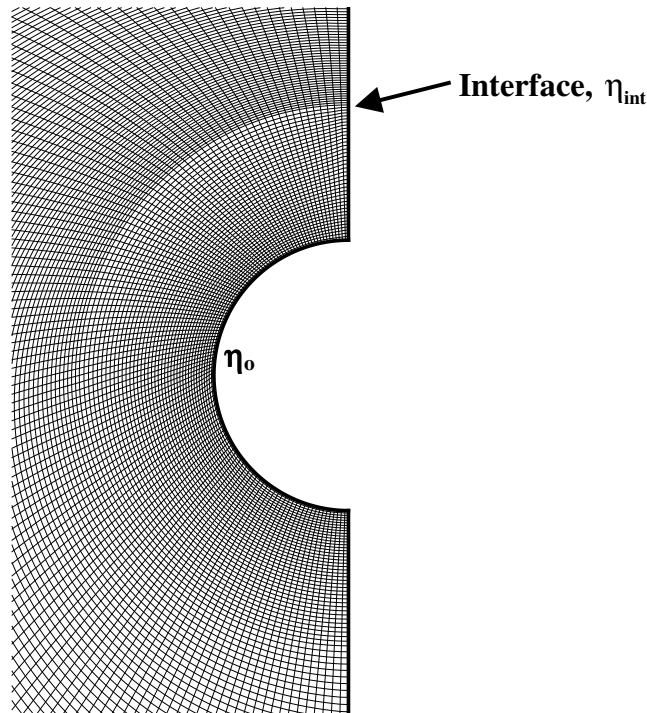
Figure 4.5 Magnified view of the computational mesh near the interface.

choice for all calculations in terms of the computational efficiency and accuracy. It should be noted that a further increase in the physical domain size or grid refinement does not produce any significant improvement in the heat transfer results (< 1%). As an additional check on the accuracy of the numerical results, an overall energy balance has been performed. All the results obtained are satisfied within 3%. The solution procedures are summarized by the flow chart shown below.
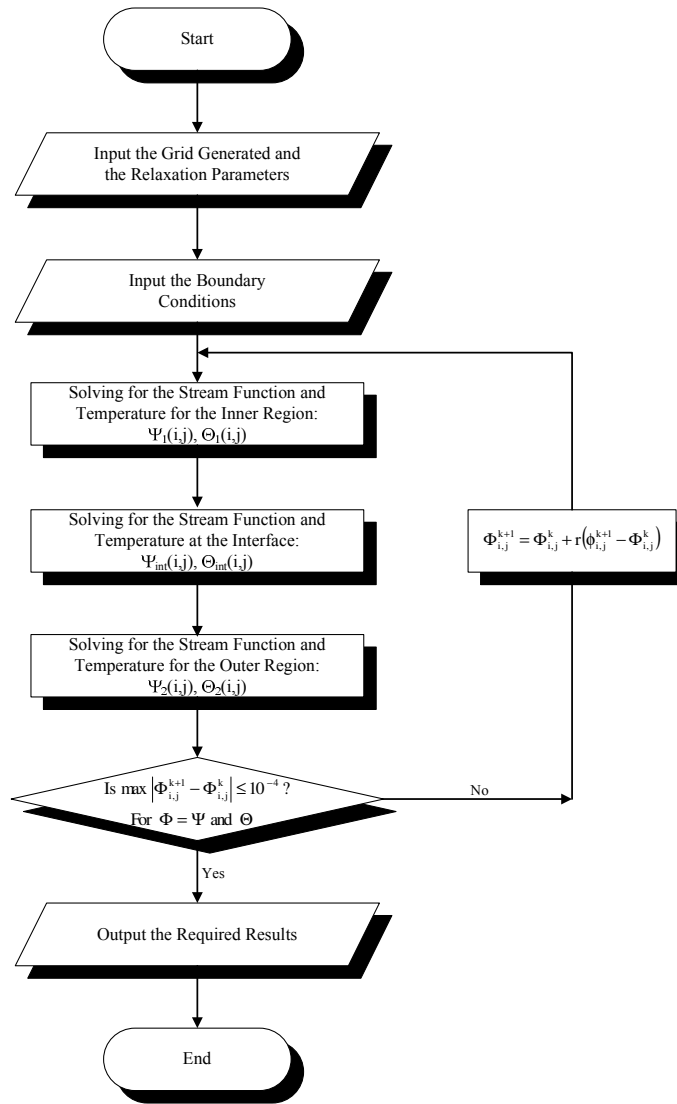
Figure 4.6 Flow chart of the numerical procedures for the study of natural convection from a buried pipe with a backfill layer.

To validate the numerical code, the present results have been tested against those reported in the literature for natural convection in a layered porous annulus. With a minimum modification of the present code, results can be readily obtained and they are in good agreement with those reported by Ngo and Lai (2000), which can be clearly observed from Figure 4.7.

4.5 Results and Discussion

To this end, numerical calculations have covered a wide range of the governing parameters (i.e., $10 \leq Ra_1 \leq 500$ and $0.1 \leq K_1/K_2 \leq 10$) for various backfill thicknesses ($0.5 \leq t/r_i \leq 2$), and they are summarized in Table 4.1.

When the excavation disturbed zone or backfill is considered, the resulting flow and temperature fields (Figures 4.8 - 4.11) are very different from those of the homogeneous one. To better observe the flow structure and temperature field at the vicinity of the buried pipe, only partial results are presented in these figures ($10 \leq X \leq$
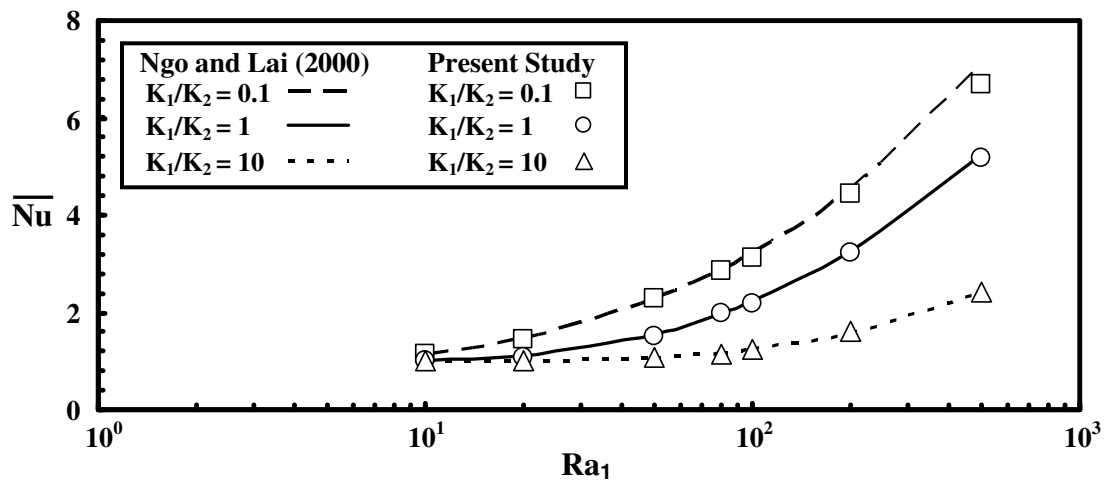
Figure 4.7 Validation of numerical results for natural convection in a layered porous annulus.

110

Table 4.1 Range of the parameters considered in the study of natural convection from a buried pipe with a backfill layer.

Parameters	Range
Rayleigh Number (Ra)	10, 20, 50, 80, 100, 200, 500
Permeability Ratio (K_1/K_2)	0.1, 1, 10
Backfill Thickness (t/r_i)	0.5, 1, 2

0, $-10 \leq Y \leq 5$). For $K_1/K_2 = 10$, it is observed that the heat transfer mode is mainly by conduction at low Rayleigh numbers (e.g., $Ra_1 = 10$), which is evident from the isotherms displayed in Figure 4.9. As the Rayleigh number (thermal buoyancy) increases, convective flow is first initiated from the inner layer (i.e., the more permeable layer) and then gradually penetrates the outer region (Figure 4.8). Due to the added flow resistance in the outer region, the flow fields for $K_1/K_2 = 10$ are weaker than those of the homogeneous case. As a result, the eye of the convective cell is confined mostly in the inner layer. For a fixed Rayleigh number, the strength of the convective cell increases with the inner layer thickness (t/r_i). A thicker inner layer provides more room for the convective cell to develop.

On the other hand, for $K_1/K_2 = 0.1$, the outer region is more permeable than the inner layer, and consequently convection is promoted. It can be observed from Figure 4.10 that convection is initiated even at a low Rayleigh number and the strength of the convective cell is notably strong when compared with that of the homogeneous case. It is interesting to note that the eye of the convective cell in this case always locates at the outer region. From the isotherms shown in Figure 4.11, it
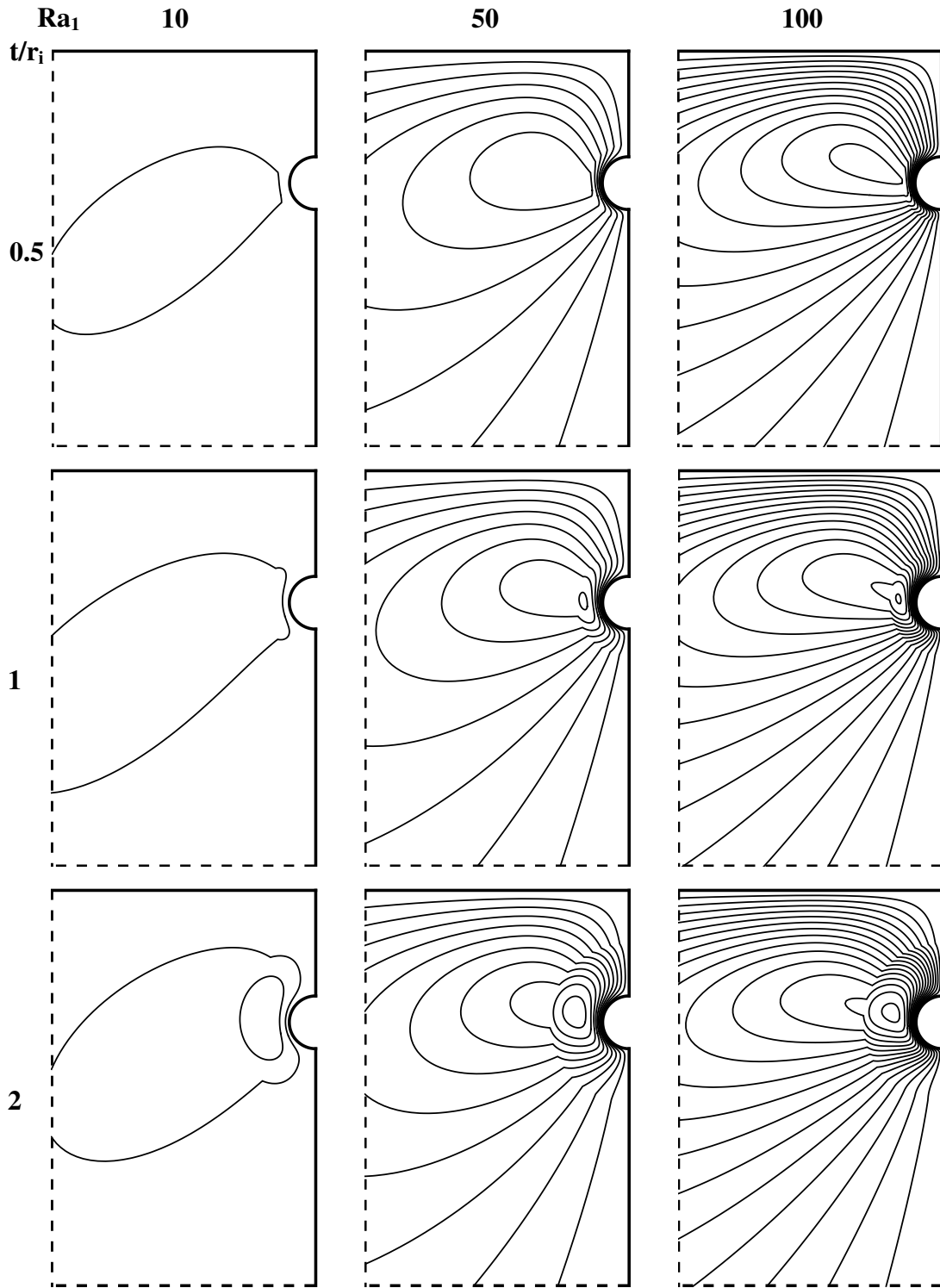
Figure 4.8 Flow fields for a buried pipe with a backfill of $K_1/K_2 = 10$ ($\Delta\Psi = 0.5$).
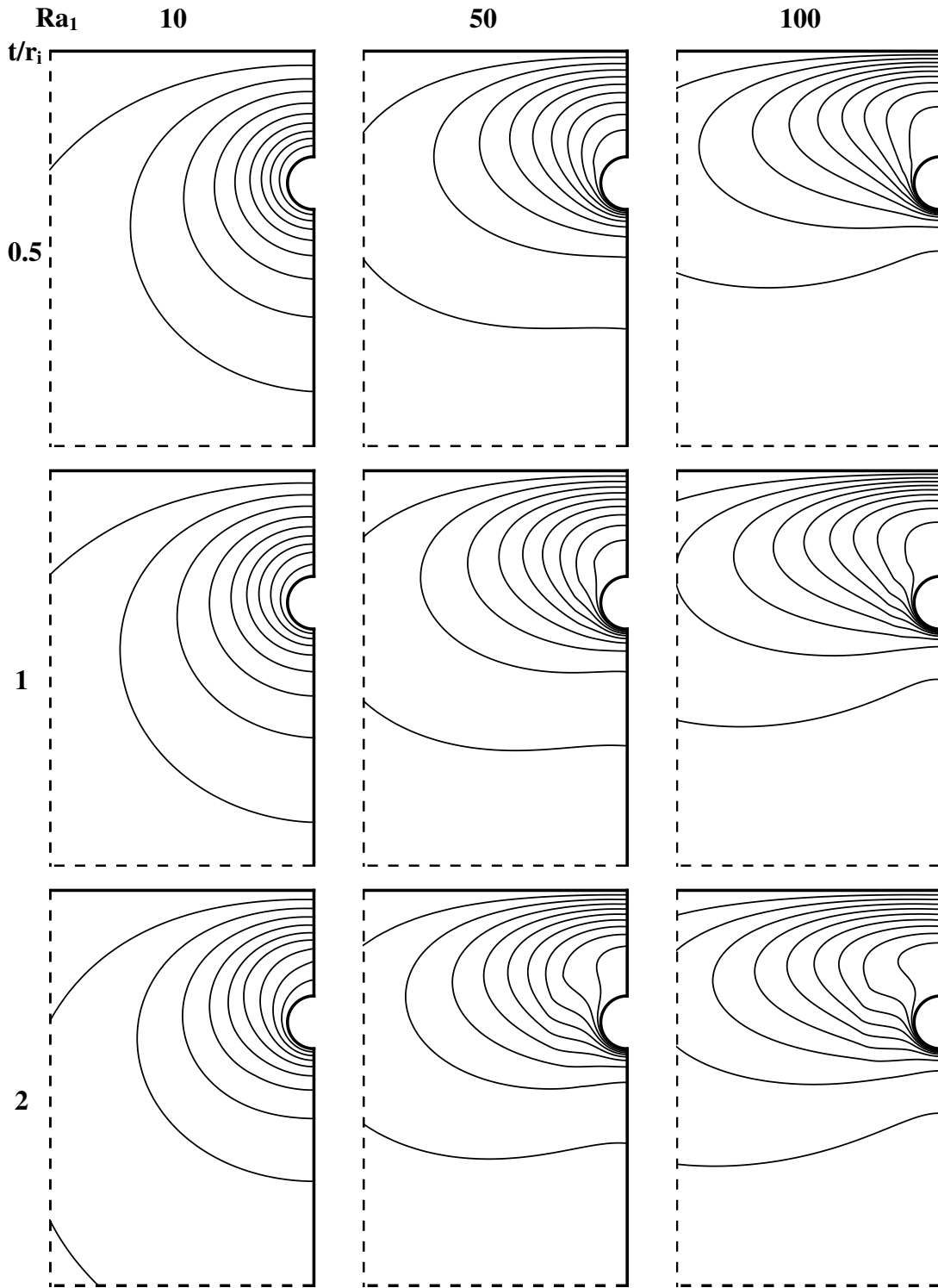
Figure 4.9 Temperature fields for a buried pipe with a backfill of $K_1/K_2 = 10$ ($\Delta\Theta = 0.1$).

Ra$_1$ 10   50   100

t/r$_i$
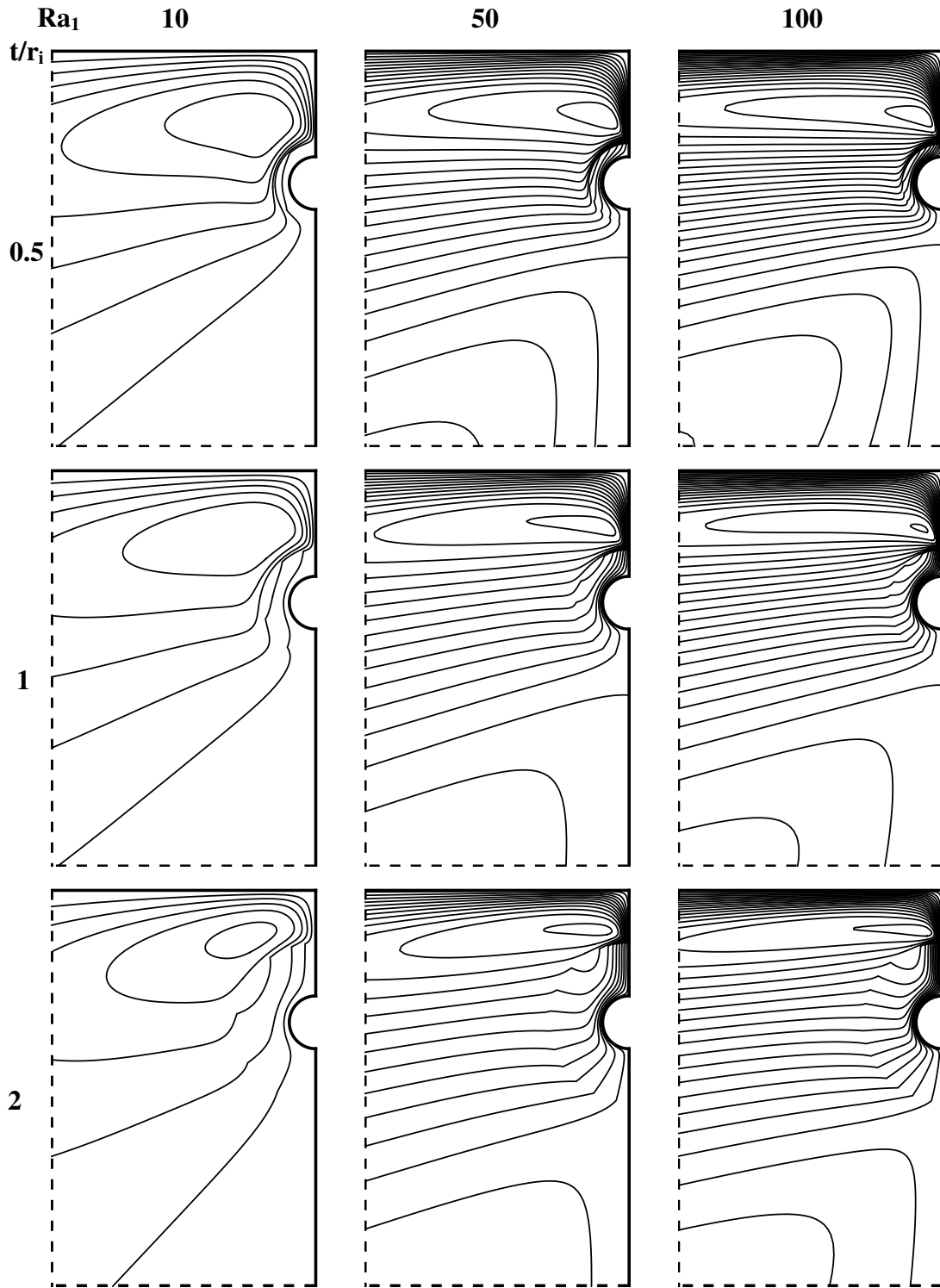
Figure 4.10 Flow fields for a buried pipe with a backfill of K$_1$/K$_2$ = 0.1 ($\Delta\Psi$ = 2).
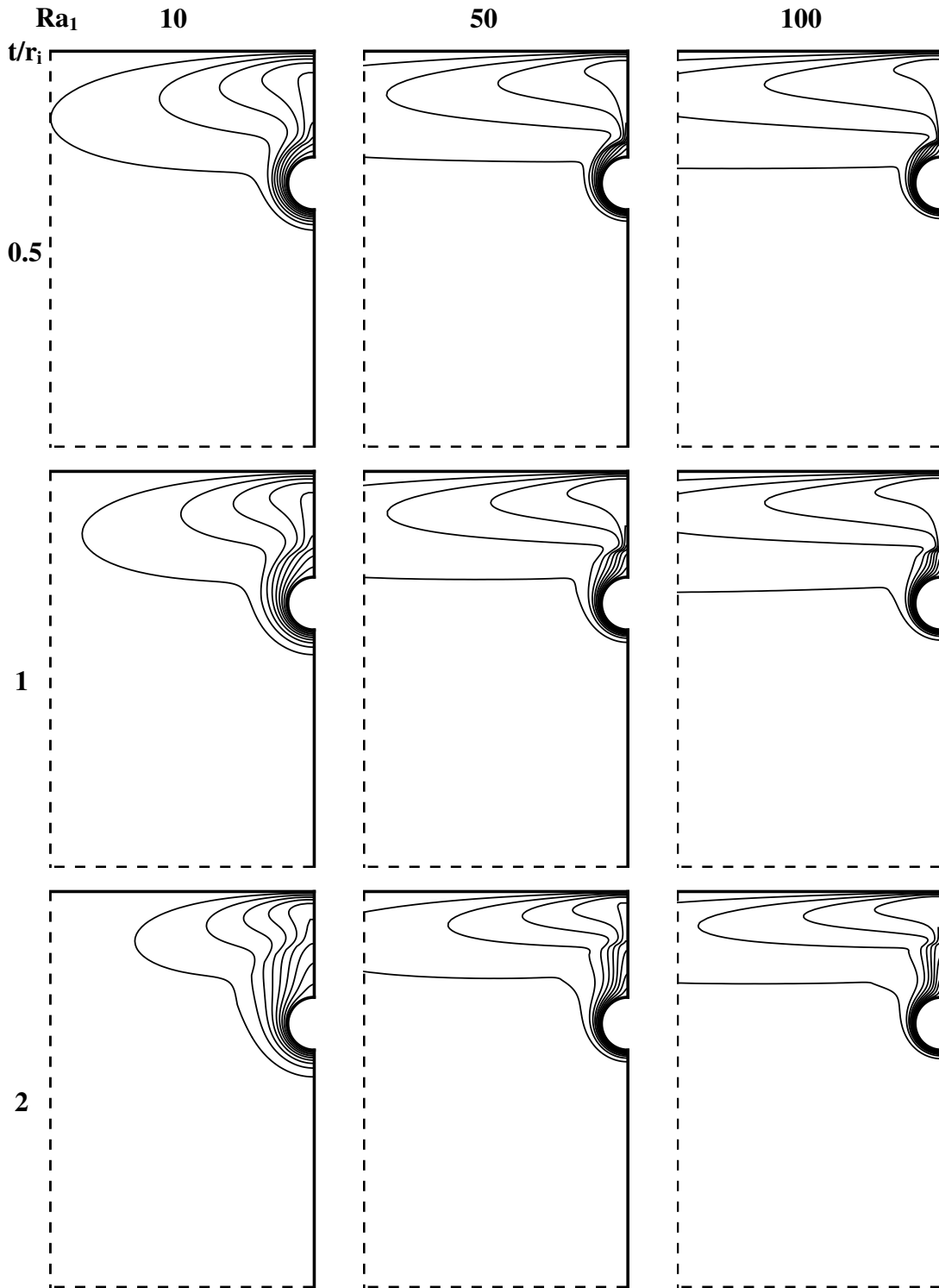
Figure 4.11 Temperature fields for a buried pipe with a backfill of $K_1/K_2 = 0.1$ ($\Delta\Theta = 0.1$).

is ascertained that heat transfer is always by convection for $K_1/K_2 < 1$. For a fixed

Rayleigh number, the temperature gradient across the inner layer decreases with an

increase in the inner layer thickness. The strength of the convective flow in the outer

layer is weakened accordingly.

For the present study, heat transfer results are evaluated in terms of the

Nusselt number at the top surface,

$$ \text{Nu} = -\int_{-w/r_i}^{0} \left.\frac{\partial \Theta}{\partial Y}\right|_{Y=d/r_i} dX, \tag{4.12} $$

which also represents the total heat flux through the top surface. For a homogeneous

porous medium, the heat transfer results can be correlated by the following equation,

$$ \text{Nu} = \text{Ra}^{\frac{1}{2}}. \tag{4.13} $$

The Nusselt numbers obtained for the present study are shown in Figure 4.12 as a
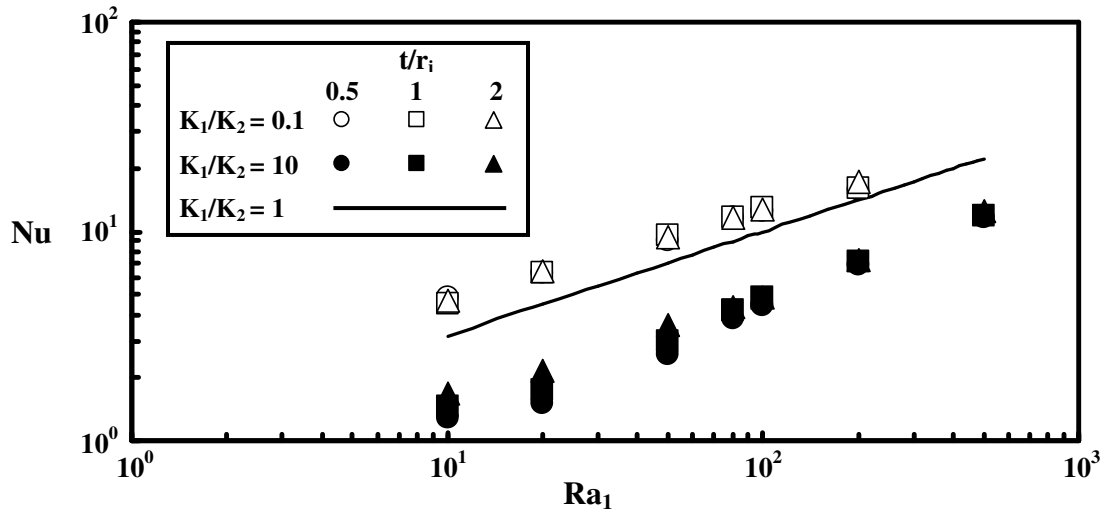
Figure 4.12 Heat transfer results for natural convection from a buried pipe with and without backfill.

function of the Rayleigh number. It is observed that the Nusselt number for a buried pipe with a backfill of $K_1/K_2 < 1$ is always larger than that of a homogeneous one while it is always smaller for a buried pipe with a backfill of $K_1/K_2 > 1$. It should be mentioned that for $K_1/K_2 < 1$, no converged solution has been obtained for high Rayleigh numbers ($Ra_1 \geq 500$) due to the nature of a highly convective flow field. It is interesting to note that the trend observed here is similar to that for a layered porous annulus (Ngo and Lai, 2000) despite that the configurations for these two cases are very different.

4.6 Concluding Remarks

The present study has considered a very fundamental problem in heat transfer. Although the problem has received considerable attention in the past, the present study addresses some critical aspects of the problem, particularly related to its applications to energy utilization and environmental protection. Based on the results obtained, one can conclude that, for the transportation of crude oil, it may be desirable to have a layer of backfill or excavation disturbed zone that is more permeable than the hosting soil ($K_1/K_2 > 1$) so that the heat loss can be minimized. In fact, this is also the most desirable condition for the purpose of environmental protection since the contamination will be confined mostly in the disturbed zone or the backfill layer in the event that a leak should develop from a pipeline or a nuclear waste canister. On the other hand, for the applications in electric power transmission, a backfill with $K_1/K_2 > 1$ may be used if overheating of transmission lines or power cables is to be avoided.

COUPLED HEAT AND MASS TRANSFER BY MIXED CONVECTION FROM A BURIED PIPE WITH LEAKAGE

5.1 Introductory Remarks

In the previous two chapters, heat transfer and fluid flow near a buried pipe in both homogeneous and heterogeneous porous medium have been examined from the natural convection perspective. Coupled heat and mass transfer resulting from a leakage on a buried pipe is the main interest in this chapter. This type of convection is frequently referred to as the double-diffusive mixed convection, where the buoyancy due to the concentration difference is as significant as that produced by the temperature difference. Despite the importance of this transport phenomenon in engineering applications, only limited reports are available in the literature that deal with double diffusive convection from a buried cylinder. One of the pioneering studies was performed by Poulikakos (1985) as he tackled the problem with perturbation method using a heat and concentration point source in an infinite porous medium. Later, Cheng and Lai (1997), Yih (1999) as well as Chamkha and Quadri (2001) investigated the double-diffusive transport phenomena from a buried cylinder. However, their studies did not consider a leakage from the pipe.

The objective of the present study is to investigate the coupled heat and mass transfer by mixed convection induced by a leakage from a cylinder buried in a porous medium. The engineering application that is closely related to this study is the

transportation of crude oil through buried pipelines. In order to reduce the pumping load and cost, crude oil is often heated to a higher temperature to reduce its viscosity for transport. In the event of a leak developed from the pipeline, one would be interested in predicting the spreading patterns of the crude oil from the accident site to the surrounding environment. Another application related to the present study is the usage of waste heat for soil heating. Sometimes it is desirable to let water seep through a buried pipe to provide subsurface irrigation and maintain the moisture level in the soil (Slegel and Davis, 1977). For either application, a prior knowledge of the flow, temperature and concentration distributions would certainly improve the effectiveness in confining the pollutants or providing subsurface heating and irrigation.

The geometry considered is a horizontal pipe with a radius of r_i embedded in a saturated porous medium at a depth of d ($d/r_i = 5$ for the present study) beneath the top surface (Figure 5.1). A crack developed on the pipe is assumed to have an angular span of 9° to produce leakage from the pipe. Two locations of the leakage are considered in the present study: one is on top and another at the bottom of the pipe. The fluid is assumed to discharge from the horizontal pipe at a radial velocity of u_R and a higher concentration of $\overline{C}_h$. The impermeable top surface is maintained at a lower temperature T_c and concentration $\overline{C}_c$ while the pipe itself is maintained at a higher temperature T_h. Since the geometry of the present problem is symmetric to the center line that contains the vertical diameter of the pipe, only one half of the physical domain is considered for computation. As illustrated in Chapter 3, the value of w/r_i
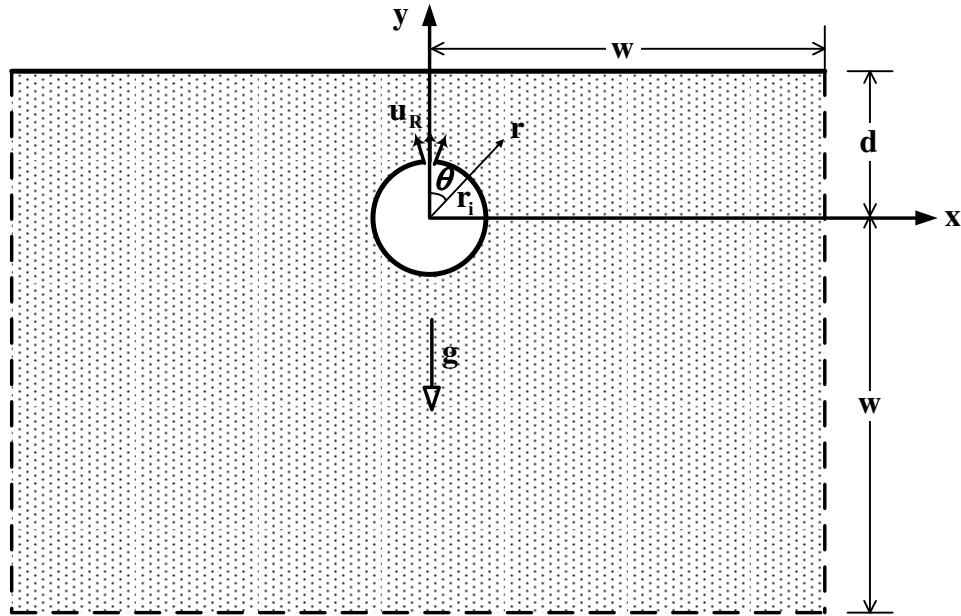
Figure 5.1 A leaking horizontal pipe embedded in a porous medium.

has been set to 30 as this ensures the domain is large enough to represent a semi-infinite medium.

5.2 Mathematical Formulation

Similar to the studies previously discussed in Chapter 3 and 4, the properties of the fluid and porous medium are assumed homogeneous and isotropic. The solid matrix is in local thermodynamics equilibrium with the saturating fluid. It is also assumed that the Darcy's law is applicable and thus the inertial and viscous effects are neglected. The governing equations for the double-diffusive convection based on Darcy's law in Cartesian coordinate system are given by

Continuity:
$$\frac{\partial u}{\partial x} + \frac{\partial v}{\partial y} = 0,$$
[5.1]

x-Momentum:
$$u = -\frac{K}{\mu}\frac{\partial p}{\partial x},$$
[5.2]

y-Momentum:
$$v = -\frac{K}{\mu}\left[\frac{\partial p}{\partial y} + \rho g\right],$$
[5.3]

Energy Equation:
$$u\frac{\partial T}{\partial x} + v\frac{\partial T}{\partial y} = \alpha\left[\frac{\partial^2 T}{\partial x^2} + \frac{\partial^2 T}{\partial y^2}\right],$$
[5.4]

Transport Equation:
$$u\frac{\partial \overline{C}}{\partial x} + v\frac{\partial \overline{C}}{\partial y} = D\left[\frac{\partial^2 \overline{C}}{\partial x^2} + \frac{\partial^2 \overline{C}}{\partial y^2}\right],$$
[5.5]

where D in the species transport equation represents the mass diffusivity.

In this study, the Boussinesq approximation is employed to account for the changes in density due to temperature and concentration difference in the body force term in the y-momentum equation. It is further assumed that density is a linear function of both temperature and concentration difference:

$$\rho = \rho_c\left[1 - \beta_T(T - T_c) - \beta_C(\overline{C} - \overline{C}_c)\right],$$
[5.6]

where β_T and β_C are the coefficient of thermal and concentration expansion, respectively. This approximation is valid only for small temperature and concentration differences, i.e., $(T - T_c) \leq O(1)$ and $(\overline{C} - \overline{C}_c) \leq O(1)$ (Gebhart et al., 1988).

Next, the following dimensionless parameters are introduced for the normalization of the governing equations,

$$X = \frac{x}{r_i}, \qquad Y = \frac{y}{r_i}, \qquad U = \frac{u}{u_R}, \qquad V = \frac{v}{u_R}, \qquad \text{[5.7a, b, c, d]}$$

$$\Theta = \frac{T - T_c}{T_h - T_c}, \qquad C = \frac{\overline{C} - \overline{C}_c}{\overline{C}_h - \overline{C}_c}, \qquad Ra = \frac{Kg\beta_T(T_h - T_c)r_i}{\alpha\nu}, \qquad [5.7e, f, g]$$

$$Le = \frac{\alpha}{D}, \qquad Pe = \frac{u_R r_i}{\alpha}, \qquad N = \frac{\beta_C(\overline{C}_h - \overline{C}_c)}{\beta_T(T_h - T_c)}. \qquad [5.7h, i, j]$$

The radius of the buried pipe is chosen as the characteristic length. Note that the characteristic velocity is different from that in the previous chapters for natural convection. The radial velocity of the leakage is used as the characteristic velocity in the present study. Temperature and concentration are normalized with the temperature and concentration difference between the cylinder and the top surface. Ra is the modified Rayleigh number as it represents the ratio of buoyancy force to viscous force. Le is the Lewis number, the ratio of thermal to mass diffusivity. Pe is the Peclet number as it is the measure of bulk heat transfer to diffusive heat transfer. N is the buoyancy ratio, the ratio of buoyancy due to concentration difference to that due to temperature difference. It is obvious that N is zero for pure thermal driven flows, infinite for mass driven flows, negative for opposing flows and positive for aiding flows.

Stream function is introduced to further simplify the governing equations,

$$U = \frac{\partial\Psi}{\partial Y}, \qquad V = -\frac{\partial\Psi}{\partial X}. \qquad [5.8a, b]$$

By introducing the stream functions, the continuity equation is satisfied automatically.

After cross-differentiated the momentum equations to eliminate the pressure terms, the dimensionless governing equations in terms of stream function are given by

$$\frac{\partial^2 \Psi}{\partial X^2} + \frac{\partial^2 \Psi}{\partial Y^2} = -\frac{Ra}{Pe}\left[\frac{\partial \Theta}{\partial X} + N\frac{\partial C}{\partial X}\right],$$ [5.9]

$$\frac{\partial \Psi}{\partial Y}\frac{\partial \Theta}{\partial X} - \frac{\partial \Psi}{\partial X}\frac{\partial \Theta}{\partial Y} = \frac{1}{Pe}\left[\frac{\partial^2 \Theta}{\partial X^2} + \frac{\partial^2 \Theta}{\partial Y^2}\right],$$ [5.10]

$$\frac{\partial \Psi}{\partial Y}\frac{\partial C}{\partial X} - \frac{\partial \Psi}{\partial X}\frac{\partial C}{\partial Y} = \frac{1}{Le \cdot Pe}\left[\frac{\partial^2 C}{\partial X^2} + \frac{\partial^2 C}{\partial Y^2}\right].$$ [5.11]

The above governing equations are then transformed to the computational domain by employing the elliptic transformation described in Chapter 2. The resultant equations are given as follows,

$$\nabla_{\xi\eta}^2 \Psi = -\frac{Ra}{Pe}\cdot\frac{1}{J}\left\{\left[\frac{\partial \Theta}{\partial \xi}\frac{\partial Y}{\partial \eta} - \frac{\partial \Theta}{\partial \eta}\frac{\partial Y}{\partial \xi}\right] + N\left[\frac{\partial C}{\partial \xi}\frac{\partial Y}{\partial \eta} - \frac{\partial C}{\partial \eta}\frac{\partial Y}{\partial \xi}\right]\right\},$$ [5.12]

$$\nabla_{\xi\eta}^2 \Theta = \frac{Pe}{J}\left[\frac{\partial \Theta}{\partial \xi}\frac{\partial \Psi}{\partial \eta} - \frac{\partial \Theta}{\partial \eta}\frac{\partial \Psi}{\partial \xi}\right],$$ [5.13]

$$\nabla_{\xi\eta}^2 C = \frac{Le \cdot Pe}{J}\left[\frac{\partial C}{\partial \xi}\frac{\partial \Psi}{\partial \eta} - \frac{\partial C}{\partial \eta}\frac{\partial \Psi}{\partial \xi}\right],$$ [5.14]

where $\nabla_{\xi\eta}^2 = \frac{\alpha}{J^2}\frac{\partial^2}{\partial \xi^2} - \frac{2\beta}{J^2}\frac{\partial^2}{\partial \xi\partial \eta} + \frac{\gamma}{J^2}\frac{\partial^2}{\partial \eta^2} + \overline{P}\frac{\partial}{\partial \xi} + \overline{Q}\frac{\partial}{\partial \eta},$ [5.15]

is the Laplacian operator in the computational domain.

5.3 Boundary Conditions

The corresponding boundary conditions for the present study are given as follows,

(a) cylinder surface: $u_r = 0,$ $T = T_h,$ $\frac{\partial \overline{C}}{\partial r} = 0.$ [5.16a, b, c]

(b) leakage location: $\qquad u_r = u_R, \qquad T = T_h, \qquad \overline{C} = \overline{C}_h.$ $\qquad$ [5.16d, e, f]

(c) top surface: $\qquad v = 0, \qquad T = T_c, \qquad \overline{C} = \overline{C}_c.$ $\qquad$ [5.16g, h, i]

(d) left boundary: $\qquad v = 0, \qquad \dfrac{\partial T}{\partial x} = 0, \qquad \dfrac{\partial \overline{C}}{\partial x} = 0.$ $\qquad$ [5.16j, k, l]

(e) bottom boundary: $\qquad u = 0, \qquad \dfrac{\partial T}{\partial y} = 0, \qquad \dfrac{\partial \overline{C}}{\partial y} = 0.$ $\qquad$ [5.16m, n, o]

(f) top right boundary: $\qquad u = 0, \qquad \dfrac{\partial T}{\partial x} = 0, \qquad \dfrac{\partial \overline{C}}{\partial x} = 0.$ $\qquad$ [5.16p, q, r]

(g) bottom right boundary: $\quad u = 0, \qquad \dfrac{\partial T}{\partial x} = 0, \qquad \dfrac{\partial \overline{C}}{\partial x} = 0.$ $\qquad$ [5.16s, t, u]

Figure 5.2 shows a schematic of the dimensionless boundary conditions. The boundary conditions in terms of the dimensionless parameters and stream functions are given below.

(a) cylinder surface: $\qquad$ (i) $\Psi = 2\pi - \theta_o$ (upward leakage), $\qquad$ [5.17a]

$\qquad\qquad\qquad\qquad$ (ii) $\Psi = \theta_o - \theta$ (downward leakage), $\qquad$ [5.17b]

$\qquad\qquad\qquad\qquad \Theta = 1, \qquad \dfrac{\partial C}{\partial R} = 0.$ $\qquad$ [5.17c, d]

(b) leakage location: $\qquad$ (i) $\Psi = 2\pi - \theta$ (upward leakage), $\qquad$ [5.17e]

$\qquad\qquad\qquad\qquad$ (ii) $\Psi = \theta_o - \theta$ (downward leakage), $\qquad$ [5.17f]

$\qquad\qquad\qquad\qquad \Theta = 1, \qquad C = 1.$ $\qquad$ [5.17g, h]

(c) top surface: $\qquad \Psi = 0, \qquad \Theta = 0, \qquad C = 0.$ $\qquad$ [5.17i, j, k]

(d) left boundary: $\qquad \dfrac{\partial \Psi}{\partial X} = 0, \qquad \dfrac{\partial \Theta}{\partial X} = 0, \qquad \dfrac{\partial C}{\partial X} = 0.$ $\quad$ [5.17l, m, n]

$$\Psi = 0, \ \Theta = 0, \ C = 0$$

(a)

$$\frac{\partial \Psi}{\partial X} = 0$$

$$\frac{\partial \Theta}{\partial X} = 0$$

$$\frac{\partial C}{\partial X} = 0$$

$$\Psi = 2\pi - \theta$$
$$C = 1$$
$$\Theta = 1$$

$$\Psi = 0, \ \frac{\partial \Theta}{\partial X} = 0, \ \frac{\partial C}{\partial X} = 0$$

$$\Psi = 2\pi - \theta_o, \ \frac{\partial C}{\partial R} = 0, \ \Theta = 1$$

$$\Psi = 2\pi - \theta_o$$
$$\frac{\partial \Theta}{\partial X} = 0$$
$$\frac{\partial C}{\partial X} = 0$$

$$\frac{\partial \Psi}{\partial Y} = 0, \ \frac{\partial \Theta}{\partial Y} = 0, \ \frac{\partial C}{\partial Y} = 0$$

$$\Psi = 0, \ \Theta = 0, \ C = 0$$

(b)

$$\frac{\partial \Psi}{\partial X} = 0$$

$$\frac{\partial \Theta}{\partial X} = 0$$

$$\frac{\partial C}{\partial X} = 0$$

$$\Psi = 0, \ \frac{\partial C}{\partial R} = 0, \ \Theta = 1$$

$$\Psi = \theta_o - \theta$$
$$C = 1$$
$$\Theta = 1$$

$$\Psi = 0, \ \frac{\partial \Theta}{\partial X} = 0, \ \frac{\partial C}{\partial X} = 0$$

$$\Psi = \theta_o - \pi$$
$$\frac{\partial \Theta}{\partial X} = 0$$
$$\frac{\partial C}{\partial X} = 0$$
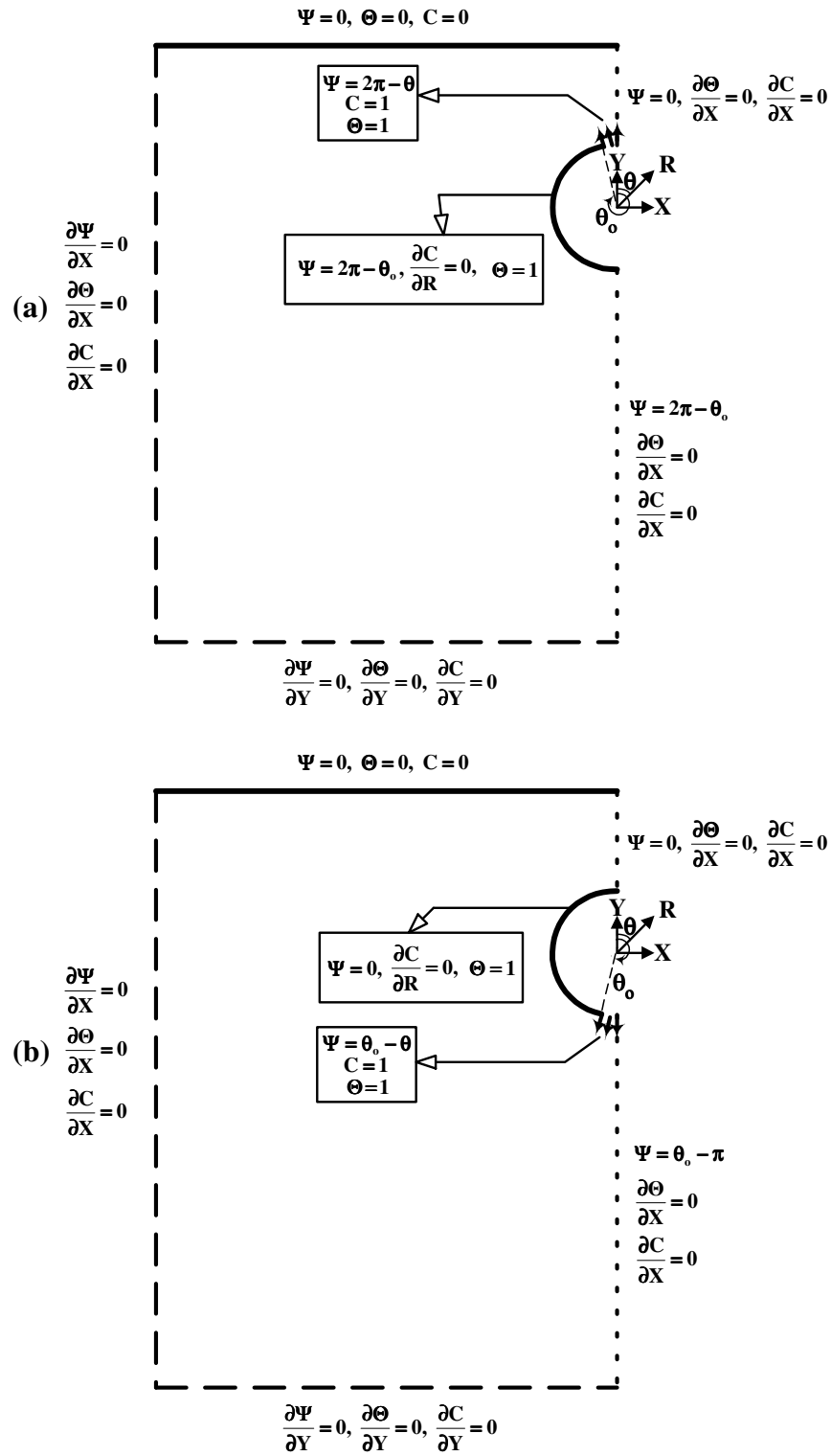
$$\frac{\partial \Psi}{\partial Y} = 0, \ \frac{\partial \Theta}{\partial Y} = 0, \ \frac{\partial C}{\partial Y} = 0$$

Figure 5.2 Dimensionless boundary conditions: (a) upward leakage and (b) downward leakage.

(e) bottom boundary: $\dfrac{\partial \Psi}{\partial Y} = 0,$ $\qquad \dfrac{\partial \Theta}{\partial Y} = 0,$ $\qquad \dfrac{\partial C}{\partial Y} = 0.$ [5.17o, p, q]

(f) top right boundary: $\Psi = 0,$ $\qquad \dfrac{\partial \Theta}{\partial X} = 0,$ $\qquad \dfrac{\partial C}{\partial X} = 0.$ [5.17r, s, t]

(g) bottom right boundary: (i) $\Psi = 2\pi - \theta_o$ (upward leakage), [5.17u]

(ii) $\Psi = \theta_o - \pi$ (downward leakage), [5.17v]

$\dfrac{\partial \Theta}{\partial X} = 0,$ $\qquad \dfrac{\partial C}{\partial X} = 0.$ [5.17w, x]

The boundary conditions are also transformed to the computational domain using the elliptic transformation described in Chapter 2 and they are given as follows,

(a) cylinder surface: (i) $\Psi = 2\pi - \theta_o$ (upward leakage), [5.18a]

(ii) $\Psi = \theta_o - \theta$ (downward leakage), [5.18b]

$\Theta = 1,$ [5.18c]

$$\frac{\partial C}{\partial \xi}\left(\sin\theta \frac{\partial Y}{\partial \eta} - \cos\theta \frac{\partial X}{\partial \eta} \right) + \frac{\partial C}{\partial \eta}\left(\cos\theta \frac{\partial X}{\partial \xi} - \sin\theta \frac{\partial Y}{\partial \xi} \right) = 0.$$

[5.18d]

(b) leakage location: (i) $\Psi = 2\pi - \theta$ (upward leakage), [5.18e]

(ii) $\Psi = \theta_o - \theta$ (downward leakage), [5.18f]

$\Theta = 1,$ $\qquad C = 1.$ [5.18g, h]

(c) top surface: $\Psi = 0,$ $\qquad \Theta = 0,$ $\qquad C = 0.$ [5.18i, j, k]

(d) left boundary: $\dfrac{\partial \Psi}{\partial \xi}\dfrac{\partial Y}{\partial \eta} - \dfrac{\partial \Psi}{\partial \eta}\dfrac{\partial Y}{\partial \xi} = 0,$ [5.18l]

$$\frac{\partial \Theta}{\partial \xi}\frac{\partial Y}{\partial \eta} - \frac{\partial \Theta}{\partial \eta}\frac{\partial Y}{\partial \xi} = 0, \qquad\qquad [5.18\mathrm{m}]$$

$$\frac{\partial C}{\partial \xi}\frac{\partial Y}{\partial \eta} - \frac{\partial C}{\partial \eta}\frac{\partial Y}{\partial \xi} = 0. \qquad\qquad [5.18\mathrm{n}]$$

(e) bottom boundary:
$$\frac{\partial \Psi}{\partial \eta}\frac{\partial X}{\partial \xi} - \frac{\partial \Psi}{\partial \xi}\frac{\partial X}{\partial \eta} = 0, \qquad\qquad [5.18\mathrm{o}]$$

$$\frac{\partial \Theta}{\partial \eta}\frac{\partial X}{\partial \xi} - \frac{\partial \Theta}{\partial \xi}\frac{\partial X}{\partial \eta} = 0, \qquad\qquad [5.18\mathrm{p}]$$

$$\frac{\partial C}{\partial \eta}\frac{\partial X}{\partial \xi} - \frac{\partial C}{\partial \xi}\frac{\partial X}{\partial \eta} = 0. \qquad\qquad [5.18\mathrm{q}]$$

(f) top right boundary:
$$\Psi = 0, \qquad\qquad [5.18\mathrm{r}]$$

$$\frac{\partial \Theta}{\partial \xi}\frac{\partial Y}{\partial \eta} - \frac{\partial \Theta}{\partial \eta}\frac{\partial Y}{\partial \xi} = 0, \qquad\qquad [5.18\mathrm{s}]$$

$$\frac{\partial C}{\partial \xi}\frac{\partial Y}{\partial \eta} - \frac{\partial C}{\partial \eta}\frac{\partial Y}{\partial \xi} = 0. \qquad\qquad [5.18\mathrm{t}]$$

(g) bottom right boundary: (a) $\Psi = 2\pi - \theta_o$ (upward leakage), $\qquad [5.18\mathrm{u}]$

(b) $\Psi = \theta_o - \pi$ (downward leakage), $\qquad [5.18\mathrm{v}]$

$$\frac{\partial \Theta}{\partial \xi}\frac{\partial Y}{\partial \eta} - \frac{\partial \Theta}{\partial \eta}\frac{\partial Y}{\partial \xi} = 0, \qquad\qquad [5.18\mathrm{w}]$$

$$\frac{\partial C}{\partial \xi}\frac{\partial Y}{\partial \eta} - \frac{\partial C}{\partial \eta}\frac{\partial Y}{\partial \xi} = 0. \qquad\qquad [5.18\mathrm{x}]$$

5.4 Numerical Methods

The transformed governing equations (Eqns. [5.12] - [5.15]) along with the boundary conditions (Eqns. [5.18]) are solved using a finite difference method similar

to those previously reported by Coulter and Güceri (1985) and Yost (1984). The control volume approach is used to derive the finite difference equations. For diffusion terms, central-difference approximation is employed. The convective terms in the energy and transport equations are discritized using the upwind scheme. A detailed description of the numerical schemes has been discussed in Chapter 3, thus only the discretized results are summarized here for brevity.

For a uniform grid (i.e., $\Delta\xi = \Delta\eta = 1$), the stream function is given by the algebraic equation

$$\Psi_P = \frac{1}{2(\overline{\alpha}_P + \overline{\gamma}_P)}\left[F_1 + F_2 + F_3 + F_4 + F_5 + F_6\right], \qquad [5.19a]$$

where $\quad F_1 = \overline{\alpha}_P\left(\Psi_E + \Psi_W\right),$ $\qquad\qquad\qquad\qquad\qquad\qquad$ [5.19b]

$$F_2 = \overline{\gamma}_P\left(\Psi_N + \Psi_S\right), \qquad\qquad\qquad\qquad\qquad [5.19c]$$

$$F_3 = -\frac{\overline{\beta}_P}{2}\left(\Psi_{NE} - \Psi_{SE} - \Psi_{NW} + \Psi_{SW}\right), \qquad [5.19d]$$

$$F_4 = \frac{J_P^2}{2}\left[\overline{P}\left(\Psi_E - \Psi_W\right) + \overline{Q}\left(\Psi_N - \Psi_S\right)\right], \qquad [5.19e]$$

$$F_5 = \frac{Ra \cdot J_P}{4Pe}\left[\left(\Theta_E - \Theta_W\right)\left(Y_N - Y_S\right) - \left(\Theta_N - \Theta_S\right)\left(Y_E - Y_W\right)\right], \qquad [5.19f]$$

$$F_6 = \frac{Ra \cdot N \cdot J_P}{4Pe}\left[\left(C_E - C_W\right)\left(Y_N - Y_S\right) - \left(C_N - C_S\right)\left(Y_E - Y_W\right)\right]. \qquad [5.19g]$$

The transformation coefficients $\overline{\alpha}_P, \overline{\beta}_P, \overline{\gamma}_P$ and J_P are given in Eqns. [2.7].

The temperature at the central node is determined to be

$$\Theta_P = \frac{T_{SUM2}}{T_{SUM1}}, \qquad\qquad\qquad\qquad\qquad [5.20a]$$

where $T_{SUM1} = A_{SUMT1} + B_{SUMT1}$, $\qquad$ [5.20b]

$T_{SUM2} = A_{SUMT2} + B_{SUMT2}$, $\qquad$ [5.20c]

$A_{SUMT1} = Pe(A_E + A_W + A_N + A_S)$, $\qquad$ [5.20d]

$B_{SUMT1} = B_{1AE} + B_{1AW} + B_{3AN} + B_{3AS} + B_{4BP} + B_{5BP}$, $\qquad$ [5.20e]

$A_{SUMT2} = Pe(A_E\Theta_E + A_W\Theta_W + A_N\Theta_N + A_S\Theta_S)$, $\qquad$ [5.20f]

$B_{SUMT2} = B_{T1} + B_{T2} + B_{T3} + B_{T4} + B_{T5}$, $\qquad$ [5.20g]

$B_{T1} = B_{1AE}\Theta_E + B_{1AW}\Theta_W - B_{1B}(\Theta_E - \Theta_W)$, $\qquad$ [5.20h]

$$B_{T2} = B_{2AE}(\Theta_{NE} + \Theta_N - \Theta_S - \Theta_{SE}) - B_{2AW}(\Theta_{NW} + \Theta_N - \Theta_S - \Theta_{SW})$$
$$- B_{2B}(\Theta_N - \Theta_S),$$ $\qquad$ [5.20i]

$B_{T3} = B_{3AN}\Theta_N + B_{3AS}\Theta_S - B_{3B}(\Theta_N - \Theta_S)$, $\qquad$ [5.20j]

$B_{T4} = B_{4AE}\Theta_E - B_{4AW}\Theta_W - B_{4B}(\Theta_N + \Theta_W + \Theta_S + \Theta_E)$, $\qquad$ [5.20k]

$B_{T5} = B_{5AN}\Theta_N - B_{5AS}\Theta_S - B_{5B}(\Theta_N + \Theta_W + \Theta_S + \Theta_E)$. $\qquad$ [5.20l]

Other coefficients such as A's (e.g., A_E, A_W, A_N and A_S) and B's (e.g., B_{1AE}, B_{1AW}, B_{1B} etc.) are given in Chapter 3.

The concentration at the central node is given by

$$C_P = \frac{C_{SUM2}}{C_{SUM1}},$$ $\qquad$ [5.21a]

where $C_{SUM1} = A_{SUMC1} + B_{SUMC1}$, $\qquad$ [5.21b]

$C_{SUM2} = A_{SUMC2} + B_{SUMC2}$, $\qquad$ [5.21c]

$A_{SUMC1} = Le \cdot Pe(A_E + A_W + A_N + A_S)$, $\qquad$ [5.21d]

$B_{SUMC1} = B_{1AE} + B_{1AW} + B_{3AN} + B_{3AS} + B_{4BP} + B_{5BP}$, $\qquad$ [5.21e]

$$A_{SUMC2} = Le \cdot Pe\,(A_E C_E + A_W C_W + A_N C_N + A_S C_S), \qquad\qquad [5.21f]$$

$$B_{SUMC2} = B_{C1} + B_{C2} + B_{C3} + B_{C4} + B_{C5}, \qquad\qquad [5.21g]$$

$$B_{C1} = B_{1AE} C_E + B_{1AW} C_W - B_{1B}(C_E - C_W), \qquad\qquad [5.21h]$$

$$\begin{aligned} B_{C2} &= B_{2AE}(C_{NE} + C_N - C_S - C_{SE}) - B_{2AW}(C_{NW} + C_N - C_S - C_{SW}) \\ &\quad - B_{2B}(C_N - C_S), \end{aligned} \qquad\qquad [5.21i]$$

$$B_{C3} = B_{3AN} C_N + B_{3AS} C_S - B_{3B}(C_N - C_S), \qquad\qquad [5.21j]$$

$$B_{C4} = B_{4AE} C_E - B_{4AW} C_W - B_{4B}(C_N + C_W + C_S + C_E), \qquad\qquad [5.21k]$$

$$B_{C5} = B_{5AN} C_N - B_{5AS} C_S - B_{5B}(C_N + C_W + C_S + C_E). \qquad\qquad [5.21l]$$

Coefficients A's and B's are the same as those shown in Eqns. [5.20]. Also, note the similarity between the discretized formulations of temperature and concentration.

A Fortran90 code has been programmed to perform the numerical calculations using Gauss-Seidel iterative scheme. In addition, a relaxation parameter has been employed to accelerate or improve convergence. Either under-relaxation or over-relaxation could be used. The selection of an adequate relaxation parameter depends on experience and some insights into the problem. For the present study, an under-relaxation parameter generally provides better results. The iteration process is terminated once the maximum error between two consecutive iterations is less than or equal to 10^{-4}.

The heat and mass transfer results are expressed in terms of the overall Nusselt and Sherwood numbers, respectively. They are defined below in the physical domain,

$$Nu = -\int_{-w/r_i}^{0} \left.\frac{\partial \Theta}{\partial Y}\right|_{Y=d/r_i} dX,$$ [5.22]

$$Sh = -\int_{-w/r_i}^{0} \left.\frac{\partial C}{\partial Y}\right|_{Y=d/r_i} dX.$$ [5.23]

The Nusselt number represents the total heat flux through the top surface, and the Sherwood number is the net mass flux through the same surface. To further assess the accuracy of the numerical results obtained, an overall energy and mass balance has been performed after each calculation. For the present study, attempts have been made to reduce the relative errors to less than three percent. The definitions of the relative errors are given below.

$$\% \text{ Error E} = \left|\frac{Nu_{in} - Nu_{out}}{Nu_{in}}\right| \times 100\%,$$ [5.24]

$$\% \text{ Error m} = \left|\frac{Sh_{in} - Sh_{out}}{Sh_{in}}\right| \times 100\%,$$ [5.25]

where

$$Nu_{in} = \int \left(-\frac{\partial \Theta}{\partial R} R\right)_{\text{cylinder surface}} d\theta + \int \left(Pe \cdot U_R \cdot \Theta \cdot R\right)_{\text{leakage}} d\theta + \int \left(-\frac{\partial \Theta}{\partial R} R\right)_{\text{leakage}} d\theta$$

$$+ \int \left(Pe \cdot U \cdot \Theta\right)_{\text{left boundary}} dY + \int \left(Pe \cdot V \cdot \Theta\right)_{\text{bottom boundary}} dX,$$

[5.26]

$$Nu_{out} = \int \left(-\frac{\partial \Theta}{\partial Y}\right)_{\text{top surface}} dX,$$ [5.27]

$$Sh_{in} = \int \left(Le \cdot Pe \cdot U_R \cdot C \cdot R\right)_{\text{leakage}} d\theta + \int \left(-\frac{\partial C}{\partial R} R\right)_{\text{leakage}} d\theta$$

$$+ \int \left(Le \cdot Pe \cdot U \cdot C\right)_{\text{left boundary}} dY + \int \left(Le \cdot Pe \cdot V \cdot C\right)_{\text{bottom boundary}} dX,$$

[5.28]

$$\text{Sh}_{\text{out}} = \int \left(-\frac{\partial C}{\partial Y} \right)_{\text{top surface}} dX. \tag{5.29}$$

In the above expressions, it has been assumed that the velocities U and V are in the positive direction. When performing the energy and mass balances, the direction of the velocities were obtained prior to the determination if the energy or mass transfers were going into or coming out of the control volume.

A grid refinement test has been performed to determine the proper grid size for the production runs. For the present study, a mesh of 121×121 is sufficient to produce acceptable results within a reasonable time frame. It is noted that a further grid refinement does not produce any significant improvement in the numerical results.

5.5 Results and Discussion

Numerical calculations for combined heat and mass transfer by mixed convection induced from a buried pipe with leakage have been performed in the present study. A parametric study has been performed over a wide range of governing parameters and they are summarized in Table 5.1. The variation of the flow structures, temperature and concentration profiles due to the effects of the buoyancy ratio N, Lewis number Le, Peclet number Pe, and leakage locations are presented and discussed in the following sections.

5.5.1 Effects of Buoyancy Ratio N

The effects of buoyancy ratio N on the flow, temperature and concentration

Table 5.1 Range of the parameters considered in the study of mixed convection from a buried pipe with leakage.

Parameters	Range
Rayleigh Number (Ra)	10, 20, 50, 80, 100, 200, 500
Buoyancy Ratio (N)	-5, 1, 5
Lewis Number (Le)	0.1, 1, 10
Peclet Number (Pe)	0.1, 1, 10
Leakage Locations	Top, Bottom

fields are first examined. As stated earlier, N is the ratio of buoyancy due to concentration difference and temperature difference. Therefore, N is zero for pure thermal driven flows, infinite for mass driven flows, negative for opposing flows and positive for aiding flows. When N is unity, the solute and thermal buoyancy forces have equal strength. For comparison and discussion that follow, the results of pure thermal convection with no leak from the pipe (Figure 3.12 - 3.13) are used as the reference.

When the leakage location is on top of the buried pipe, the plots of streamlines, temperature and concentration profiles are given in Figures 5.3, 5.4 and 5.5, respectively. Since the concentration profiles are mostly confined to a region near the leakage location, only the results at the vicinity of the buried pipe are shown (i.e., $-10 \le X \le 0, -10 \le Y \le 5$). For N = 1, the resulting flow and temperature fields are quite similar to those of the thermal buoyancy driven flows presented in Figures 3.12 and 3.13. As the Rayleigh number increases, the convection becomes more pronounced. With an increase in the buoyancy ratio (i.e., aiding flows), the strength of the convective cell increases considerably due to the additional contribution from

Figure 5.3 Effects of buoyancy ratio (N) on the flow fields with upward leakage, Le = 0.1, Pe = 1; (a) Ra = 10, (b) Ra = 50, (c) Ra = 100 ($\Delta\Psi$ = 1).

Figure 5.4 Effects of buoyancy ratio (N) on the temperature fields with upward leakage, Le = 0.1, Pe = 1; (a) Ra = 10, (b) Ra = 50, (c) Ra = 100 ($\Delta\Theta$ = 0.1).

(a) Ra = 10   **(b) Ra = 50**   **(c) Ra = 100**

N = 5

N = 1

N = -5

Figure 5.5 Effects of buoyancy ratio (N) on the concentration fields with upward leakage, Le = 0.1, Pe = 1; (a) Ra = 10, (b) Ra = 50, (c) Ra = 100 (ΔC = 0.1).

the solute buoyancy. A steeper temperature gradient at the lower portion of the buried pipe is observed, and the concentration plumes are lifted upward. For opposing flows at N = -5, the solute buoyancy force is in the opposite direction of the thermal buoyancy, which leads to a more complicated flow field with multicellular convection. As seen in Figure 5.3(c), three recirculating cells are observed at a high Rayleigh number (Ra = 100). The convective cell closest to the buried pipe and the outermost cell rotate in the clockwise direction whereas the one in between those two cells circulates in the counterclockwise direction. From the isotherms shown in Figure 5.4, reversed thermal plumes are observed to appear near the leak. Also from the isoplets shown in Figure 5.5, areas influenced by both temperature and concentration fields are shifted downward. In general, the buoyancy ratio has a more pronounced influence on the temperature field than the concentration field.

When the leakage occurs at the bottom of the buried pipe, the plots of flow, temperature and concentration fields are presented in Figures 5.6, 5.7 and 5.8, respectively. Again it is observed that convection becomes stronger with an increase in the Rayleigh number and buoyancy ratio. As the buoyancy ratio increases (aiding flows), both the temperature and concentration profiles are lifted upward. Also, note the similarity between the flow and temperature fields despite the change of the leakage location from top to bottom of the pipe. On the other hand, for the opposing flows (N < 0), the concentration profile is shifted downward. Since the leakage location is now at the bottom of the buried pipe, another thermal plume is issued out of the buried pipe near the leakage. For N < 0, the primary flow is in reversed (clockwise) direction and it first descends towards the buried pipe and then discharges
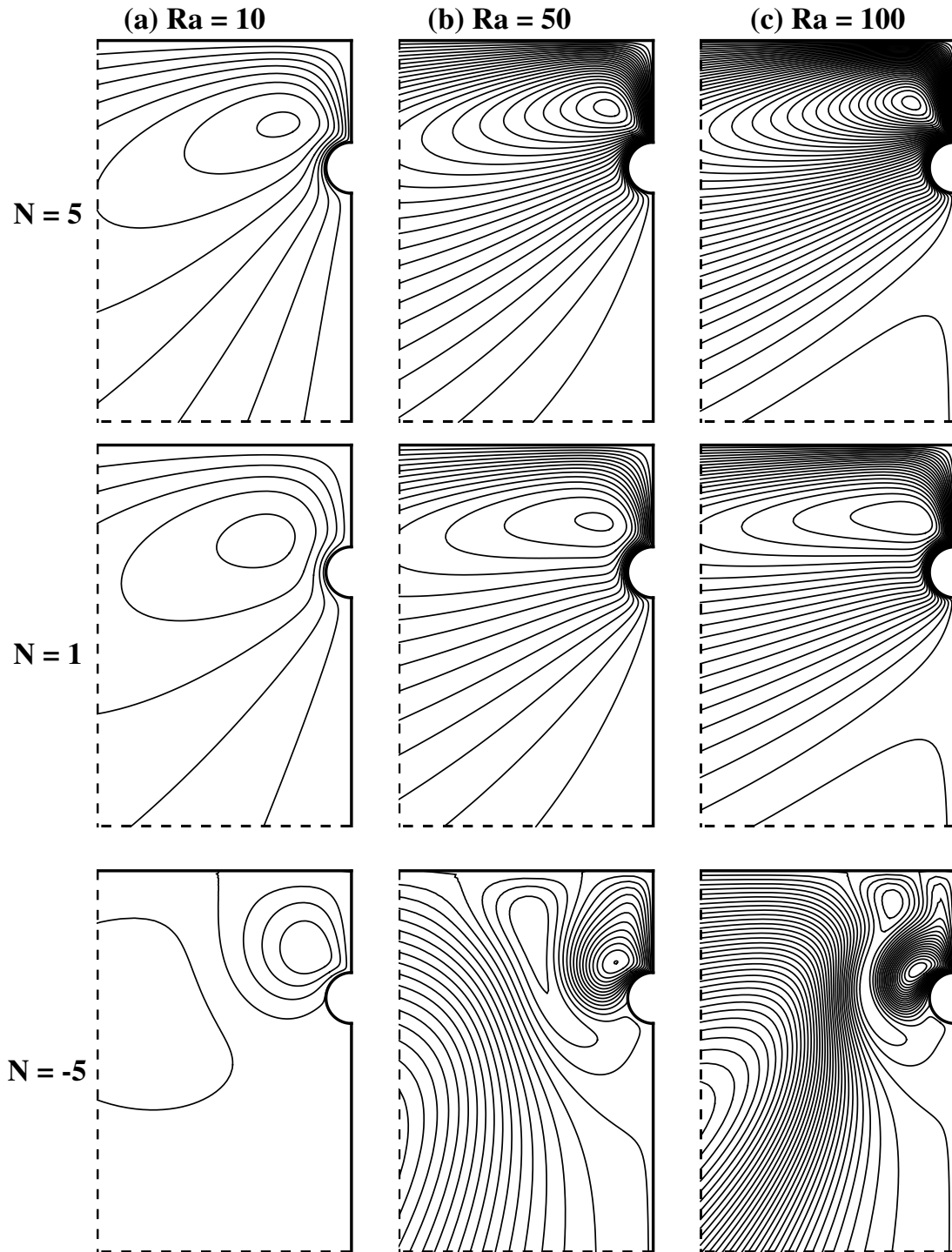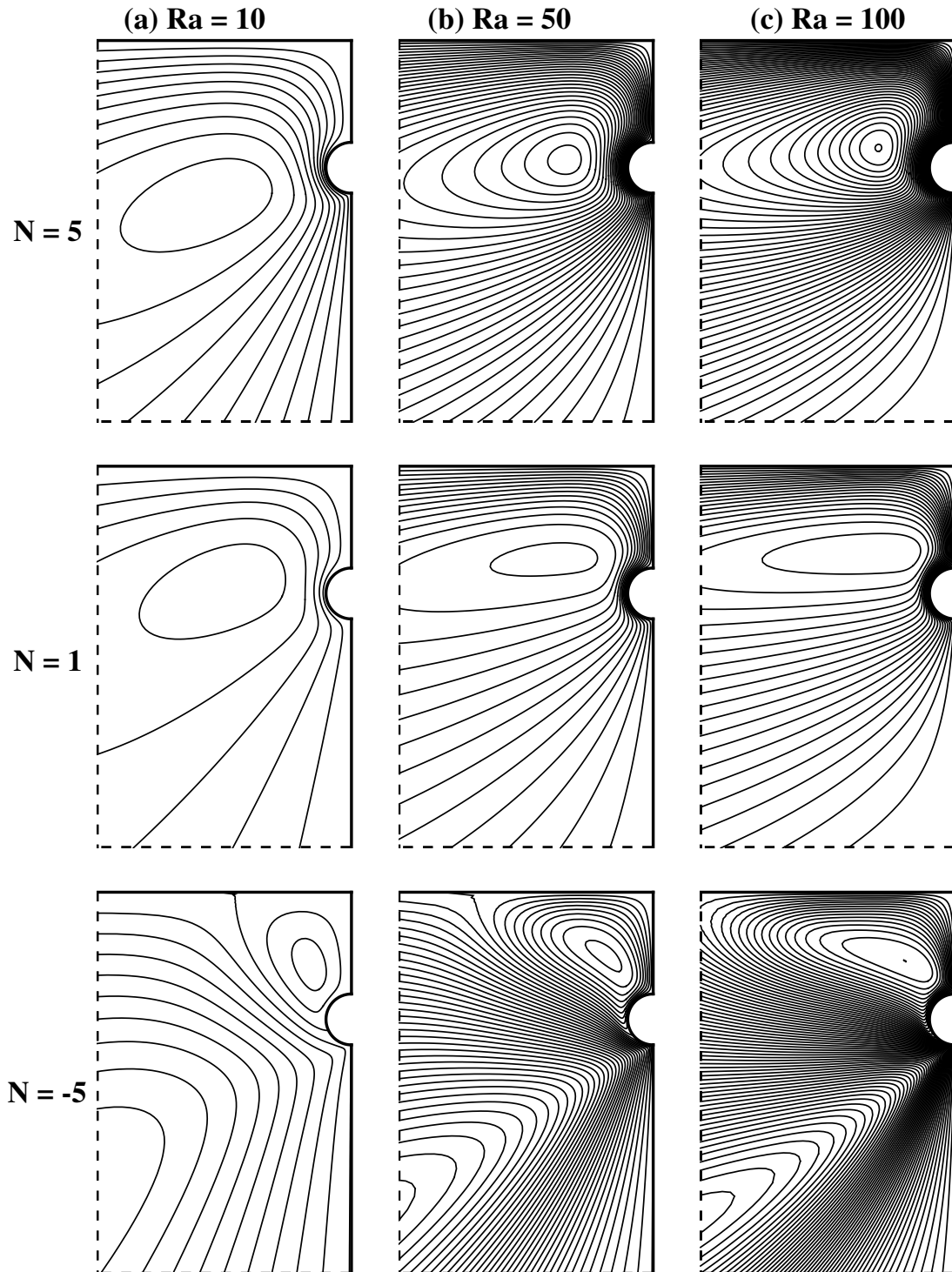
Figure 5.6 Effects of buoyancy ratio (N) on the flow fields with downward leakage, Le = 0.1, Pe = 1; (a) Ra = 10, (b) Ra = 50, (c) Ra = 100 ($\Delta\Psi$ = 1).
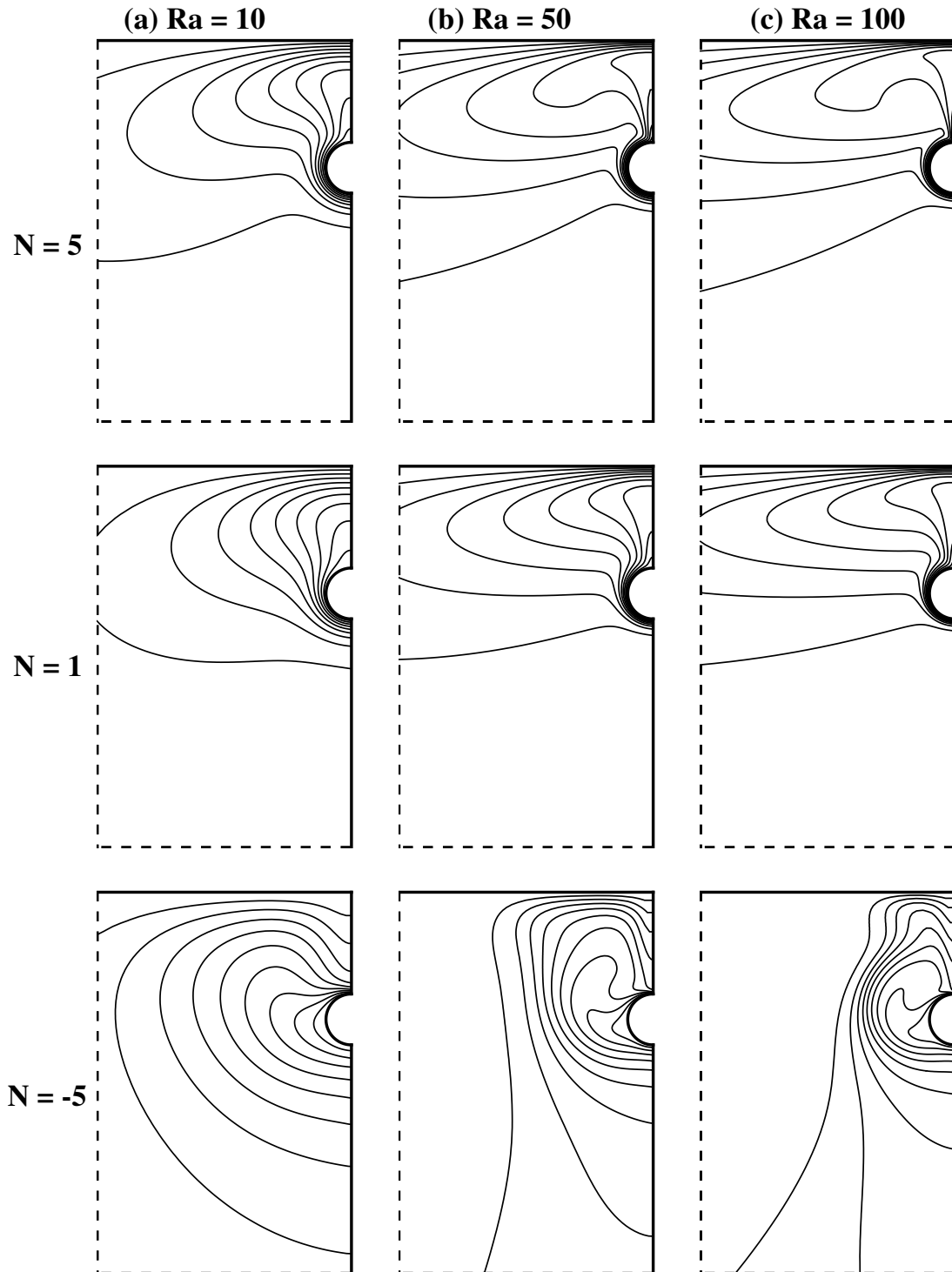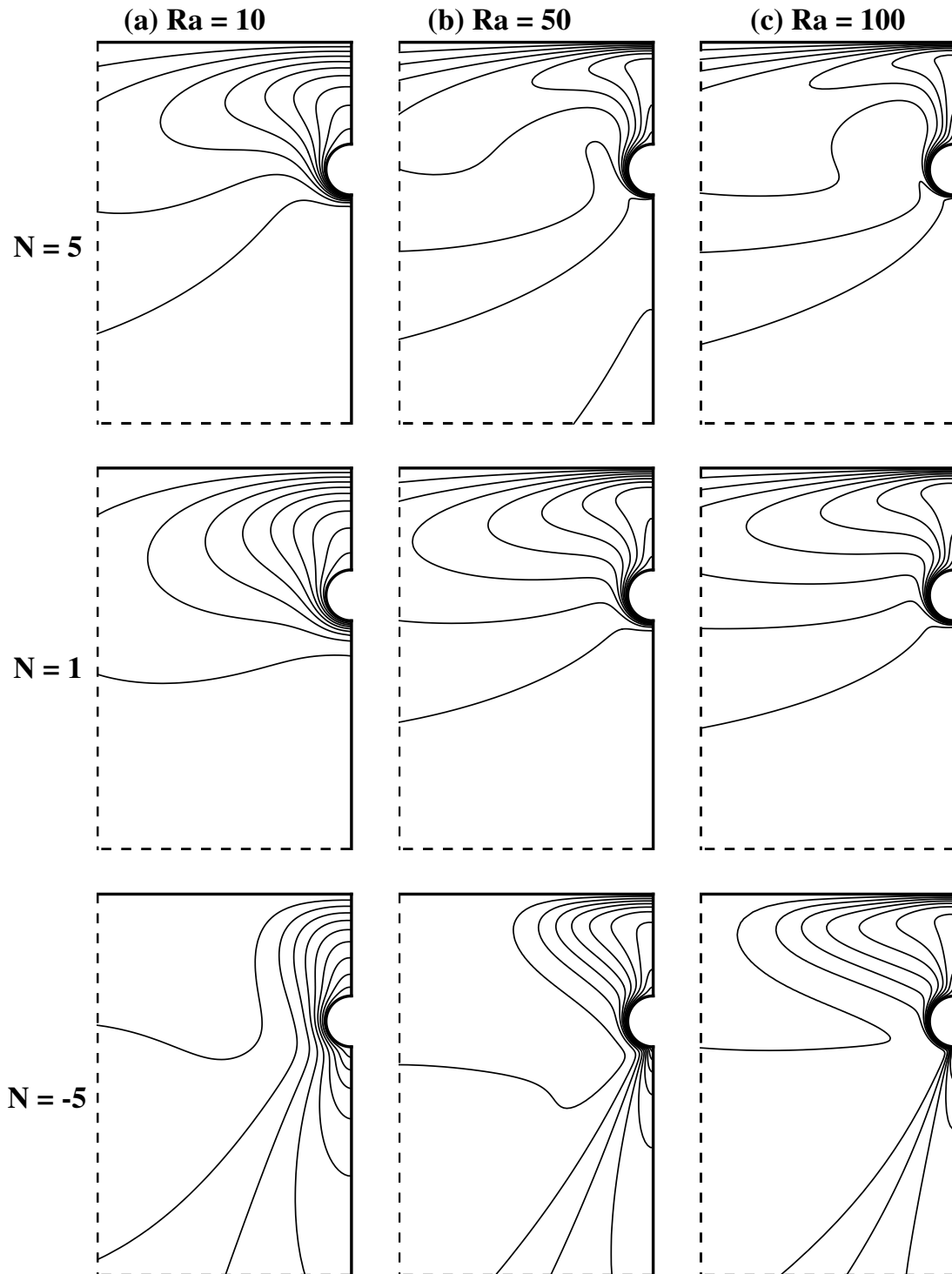
Figure 5.7 Effects of buoyancy ratio (N) on the temperature fields with downward leakage, Le = 0.1, Pe = 1; (a) Ra = 10, (b) Ra = 50, (c) Ra = 100 ($\Delta\Theta$ = 0.1).

139

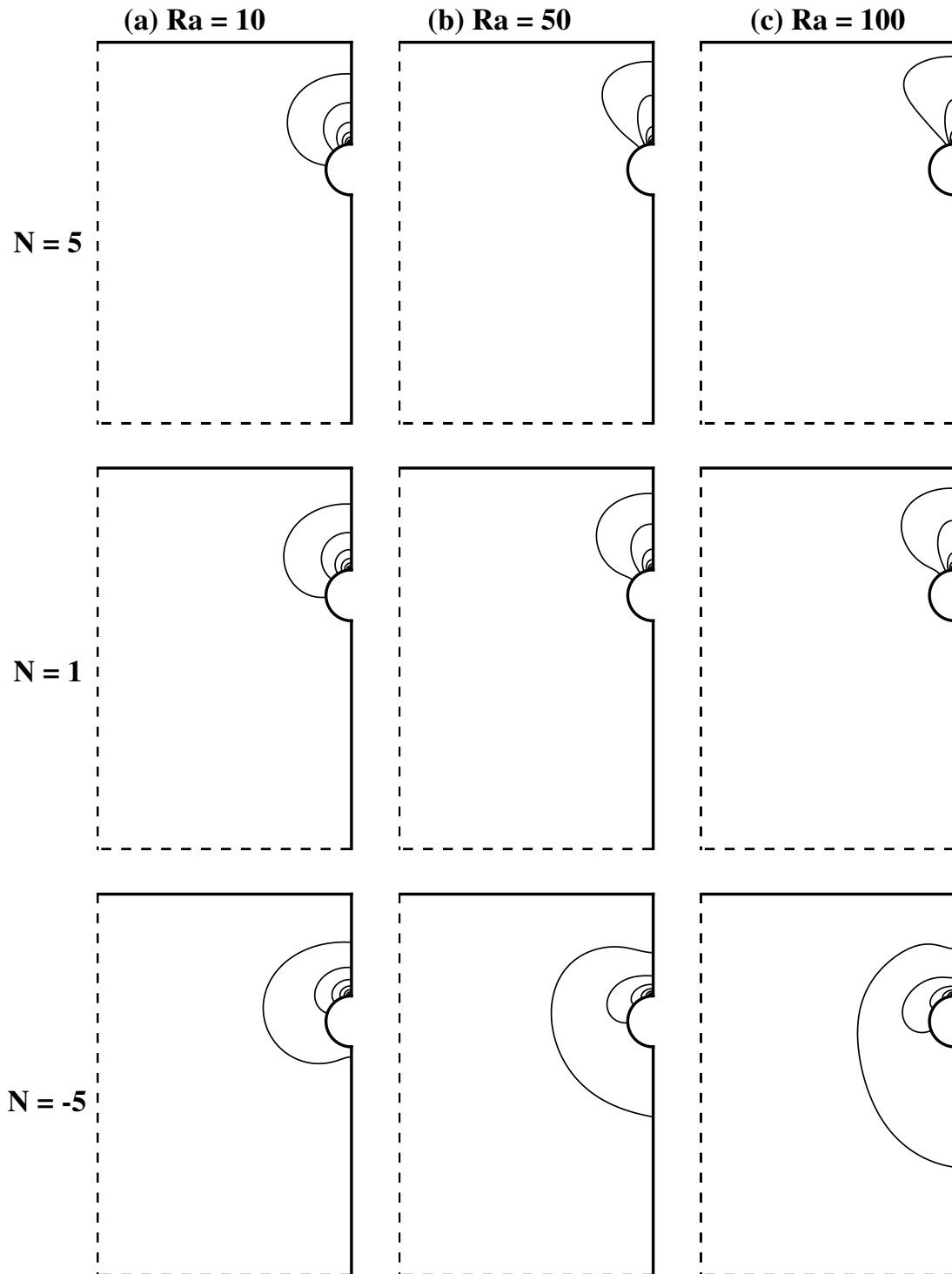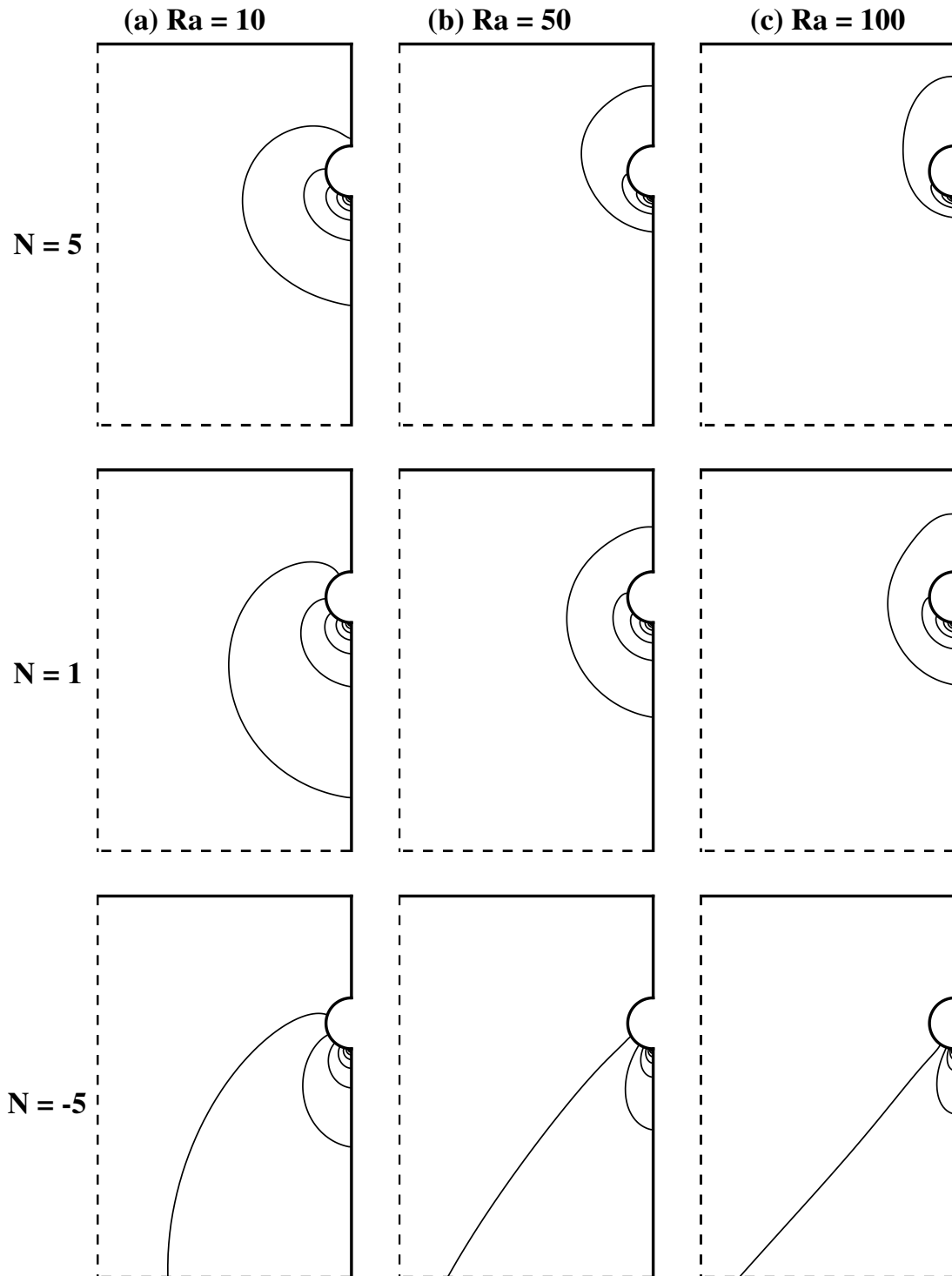**Figure 5.8** Effects of buoyancy ratio (N) on the concentration fields with downward leakage, Le = 0.1, Pe = 1; (a) Ra = 10, (b) Ra = 50, (c) Ra = 100 (ΔC = 0.1).

to the lower boundary. There is a secondary cell rotating in the counterclockwise direction near the top of the buried pipe. The strength of the secondary cell increases with the Rayleigh number.

5.5.2 Effects of Lewis Number Le

In this section, the effects of Lewis number on the flow, temperature and concentration fields are examined. Lewis number is a physical property, a measure of the ratio of thermal diffusivity to mass diffusivity. For upward leakage, the flow, temperature and concentration fields are shown in Figures 5.9, 5.10 and 5.11, respectively, for various Lewis numbers and buoyancy ratios.

When N = 1, it is observed that the change in Lewis number has little effect on both flow and temperature fields, but it has a more pronounced effect on the concentration fields. The concentration profiles are shifted upwards and confined to a narrow region near the centerline as the Lewis number increases. For aiding flows (N = 5), an increase in the Lewis number leads to a slightly weakened flow field. As the Lewis number increases, the temperature profiles are shifted downwards while the concentration profiles are shifted upwards. For opposing flows (N = -5), the trend is just reversed. An increase in the Lewis number leads to a temperature profile lifted upward and a concentration profile shifted downward.

For downward leakage (Figures 5.12 - 5.14), a similar trend is observed in the variation of the flow, temperature and concentration fields with the Lewis number despite the change in the leakage location. A particular phenomenon that is worth mentioning is that for opposing flows, the strength of the secondary cell on top of the

(a) N = -5 **(b) N = 1** **(c) N = 5**

Le = 0.1

Le = 1

Le = 10
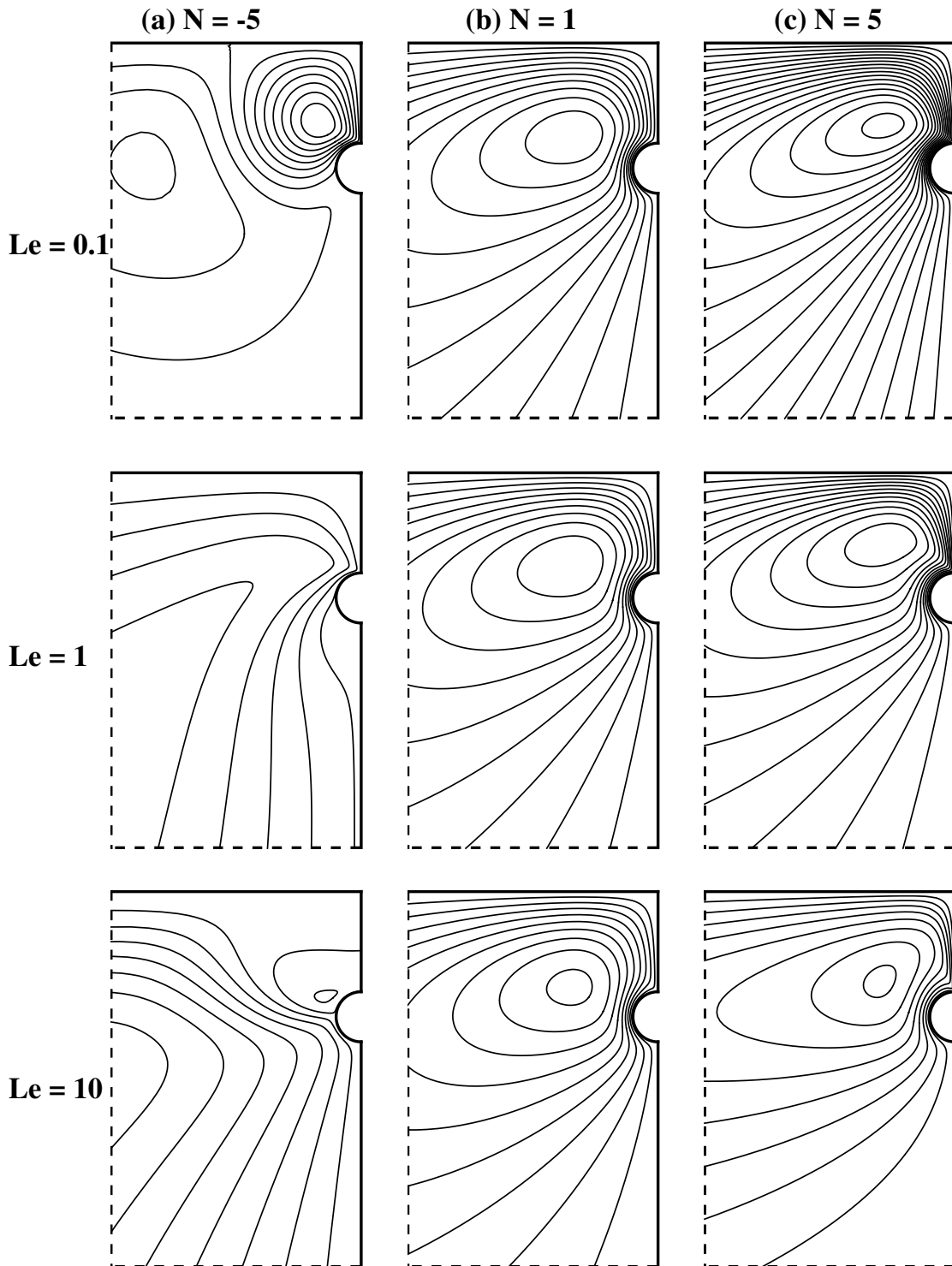
Figure 5.9 Effects of Lewis number (Le) on the flow fields with upward leakage, Ra = 10, Pe = 1; (a) N = -5, (b) N = 1, (c) N = 5 ($\Delta\Psi = 0.5$).
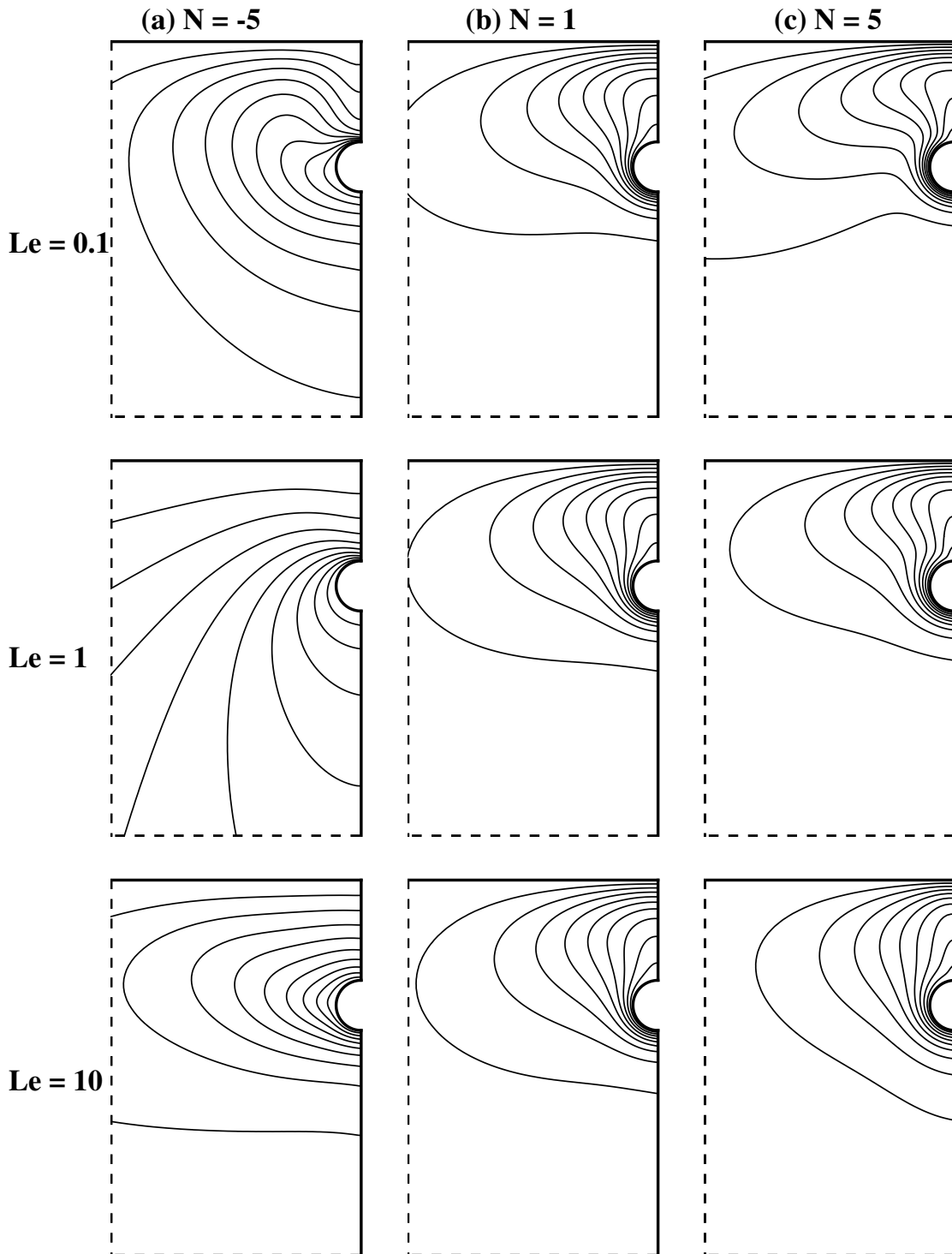
Figure 5.10 Effects of Lewis number (Le) on the temperature fields with upward leakage, Ra = 10, Pe = 1; (a) N = -5, (b) N = 1, (c) N = 5 ($\Delta\Theta = 0.1$).
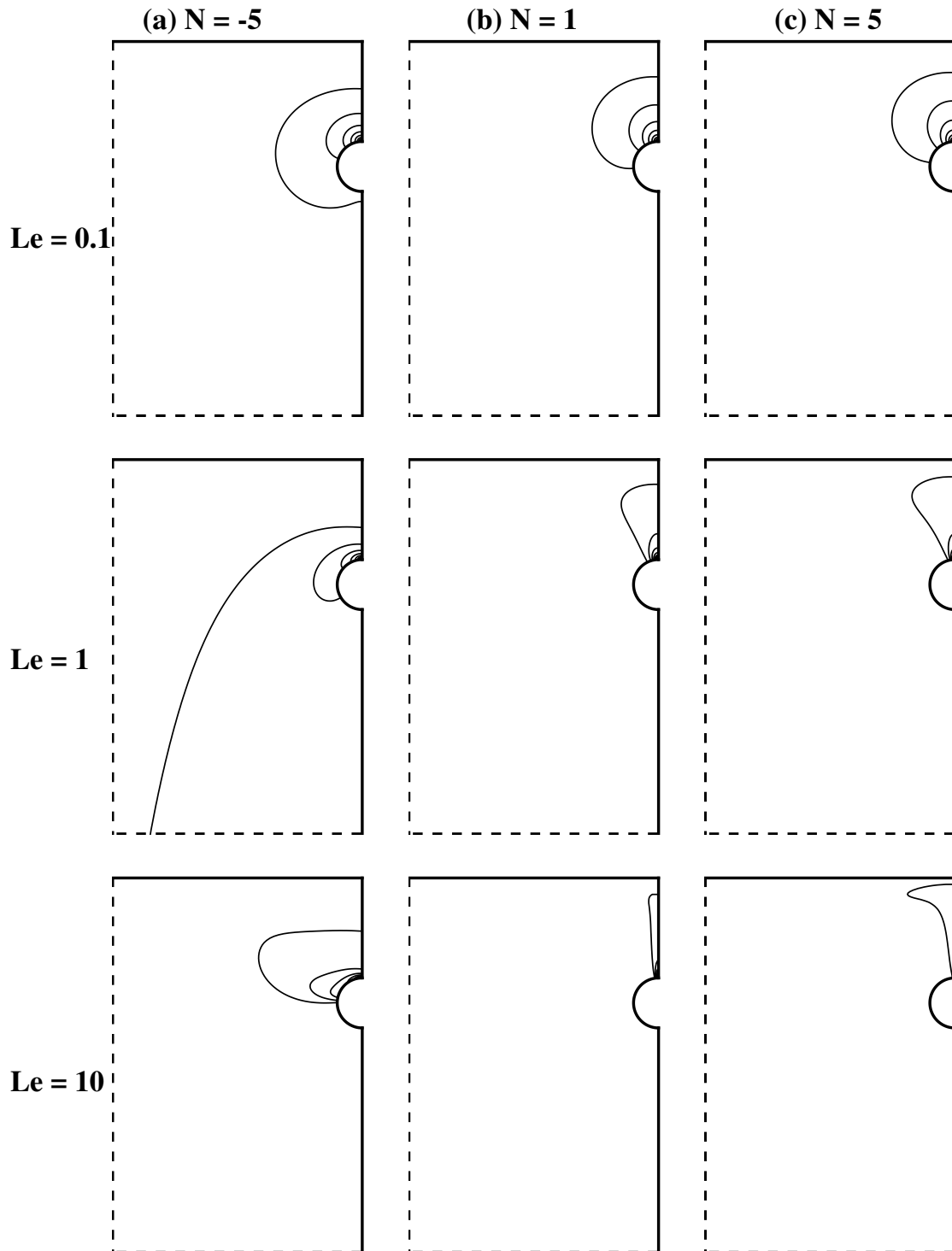
Figure 5.11 Effects of Lewis number (Le) on the concentration fields with upward leakage, Ra = 10, Pe = 1; (a) N = -5, (b) N = 1, (c) N = 5 (ΔC = 0.1).
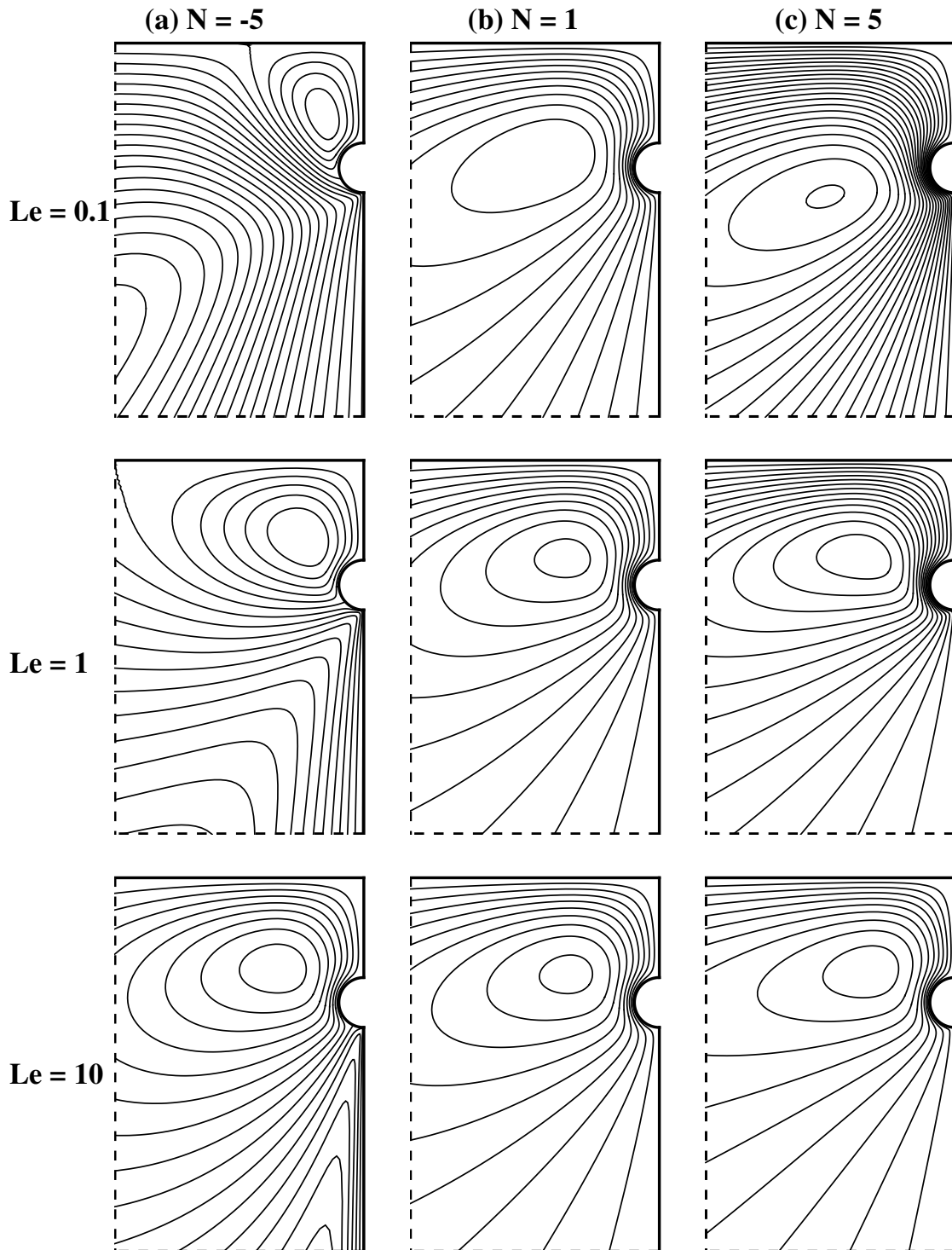
Figure 5.12 Effects of Lewis number (Le) on the flow fields with downward leakage, Ra = 10, Pe = 1; (a) N = -5, (b) N = 1, (c) N = 5 (ΔΨ = 0.5).

(a) N = -5   **(b) N = 1**   **(c) N = 5**

Le = 0.1

Le = 1

Le = 10
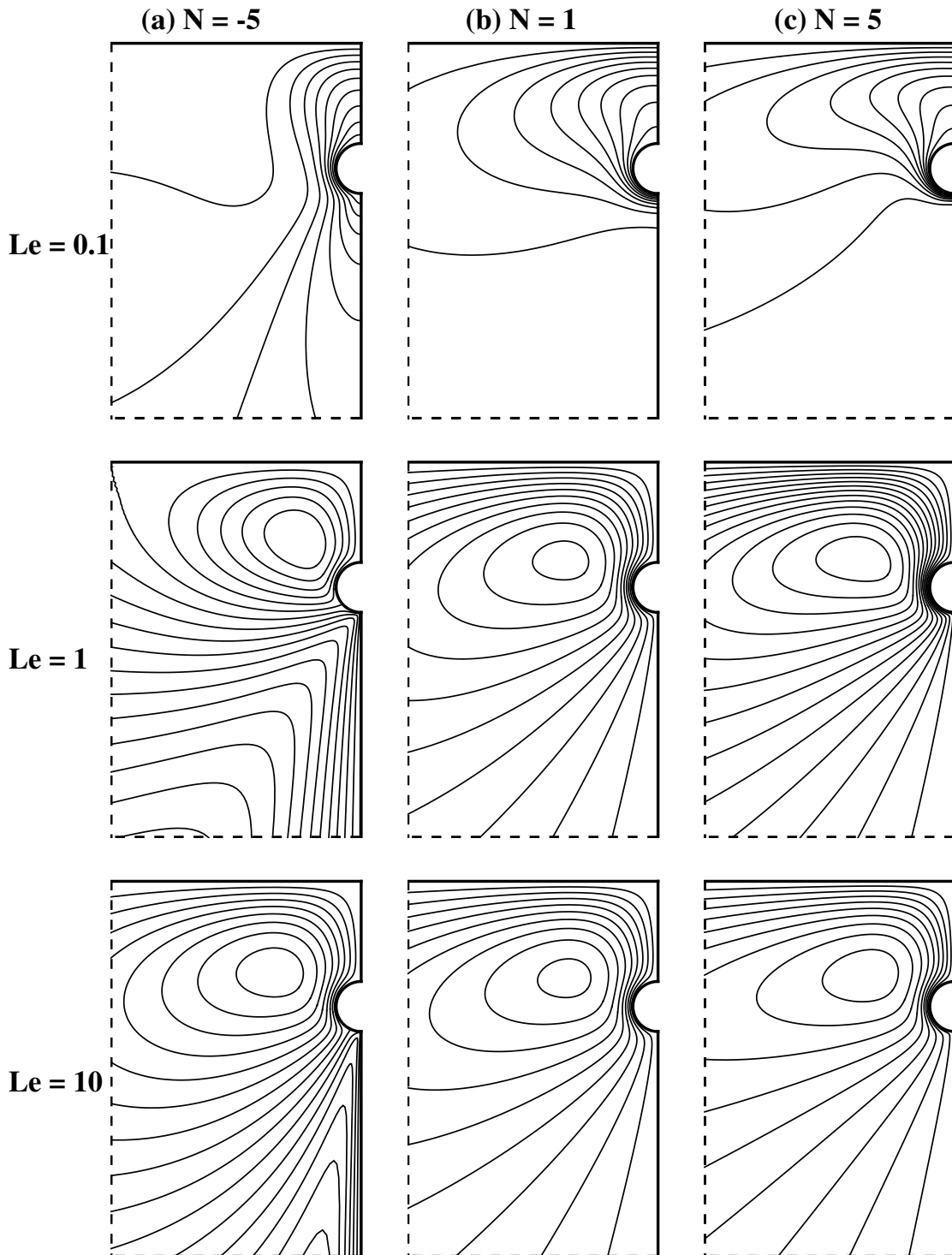
Figure 5.13 Effects of Lewis number (Le) on the temperature fields with downward leakage, Ra = 10, Pe = 1; (a) N = -5, (b) N = 1, (c) N = 5 ($\Delta\Theta = 0.1$).
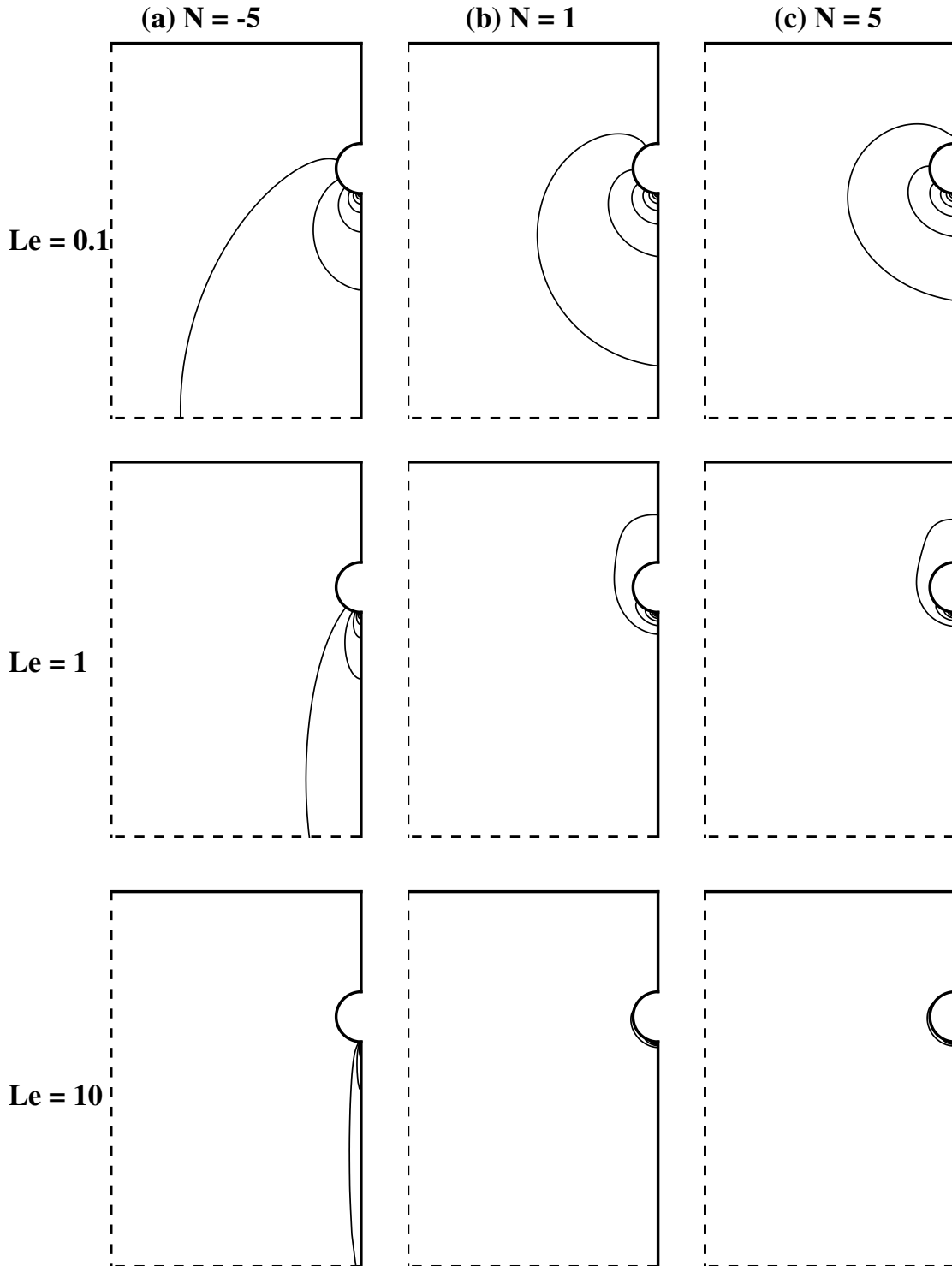
Figure 5.14 Effects of Lewis number (Le) on the concentration fields with downward leakage, Ra = 10, Pe = 1; (a) N = -5, (b) N = 1, (c) N = 5 (ΔC = 0.1).

buried pipe increases with the Lewis number, indicating that the solute buoyancy is suppressed by the thermal buoyancy. In general, for a fixed buoyancy ratio, Lewis number has a more dominant effect on the flow and concentration fields than the temperature field. It should be noted that with the combination of high Rayleigh numbers and Lewis numbers, the flow field for opposing flows becomes extremely unstable, and no converged solution is obtained.

5.5.3 Effects of Peclet Number Pe

To examine the effects of Peclet number, the plots of flow, temperature and concentration fields are presented in Figures 5.15 - 5.17 for upward leakage and Figures 5.18 - 5.20 for downward leakage. For a fixed buoyancy ratio, the strength of convective flow becomes more pronounced with an increase in the Peclet number (Figure 5.15 and 5.18), particularly for the opposing flows. From the isotherms in Figures 5.16 and 5.19, it is observed that the temperature profiles are not greatly affected by the Peclet number for aiding flows. Since the crack is relatively small, the flow inertia of the discharged fluid has little effect on the buoyancy. However, for opposing flows with an upward leakage, the flow inertia of the discharged fluid can effectively suppress the thermal plume which normally arises from the pipe (Figure 5.16a). As a result, the temperature profiles are shifted downward with an increase in the flow inertia. For opposing flows with a downward leakage, the thermal plume although survives but its area of influence is confined to a smaller region as seen in Figure 5.19a.

The effects of Peclet number are most obvious from the concentration fields
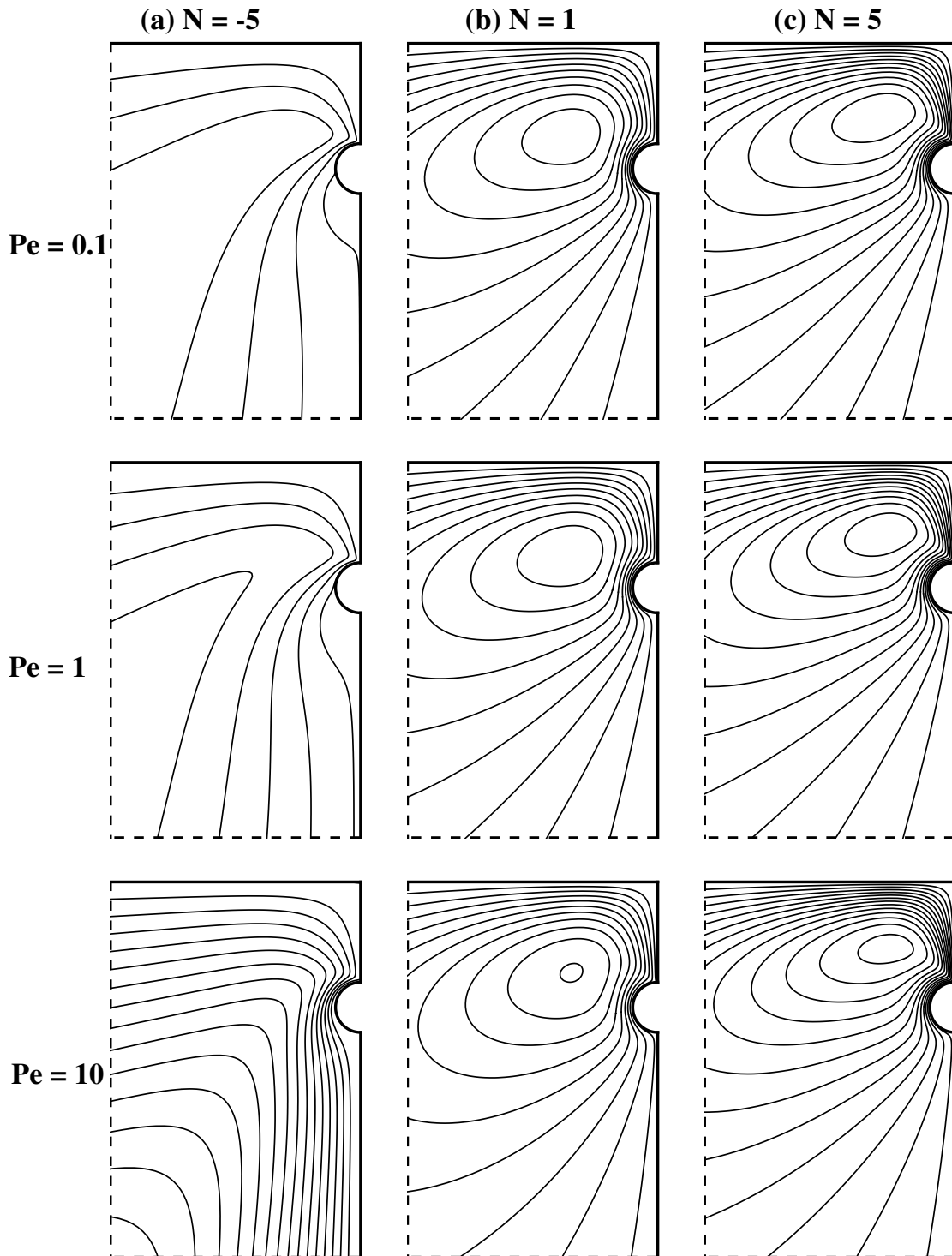
Figure 5.15 Effects of Peclet number (Pe) on the flow fields with upward leakage, Le = 1, Ra = 10; (a) N = -5, (b) N = 1, (c) N = 5 ($\Delta\Psi$ = 5, 0.5 and 0.05 for Pe = 0.1, 1 and 10, respectively).
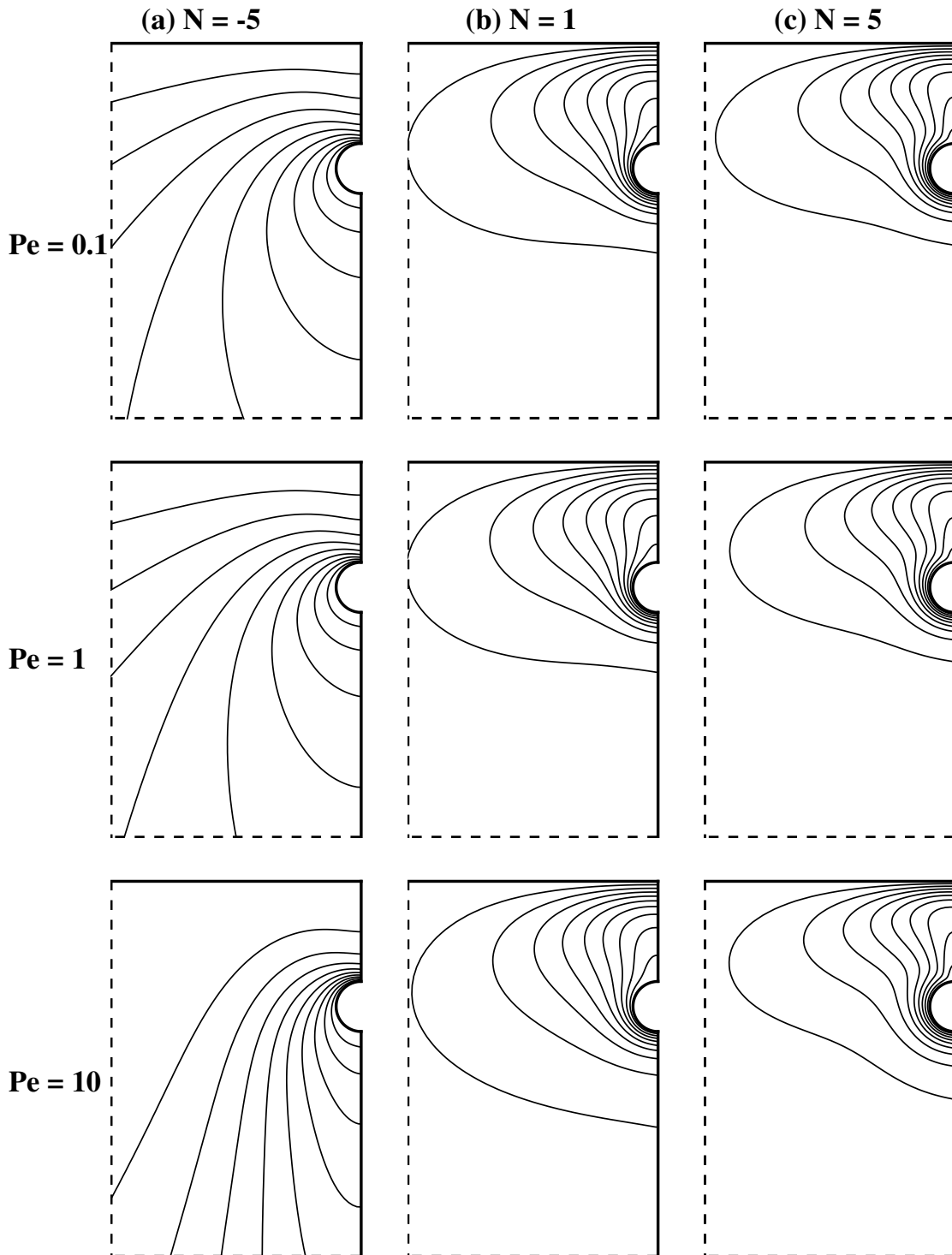
Figure 5.16 Effects of Peclet number (Pe) on the temperature fields with upward leakage, Le = 1, Ra = 10; (a) N = -5, (b) N = 1, (c) N = 5 ($\Delta\Theta$ = 0.1).
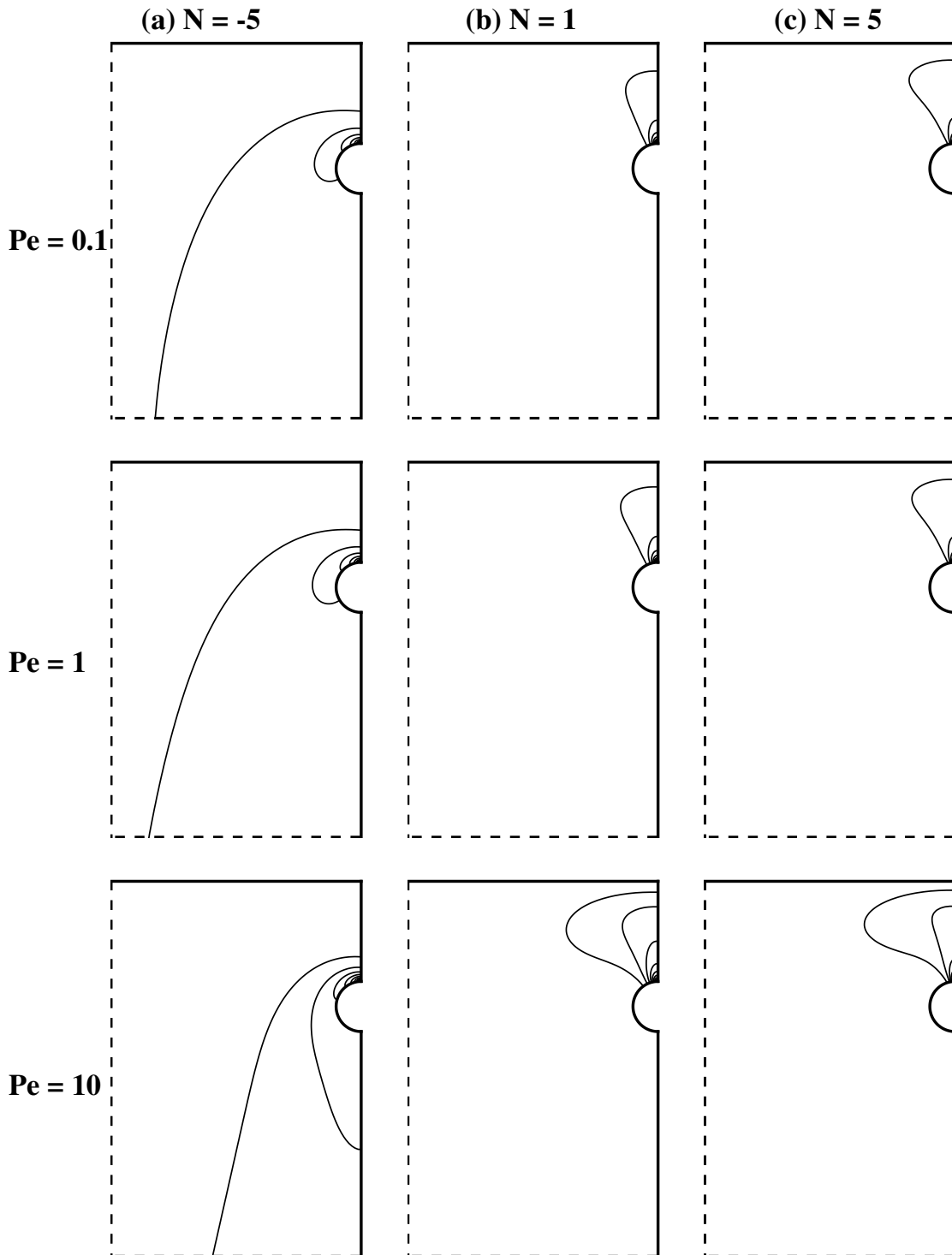
Figure 5.17 Effects of Peclet number (Pe) on the concentration fields with upward leakage, Le = 1, Ra = 10; (a) N = -5, (b) N = 1, (c) N = 5 (ΔC = 0.1).
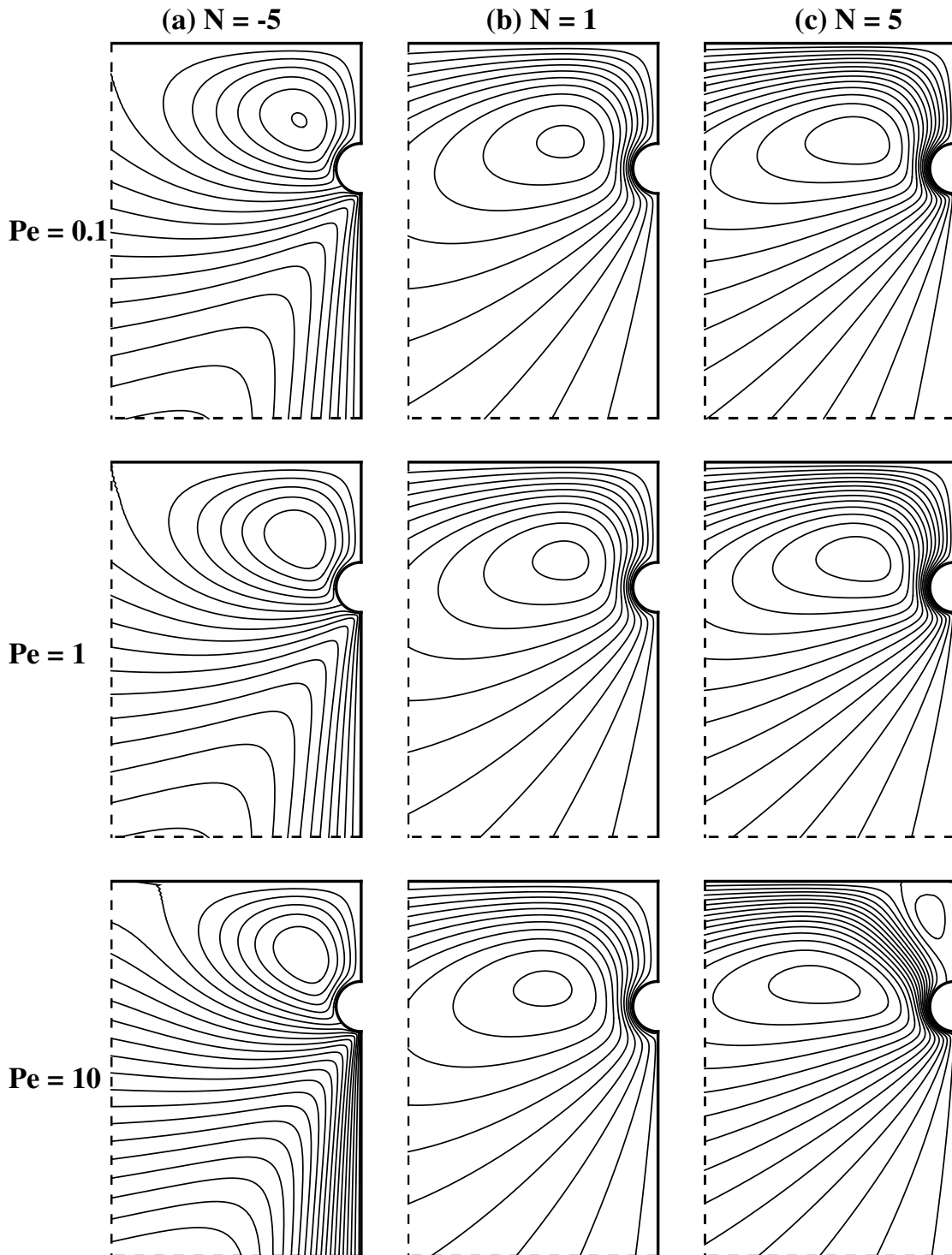
Figure 5.18 Effects of Peclet number (Pe) on the flow fields with downward leakage, Le = 1, Ra = 10; (a) N = -5, (b) N = 1, (c) N = 5 ($\Delta\Psi$ = 5, 0.5 and 0.05 for Pe = 0.1, 1 and 10, respectively).
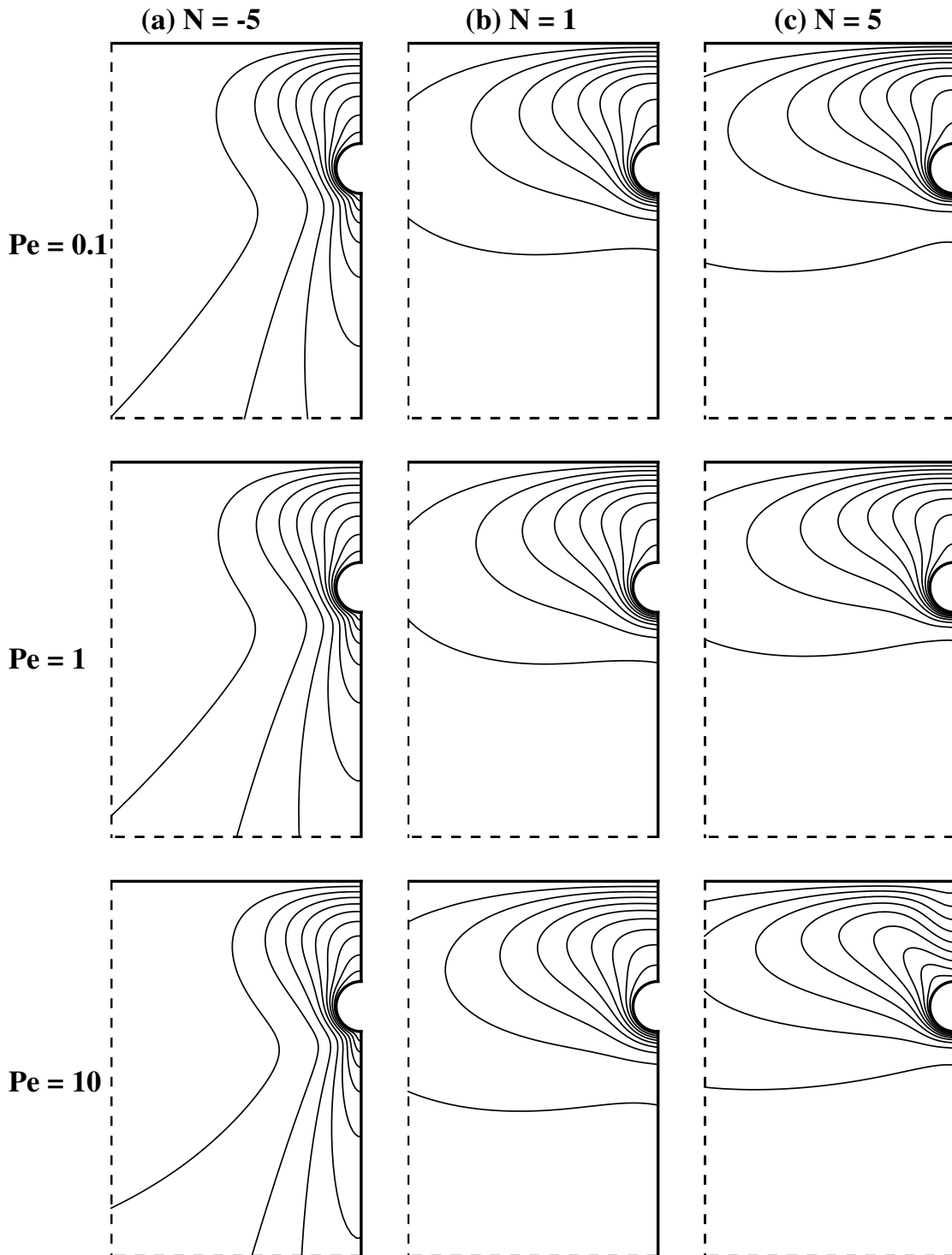
Figure 5.19 Effects of Peclet number (Pe) on the temperature fields with downward leakage, Le = 1, Ra = 10; (a) N = -5, (b) N = 1, (c) N = 5 ($\Delta\Theta$ = 0.1).
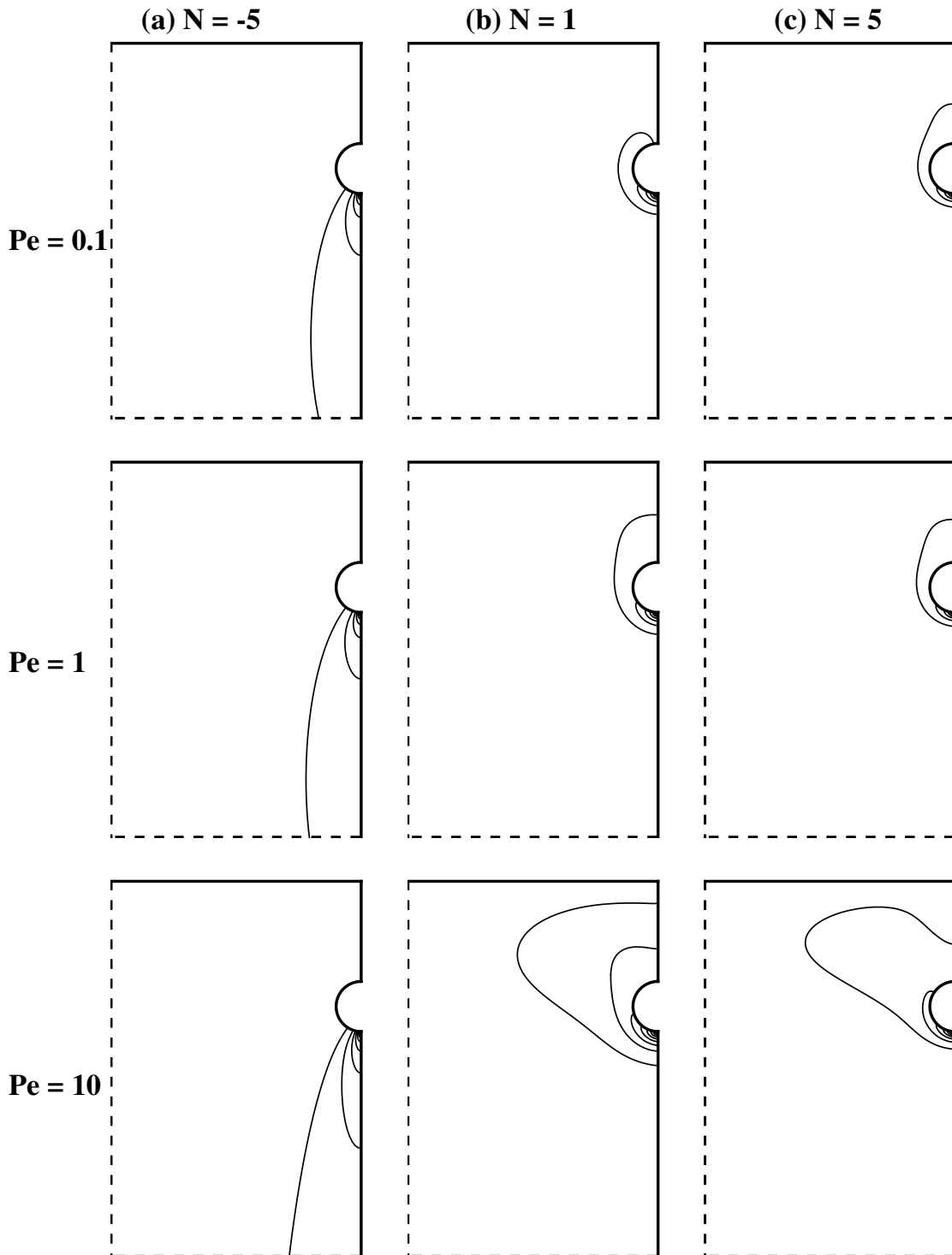
Figure 5.20 Effects of Peclet number (Pe) on the concentration fields with downward leakage, Le = 1, Ra = 10; (a) N = -5, (b) N = 1, (c) N = 5 (ΔC = 0.1).

(Figures 5.17 and 5.20). With an increase in the Peclet number, there is an upward spreading of the concentration profiles for aiding flows no matter where the leakage location is, and a downward contraction for opposing flows. It is interesting to observe that the contaminant is mostly confined to a small region near the crack for opposing flows; it never reaches the top surface even when the Peclet number is significantly increased.

5.5.4 Heat and Mass Transfer Results

For the present study, heat and mass transfer results are expressed in terms of the Nusselt and Sherwood numbers at the top surface, respectively. Basically the Nusselt number is a measure of the total heat flux across the top surface whereas the Sherwood number is the total mass flux across the same surface. The plots of Nusselt and Sherwood numbers as a function of the Rayleigh and Lewis numbers are presented in Figures 5.21 and 5.22 for upward leakage and in Figures 5.23 and 5.24 for downward leakage.

For upward leakage, the change in the buoyancy ratio has a more significant effect on the Nusselt number when the Lewis number is less than or equal to unity. In general, the Nusselt number increases for aiding flows and decreases for opposing flows. It is apparent that for opposing flows, the solute buoyancy suppresses the thermal buoyancy and hence reduces the heat transfer. A similar trend is observed when the leakage location is at the bottom of the pipe. For aiding flows with upward and downward leakage, the cases with Le < 1 yield a higher heat transfer rate than those with Le > 1. Notice that, from Figure 5.21(c), converged solutions are only
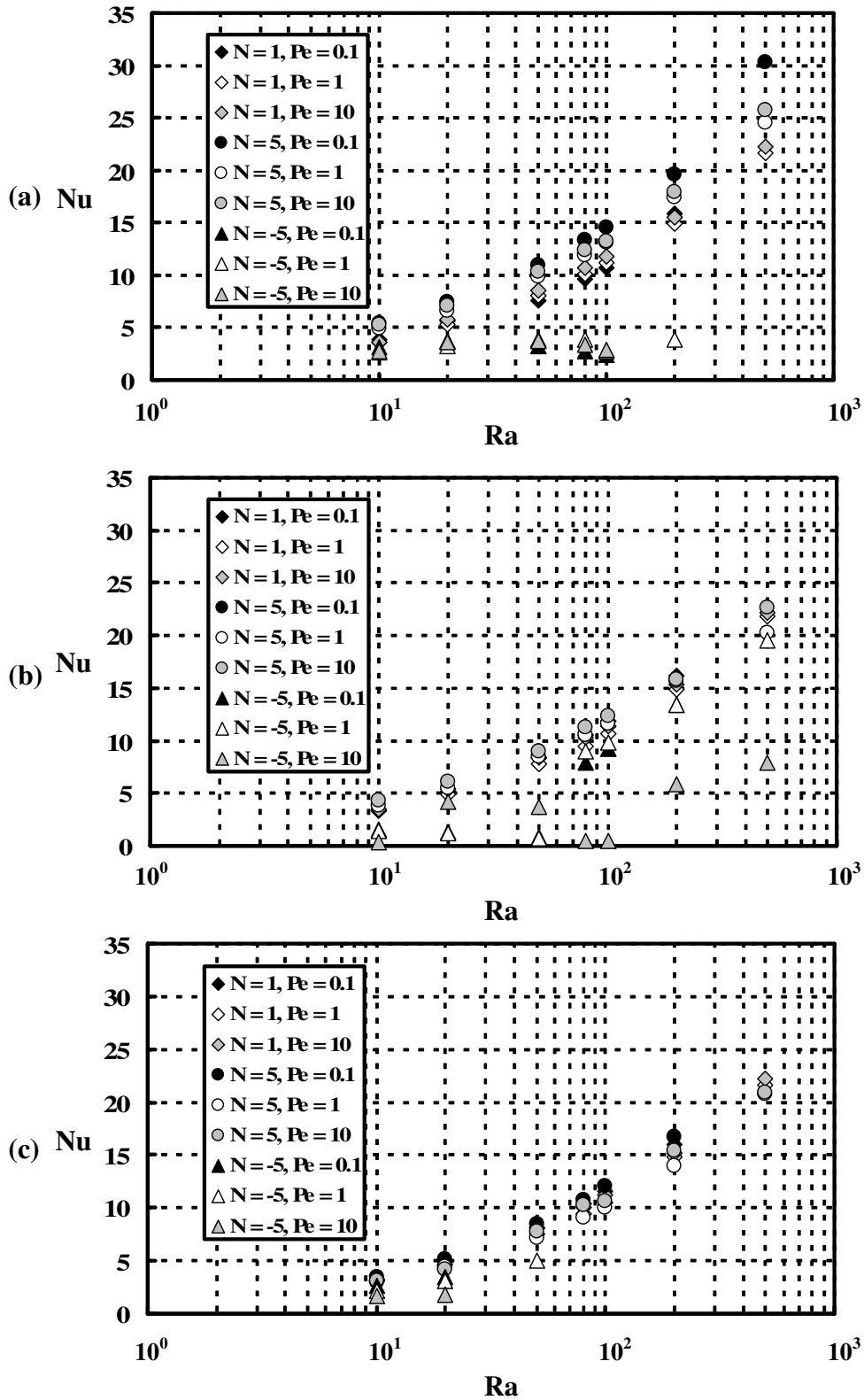
Figure 5.21 Heat transfer results with upward leakage, (a) Le = 0.1, (b) Le = 1, (c) Le = 10.
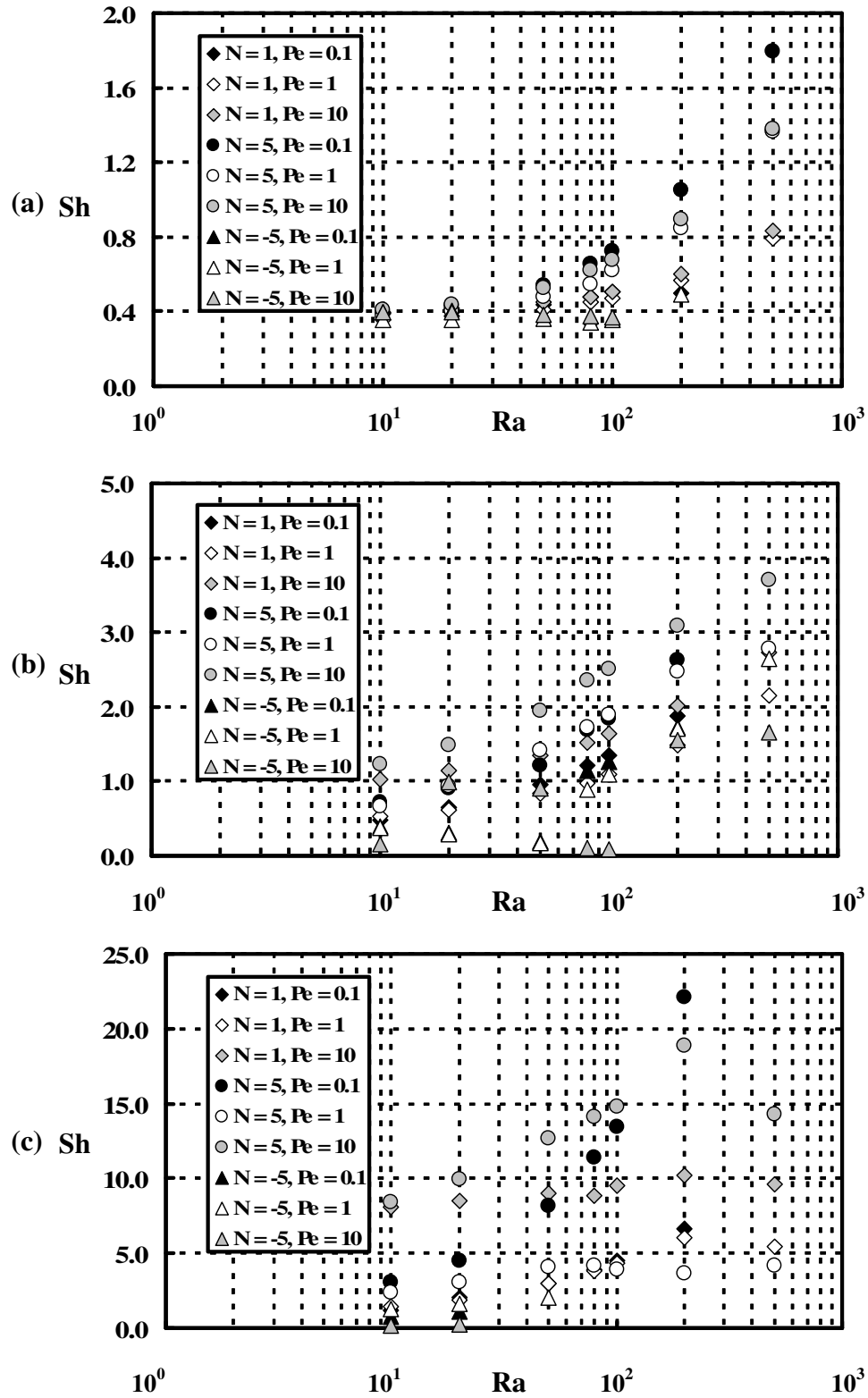
Figure 5.22 Mass transfer results with upward leakage, (a) Le = 0.1, (b) Le = 1, (c) Le = 10.
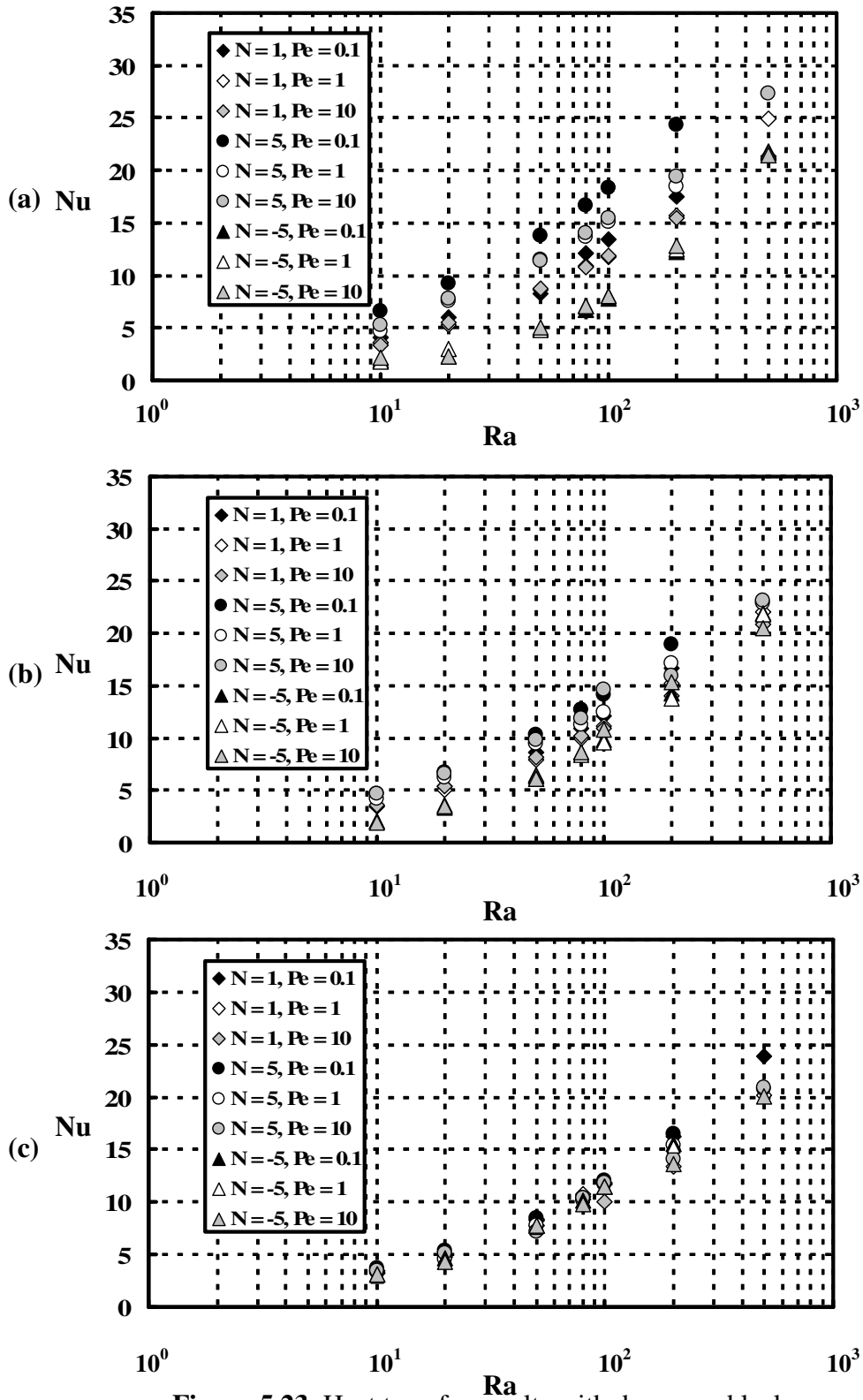
Figure 5.23 Heat transfer results with downward leakage,
(a) Le = 0.1, (b) Le = 1, (c) Le = 10.
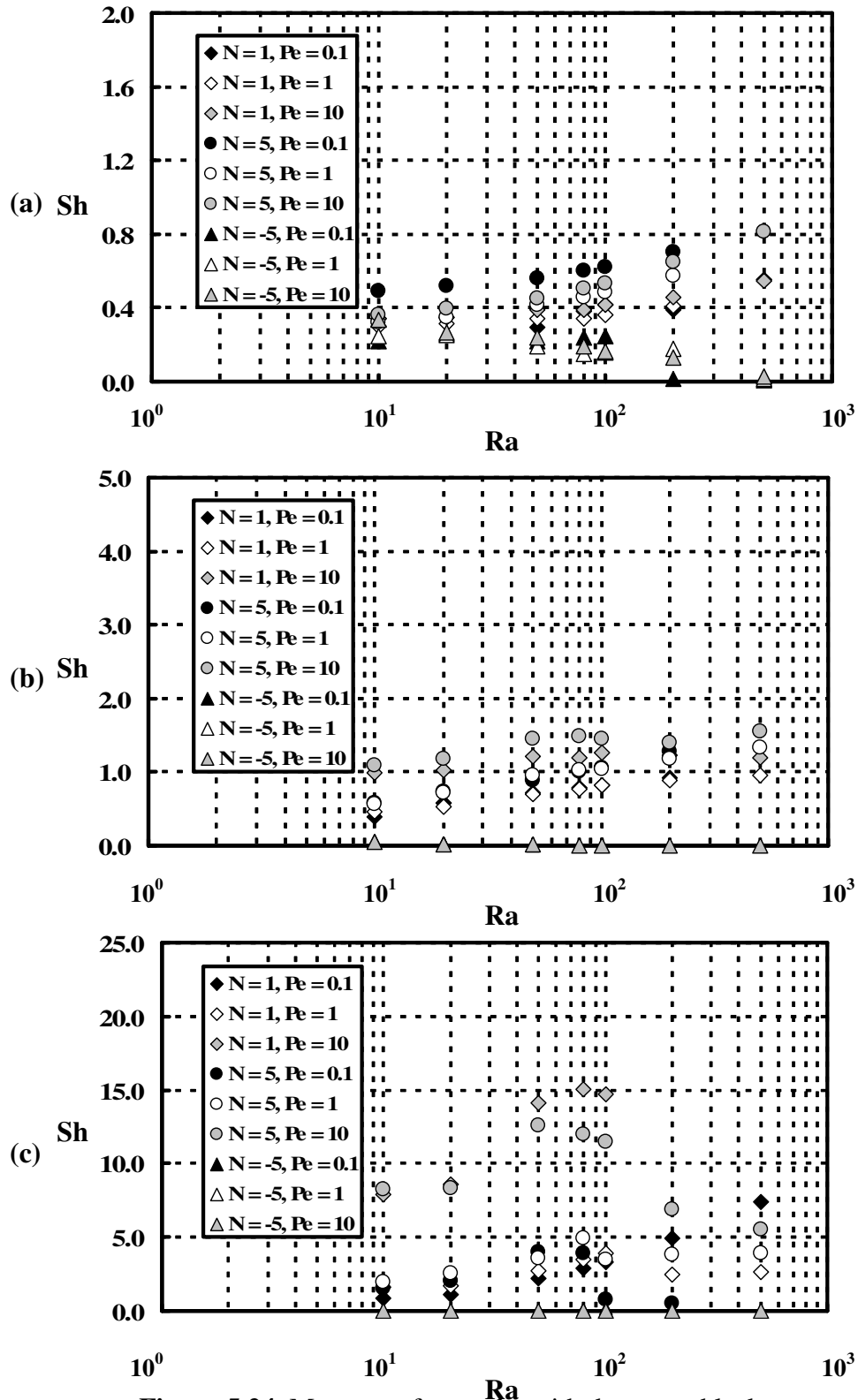
Figure 5.24 Mass transfer results with downward leakage,
(a) Le = 0.1, (b) Le = 1, (c) Le = 10.

possible at low Rayleigh numbers for opposing flows with upward leakage and Le =
10. The flow fields become highly unstable when the Rayleigh number is large. The
instability is attributed to the unbalanced interactions among flow inertia, thermal
buoyancy and solute buoyancy. Under the same conditions, the flow is more stable
when the leakage occurs at the bottom of the buried pipe. For both leakage locations,
the effects of the flow inertia (Peclet number) are more obvious when Le $\leq$ 1.
Generally, heat transfer is enhanced when the leakage location is moved from the top
to the bottom of the buried pipe.

For the mass transfer results (Figures 5.22 and 5.24), the data are more
scattered than the heat transfer results, which indicates that the effects of the
governing parameters such as N, Le, Pe and the leakage location are more significant
on the concentration field than the temperature field. For both upward and downward
leakages, the Sherwood number increases for aiding flows but decreases for opposing
flows. It is observed that the effects of Lewis number are more dominant on the
Sherwood number than the Nusselt number. The Sherwood number increases
significantly with the Lewis number for aiding flows, but approaches zero for
opposing flows. When the leakage is on top of the buried pipe, the solute buoyancy is
acting downwards for opposing flows; hence only a small fraction of the mass fluxes
crosses the top boundary. Virtually no mass is transferred through the top surface
when the leakage is at the bottom of the buried pipe for opposing flows. This result is
consistent with the observation from the isoplets shown previously. Again, the
effects of Peclet number are more pronounced on the Sherwood number than the
Nusselt number. For aiding flows with Le $\geq$ 1, the mass transfer increases with the

Peclet number regardless of the location of the leakage. In general, mass transfer rate is greater when the leakage is on top of the buried pipe than at the bottom of the buried pipe.

5.6 Concluding Remarks

Combined heat and mass transfer by mixed convection from a buried pipe with leakage has been numerically examined in this study. The effects of buoyancy ratio, Lewis number, Peclet number and leakage location on the heat and mass transfer results are examined. It has been found that Nusselt and Sherwood number increases for aiding flows, but decreases for opposing flows. The solute buoyancy is in the opposite direction of the thermal buoyancy for opposing flows, hence it suppresses the thermal buoyancy and reduces the heat and mass transfer rates across the top surface.

Lewis number has a more dominant effect on the mass transfer than the heat transfer. The changes of the concentration profiles with Lewis numbers are more obvious than those of the isotherms. For aiding flows, Nusselt number increases but Sherwood number decreases for Le < 1 while the trend is reversed for Le > 1.

Peclet number also has a more significant effect on the mass transfer than the heat transfer. Sherwood number increases with the Peclet number for aiding flows with Le ≥ 1. On the other hand, the variations of Nusselt number with Peclet number are more obvious for Le ≤ 1. The mass transfer rate increases when the leakage is on top of the buried pipe while the heat transfer rate is enhanced when the leakage is at the bottom of the buried pipe.

CHAPTER **VI**

FLOW VISUALIZATION EXPERIMENT

6.1 Introductory Remarks

Flow visualization methods have been employed extensively in the study of transport phenomena occurred in nature. Pioneers such as Osborne Reynolds, Ludwig Prandtl and Ernst Mach have all conducted flow visualization experiments in developing fundamental theories of fluid mechanics and aerodynamics. Reynolds (1883) studied the transition from laminar to turbulent flow by injecting dye into the water flowing through a long circular pipe. Through this study, he identified a critical parameter, the Reynolds number, which governs this flow transition. Prandtl (1904) investigated flow along a flat plate using tracing particles, and his results ultimately led to the development of boundary layer theory. Mach mastered visualization techniques such as the shadowgraph and Schlieren photography method in studying supersonic flow. In 1877, he presented his infamous paper "Photographische Fixierung der durch Projektile in der Luft eingeleiten Vorgange," which showed a historic photograph of shock waves formed by the nose of a bullet traveling faster than the speed of sound, to the Academy of Sciences in Vienna.

Yang (1994, 2001) provided a summary of both the conventional (i.e., the first generation method) and computer-assisted (i.e., the second generation method) flow visualization techniques. He also demonstrated how these visualization techniques can be utilized in science and technology. Some remarkable photographs of fluid flow in fundamental research and engineering applications can be found in an album

compiled by the Japan Society of Mechanical Engineers (1988). To the best knowledge of the author, Bear (1972) provided the most comprehensive discussion on the experimental methods for flow through porous media, which include the sand box analogy, the electric analogy, the membrane analogy and the Hele-Shaw analogy.

Each of the analogies mentioned above has its pros and cons. For example, the sand box analogy is basically a model simulates a reduced scale of the natural porous medium (e.g., an aquifer) while maintains its similarity (i.e., geometric, kinematic and dynamic similarity). This analogy has been used quite substantially in petroleum reservoir engineering to investigate different fluid drives (e.g., water, gas and solvent) in oil fields. Electric analogy is another technique employed in studies related to flow in porous media, and it includes (a) the continuous electric analogy, (b) the discrete electric analogy and (c) the ion motion analogy. The underlying principle of these techniques is based on the similarity between Darcy's law (which governs the flow through a porous medium) and Ohm's law (which governs the electric current flow through a conductor). By the same token, the differential equation for equilibrium of forces acting on a uniformly stretched membrane is analogous to the equation for flow through a porous medium, and this method is referred to as the membrane analogy. Owing to the difficulty associated with the visualization of actual fluid motion in porous media, the Hele-Shaw analogy perhaps is the most suitable to obtain the flow pattern. Hence it has been adopted in the present study. The discussion of the Hele-Shaw analogy is presented in the next section in greater details.

6.2 Hele-Shaw Analogy

Henry Selby Hele-Shaw, an English engineer, first considered a viscous flow in a narrow gap of a cell consisting of two parallel plates. He suggested that such flow was analogue to a two-dimensional potential flow (Hele-Shaw, 1898a, b). This method was later named after him, and it was referred to as the Hele-Shaw analogy, also known as the viscous flow analogy. Since then, the Hele-Shaw analogy has been related to linear potential flow analysis (i.e., Laplace equation) and used widely in various applications, namely the reservoir engineering, seepage study and groundwater research. A brief literature review that outlines the usage of Hele-Shaw cell is given herein.

Wooding (1960) performed stability analysis for a viscous fluid with variable density in a Hele-Shaw cell. The critical Rayleigh number at neutral stability based on asymptotic expansion was derived for flow in a long vertical rectangular channel. The experimental result obtained from the Hele-Shaw cell was roughly 4% higher than the predicted value. Horne and O'Sullivan (1974) examined the stability of natural convective flow in a porous medium heated uniformly and non-uniformly from below. Both steady and fluctuating flows were reported for uniform heating condition whereas the convective flow due to the non-uniform heat source was found to be periodically oscillatory. The experimental result using a Hele-Shaw cell was consistent with the numerical work. Hartline and Lister (1977) visualized the convective flow in a Hele-Shaw cell using Baker's (1966) pH-indicator technique. This technique has the capability to obtain the flow patterns and velocity

measurements. The experimental results validated the Rayleigh number prediction for the onset of convection.

Koster (1982, 1985) collaborated with his colleague Müller (Koster and Müller, 1982 and 1984) and conducted a series of studies related to convective flow in a Hele-Shaw cell heated from below. The temperature fields were obtained using the holographic real-time interferometry along with local measurements by thermocouples. Two Hele-Shaw cells were considered: (a) Hele-Shaw gaps, with large horizontal extent (Koster, 1982; Koster and Müller, 1982), and (b) Hele-Shaw slots, with larger vertical than horizontal extent (Koster, 1985; Koster and Müller, 1984). In the Hele-Shaw gap experiments, the time-dependent flow was initiated and driven by the instability of the horizontal thermal boundary layer. The exhibition of complicated flow structures was also observed in the Hele-Shaw slot. The flow pattern could be periodic, quasi-periodic or completely stochastic.

More recently, Vorontsov et al. (1991) performed both theoretical and experimental analysis on natural convection in a Hele-Shaw cell subjected to constant wall temperature and uniform wall heat flux. Thermocouples were used to measure the temperature profiles near the thermal boundary layer on the heated wall. The thermograms of the Hele-Shaw convective flow were obtained using an optomechanical infrared imaging system. The theoretical results based on the similarity analysis with boundary layer approximation were in good agreement with the experimental results. Furthermore, the similarity equations were in the same form as those considered by Cheng and Minkowycz (1977) for porous media. Once again, it confirmed that natural convection in a porous medium is analogue to free

convective flow in a Hele-Shaw cell. In the same year, Safonov (1991) investigated

mixed convection around a heated cylinder in a Hele-Shaw cell using finite difference

method. A correlation was proposed for the heat transfer results from the cylinder

when the free-stream velocity was perpendicular to the gravitational force. The

numerical solutions agreed with the proposed correlation within 7%.

Among the literature reviewed thus far, Cheng's experimental work (1996)

was most closely related to the present study. Using a Hele-Shaw cell, he obtained

the flow patterns induced by a buried heated pipe in a porous medium subject to both

permeable and impermeable top boundaries. The focus of his study was to

investigate the effects of aiding and opposing external cross-flow on the convective

flow patterns. However, the natural convection results (i.e., in the absence of cross-

flow) was also presented, and it showed two distinct symmetrical recirculating cells

formed above the heated pipe. The flow fields (Figure 3.12) obtained from the

present numerical study compared quantitatively well with Cheng's visualized results

(1996) despite the absence of the simulated Rayleigh number value.

The Hele-Shaw analogy is not limited for its use in visualizing the flow

pattern of potential flows (such as those in porous media reviewed thus far), it has

other significant scientific value. Polubarinova-Kochina (1945a, b and 1962) was

among those researchers who applied Hele-Shaw flow to study groundwater flow.

However, she realized that there was a need to separate the saturated and dry region

with a free boundary when modeled groundwater flows. Polubarinova-Kochina

(1945a and b) and Galin (1945) developed a complex-variable method to obtain the

exact solution for this Stefan-type moving boundary problem. Polubarinova-Kochina

(1945b) also obtained a close agreement between the exact solutions and the flows visualized in her Hele-Shaw cell. The fact that this nonlinear problem can be readily analyzed using the Hele-Shaw analogy has become the basis for studies involving melting and freezing of materials in industrial processes such as steel making, laser welding, and semiconductor fabrication. In a recent paper, Ockendon and Howison (2002) paid tribute to Polubarinova-Kochina and Hele-Shaw, and examined the impact of their work on modern mathematics, natural science and applications in industry.

In a classical paper, Saffman and Taylor (1958) presented the penetration of a fluid into a porous medium (or Hele-Shaw cell) containing a more viscous liquid. They discovered the viscous fingering phenomena in the Hele-Shaw cell when two immiscible fluids with different viscosity come into contact with one other. This instability of interface is now commonly known as the Saffman-Taylor instability although the first instability analysis of the viscous fingering should be attributed to Hill (1952), and a similar study was also reported by Chuoke et al. (1959) around the same period. All these works laid the foundation and stimulated numerous studies which were significant from both theoretical and practical point of view. From the theoretical aspect, the Saffman-Taylor instability represented the ill-posedness of problem considered by Polubarinova-Kochina (1945a and b) and Galin (1945), hence it posed challenges and sparked tremendous research efforts in the branch of applied mathematics. From the practical viewpoint, the understanding of the interface between two fluids (e.g., water and oil) is essential in advancing applications such as the secondary and tertiary oil recovery methods used in the petroleum industry. For a

more detailed review on the subject of viscous fingering phenomena in Hele-Shaw cell, readers are referred to Howison (1986) and Saffman (1986). Homsy (1987) also reviewed the fingering phenomena with an emphasis on the mechanisms involved in porous media.

The Hele-Shaw analogy also finds its applications in bioengineering and microelectromechanical systems (MEMS). For example, Pozrikidis (1994) studied the motion of particles in a Hele-Shaw cell with an interest in its application to the motion of red blood cells through the interalveoral septum (Fung, 1984). In particular, the force and torque exerted on the particles due to the flow, and the effect of the particle shape on the flow structure as well as particle motion were examined. Lorenz and Zahn (2003) explored the potential applications of ferrofluid in the magnetic-field-driven microfluidic devices using a Hele-Shaw cell. Also, since electrowetting has become a popular mechanism for microfluidic actuations (Cho et al., 2003; Lu et al., in press) proposed a diffuse interface model to predict the motion of electrowetting droplets in a Hele-Shaw cell.

In short, the Hele-Shaw analogy has been a well established practice in various fields over the years due to its simplicity. The ease of relating Hele-Shaw flows to other linear potential flows and the capability of revealing flow patterns are important characteristics of this analogy.

6.3 Motivation and Objective of Present Study

As stated in the last section, the comparison between the present numerical work (Chapter 3) and Cheng's Hele-Shaw experimental work (1996) has shown

excellent agreement in the flow patterns for natural convection in a homogeneous porous medium induced from a heated pipe. The Hele-Shaw analogy is thus adopted in the present study to visualize flow in a heterogeneous porous medium. The objective is to construct a Hele-Shaw cell with different gap widths to simulate a porous medium with distinct permeabilities. The flow patterns can then be visualized using time-elapsed photography with the aid of tracing particles. It is hoped that the experimental work conducted here can lend support to the numerical work presented in Chapter 4. The visualization experiment is set up to investigate how a step change in the permeability of the backfill would affect the flow patterns from a heated buried pipe. Both permeable and impermeable top surfaces with different buoyancy strengths are considered in this experiment.

6.4 Porous Medium and Hele-Shaw Cell

To illustrate mathematically that the governing equation for an incompressible viscous flow in a Hele-Shaw cell is analogous to Darcy's law for flow in a porous medium, let's consider the Hele-Shaw cell shown in Figure 6.1. The cell consists of
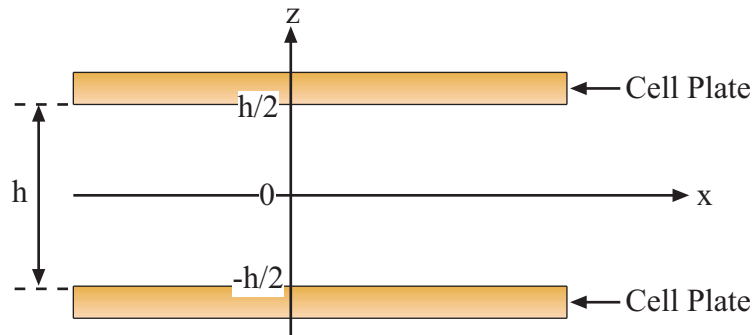
Figure 6.1 Flow in a Hele-Shaw cell.

two parallel plates separated by a gap width h. The coordinate system employed is also indicated in the figure.

For an incompressible flow, the governing equations are based on the Navier-Stokes equations given as follows,

$$\frac{\partial u}{\partial t} + u\frac{\partial u}{\partial x} + v\frac{\partial u}{\partial y} + w\frac{\partial u}{\partial z} = g_x - \frac{1}{\rho}\frac{\partial p}{\partial x} + \nu\left(\frac{\partial^2 u}{\partial x^2} + \frac{\partial^2 u}{\partial y^2} + \frac{\partial^2 u}{\partial z^2}\right),$$ [6.1a]

$$\frac{\partial v}{\partial t} + u\frac{\partial v}{\partial x} + v\frac{\partial v}{\partial y} + w\frac{\partial v}{\partial z} = g_y - \frac{1}{\rho}\frac{\partial p}{\partial y} + \nu\left(\frac{\partial^2 v}{\partial x^2} + \frac{\partial^2 v}{\partial y^2} + \frac{\partial^2 v}{\partial z^2}\right),$$ [6.1b]

$$\frac{\partial w}{\partial t} + u\frac{\partial w}{\partial x} + v\frac{\partial w}{\partial y} + w\frac{\partial w}{\partial z} = g_z - \frac{1}{\rho}\frac{\partial p}{\partial z} + \nu\left(\frac{\partial^2 w}{\partial x^2} + \frac{\partial^2 w}{\partial y^2} + \frac{\partial^2 w}{\partial z^2}\right).$$ [6.1c]

The flow is assumed to be steady and two-dimensional (w = 0). For creeping or highly viscous flows, the viscous terms on the right hand side is more dominant; hence the convective terms on the left hand side are neglected. In the absence of body forces, the Navier-Stokes equations are reduced to

$$\frac{\partial p}{\partial x} = \mu\left(\frac{\partial^2 u}{\partial x^2} + \frac{\partial^2 u}{\partial y^2} + \frac{\partial^2 u}{\partial z^2}\right),$$ [6.2a]

$$\frac{\partial p}{\partial y} = \mu\left(\frac{\partial^2 v}{\partial x^2} + \frac{\partial^2 v}{\partial y^2} + \frac{\partial^2 v}{\partial z^2}\right).$$ [6.2b]

Since the gap width is sufficiently small, it is reasonable to assume that the second derivatives of the velocity with respect to x and y are small compared to those with respect to the z-direction. The governing equations for the Hele-Shaw flow can be further reduced to

$$\frac{\partial p}{\partial x} = \mu \frac{\partial^2 u}{\partial z^2}, \quad\quad\quad [6.3a]$$

$$\frac{\partial p}{\partial y} = \mu \frac{\partial^2 v}{\partial z^2}. \quad\quad\quad [6.3b]$$

Integrating the above equations twice and subjecting to the following no-slip boundary conditions,

$$\text{At } z = \frac{h}{2}, \quad u = 0 \quad \text{and} \quad v = 0, \quad\quad\quad [6.4a]$$

$$\text{At } z = -\frac{h}{2}, \quad u = 0 \quad \text{and} \quad v = 0, \quad\quad\quad [6.4b]$$

the velocity components are determined to be

$$u = \frac{1}{2\mu} \frac{\partial p}{\partial x}\left(z^2 - \frac{h^2}{4}\right), \quad\quad\quad [6.5a]$$

$$v = \frac{1}{2\mu} \frac{\partial p}{\partial y}\left(z^2 - \frac{h^2}{4}\right). \quad\quad\quad [6.5b]$$

The average velocities in the Hele-Shaw cell are given by

$$\bar{u} = \frac{1}{h}\int_{-h/2}^{h/2} u \, dz, \quad\quad\quad [6.6a]$$

$$\bar{v} = \frac{1}{h}\int_{-h/2}^{h/2} v \, dz. \quad\quad\quad [6.6b]$$

Combining Eqns. [6.5] and [6.6], one yields

$$\bar{u} = -\frac{h^2}{12\mu} \frac{\partial p}{\partial x}, \quad\quad\quad [6.7a]$$

$$\bar{v} = -\frac{h^2}{12\mu} \frac{\partial p}{\partial y}. \quad\quad\quad [6.7b]$$

According to Darcy's law, the volume-averaged velocities for flow in a porous medium are given by

$$\bar{u} = -\frac{K}{\mu}\frac{\partial p}{\partial x} \ , \qquad\qquad\qquad\qquad [6.8a]$$

$$\bar{v} = -\frac{K}{\mu}\frac{\partial p}{\partial y}. \qquad\qquad\qquad\qquad [6.8b]$$

By comparing the expressions for the velocities in Eqns. [6.7] and [6.8], one can obtain the following relationship

$$h = \sqrt{12K}. \qquad\qquad\qquad\qquad [6.9]$$

Hence, the analogy between the flow in a Hele-Shaw cell and Darcy's flow in a porous medium is established. With this analogy, one can model a porous medium with a given permeability by properly selecting the gap width of the Hele-Shaw cell. However, there are some limitations associated with the Hele-Shaw analogy. For example, this analogy is only valid for laminar flows, and it cannot accommodate any lateral dispersion and instabilities effects. Obviously, the pros of Hele-Shaw analogy are its simplicity in design and relatively inexpensive to construct the experimental setup.

In this study, Hele-Shaw cells with different gap widths (Figure 6.2) were constructed to simulate a porous medium with distinct permeabilities around a buried pipe. For cell A, the gap width immediate around a copper pipe was set to be 3/8 inch (h_1) and that for the outer region was 1/8 inch (h_2). Hence, a buried pipe with a backfill of $K_1/K_2 = 9$ was modeled in this setup. The top portion of the Hele-Shaw cell has the widest gap width ($h_3 = 1$ inch) such that a permeable top boundary can be
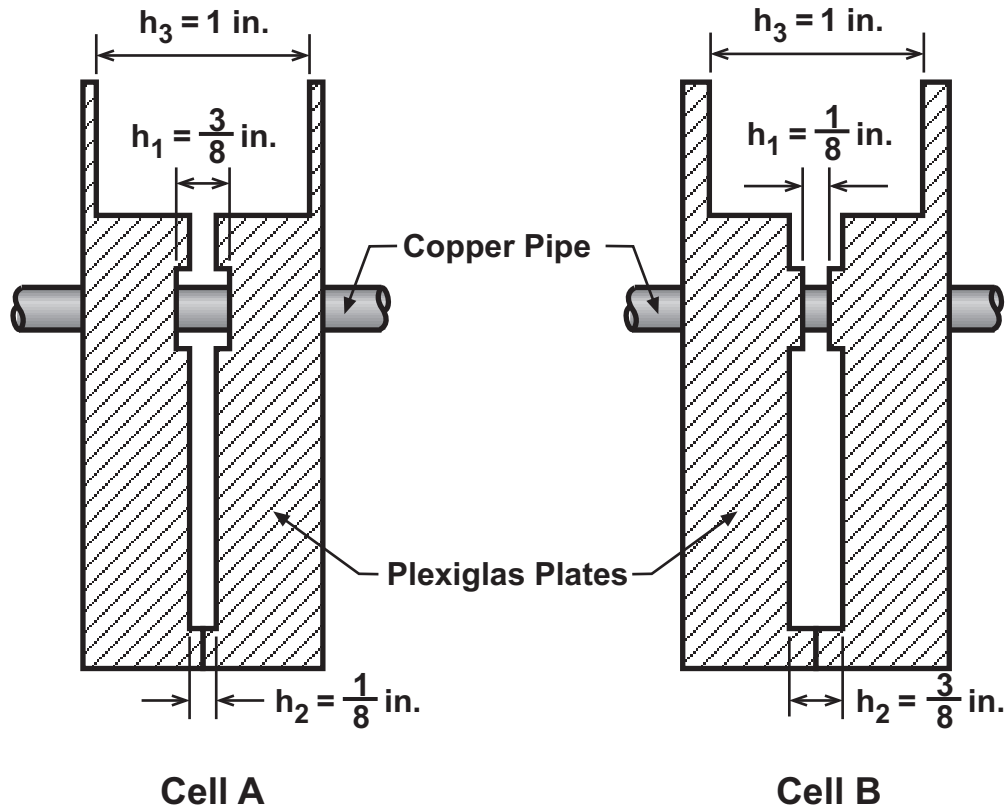
Figure 6.2 Cross-sectional view of the Hele-Shaw cells constructed for the present study.

modeled. The cell can then be sealed to set up an impermeable top boundary. On the other end, cell B was constructed to simulate a backfill of $K_1/K_2 = 0.11$ around a buried pipe. The details of experimental setup and apparatus are discussed next.

6.5 Experimental Setup and Apparatus

The experimental apparatus for the present study consists of four main units: (a) Hele-Shaw cell unit, (b) Heated pipe unit, (c) Reservoir unit, and (d) Imaging unit. A complete description of components and specifications is listed in Table 6.1. The details of each unit of the experimental setup are described as follows.

Table 6.1 List of the components of the experimental apparatus and their specifications.

Component	Specification/Manufacturer	Unit
Hele-Shaw Cell	<u>Cell A:</u> Two 1/2 in. thick and 32 in. x 22 in. Plexiglas; One 1/8 in. thick and 1 in. wide U-shape Plexiglas (Figure 6.4) <u>Cell B:</u> Two 1/2 in. thick and 32 in. x 22 in. Plexiglas; One 3/8 in. thick and 1 in. wide U-shape Plexiglas; Two 1/8 in. thick, 3 in. OD x 1 in. ID donut-shape Plexiglas (Figure 6.5) Weld-On #16 clear, medium bodied solvent cement for joining acrylic; GE Silicone II 100% clear silicone sealant; ColorPlace fast dry spray paint (black); Four Watts PL-200 1/4 in. x 1/4 in. nylon barb splicers; Midwest Fastener Corp. Phillips pan machine screws zinc 8-32 x 2 in. & 8-32 x 1-1/2 in.; machine screw hex nuts coarse thread zinc 8-32; #8 flat washers zinc	Cell
Tracing Particles	Gliterex Corp. Poly Flakes polyester glitter	Cell
Silicone Oil	10 bottles of Fisher Scientific 500 ml silicone oil	Cell
Base Support	Two 1/2 in. thick and 4 ft. x 2 ft. plywood; Two sets of shelf brackets (10 in. x 12 in. and 9 in. x 11 in.); 8x 1/2in. Phillips sheet metal screws	Cell
Copper Pipe	Two 6 in. long of 1 in. diameter copper tubing	Heated Pipe
Tubing	4 ft. of 1/2 in. OD x 3/8 in. ID vinyl tubing	Heated Pipe
Tube Fittings	Four Watts PL-741 nylon barb to MIP adapters 1 in. x 1/2 in.	Heated Pipe
Hose Clamps	Four 1/2 in. hose clamps	Heated Pipe
Isothermal Bath	Fisher Scientific Isotemp 3013P	Heated Pipe
Funnel	Flotool multipurpose funnel	Reservoir
Valve	Kbi 1/2 in. chlorinated poly vinyl chloride ball valve (CBV-0500-S)	Reservoir
Tubing	6 ft. of 3/8 in. OD x 1/4 in. ID vinyl tubing	Reservoir
Tube Fittings	3/8 in. comp x 3/8 in. MPT Co; 3/8 in. HB x 3/8 in. MPT Barb	Reservoir
Support	13 in. x 3.5 in. x 1.5 in. wooden block; 3 ft. x 3.5 in. x 0.75 in. wooden sheet; 8x 2 in. flat head Phillips sheet metal screws; Two 1/2 in. RIG pipe straps; One 3/8 in. RIG pipe strap	Reservoir
Camera	Minolta Maxxum 7000i autofocus SLR camera	Imaging
Films	Kodak Professional BW400CN ISO400 35mm black and white 24-exposure film	Imaging
Tripod	Samsonite	Imaging

(a) Hele-Shaw cell unit: Two Hele-Shaw cells were constructed using four pieces of Plexiglas of 1/2 inch thickness cut to a dimension of 32 inches by 22 inches. They were machined using a computer numerical control (CNC) machine. The dimensions and assembly of the Hele-Shaw cells A and B are shown in Figure 6.3 and 6.4, respectively. The dimensions of the Hele-Shaw cells were selected such that they could be handled using the CNC machine in the machine shop of the School of Aerospace and Mechanical Engineering. Once the Plexiglas was machined using the CNC machine, it lost its transparency. The front Plexiglas wall was polished using sand papers and liquid polishers (Table 6.2) to restore its transparency for the flow visualization purpose while the back Plexiglas wall was painted black to enhance the visibility of the tracing particles.

A one-inch-diameter hole was drilled at the center of the cell for the installation of a copper pipe to simulate a buried heated pipe. Two 1/4 inch holes were drilled at the back side of the Hele-Shaw cell for connecting tubing to the reservoir unit. Three edges of the Hele-Shaw cell were also drilled with 1/4 inch holes to accommodate bolts and nuts for fastening purpose. The front and back Plexiglas walls along with the spacer were then aligned and glued together using

Table 6.2 Items used to restore the transparency of Plexiglas.

Novus Plastic Polish No. 3: Heavy Scratch Remover
Novus Plastic Polish No. 2: Fine Scratch Remover
Novus Plastic Polish No. 1: Plastic Clean & Shine
Kleenmaster Brillianize Plastics Polish & Fine Finish
GatorGrit Waterproof Sandpaper 600-b (Ultra Fine)
GatorGrit Waterproof Sandpaper 1500-b (Mirror Fine)

(a)

(b)

(c)

(d)
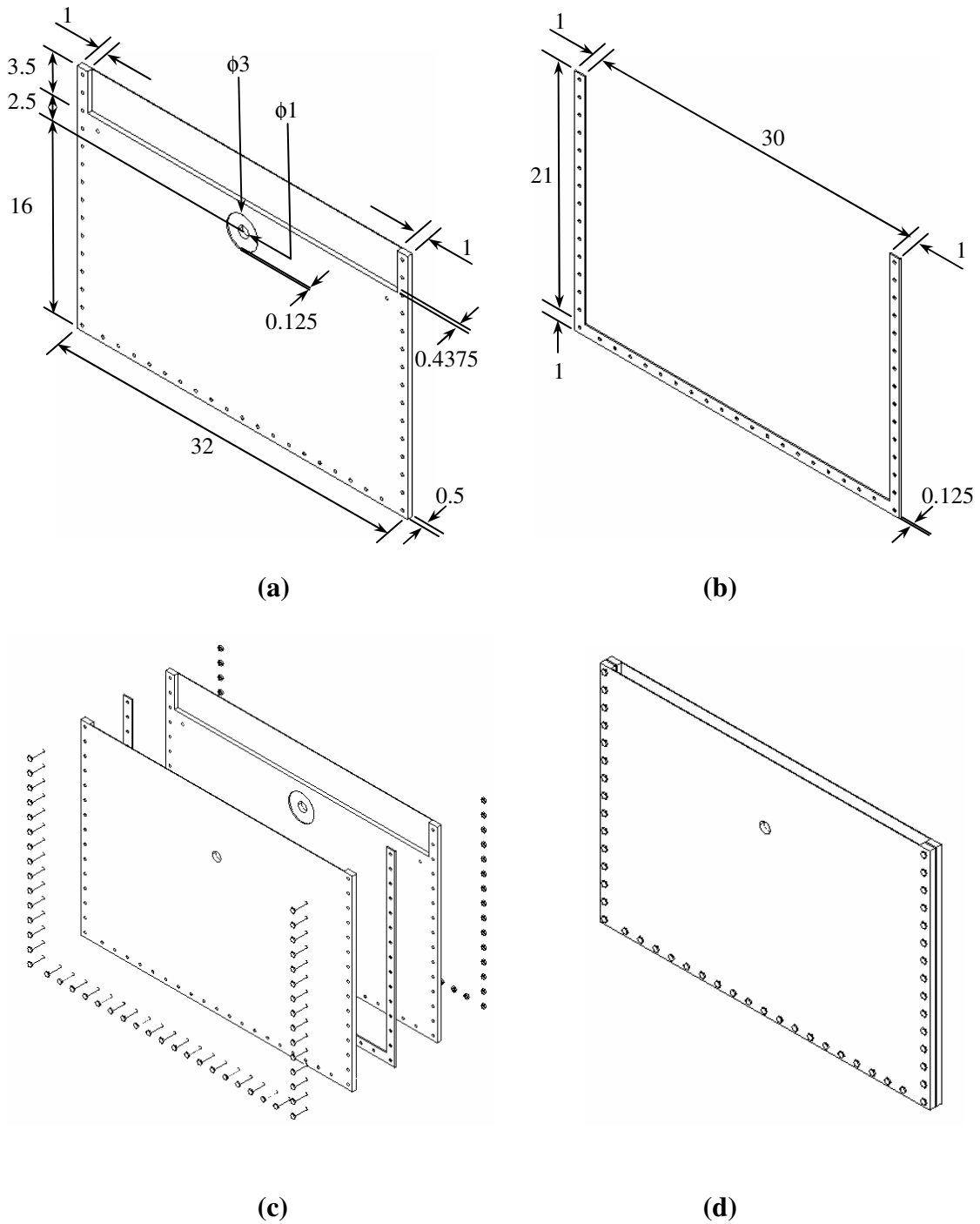
Figure 6.3 The dimensions of Hele-Shaw cell A (in inches): (a) the front/back wall, (b) the spacer, (c) the assembly components and, (d) the assembled cell.

(a)

(b)

(c)

(d)
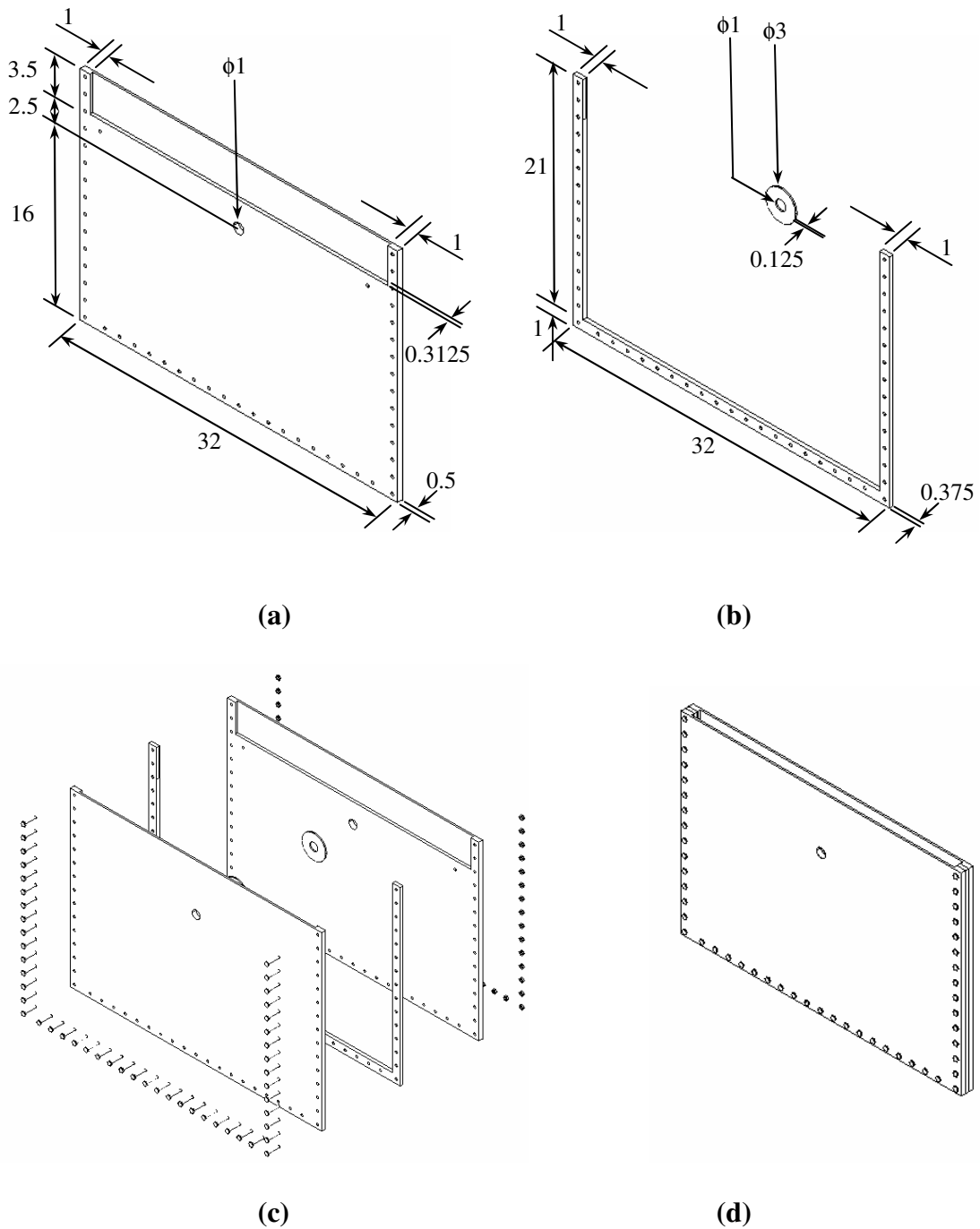
Figure 6.4 The dimensions of Hele-Shaw cell B (in inches): (a) the front/back wall, (b) the spacers, (c) the assembly components and, (d) the assembled cell.

Weld-On #16 clear solvent cement to form a complete Hele-Shaw cell. In addition, they were bolted together and sealed with silicon sealant such that the cell could withstand the pressure build-up once it was filled with silicone oil. The same assembling procedures were applied to construct the second Hele-Shaw cell. The components of Hele-Shaw cell B included two donut-shape spacers (Figure 6.4c): one transparent and one painted black. Extra care was exercised to glue the transparent spacer to the front Plexiglas wall as it would become part of the test section (viewing area). Clear Weld-On #16 solvent cement was applied evenly on the transparent spacer and then pressed firmly to the Plexiglas front wall to avoid bubbles being formed. The assembled cells were left to cure for 24 hours, and were tested for leaks using water.

The next step was to build a base support for the Hele-Shaw cell. Four triangle brackets were secured to a 4-feet by two-feet plywood such that the Hele-Shaw cell could be placed into the slot. For the present experiment, the Hele-Shaw cells were filled with silicone oil. The silicone oil was chosen because of its high viscosity. Glitter was used as the tracing particles. Most glitter available on the market tends to be heavy and they settle when immersed in a liquid. Glitter with high reflective index and capable of remaining suspended in the silicone oil was selected. Photographs of the Hele-Shaw cell units are shown in Figure 6.5.

(b) Heated pipe unit: A one-inch copper pipe was inserted through the center of the Hele-Shaw cell to simulate a buried pipe. Due to the tight tolerance of the drilled center hole and copper pipe, it was important not to exert pressure on the Plexiglas when installing the pipe to avoid alteration in the designed gap widths. A
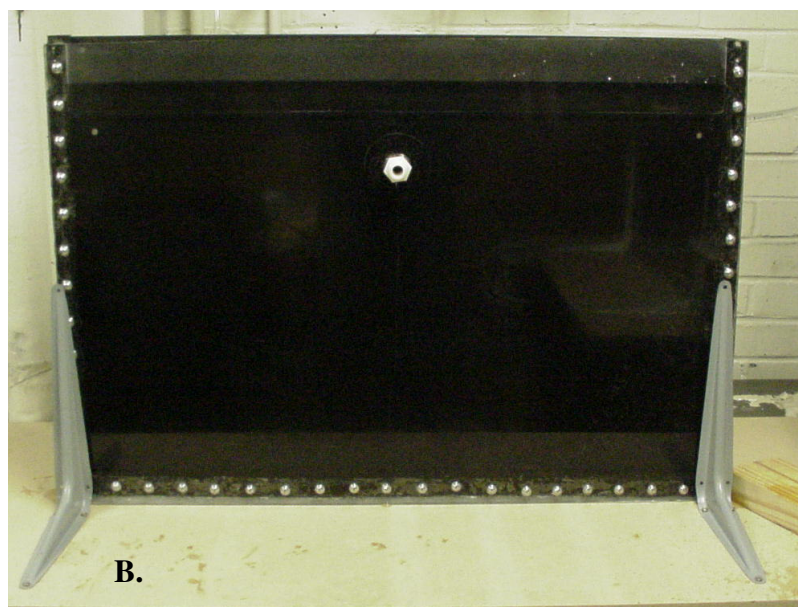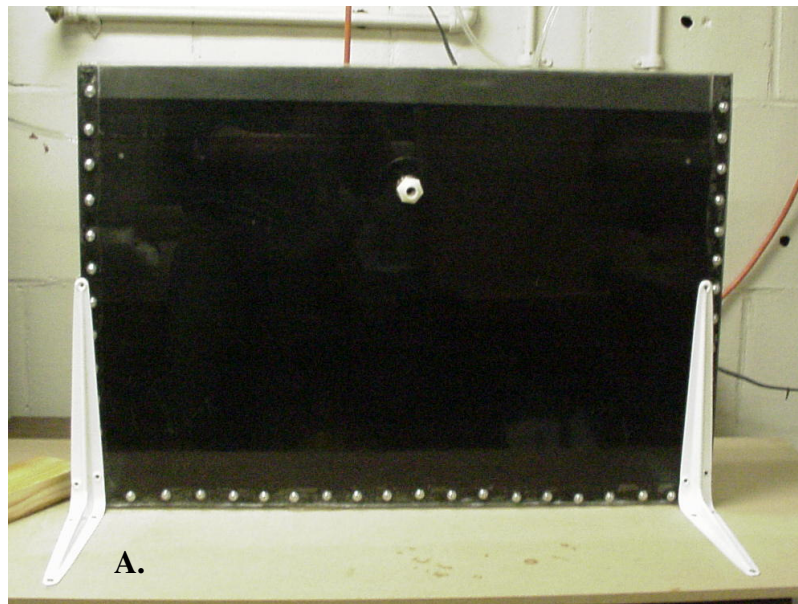
Figure 6.5 Hele-Shaw cells A and B.

1/2 inch OD vinyl tubing was connected to the copper pipe through proper tube fittings and allowing the water from the constant temperature bath to circulate through a loop. The water temperature controlled by the Fisher Scientific Isotemp bath served as a heat source to produce thermal buoyancy for the formation of convective cells. Copper was chosen as the material for the pipe for its high thermal conductivity. Silicon sealant was applied to the interconnections of components, and hose clamps were used to secure the tubing to prevent leak. The assembly of the heated pipe unit is shown in Figure 6.6.

(c) Reservoir unit: The main purpose of the reservoir unit was to supply the silicone oil and tracing particles to the gap of the Hele-Shaw cell. This unit consisted of a funnel with vinyl tubing attached to the back of the Hele-Shaw cell unit. The flow of silicone oil and tracing particles was regulated using a ball valve. Two tube fittings were needed to connect the valve to the funnel, and from the valve to the vinyl tubing. All these components were then secured to a base using three pipe
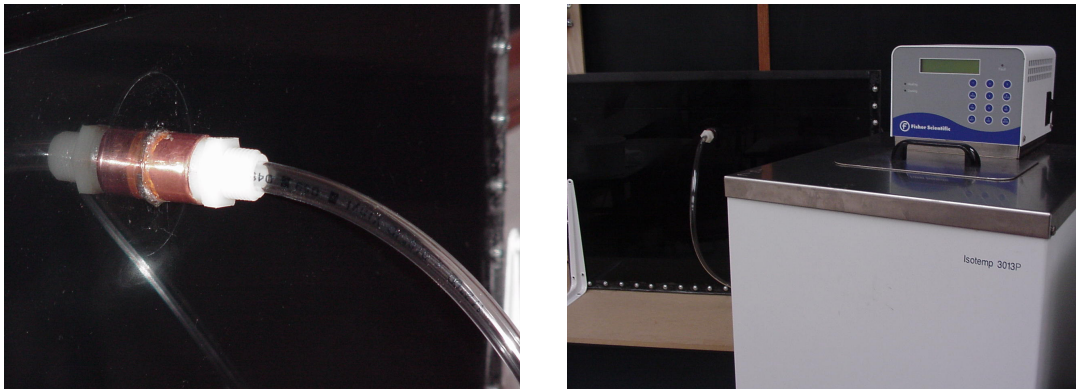
Figure 6.6 Heated pipe unit.

straps (Figure 6.7). Another function of the reservoir unit is for the drainage of silicone oil.

(d) Imaging unit: The flow patterns were captured using an autofocus single-lens reflex (SLR) camera with black and white films. The camera was mounted on a tripod to obtain still images. Figure 6.8 shows the imaging unit used in this experiment. The lighting of the laboratory and appropriate light sources were adjusted for best image quality. The optimum combination of aperture size and shuttle speed was determined by trials. By manually adjusting these settings, one has full control of exposure. The aperture size is related to the sharpness of the object. Generally, a large aperture (e.g., f/2 or f/2.8 etc.) will isolate the object in focus from its background while a small aperture (e.g., f/22 or f/16 etc.) will provide sharpness on both foreground and background. On the other hand, the shuttle speed is related to how fast the shuttle curtain opens and closes during an exposure. Having the option
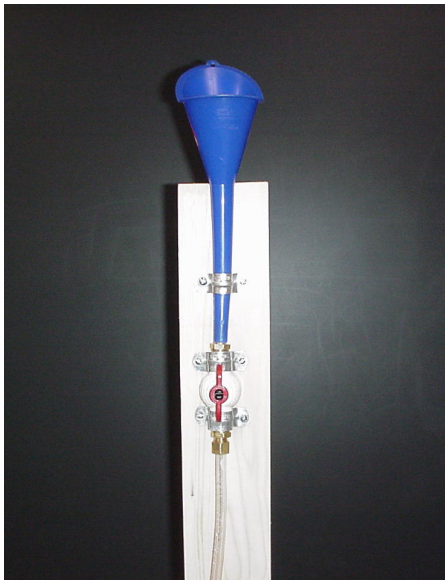
Figure 6.7 Reservoir unit.

Figure 6.8 Imaging unit.

of manually setting the shuttle speed is ideal when taking picture of an object in motion. The shuttle speed ranges from 1/4000 of a second to a full 30 seconds. One can freeze the object in motion using a fast shuttle speed such as 1/4000 or 1/2000 of a second while a slower shuttle speed (e.g., 15 or 30 seconds) will blur the motion and make the object appears to be flowing. This becomes an essential part of this visualization experiment as our objective is to capture the motion of the tracing particles and present the overall flow field.

6.6 Experimental Procedures

The experimental procedures are outlined as follows:

1. The first step of the experiment was to make sure that all units were connected and secured properly. A complete experimental setup is shown in Figure 6.9.

Figure 6.9 Hele-Shaw flow visualization setup.

2. The Hele-Shaw cell was filled with silicone oil and tracing particles using the reservoir unit.

3. The water inside the constant temperature bath was filled up to its appropriate level. The constant temperature bath was then turned on, and the temperature was set to 70 $^{\circ}$C.

4. Once the temperature reached the preset value, one needed to ensure that the tracing particles were distributed evenly and fully suspended in the cell by stirring the silicone oil with a thin rod. Undesired air bubbles trapped in the cell were also removed.

5. The Hele-Shaw cell was left for the flow within the cell to reach steady-state.

6. Meanwhile, the light of the laboratory was turned off, and appropriate light sources were directed to the Hele-Shaw cell. The light sources were adjusted to produce the most reflections from the tracing particles.

7. Photographs were taken using an aperture of f/8 and a shuttle speed of 15 seconds. These settings were pre-determined by trials to obtain the best image quality.

8. Steps 4-7 were repeated for a pipe temperature of 95 $^{\circ}$C to simulate different strength of buoyancy.

9. The same procedures (Steps 1-8) were then repeated for Hele-Shaw cell B.

    The Hele-Shaw cells constructed were first used to simulate a porous layer with a permeable top boundary. Once that portion of the experiment was completed, the top was sealed using a top plate to model a porous layer with an impermeable top boundary. The same experiment procedures were then repeated for both sealed Hele-Shaw cells.

6.7 Results and Discussion

The buoyancy induced convection in Hele-Shaw cell due to a heated pipe were examined for both permeable and impermeable top boundary. As mentioned previously, Hele-Shaw cell with different gap widths was constructed to model a porous layer with distinct permeabilities. For Hele-Shaw cell A, the gap width immediate around the copper pipe was 3/8 inch (h_1) while the gap width for the outer region was 1/8 inch (h_2). Hence, a buried pipe with a backfill of $K_1/K_2 = 9$ was modeled in this particular setup. On the other end, Hele-Shaw cell B was constructed to model a backfill of $K_1/K_2 = 0.11$ around a buried pipe.

6.7.1 Results for Hele-Shaw Cells with Permeable Top Boundary

Figure 6.10 (a) shows the flow field in Hele-Shaw cell A with a permeable top boundary subjected to a pipe temperature of 70 ^{o}C. The heated fluid rises along the pipe, and a jet stream of fluid can be observed at the top of the pipe issuing upwards through the permeable boundary. As the fluid hits the free surface, two symmetrical recirculating cells are formed in the top layer. From the figure, it can be seen that most fluid is drawn from the top region of the cell towards the pipe. As the pipe temperature is increased from 70 ^{o}C to 95 ^{o}C (Figure 6.10(b)), the strength of the buoyancy cells increases. More fluid away from the pipe is affected and drawn to the inner region.

On the other hand, the flow field in Hele-Shaw cell B with a permeable top boundary subject to a pipe temperature of 70 ^{o}C and 95 ^{o}C is shown in Figure 6.11. Both flow fields share the same characteristics. Since the permeability immediate

(a)

(b)
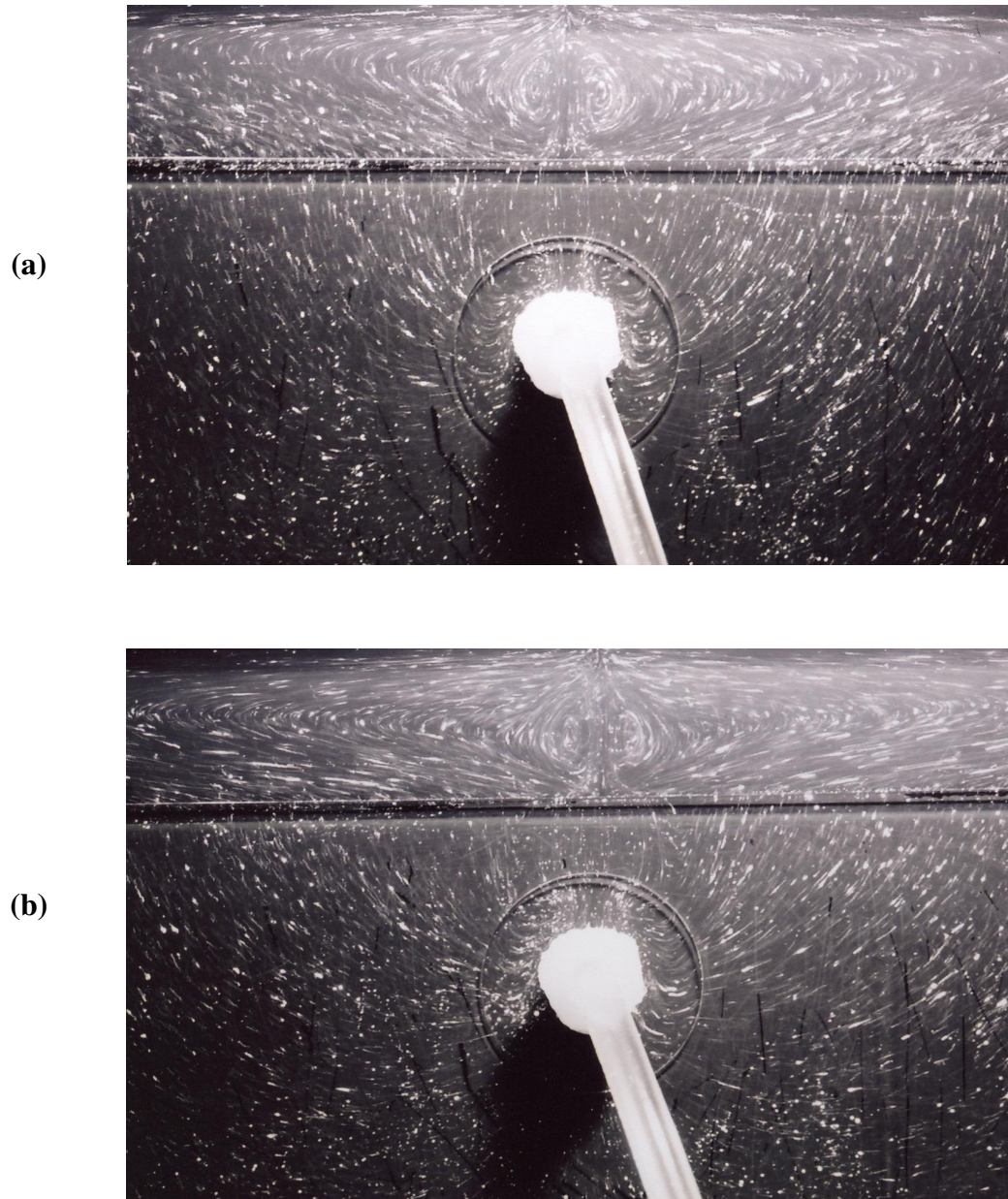
Figure 6.10 Experimental results for Hele-Shaw cell A with permeable top boundary subject to pipe temperature of (a) 70 $^{\circ}$C and (b) 95 $^{\circ}$C.
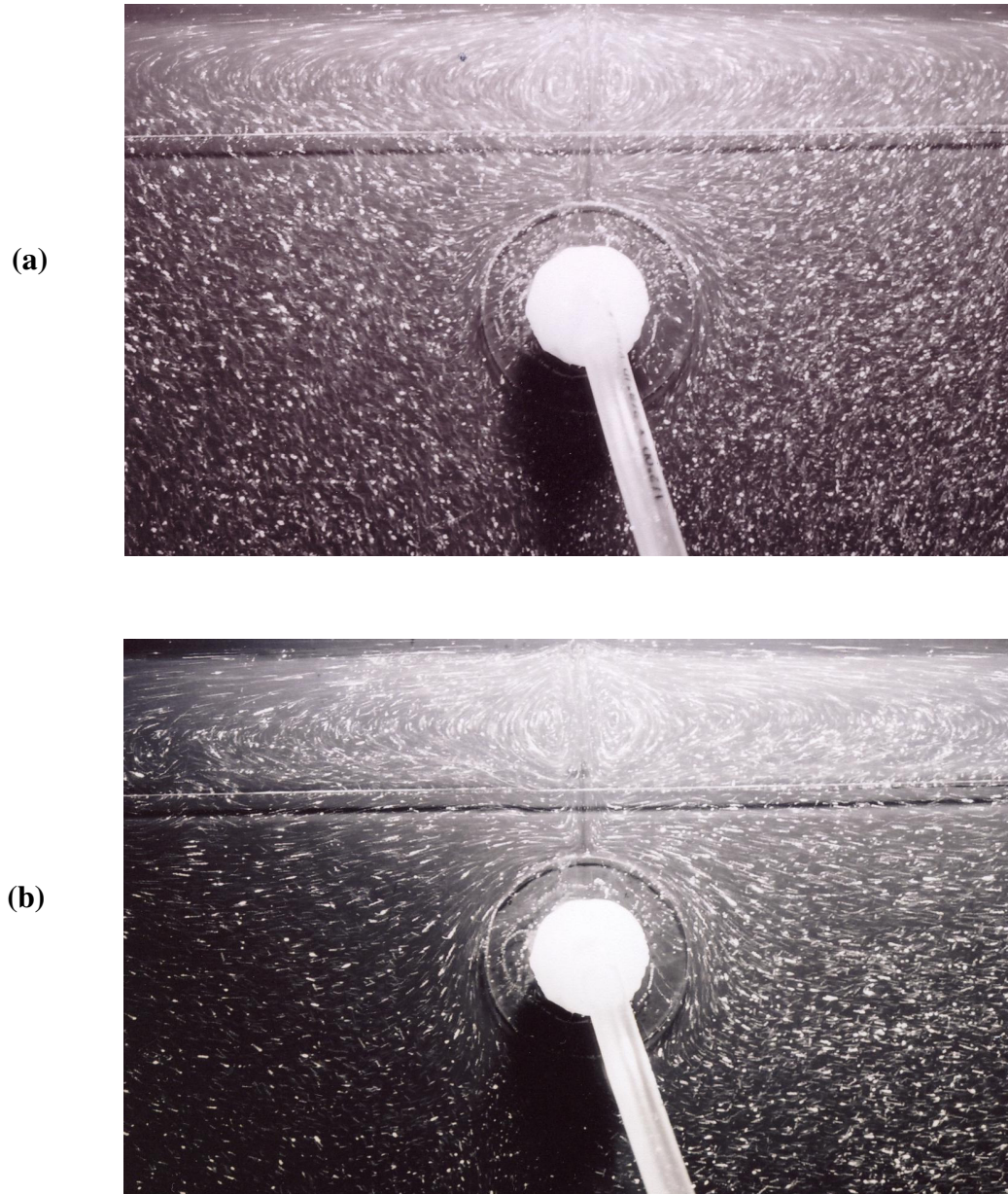
Figure 6.11 Experimental results for Hele-Shaw cell B with permeable top boundary subject to pipe temperature of (a) 70 $^{\circ}$C and (b) 95 $^{\circ}$C.

around the pipe is less permeable than the outer region, most tracing particles stay in the more permeable layer and rise along the interface to the top. Few particles are able to penetrate the less permeable layer. The formation of two symmetrical recirculating cells of equal strength is also observed in the top layer. The strength of the buoyancy cells increases with the pipe temperature. Unlike the flow field in Hele-Shaw cell A, less fluid is drawn from the top layer.

Particular attention is also focused on the fluid flowed through the permeable top boundary. It can be seen from both Figures 6.10 and 6.11 that the slopes of streamlines traced by the particles are not continuous and deflected as they cross the top boundary. This phenomenon was caused by the change in the velocity due to the abrupt alteration in the gap width of the Hele-Shaw cell. Recall that for the Hele-Shaw flow to adequately represent the flow in a porous medium, the velocity in the z-direction is assumed to be zero (i.e., w = 0). Hence, if the change in the gap width is not gradual enough, this assumption is no longer valid, which in turn causes the flow field near that interface not depicting a real flow situation. The Hele-Shaw cells constructed for this experiment are intended to simulate a fluid layer overlying on top of a porous medium.

6.7.2 Results for Hele-Shaw Cells with Impermeable Top Boundary

The flow field in a heterogeneous porous medium with an impermeable top boundary is examined next. The numerical study for this case of convective flow was discussed in Chapter 4, and the result corresponding to the experimental condition was reproduced for comparison. Due to symmetry, the numerical result is shown on

the left while the visualized flow field is shown on the right. The properties of silicone oil (Leong, 2002) as well as the simulated parameters are listed in Tables 6.3 and 6.4, respectively.

Table 6.3 Physical properties of the silicone oil.

Thermal diffusivity (α)	7×10^{-8} m^2/s
Coefficient of thermal expansion (β_T)	0.00104 ^{o}C^{-1}
Kinematic viscosity (ν)	50.3×10^{-4} m^2/s

Table 6.4 Simulated parameters for the flow visualization experiment.

Hele-Shaw cell A:

Gap width of the inner layer (h$_1$)	0.0095 m
Gap width of the outer layer (h$_2$)	0.0032 m
Permeability of the inner layer $\left(K_1 = \dfrac{h_1^2}{12} \right)$	7.56×10^{-6} m^2
Permeability ratio (K$_1$/K$_2$)	9
Radius of the copper pipe (r$_i$)	0.013 m
Ambient temperature (T$_c$)	27 ^{o}C
Rayleigh number $\left(Ra_1 = \dfrac{K_1 g \beta_T (T_h - T_c) r_i}{\alpha \nu} \right)$	
For pipe temperature (T$_h$) = 70 ^{o}C:	120
For pipe temperature (T$_h$) = 95 ^{o}C:	189

Hele-Shaw cell B:

Gap width of the inner layer (h$_1$)	0.0032 m
Gap width of the outer layer (h$_2$)	0.0095 m
Permeability of the inner layer $\left(K_1 = \dfrac{h_1^2}{12} \right)$	8.4×10^{-7} m^2
Permeability ratio (K$_1$/K$_2$)	0.11
Radius of the copper pipe (r$_i$)	0.013 m
Ambient temperature (T$_c$)	27 ^{o}C
Rayleigh number $\left(Ra_1 = \dfrac{K_1 g \beta_T (T_h - T_c) r_i}{\alpha \nu} \right)$	
For pipe temperature (T$_h$) = 70 ^{o}C:	13
For pipe temperature (T$_h$) = 95 ^{o}C:	21

As clearly shown in Figure 6.12, the predicted flow field is similar to that observed from the experiment. The pipe temperature in this case was set to 70 $^{\circ}$C while the corresponding numerical result was presented for $Ra_1 = 120$ and $K_1/K_2 = 9$. It can be seen that the fluid rises along the pipe wall due to buoyancy while drawing fluid from the less permeable region. Because of the impermeable top boundary, the fluid alters its course and redirects downwards, but is carried away almost immediately by the buoyancy force and thus forming a circulating convective cell. This circulating cell is confined mostly in the more permeable inner layer. As the pipe temperature is increased to 95 $^{\circ}$C, the strength of the buoyancy increases correspondingly as seen in Figure 6.13.

For Hele-Shaw cell B, the outer region is more permeable than the inner region, and the results are shown in Figures 6.14 and 6.15 for different pipe temperatures. The flow field obtained from the experiment resembled that predicted by the numerical study. Convection remains in the layer with a higher permeability. Although the location of the eye of the recirculating cell observed from the experiment is lower than that predicted by numerical simulation, both results indicate that the circulating cell prevails in the outer region. It is also noted that the overall strength of the buoyancy cell in this case is stronger than those seen from Hele-Shaw cell A.

Another observation from the experiment is that the overall settling velocity of tracing particle in Hele-Shaw cell B is faster than that in cell A due to a wider gap width. The capillary force within Hele-Shaw cell A with a smaller gap width is greater, hence slows down the settling velocity. As such, the streamline traced by the

(a)   **(b)**
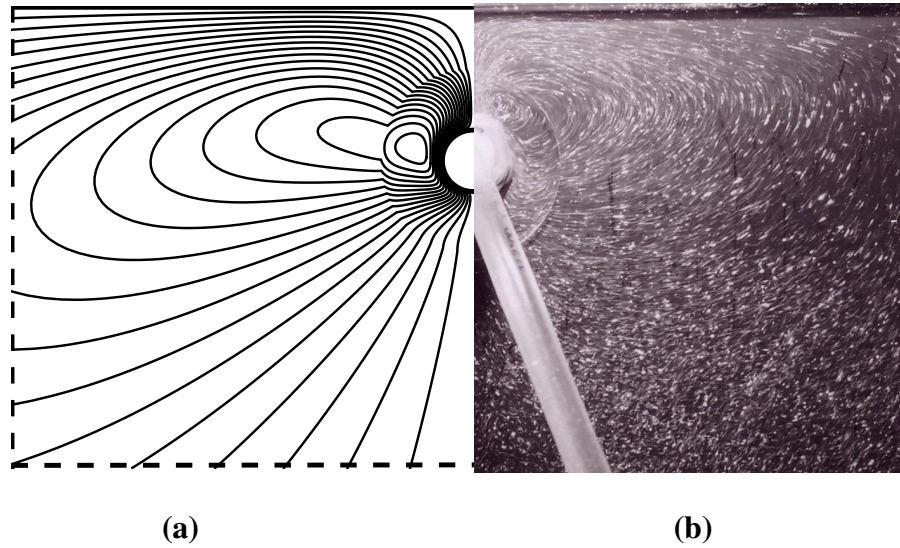
Figure 6.12 Comparison of convective flow fields of Hele-Shaw cell A between (a) numerical result at $Ra_1 = 120$ and $K_1/K_2 = 9$ ($\Delta\Psi = 0.5$), and (b) experimental result observed at a pipe temperature of 70 $^{\circ}$C.

(a)   **(b)**
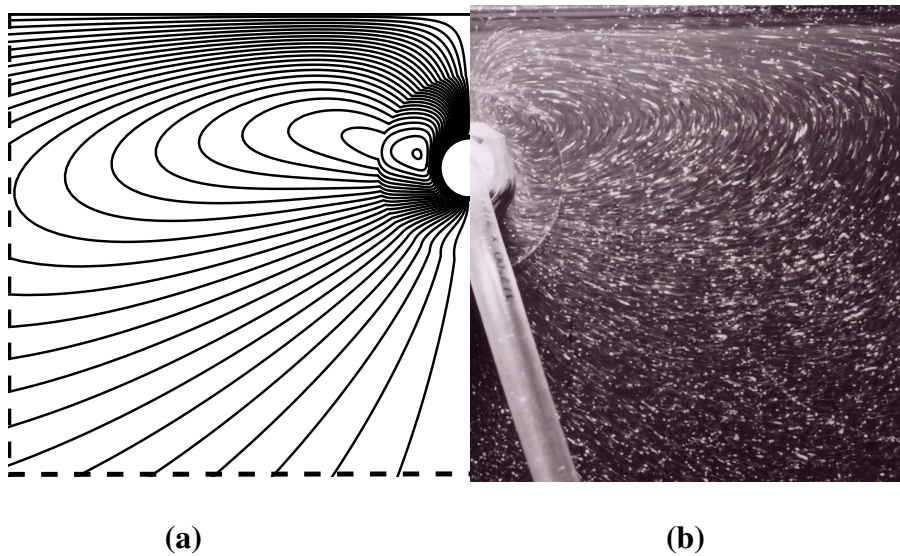
Figure 6.13 Comparison of convective flow fields of Hele-Shaw cell A between (a) numerical result at $Ra_1 = 189$ and $K_1/K_2 = 9$ ($\Delta\Psi = 0.5$), and (b) experimental result observed at a pipe temperature of 95 $^{\circ}$C.

(a)   **(b)**
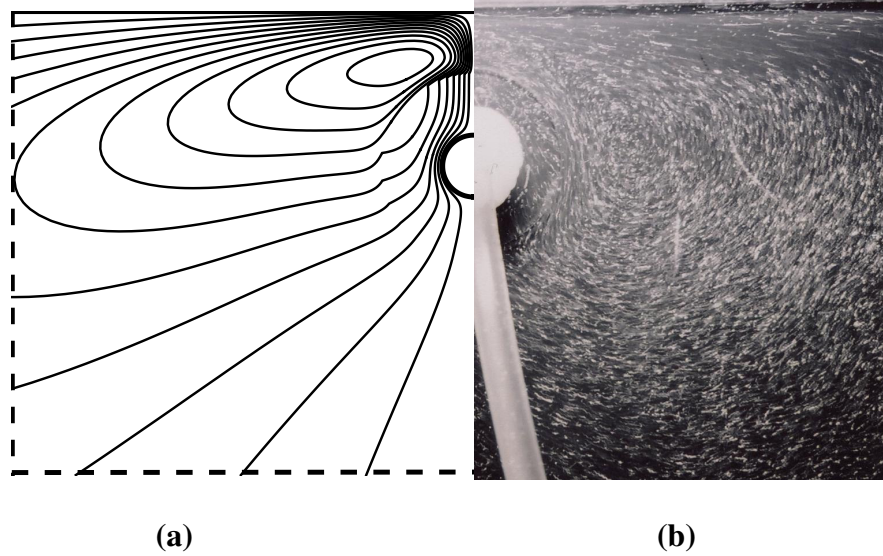
Figure 6.14 Comparison of convective flow fields of Hele-Shaw cell B between (a) numerical result at $Ra_1 = 13$ and $K_1/K_2 = 0.11$ ($\Delta\Psi = 1$), and (b) experimental result observed at a pipe temperature of 70 $^{\circ}$C.

(a)   **(b)**
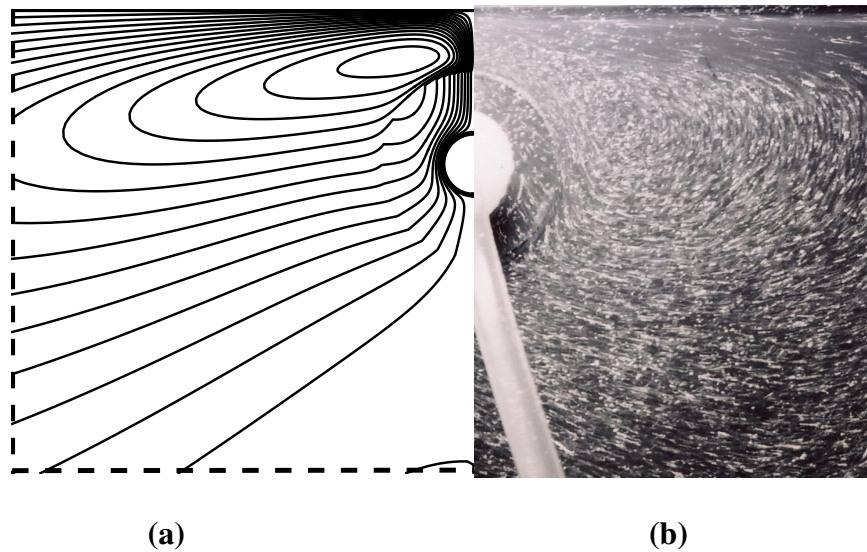
Figure 6.15 Comparison of convective flow fields of Hele-Shaw cell B between (a) numerical result at $Ra_1 = 21$ and $K_1/K_2 = 0.11$ ($\Delta\Psi = 1$), and (b) experimental result observed at a pipe temperature of 95 $^{\circ}$C.

particles shown here may not depict the actual velocity of the particles due solely to buoyancy effect.

6.8 Concluding Remarks

Hele-Shaw cells with various gap widths were constructed to simulate porous media with distinct permeabilities. Visualization experiments were conducted for both permeable and impermeable top boundary subjected to various pipe temperatures. The Hele-Shaw flow patterns formed by tracing particles were captured successfully using time-elapsed photography.

The flow field observed for the permeable top boundary has distinct characteristics and is different from that with impermeable top boundary. Interaction between the fluid layer on top of the permeable boundary and the simulated porous region constitutes a vital part of the convective flow. This can be seen evidently through the formation of the circulating cells in the fluid layer on top of the cell. The numerical work presented for the cases with an impermeable top boundary compares well with the visualized flow field. The presence of a recirculating cell in the more permeable layer is predicted, and the flow patterns based on the numerical study closely resemble the actual flow field.

CHAPTER **VII**

CONCLUSIONS AND FUTURE WORK

7.1 Introductory Remarks

Heat and mass transfer from a buried pipe has been a subject of great interest. Its engineering applications include the underground pipelines for gas and oil, power cables and the disposal of nuclear wastes. For these applications, the temperature of pipe or canister is usually higher than that of surroundings due to artificial (reduction of viscosity for oil transportation) or natural (ohm heating from transmission cables and decay heating from nuclear wastes) causes. Heat conduction and natural convection induced from a heated pipe buried in a homogeneous porous medium has been examined in Chapter 3.

However in reality, the soil structure near the buried site is usually modified from its original state in the excavation process or in the mining process for a nuclear waste repository. Backfill is also often added to the buried pipes and waste canisters. Thus, the soil or bed rock that hosts the pipes and waste canisters are heterogeneous in nature. The effects of permeability variation in the porous medium on the heat transfer results have been investigated in Chapter 4.

Another application of interest is in the event of a leak developed from the pipeline. The prediction of the spreading patterns of the crude oil from the accident site to its surroundings is essential for environmental protection. Also closely related to this study is the usage of waste heat for soil heating and providing subsurface irrigation by letting water seep through the pipe. Chapter 5 investigates the coupled

heat and mass transfer by mixed convection induced by a leakage from a pipe buried in a porous medium.

The Hele-Shaw analogy is adopted in Chapter 6 to model flow in a heterogeneous porous medium by constructing Hele-Shaw cells with various gap widths. Using time-elapsed photography with the aid of tracing particles, the flow patterns can be revealed. The objective of this experimental work is to lend support to the numerical work presented in Chapter 4.

7.2 Summary of Results

The numerical solutions obtained for conduction and natural convection in the present study are in excellent agreement with the previous analytical work. The conductive heat transfer for an isothermal top surface is determined to be 1.43, which is within 5% of the analytical solution provided by Eckert and Drake (1959). As for the study of natural convection, Nusselt number is found to be a function of the square root of the Rayleigh number, which also compares well with the perturbation solutions provided by Himasekhar and Bao (1987) for small Rayleigh numbers.

7.2.1 Effects of Backfill on Heat Transfer from a Buried Pipe

Chapter 4 addresses some critical aspects in engineering applications related to energy utilization and environmental protection. The numerical results suggest that the heat loss can be minimized by having a layer of backfill or excavation disturbed zone that is more permeable than the hosting soil ($K_1/K_2 > 1$). This is the best scenario for the transportation of crude oil. In fact, this is also the most desirable

condition for environmental protection since the contamination will be confined

mostly in the backfill layer in the event that a leak should develop from a pipeline or

a nuclear waste canister. On the other hand, a backfill with $K_1/K_2 < 1$ may be

preferred if overheating of transmission lines or power cables is to be avoided.

7.2.2 Double-Diffusive Mixed Convection Induced by Leakage

Numerical study on double-diffusive mixed convection from a buried pipe

with leakage has been performed in Chapter 5. The effects of governing parameters

such as the buoyancy ratio, Lewis number, Peclet number and leakage location on the

heat and mass transfer results are examined. The results suggest that Nusselt and

Sherwood numbers increase for aiding flows, but decrease for opposing flows. It is

also found that Sherwood number increases when the leakage is on top of the buried

pipe while Nusselt number increases when the leakage is at the bottom of the pipe.

Both Lewis number and Peclet number have a more dominant effect on the mass

transfer than heat transfer. For aiding flows, Nusselt number increases but Sherwood

number decreases for Le < 1 while the trend is reversed for Le > 1. Sherwood

number increases with the Peclet number for aiding flows with Le $\geq$ 1. On the other

hand, the variations of Nusselt number with Peclet number are more obvious for Le $\leq$

1.

7.2.3 Hele-Shaw Flow Visualization Experiment

Flow visualization experiments were conducted using two Hele-Shaw cells

with different gap widths, which simulated a porous medium with a backfill layer of

different permeability. Both permeable and impermeable top boundaries subjected to different pipe temperatures were considered in the experiment. The flow patterns formed by tracing particles were revealed through time-elapsed photography. The numerical results for the impermeable top boundary presented in Chapter 4 compared well with the visualized flow fields from experiments. The presence of the recirculating cell in the more permeable layer was confirmed, and the flow patterns closely resembled the actual flow field.

7.3 Recommended Future Work

Although the present study has addressed some fundamental problems related to buoyancy transport in porous media near a buried pipe, additional work is needed for the advancement of knowledge in this field. With the success from the visualization experiment, one notices that the flow patterns for the permeable top boundary were quite different from those of an impermeable top boundary. Hence, the next logical step is to develop a numerical model and compare the computational results to the observed flow fields. In fact, for many applications in geophysics and porous insulation, a fluid layer is often found to superimpose on a porous layer. Let's consider a simpler problem in which the porous medium is homogeneous instead of heterogeneous, as shown in Figure 7.1. The problem of interest is to determine the extent that heat generated from the buried pipe will affect the superimposed fluid layer.

The governing equations for the fluid layer are based on Navier-Stokes equations, and they are expressed in terms of the stream functions and vorticity (Ω)
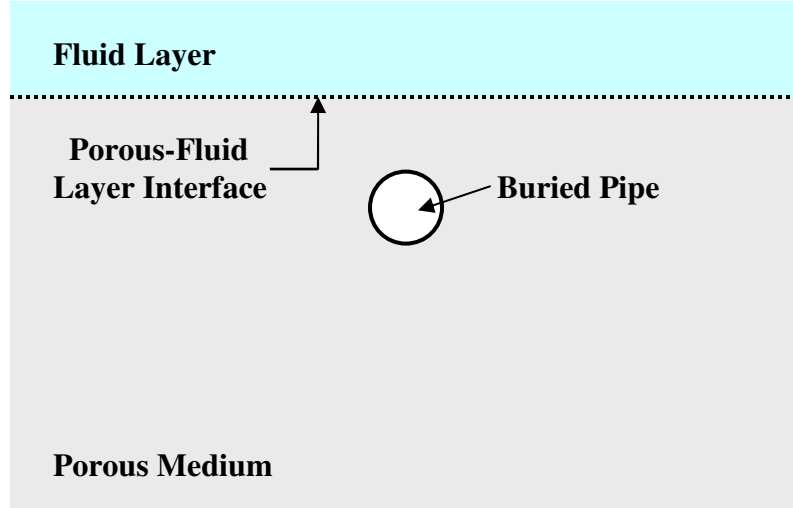
Figure 7.1 Superimposed fluid and porous layers with a buried horizontal pipe.

in the computational domain as follows

$$\nabla^2_{\xi\eta} \Psi_f = -\Omega_f \quad, \tag{7.1}$$

$$\nabla^2_{\xi\eta} \Omega_f = -\frac{Ra}{J}\left[\frac{\partial \Theta_f}{\partial \xi}\frac{\partial Y}{\partial \eta} - \frac{\partial \Theta_f}{\partial \eta}\frac{\partial Y}{\partial \xi}\right] + \frac{1}{J\cdot Pr}\left[\frac{\partial \Omega_f}{\partial \xi}\frac{\partial \Psi_f}{\partial \eta} - \frac{\partial \Omega_f}{\partial \eta}\frac{\partial \Psi_f}{\partial \xi}\right] \quad, \tag{7.2}$$

$$\nabla^2_{\xi\eta} \Theta_f = \frac{1}{J}\left[\frac{\partial \Theta_f}{\partial \xi}\frac{\partial \Psi_f}{\partial \eta} - \frac{\partial \Theta_f}{\partial \eta}\frac{\partial \Psi_f}{\partial \xi}\right] \quad, \tag{7.3}$$

where $\quad \nabla^2_{\xi\eta} = \dfrac{\overline{\alpha}}{J^2}\dfrac{\partial^2}{\partial \xi^2} - \dfrac{2\overline{\beta}}{J^2}\dfrac{\partial^2}{\partial \xi \partial \eta} + \dfrac{\overline{\gamma}}{J^2}\dfrac{\partial^2}{\partial \eta^2} + \overline{P}\dfrac{\partial}{\partial \xi} + \overline{Q}\dfrac{\partial}{\partial \eta}.$ $\tag{7.4}$

and the subscript "f" indicates fluid layer. The Prandtl number and Rayleigh number

are defined as

$$Pr = \frac{\nu}{\alpha_f} \quad, \qquad \text{and} \qquad Ra = \frac{g\beta_T(T_h - T_c)r_i^3}{\alpha_f \nu} \quad . \tag{7.5a, b}$$

For the porous layer, the governing equations are based on Darcy-Extended Brinkman model (Oosthuizen and Naylor, 1996), and they are expressed in the computational domain as follows

$$\nabla_{\xi\eta}^2 \Psi_{pm} = -\Omega_{pm} \quad , \tag{7.6}$$

$$\nabla_{\xi\eta}^2 \Omega_{pm} = -\frac{Ra}{J}\left[\frac{\partial\Theta_{pm}}{\partial\xi}\frac{\partial Y}{\partial\eta} - \frac{\partial\Theta_{pm}}{\partial\eta}\frac{\partial Y}{\partial\xi}\right] + \frac{\Omega_{pm}}{Da} + \frac{1}{J\cdot Pr}\left[\frac{\partial\Omega_{pm}}{\partial\xi}\frac{\partial\Psi_{pm}}{\partial\eta} - \frac{\partial\Omega_{pm}}{\partial\eta}\frac{\partial\Psi_{pm}}{\partial\xi}\right] ,$$

$$\tag{7.7}$$

$$\nabla_{\xi\eta}^2 \Theta_{pm} = \frac{\alpha_f}{\alpha_{pm}}\frac{1}{J}\left[\frac{\partial\Theta_{pm}}{\partial\xi}\frac{\partial\Psi_{pm}}{\partial\eta} - \frac{\partial\Theta_{pm}}{\partial\eta}\frac{\partial\Psi_{pm}}{\partial\xi}\right] , \tag{7.8}$$

where the Darcy number is defined by $Da = K/r_i^2$, and the subscript "pm" indicates porous medium layer. It is noted that when the porous layer is saturated with the same fluid as the fluid layer, the ratio α_f/α_{pm} reduces to k_f/k_{pm}. With minimum modification, the numerical techniques described in Chapter 2 can be applied here to obtain the discretize equations.

The appropriate conditions need to be specified at the interface between the porous and fluid layers are the continuity of temperature, heat flux, normal and tangential velocity, shear stress and pressure:

$$\Theta_f = \Theta_{pm} , \tag{7.9a}$$

$$\frac{\partial\Theta_f}{\partial Y} = \frac{k_{pm}}{k_f}\frac{\partial\Theta_{pm}}{\partial Y} , \tag{7.9b}$$

$$\frac{\partial\Psi_f}{\partial Y} = \frac{\partial\Psi_{pm}}{\partial Y} , \tag{7.9c}$$

$$\Psi_f = \Psi_{pm} , \tag{7.9d}$$

$$\Omega_f = \Omega_{pm} \, , \tag{7.9e}$$

$$\frac{\partial \Omega_f}{\partial Y} = \frac{\partial \Omega_{pm}}{\partial Y} + \frac{1}{Da} \frac{\partial \Psi_{pm}}{\partial Y} \quad . \tag{7.9f}$$

The concept of the imaginary nodal point presented in Chapter 4 will be needed to implement the interface conditions. However, a more complicated derivation is expected. With the completion of this new study, one should be able to compare the numerical results with the flow patterns observed in the present study.

REFERENCES

Alazmi, B. and Vafai, K., "Analysis of Variants within the Porous Media Transport Models," *Journal of Heat Transfer*, Vol. 122, pp. 303-326, 2000.

Alazmi, B. and Vafai, K., "Analysis of Fluid Flow and Heat Transfer Interfacial Conditions between a Porous Medium and a Fluid Layer," *International Journal of Heat and Mass Transfer*, Vol. 44, pp. 1735-1749, 2001.

Badr, H. M. and Pop, I., "Combined Convection from an Isothermal Horizontal Rod Buried in a Porous Medium," *International Journal of Heat and Mass Transfer*, Vol. 31, pp. 2527-2541, 1988.

Baker, D. J., "A Technique for the Precise Measurement of Small Fluid Velocities," *Journal of Fluid Mechanics*, Vol. 26, pp. 573-575, 1966.

Bau, H. H., "Convective Heat Losses from a Pipe Buried in a Semi-Infinite Porous Medium," *International Journal of Heat and Mass Transfer*, Vol. 27, pp. 2047-2056, 1984.

Bau, H. H. and Sadhal, S. S., "Heat Losses from a Fluid Flowing in a Buried Pipe," *International Journal of Heat and Mass Transfer*, Vol. 25, pp. 1621-1629, 1982.

Bear, J., *Dynamics of Fluids in Porous Media*, Dover Publications, New York, 1972.

Bear, J. and Bachmat, Y., *Introduction to Modeling of Transport Phenomena in Porous Media*, Kluwer Academic Publishers, Dordrecht, 1990.

Bear, J. and Verruijt, A., *Modeling Groundwater Flow and Pollution*, D. Reidel Publishing, Dordrecht, 1987.

Beavers, G. S. and Joseph, D. D., "Boundary Conditions at a Naturally Permeable Wall," *Journal of Fluid Mechanics*, Vol. 30, pp. 197-207, 1967.

Beavers, G. S., Sparrow, E. M. and Magnuson, R. A., "Experiments on Coupled Parallel Flows in a Channel and a Bounding Medium," *Journal of Basic Engineering*, Vol. 92, pp. 843-848, 1970.

Beavers, G. S., Sparrow, E. M. and Masha, B. A., "Boundary Conditions at a Porous Surface which Bounds a Fluid Flow," *AIChe Journal*, Vol. 20, pp. 596-597, 1974.

Beckermann, C., Ramadhyani, S. and Viskanta, R., "Natural Convection Flow and Heat Transfer between a Fluid Layer and a Porous Layer inside a Rectangular Enclosure," *Journal of Heat Transfer*, Vol. 109, pp. 363-370, 1987.

References

Bejan, A., "Natural Convection in an Infinite Porous Medium with a Concentrated Heat Source," *Journal of Fluid Mechanics*, Vol. 89, pp. 97-107, 1978.

Bejan, A., Dincer, I., Lorente, S., Miguel, A. F., and Reis A. H., *Porous and Complex Flow Structures in Modern Technologies*, Springer, New York, 2004.

Bird, R. B., Stewart, W. E. and Lightfoot, E. N., *Transport Phenomena*, Wiley, New York, 1960.

Bishop, W. P. and Hollister, C. D., "Sea-bed Disposal-Where to Look," *Nuclear Technology*, Vol. 24, pp. 425-443, 1974.

Boberg, T. C., *Thermal Methods of Oil Recovery*, John Wiley & Sons, New York, 1988.

Bradean, R., Ingham, D. B., Heggs, P. J. and Pop, I., "Unsteady Free Convection Adjacent to an Impulsively Heated Horizontal Circular Cylinder in Porous Media," *Numerical Heat Transfer, Part A*, Vol. 31, pp. 325-346, 1997.

Bradean, R., Ingham, D. B., Heggs, P. J. and Pop, I., "Mixed Convection Adjacent to a Suddenly Heated Horizontal Circular Cylinder Embedded in a Porous Medium," *Transport in Porous Media*, Vol. 32, pp. 329-355, 1998.

Brown, S. N. and Simpson, C. J., "Collision Phenomena in Free-Convection Flow over a Sphere," *Journal of Fluid Mechanics*, Vol. 124, pp. 123-137, 1982.

Carslaw, H. S. and Jaeger, J. C., *Conduction of Heat in Solids*, 2nd ed., Oxford University Press, London, 1959.

Chamkha, A. and Quadri, M. M., "Heat and Mass Transfer from a Permeable Cylinder in a Porous Medium with Magnetic Field and Heat Generation/Absorption Effects," *Numerical Heat Transfer Part A: Applications*, Vol. 40, pp. 387-401, 2001.

Chang, W. J. and Weng, C. I, "Heat and Mass Transfer in Porous Material," in *Transport Phenomena in Porous Media II*, D. B. Ingham and I. Pop (Eds.), Pergamon, Oxford, 2002.

Chapra, S. C. and Canale, R. P., *Numerical Methods for Engineers*, 4th ed., McGraw-Hill, New York, 2002.

Chen, C. K. and Hsiao, S. W., "Transport Phenomena in Enclosed Porous Cavities, in *Transport Phenomena in Porous Media*, D. B. Ingham and I. Pop (Eds.), Pergamon, Oxford, 1998.

Chen, F. and Chen C. F., "Onset of Finger Convection in a Horizontal Porous Layer Underlying a Fluid Layer," *Journal of Heat Transfer*, Vol. 110, pp. 403-409, 1988.

Chen, F. and Chen C. F., "Experimental Investigation of Convective Stability in a Superposed Fluid and Porous Layer when Heated from Below," *Journal of Fluid Mechanics*, Vol. 207, pp. 311-321, 1989.

Chen, F. and Chen C. F., "Convection in Superposed Fluid and Porous Layers," *Journal of Fluid Mechanics*, Vol. 234, pp. 97-119, 1992.

Cheng, E. *Experimental Visualization and Analytical Study of Convective Flow Around a Buried Heated Pipe*, Master Thesis, University of Oklahoma, 1996.

Cheng, E. S. and Lai, F. C., "Heat and Mass Transfer from a Buried Pipe," 32nd Thermophysics Conference, Atlanta, GA, AIAA Paper 97-2517, 1997.

Cheng, P., "Combined Free and Forced Boundary Layer Flows about Inclined Surfaces in a Porous Medium," *International Journal of Heat and Mass Transfer*, Vol. 20, pp. 807-814, 1977.

Cheng, P., "Heat Transfer in Geothermal Systems," *Advances in Heat Transfer*, Vol. 14, pp. 1-105, 1978.

Cheng, P., ME 627 Class Notes, University of Hawaii, 1980.

Cheng, P., "Mixed Convection about a Horizontal Cylinder and a Sphere in a Fluid Saturated Porous Medium," *International Journal of Heat and Mass Transfer*, Vol. 25, pp. 1245-1247, 1982.

Cheng, P. and Minkowycz, W. J., "Free Convection about a Vertical Flat Plate Embedded in a Saturated Porous Medium with Application to Heat Transfer from a Dike," *Journal of Geophysics Research*, Vol. 82, pp. 2040-2044, 1977.

Cho, S. K., Moon, H., and Kim, C.-J., "Creating, Transporting, Cutting, and Merging Liquid Droplets by Electrowetting-Based Actuation for Digital Microfluidic Circuits," *Journal of Microelectromechanical Systems*, Vol. 12, pp. 70-80, 2003.

Choi, C. Y. and Waller, P. M., "Momentum Transport Mechanism for Water Flow over Porous Media," *Journal of Environmental Engineering*, Vol. 123, pp. 792-799, 1997.

Chouke, R. L., van Meurs, P., and van der Poel, C., "The Instability of Slow, Immiscible, Viscous Liquid-Liquid Displacements in Permeable Media," *American Institute of Mining Engineers Transactions*, Vol. 216, pp. 188-194, 1959.

References

Christopher, D. M. and Wang, B.-X., "Non-Darcy Natural Convection around a Horizontal Cylinder Buried Near the Surface of a Fluid-Saturated Porous Medium," *International Journal of Heat and Mass Transfer*, Vol. 36, pp. 3663-3669, 1993.

Collins, R. E., *Flow of Fluids through Porous Materials*, 2nd Reprint, Research & Engineering Consultants, 1990.

Coulter, J. P. and Güceri, S. I., "Laminar and Turbulent Natural Convection in Irregularly Shaped Enclosures," *Center for Composite Materials Report*, University of Delaware, 1985.

Darcy, H. P. G., *Les Fontaines Publiques de la Ville de Dijon*. Victor Dalmont, Paris 1856.

Dhir, V. K., "Remediation of Soils Contaminated with Hydrocarbons," in *Handbook of Porous Media*, K. Vafai (Ed.), Chapter 18, Marcel Dekker, New York, 2000.

Donaldson, I. G., "Temperature Gradient in the Upper Layers of the Earth's Crust Due to Convective Water Flows," *Journal of Geophysical Research*, Vol. 67, pp. 3449-3459, 1962.

Dullien, F. A. L., *Porous Media: Fluid Transport and Pore Structure*, 2nd ed., Academic Press, New York, 1992.

Eckert, E. R. G. and Drake, R. M., *Heat and Mass Transfer*, McGraw-Hill, New York, 1959.

Edwards, L. M., Chilingar, G. V., Rieke III, H. H., and Ferte, W. H. (Eds.), *Handbook of Geothermal Energy*, Gulf Publishing, Houston, 1982.

Ehrenman, G., "Not a Drop to Drink," *Mechanical Engineering*, Vol. 125, pp. 46-49, 2003.

Fand, R. M. and Keswani, K. K., "Combined Natural and Forced Convection Heat Transfer from Horizontal Cylinders to Water," *International Journal of Heat and Mass Transfer*, Vol. 16, pp. 1175-1191, 1973.

Fand, R. M. and Phan, R. T., "Combined Forced and Natural Convection Heat Transfer from a Horizontal Cylinder Embedded in a Porous Medium," *International Journal of Heat and Mass Transfer*, Vol. 30, pp. 1351-1358, 1987.

Fand, R. M., Steinberger, T. E. and Cheng, P., "Natural Convection Heat Transfer from a Horizontal Cylinder Embedded in a Porous Medium," *International Journal of Heat and Mass Transfer*, Vol. 29, pp. 119-133, 1986.

References

Farouk, B. and Shayer, H., "Natural Convection around a Heated Cylinder in a Saturated Porous Medium," *Journal of Heat Transfer*, Vol. 110, pp. 642-648, 1988.

Fernandez, R. T. and Schrock, V. E., "Natural Convection from Cylinders Buried in a Liquid-Saturated Porous Medium," *Proceedings of the International Heat Transfer Conference*, Munich, Vol. 2, pp. 335-340, 1982.

Fritton, D. D. and Martsolf, J. D., "Soil Heat Flow under an Orchard Heater," *Soil Science Society of America Journal*, Vol. 44, pp. 13-16, 1980.

Fung, Y. C., *Biodynamics: Circulation*, Springer-Verlag, New York, 1984.

Galin, L. A., "Unsteady Filtration with a Free Surface," *Doklady Akademii Nauk SSSR*, Vol. 47, pp. 246-249, 1945. (in Russian)

Ganapathy, R., "Free Convective Heat and Mass Transfer Flow Induced by an Instantaneous Point Source in an Infinite Porous Medium," *Fluid Dynamics Research*, Vol. 14, pp. 313-329, 1994.

Gartling, D. K. and Hickox, C. E., "MARIAH – A Finite Element Computer Program for Incompressible Porous Flow Problem," SAND79-1623, Sandia National Laboratories, Albuquerque, New Mexico, 1980.

Gebhart, B., Jaluria, Y., Mahajan, R. L. and Sammakia, B., *Buoyancy-Induced Flows and Transport*, Hemisphere Publishing, New York, 1988.

Gilver, R. C. and Altobelli, S. A., "A Determination of the Effective Viscosity for the Brinkman-Forchheimer Flow Model," *Journal of Fluid Mechanics*, Vol. 258, pp. 355-370, 1994.

Hartline, B. K., and Lister, C. R. B., "Thermal Convection in a Hele-Shaw Cell," *Journal of Fluid Mechanics*, Vol. 79, pp. 379-389, 1977.

Hele-Shaw, H. S., "The Flow of Water," *Nature*, Vol. 58, pp. 33-36, 1898a.

Hele-Shaw, H. S., ""Investigation of the Nature of the Surface Resistance of Water and of Streamline Motion under Certain Experimental Conditions," *Transactions of the Royal Institution of Naval Architects,* London, Vol. 40, pp. 218-221, 1898b.

Hickox, C. E., "Thermal Convection at Low Rayleigh Number from Concentrated Sources in Porous Media," *Journal of Heat Transfer*, Vol. 103, pp. 232-236, 1981.

Hickox, C. E. and Watts, H. A., "Steady Thermal Convection from a Concentrated Source in a Porous Medium," *Journal of Heat Transfer*, Vol. 102, pp. 248-253, 1980.

References

Hill, S., "Channeling in Packed Columns," *Chemical Engineering Science*, Vol. 19, pp. 247-253, 1952.

Hillel, D., *Introduction to Soil Physics*, Academic Press, Orlando, 1982.

Himasekhar, K. and Bau, H. H., "Thermal Convection Associated with Hot/Cold Pipes Buried in a Semi-Infinite, Saturated, Porous Medium," *International Journal of Heat Transfer*, Vol. 30, pp. 263-273, 1987.

Himasekhar, K. and Bau, H. H., "Thermal Convection around a Heat Source Embedded in a Box Containing a Saturated Porous Medium," *Journal of Heat Transfer*, Vol. 110, pp. 649-654, 1988.

Holzbecher, E., *Modeling Density-Driven Flow in Porous Media*, Springer-Verlag, Berlin, 1998.

Homsy, G. M., "Viscous Fingering in Porous Media," *Annual Review of Fluid Mechanics*, Vol. 19, pp. 271-311, 1987.

Horne, R. N., and O'Sullivan, M. J., "Oscillatory Convection in a Porous Medium Heated from Below," *Journal of Fluid Mechanics*, Vol. 66, pp. 339-352, 1974.

Howison, S. D., "Fingering in Hele-Shaw Cells," *Journal of Fluid Mechanics*, Vol. 167, pp. 439-453, 1986.

Hsiao, S.-W., Cheng, P. and Chen, C.-K., "Non-Uniform Porosity and Thermal Dispersion Effects on Natural Convection about a Heated Horizontal Cylinder in an Enclosed Porous Medium," *International Journal of Heat and Mass Transfer*, Vol. 35, pp. 3407-3418, 1992.

Hsu, C. T. and Cheng, P., "Thermal Dispersion in a Porous Medium," *International Journal of Heat and Mass Transfer*, Vol. 33, pp. 1587-1597, 1990.

Huang, M. J., Yih, K. A., Chou, Y. L., and Chen, C. K., "Mixed Convection Flow over a Horizontal Cylinder or a Sphere Embedded in a Saturated Porous Medium," *Journal of Heat Transfer*, Vol. 108, pp. 469-471, 1986.

Incropera, F. P. and DeWitt, D. P., *Introduction to Heat Transfer*, 3rd ed., John Wiley & Sons, New York, 1996.

Ingham, D. B., Merkin, J. H., and Pop, I., "The Collision of Free Convection Boundary Layers on a Horizontal Cylinder Embedded in a Porous Medium," *Quarterly Journal of Mechanics and Applied Mathematics*, Vol. 36, pp. 313-335, 1983.

Ingham, D. B. and Pop, I., "Natural Convection about a Heated Horizontal Cylinder in a Porous Medium," *Journal of Fluid Mechanics*, Vol. 184, pp. 157-181, 1987.

Ingham, D. B. and Pop, I. (Eds.), *Transport Phenomena in Porous Media*, Pergamon, Oxford, 1998.

Ingham, D. B. and Pop, I. (Eds.), *Transport Phenomena in Porous Media II*, Pergamon, Oxford, 2002.

James, D. F. and Davis, A. M. J., "Flow at the Interface of a Model Fibrous Porous Medium," *Journal of Fluid Mechanics*, Vol. 426, pp. 47-72, 2001.

The Japan Society of Mechanical Engineers (Ed.), *Visualized Flow: Fluid Motion in Basic and Engineering Situations Revealed by Flow Visualization*, Pergamon Press, Oxford, 1988.

Kaviany, M., *Principles of Heat Transfer in Porous Media*, 2nd ed., Springer-Verlag, New York, 1995.

Khonsari, M. M. and Booser, E. R., *Applied Tribology: Bearing Design and Lubrication*, John Wiley & Sons, New York, 2001.

Knox, R. C., Sabatini, D. A. and Canter, L. W., *Subsurface Transport and Fate Processes*, Lewis Publishers, Boca Raton, 1993.

Knupp, P., and Steinberg, S., *Fundamentals of Grid Generation*, CRC Press, Boca Raton, 1993.

Kolodziej, J. A., "Influence of the Porosity of a Porous Medium on the Effective Viscosity in Brinkman's Filtration Equation," *Acta Mechanica*, Vol. 75, pp. 241-254, 1988.

Koo, M.-H., and Leap, D. I., "Modeling Three-Dimensional Groundwater Flows by the Body-Fitted Coordinate (BFC) Method: II. Free and Moving Boundary Problems," *Transport in Porous Media*, Vol. 30, pp. 345-362, 1998.

Koster, J. N., "Heat Transfer in Vertical Gaps," *International Journal of Heat and Mass Transfer*, Vol. 25, pp. 426-428, 1982.

Koster, J. N., "Time Dependent Heat Transfer in Hele-Shaw Slots," *International Communications in Heat and Mass Transfer*, Vol. 12, pp. 159-167, 1985.

Koster, J. N., and Müller, U., "Free Convection in Vertical Gaps," *Journal of Fluid Mechanics*, Vol. 125, pp. 429-451, 1982.

Koster, J. N., and Müller, U., "Oscillatory Convection in Vertical Slots," *Journal of Fluid Mechanics*, Vol. 139, pp. 363-390, 1984.

Kuznetsov, A. V., "Influence of the Stress Jump Condition at the Porous-Medium/Clear Fluid Interface on a Flow at a Porous Wall," *International Communications in Heat and Mass Transfer*, Vol. 24, pp. 401-410, 1997.

Lage, J. L., "The Fundamental Theory of Flow through Permeable Media from Darcy to Turbulence," in *Transport Phenomena in Porous Media*, D. B. Ingham and I. Pop (Eds.), Pergamon, Oxford, 1998.

Lai, F. C., *Free and Mixed Convection in Porous Media*, Ph. D. Dissertation, University of Delaware, 1988.

Lai, F. C., Natural Convection from a Concentrated Heat Source in a Saturated Porous Medium," *International Communications in Heat and Mass Transfer*, Vol. 17, pp. 791-800, 1990.

Lai, F. C., "Mixed Convection in Porous Media," in *Handbook of Porous Media*, K. Vafai (Ed.), Chapter 14, Marcel Dekker, New York, 2000.

Leong, J. C., *Heat Transfer and Fluid Flow in Rotating Cylinders with a Porous Sleeve*, Ph. D. Dissertation, University of Oklahoma, 2002.

Lew, H. S. and Fung, Y. C., "Formulation of s Statistical Equation of Motion of a Viscous Fluid in an Anisotropic Non-Rigid Porous Solid," *International Journal of Solids Structures*, Vol. 6, pp. 1323-1340, 1970.

Lorenz, C., and Zahn, M., "Hele-Shaw Ferrohydrodynamics for Rotating and dc Axial Magnetic Fields," *Physics of Fluids: Gallery of Fluid Motion*, Vol. 15, pp. S4, 2003.

Lu, H.-W., Glasner, K., Bertozzi, A. L., and Kim, C.-J., "A Diffuse Interface Model for Electrowetting Droplets in a Hele-Shaw Cell," *Journal of Fluid Mechanics*, in press.

Lundgren, T. S., "Slow Flow through Stationary Random Beds and Suspension of Spheres," *Journal of Fluid Mechanics*, Vol. 51, pp. 273-299, 1972.

Mamou, M., "Stability Analysis of Double-Diffusive Convection in Porous Enclosures," in *Transport Phenomena in Porous Media II*, D. B. Ingham and I. Pop (Eds.), Pergamon, Oxford, 2002.

Mastin, C. W., and Thompson, J. F., "Elliptic Systems and Numerical Transformations," *Journal of Mathematical Analysis and Applications*, Vol. 62, pp. 52-62, 1978.

McKibbin, R., "Mathematical Models for Heat and Mass Transport in Geothermal Systems," in *Transport Phenomena in Porous Media*, D. B. Ingham and I. Pop (Eds.), Elsevier Science, Oxford, 1998.

McKibbin, R., and O'Sullivan, M. J., "Onset of Convection in a Layered Porous Medium Heated from Below," *Journal of Fluid Mechanics*, Vol. 96, pp. 375-393, 1980.

McKibbin, R., and O'Sullivan, M. J., "Heat Transfer in a Layered Porous Medium Heated from Below," *Journal of Fluid Mechanics*, Vol. 111, pp. 141-173, 1981.

Merkin, J. H., "Free Convection Boundary Layers on Axisymmetric and Two-Dimensional Bodies of Arbitrary Shape in a Saturated Porous Medium," *International Journal of Heat and Mass Transfer*, Vol. 22, pp. 1461-1462, 1979.

Mills, A. F., *Basic Heat and Mass Transfer*, 2nd ed., Prentice Hall, New Jersey, 1999.

Minkowycz, W. J., Cheng, P., and Chang, C. H., "Mixed Convection about a Non-Isothermal Cylinder and Sphere in a Porous Medium," *Numerical Heat Transfer*, Vol. 8, pp. 349-359, 1985.

Mojtabi, A. and Charrier-Mojtabi, M.-C., "Double-Diffusive Convection in Porous Media," in *Handbook of Porous Media*, K. Vafai (Ed.), Chapter 13, Marcel Dekker, New York, 2000.

Muralidhar, K., Baunchalk, R. A., and Kulacki, F. A., "Natural Convection in a Horizontal Porous Annulus with a Step Distribution in Permeability," *Journal of Heat Transfer*, Vol. 108, pp. 889-893, 1986.

Nakayama, A. and Ashizawa, T., "A Boundary Layer Analysis of Combined Heat and Mass Transfer by Natural Convection from a Concentrated Source in a Saturated Porous Medium," *Applied Scientific Research*, Vol. 56, pp. 1-11, 1996.

Nakayama, A. and Koyama, H., "Free Convection Heat Transfer over a Nonisothermal Body of Arbitrary Shape Embedded in a Fluid-Saturated Porous Medium," *Journal of Heat Transfer*, Vol. 109, pp. 125-130, 1987.

Neale, G. and Nader, W., "Practical Significant of Brinkman's Extension of Darcy's Law: Coupled Parallel Flows within a Channel and a Bounding Porous Medium," *Canadian Journal of Chemical Engineering*, Vol. 52, pp. 475-478, 1974.

References

Neilson, D. G. and Incropera, F. P., "Double-Diffusive Flow and Heat Transfer for a Cylindrical Source Submerged in a Salt-Stratified Solution," *International Journal of Heat and Mass Transfer*, Vol. 30, pp. 2559-2570, 1987.

Nield, D. A., "Onset of Convection in a Fluid Layer Overlying a Layer of a Porous Medium," *Journal of Fluid Mechanics*, Vol. 81, pp. 513-522, 1977.

Nield, D. A., "The Limitations of the Brinkman-Forchheimer Equation in Modeling Flow in a Saturated Porous Medium and at an Interface," *International Journal of Heat and Fluid Flow*, Vol. 12, pp. 269-272, 1991.

Nield, D. A., "Closure Statements on the Brinkman-Forchheimer-Extended Darcy Model," *International Journal of Heat and Fluid Flow*, Vol. 17, pp. 34-35, 1996.

Nield, D. A., "Modeling Fluid Flow in Saturated Porous Media and at Interfaces," in *Transport Phenomena in Porous Media II*, D. B. Ingham and I. Pop (Eds.), Pergamon, Oxford, 2002.

Nield, D. A. and Bejan, A., *Convection in Porous Media*, 2nd ed., Springer-Verlag, New York, 1999.

Ngo, C. C., *Natural Convection in a Layered Porous Annulus*, Master Thesis, University of Oklahoma, 1999.

Ngo, C. C. and Lai, F. C., "Effective Permeability for Natural Convection in a Layered Porous Annulus," *Journal of Thermophysics and Heat Transfer*, Vol. 14, pp. 363-367, 2000.

Ngo, C. C. and Lai, F. C., "Coupled Heat and Mass Transfer by Mixed Convection from a Buried Pipe with Leakage," *Proceedings of the 2003 National Heat Transfer Conference* (CD-ROM), NHTC2003-47285, 2003.

Ngo, C. C. and Lai, F. C., "Effects of Backfill on Heat Transfer from a Buried Pipe," *Journal of Heat Transfer*, Vol. 127, pp. 780-784, 2005.

Ochoa-Tapia, J. A. and Whitaker, S., "Momentum Transfer at the Boundary between a Porous Medium and a Homogeneous Fluid I: Theoretical Development," *International Journal of Heat and Mass Transfer*, Vol. 38, pp. 2635-2646, 1995a.

Ochoa-Tapia, J. A. and Whitaker, S., "Momentum Transfer at the Boundary between a Porous Medium and a Homogeneous Fluid II: Comparison with Experiments," *International Journal of Heat and Mass Transfer*, Vol. 38, pp. 2647-2655, 1995b.

References

Ochoa-Tapia, J. A. and Whitaker, S., "Heat Transfer at the Boundary between a Porous Medium and a Homogeneous Fluid," *International Journal of Heat and Mass Transfer*, Vol. 40, pp. 2691-2707, 1997.

Ockendon, H., and Howison, S. D., "Kochina and Hele-Shaw in Modern Mathematics, Natural Science and Industry," *Journal of Applied Mathematics and Mechanics*, Vol. 66, pp. 505-512, 2002.

Oosthuizen, P. H., "Natural Convective Heat Transfer in Porous-Media-Filled Enclosures," in *Handbook of Porous Media*, K. Vafai (Ed.), Chapter 11, Marcel Dekker, New York, 2000.

Oosthuizen, P. H. and Naylor, D., "Natural Convective Heat Transfer from a Cylinder in an Enclosure Partly Filled with a Porous Medium," *International Journal of Numerical Methods for Heat and Fluid Flow*, Vol. 6, pp. 51-63, 1996.

Pan, C. P., and Lai, F. C., "Re-examination of Natural Convection in a Horizontal Layered Porous Annulus," *Journal of Heat Transfer*, Vol. 118, pp. 990-992, 1996.

Patankar, S. V., *Numerical Heat Transfer and Fluid Flow*, Hemisphere, New York, 1980.

Pennes, H. H., "Analysis of Tissue and Arterial Blood Temperatures in the Resting Human Forearm," *Journal of Applied Physiology*, Vol. 1, pp. 93-122, 1948.

Phillips, O. M. *Flow and Reactions in Permeable Rocks*, Cambridge University Press, Cambridge, 1991.

Polubarinova-Kochina, P. Ya., "On the Displacement of the Oilfield Boundary," *Doklady Akademii Nauk SSSR*, Vol. 47, pp. 254-257, 1945a. (in Russian)

Polubarinova-Kochina, P. Ya., "On Unsteady Motions in the Theory of Filtration," *Prikladnaya Matematika i Mekhanika*, Vol. 9, pp. 76-90, 1945b. (in Russian)

Polubarinova-Kochina, P. Ya., *Theory of Ground Water Movement*, Translated from Russian by J. M., Roger De Wiest, Princeton University Press, New Jersey, 1962.

Pop, I. and Ingham, D. B., *Convective Heat Transfer: Mathematical and Computational Modelling of Viscous Fluids and Porous Media*, Pergamon, Oxford, 2001.

Pop, I., Ingham, D. B. and Bradean, R., "Transient Free Convection about a Horizontal Circular Cylinder in a Porous Medium with Constant Surface Flux Heating," *Acta Mechanica*, Vol. 119, pp. 79-91, 1996.

Pop, I., Ingham, D. B. and Cheng, P., "Transient Free Convection about a Horizontal Circular Cylinder in a Porous Medium," *Fluid Dynamics Research*, Vol. 12, pp. 295-305, 1993.

Poulikakos, D., "On Buoyancy Induced Heat and Mass Transfer from a Concentrated Sources in an Infinite Porous Medium," *International Journal of Heat and Mass Transfer*, Vol. 28, pp. 621-629, 1985.

Poulikakos, D. and Bejan, A., "Natural Convection in Vertically and Horizontally Layered Porous Media Heated from the Side," *International Journal of Heat and Mass Transfer*, Vol. 26, pp. 1805-1814, 1983.

Pozrikidis, C., "The Motion of Particles in the Hele-Shaw Cell," *Journal of Fluid Mechanics*, Vol. 261, pp. 199-222, 1994.

Prandtl, L., "Über Flüssigkeitsbewegung bei sehr Kleiner Reibung," *Proceedings of the 3rd International Mathematical Congress*, Heidelberg, 1904.

Rana, R., Horne, R. N. and Cheng, P., "Natural Convection in a Multilayered Geothermal Reservoir," *Journal of Heat Transfer*, Vol. 101, pp. 411-416, 1979.

Reddi, L. N., *Seepage in Soils: Principles and Applications*, John Wiley & Sons, New Jersey, 2003.

Reddi, L. N. and Inyang, H. I., *Geoenvironmental Engineering – Principles and Applications*, Marcel Dekker, New York, 2000.

Reynolds, O., "An Experimental Investigation of the Circumstances Which Determine Whether the Motion of Water Shall Be Direct or Sinuous, and of the Law of Resistance in Parallel Channels," *Philosophical Transactions of the Royal Society*, Vol. 174, pp. 935-982, 1883.

Richardson, S., "A Model for the Boundary Condition of a Porous Material, Part II," *Journal of Fluid Mechanics*, Vol. 49, pp. 327-336, 1971.

Saffman, P. G., "Viscous Fingering in Hele-Shaw Cells," *Journal of Fluid Mechanics*, Vol. 173, pp. 73-94, 1986.

Saffman, P. G., and Taylor, G., "The Penetration of a Fluid into a Porous Medium or Hele-Shaw Cell Containing a More Viscous Liquid," *Proceedings of the Royal Society of London, Series A*, Vol. 245, pp. 312-329, 1958.

Safonov, S. A., "Mixed Convection around a Circular Cylinder in a Hele-Shaw Cell," *Journal of Applied Mechanics and Technical Physics*, Vol. 32, pp. 356-359, 1991.

Sahraoui, M. and Kaviany, M., "Slip and No-Slip Velocity Boundary Conditions at Interface of Porous, Plain Media," *International Journal of Heat and Mass Transfer*, Vol. 35, pp. 927-943, 1992.

Sahraoui, M. and Kaviany, M., "Slip and No-Slip Temperature Boundary Conditions at the Interface of Porous, Plain Media: Convection," *International Journal of Heat and Mass Transfer*, Vol. 37, pp. 1029-1044, 1994.

Sano, T., "Mixed Convection around a Horizontal Circular Cylinder Immersed in a Darcy Flow," *Journal of Engineering Mathematics*, Vol. 27, pp. 221-232, 1993.

Scheidegger, A. E., *The Physics of Flow through Porous Media*, 3rd ed., University of Toronto Press, Toronto, 1974.

Schlichting, H., *Boundary Layer Theory*, 4th ed., McGraw Hill, New York, 1960.

Schumacher, M. M. (Ed.), *Enhanced Oil Recovery – Secondary and Tertiary Methods*, Noyes Data, New Jersey, 1978.

Scott, M. R. and Watts, H. A., "A Systematic Collection of Codes for Solving Two-Point Boundary Value Problems," in *Numerical Methods for Differential Systems-Recent Developments in Algorithms, Software, and Applications*, L. Lapidus and W. Schiesser (Eds.), Academic Press, New York, 1976.

Scott, M. R. and Watts, H. A., "Computational Solution of Nonlinear Two-Point Boundary Value Problems," SAND77-0091, Sandia Laboratories, Albuquerque, New Mexico, 1977.

Shanks, D., "Non-Linear Transformations of Divergent and Slowly Convergent Sequences," *Journal of Mathematics and Physics*, Vol. 34, pp. 1-42, 1955.

Simpson, C. J. and Stewartson, K., "A Singularity in an Unsteady Free-Convection Boundary Layer," *Quarterly Journal of Mechanics and Applied Mathematics*, Vol. 35, pp. 291-304, 1982.

Slegel, D. L. and Davis, L. R., "Transient Heat and Mass Transfer in Soils in the Vicinity of Heated Porous Pipes," *Journal of Heat Transfer*, Vol. 99, pp. 541-546, 1977.

Smith, L. A. and Hinchee, R. E., *In Situ Thermal Technologies for Site Remediation*, Lewis Publishers, Boca Raton, 1993.

Somerton, C. W. and Catton, I., "On the Thermal Instability of Superposed Porous and Fluid Layers," *Journal of Heat Transfer*, Vol. 104, pp. 160-165, 1982.

References

Stoessell, R. K., "Mass Transport in Sandstones Around Dissolving Plagioclase Grains," *Geology*, Vol. 15, pp. 295-298, 1987.

Strohle, J., Knaus, H., Schnell, U., and Hein, K. R. G., "A Radiation Model for the Numerical Simulation of Coal-Fired Furnaces Using Body-Fitted Grids," *Combustion Science and Technology*, Vol. 153, pp. 127-140, 2000.

Taylor, G. I., "A Model for the Boundary Condition of a Porous Material, Part I," *Journal of Fluid Mechanics*, Vol. 49, pp. 319-326, 1971.

Thompson, J. F. (Ed.), *Numerical Grid Generation*, Elsevier Science Publishing, New York, 1982.

Thompson, J. F., Soni, B. K. and Weatherill, N. P. (Eds.), *Handbook of Grid Generation*, CRC Press, New York, 1999.

Thompson, J. F., Warsi, Z. U. A. and Mastin, C. W., "Boundary-Fitted Coordinates Systems for Numerical Solution of Partial Differential Equations-A Review," *Journal of Computational Physics*, Vol. 47, pp. 1-108, 1982.

Thiyagarajan, R. and Yovanovich, M. M., "Thermal Resistance of a Buried Cylinder with Constant Flux Boundary Condition," *Journal of Heat Transfer*, Vol. 96, pp. 249-250, 1974.

Trevisan, O. V. and Bejan, A., "Combined Heat and Mass Transfer by Natural Convection in a Porous Medium," *Advances in Heat Transfer*, Vol. 20, pp. 315-352, 1990.

Vafai, K. (Ed.), *Handbook of Porous Media*, Marcel Dekker, New York, 2000.

Vafai, K. and Kim, S. J., "Fluid Mechanics of the Interface Region between a Porous Medium and a Fluid Layer-An Exact Solution," *International Journal of Heat and Fluid Flow*, Vol. 11, pp. 254-256, 1990.

Vafai, K. and Kim, S. J., "On the Limitations of the Brinkman-Forchheimer-Extended Darcy Equation," *International Journal of Heat and Fluid Flow*, Vol. 16, pp. 11-15, 1995.

Vafai, K. and Thiyagaraja, R., "Analysis of Flow and Heat Transfer at the Interface Region of a Porous Medium," *International Journal of Heat and Mass Transfer*, Vol. 30, pp. 1391-1405, 1987.

Vafai, K. and Tien, C. L., "Boundary and Inertia Effects on Convective Mass Transfer in Porous Media," *International Journal of Heat and Mass Transfer*, Vol. 25, pp. 1183-1190, 1980.

Vafai, K. and Tien, C. L., "Boundary and Inertia Effects on Flow and Heat Transfer in Porous Media," *International Journal of Heat and Mass Transfer*, Vol. 26, pp. 195-203, 1981.

Vorontsov, S. S., Gorin, A. V., Nakoryakov, V. Ye., Khoruzhenko, A. G., and Chupin, V. M., "Natural Convection in a Hele-Shaw Cell," *International Journal of Heat and Mass Transfer*, Vol. 34, pp. 703-709, 1991.

Wang, C. Y. and Cheng, P., "Multiphase Flow and Heat Transfer in Porous Media," *Advances in Heat Transfer*, Vol. 30, pp. 93-196, 1997.

Whitaker, S., "Coupled Transport in Multiphase Systems: A Theory of Drying," *Advances in Heat Transfer*, Vol. 31, pp. 1-104, 1998.

Withers, B. and Vipond, S., *Irrigation Design and Practice*, 2nd ed., Cornell University Press, New York, 1980.

Wooding, R. A., "Instability of a Viscous Liquid of Variable Density in a Vertical Hele-Shaw Cell," *Journal of Fluid Mechanics*, Vol. 7, pp. 501-515, 1960.

Wooding, R. A., "Convection in a Saturated Porous Medium at Large Rayleigh Number or Peclet Number," *Journal of Fluid Mechanics*, Vol. 15, pp. 527-544, 1963.

Wulff, W., "The Energy Conservation Equation for Living Tissue," *IEEE Transactions on Biomedical Engineering*, Vol. 21, pp. 494-495, 1974.

Yang, W.-J. (Ed.), *Handbook of Flow Visualization*, 2nd ed., Hemisphere Publishing Corporation, New York, 2001.

Yang, W.-J., *Computer-Assisted Flow Visualization: Second Generation Technology*, CRC Press, Boca Raton, 1994.

Yih, C.-S., *Dynamics of Nonhomogeneous Fluids*, MacMillan, New York, 1965.

Yih, K. A., "Coupled Heat and Mass Transfer by Natural Convection Adjacent to a Permeable Horizontal Cylinder in a Saturated Porous Medium," *International Communications in Heat and Mass Transfer*, Vol. 26, pp. 431-440, 1999.

Yong, R. N., Mohamed A. M. O. and Warkentin, B. P., *Principles of Contaminant Transport in Soils*, Elsevier Science Publishers, Amsterdam, 1992.

Yost, B. A., *The Analysis of Fluid Flow/Solidification Problems in Arbitrarily Shaped Domains*, Ph. D. Dissertation, University of Delaware, 1984.

References

Zhou, M. J. and Lai, F. C., "Aiding and Opposing Mixed Convection from a Cylinder in a Saturated Porous Medium," *Journal of Porous Media*, Vol. 5, pp. 103-111, 2002.

APPENDIX: NOMENCLATURE

Bi   Biot number, hr_i/k_{pm}

C   dimensionless concentration, $(\overline{C} - \overline{C}_c)/(\overline{C}_h - \overline{C}_c)$

$\overline{C}$ concentration, $[kg/m^3]$

c_p heat capacity, $[J/kg \cdot K]$

d   burial depth, $[m]$

D   mass diffusivity, $[m^2]$

Da   Darcy number, K/r_i^2

E   energy transfer, $[J]$

g   gravitational acceleration, $[m/s^2]$

h   heat transfer coefficient, $[W/m^2 \cdot K]$

h   gap width of Hele-Shaw cell, $[m]$

J   Jacobian of the coordinate transformation

k   thermal conductivity, $[W/m \cdot K]$

K   permeability, $[m^2]$

$\overline{K}$ hydraulic conductivity, $\rho gK/\mu$, $[m^2]$

Le   Lewis number, α/D

m   mass flow, $[kg/s]$

N   buoyancy ratio, $\beta_C(\overline{C}_h - \overline{C}_c)/\beta_T(T_h - T_c)$

Nu   Nusselt number, hr_i/k_f

p   pressure, $[Pa]$

$\overline{P}$	grid control function in the ξ-direction
Pe	Peclet number, $u_R r_i/\alpha$
Pr	Prandtl number, ν/α
Q	heat transfer, [J]
$\overline{Q}$	grid control function in the η-direction
r	radial direction in polar coordinate, [m]
r_i	radius of buried pipe, [m]
R	dimensionless radial distance
Ra	Rayleigh number, $Kg\beta_T(T_h - T_c)r_i/\alpha\nu$
Sh	Sherwood number, hr_i/D
T	temperature, [K]
t	backfill layer thickness, [m] or time, [s]
u, v, w	Darcy velocity in the x-, y- and z-direction, [m/s]
$\overline{u}, \overline{v}$	average velocity in Hele-Shaw cell, [m/s]
U, V, W	dimensionless velocity in the X-, Y- and Z-direction
u_R	discharged radial velocity from the leakage, [m/s]
w	width of the physical domain, [m]
x, y, z	Cartesian coordinates, [m]
X, Y, Z	dimensionless Cartesian coordinates

Greek Symbol

α	thermal diffusivity of porous medium, $k/(\rho c_p)_f$, [m^2/s]

$\overline{\alpha}, \overline{\beta}, \overline{\gamma}$ coefficients of coordinate transformation

α_{BJ} Beavers and Joseph slip coefficient

β_C coefficient of concentration expansion, $[m^3/kg]$

β_T coefficient of thermal expansion, $[1/K]$

δ allowable error

ϕ porosity of porous medium

Φ field variables such as C, Θ and Ψ

μ dynamic viscosity, $[kg/m{\cdot}s]$

μ_e effective viscosity in Brinkman-Forchheimer-extended Darcy equation, $[m^2/s]$

ν kinematic viscosity, $[m^2/s]$

θ angular direction in polar coordinate

Θ dimensionless temperature, $(T - T_c)/(T_h - T_c)$

ρ density, $[kg/m^3]$

τ dimensionless time

ξ, η body-fitted coordinates

Ψ dimensionless stream function

Ω dimensionless vorticity

Subscript

c   cold surface

f   fluid

h   hot surface

i   index of sublayer

int   interface

pm   porous medium

1   index of inner sublayer

2   index of outer sublayer

Mathematical Symbol

exp( )   exponential function

erfc( )   error function

O( )   order of magnitude

sign( )   sign function operator

∇ gradient operator

$\nabla^2_{\xi\eta}$ Laplacian in body fitted coordinates